



UNIVERSITÀ DEGLI STUDI DI TRIESTE

DIPARTIMENTO DI MATEMATICA E GEOSCIENZE

XXI CYCLE OF THE ITALIAN DOCTORAL RESEARCH PROGRAMME IN

EARTH SCIENCES AND FLUID MECHANICS

DISCIPLINARY SECTOR: GEO/11

Low-frequency Reconstruction Methods for Elastic Parameter Estimation

Author:

Luca BIANCHIN

Luca Bianchin

Coordinator of the Ph.D programme:

Prof. Pierpaolo OMARI

Pierpaolo Omari

Supervisors:

Prof. Michele PIPAN

Michele Pipan

Asst. Prof. Emanuele FORTE

Co-Supervisor:

Vittorio DE TOMASI

Vittorio De Tomasi

ACADEMIC YEAR 2017/2018

UNIVERSITÀ DEGLI STUDI DI TRIESTE

Abstract

Low-frequency Reconstruction Methods for Elastic Parameter Estimation

The thesis aims at discussing new methods for the estimation of the absolute value of subsurface mechanical properties from geophysical data collected at the earth surface. The research was prompted by the problem of estimating the acoustic impedance at depth from post-stack seismic reflection data. The problem is manifold, here the discussion is focused on the reconstruction of the low-frequency components of the acoustic impedance. The proposed solution is the harmonic reconstruction by means of autoregressive and sparsity-based models, with the integration of ancillary information that are typically available as a result of seismic imaging. Such approach is named CARV method, and its application is shown to provide a geologically sound estimate of selected features of the acoustic impedance on high-quality seismic data.

The thesis also analyses the problem of the elastic parameter inversion from multichannel seismic data: the focus is both on the recovery of the missing information at low-frequency, and on solving the indeterminacy of the Amplitude Versus Angle problem when a limited range of incident ray-paths are available. Analogously to the post-stack case, the reconstruction of the low frequency information leads to a recursive estimation of the elastic impedance at the incidence angle the data refer to. Two novel approaches to pre-stack inversion are proposed. Both methods appear theoretically sound on synthetic cases, but due to the poorer Signal to Noise ratio that characterises pre-stack with respect to post-stack data, and to the challenge to properly set geologic constraints at depth on elastic impedance, no definitive success is evidenced on real data.

To solve the pre-stack inversion problem for a set of three mechanical parameters, a priori information on their mutual correlations is required. Regularisation methods from Rock Physics relationships have been investigated to stabilise the Amplitude versus Angle inversion problem, and to evaluate the robustness of the results to the presence of noise in the data. In particular, the effects of the maximum incidence angle, the background Poisson ratio, the degree of correlation between the elastic parameters have been analysed. Such analysis widens the current state of the art on the topic, with potential application in the field of feasibility studies. The novel methods for acoustic and elastic parameter estimation are theoretically discussed, controlled on synthetic scenarios, and validated, where possible, on real marine and land seismic data. An extension of the post-stack inversion approach is attempted on a Ground Penetrating Radar profile recorded over a glacier.

Acknowledgements

I wish to thank all the people who helped me with outstanding patience during the last four years. I thank all who tried to teach geophysics to an engineer. A particular thank goes to Vittorio De Tomasi for his insightful guidance that went far beyond the mere recommendations for the development of the thesis. Mauricio Sacchi deserves a special mention for the enthusiastic personal and professional experience he allowed me within his group at University of Alberta. I am glad of all the conversations I had with him and with all the people in Edmonton. I own a debt of gratitude to my supervisors Michele Pipan and Emanuele Forte for their help. They patiently tutored my research and they really made me progress both personally and professionally. Together with my supervisors, I thank all the people at EGG group, Anna Del Ben, Arianna Mocnik, and Matteo Dossi who shared a lot of their time with me: each of them was a good teacher during these years. I am very grateful to Lorenzo Russo for his recommendations, to all the reviewers, for helping me to understand my own research, and to many others that is impossible to list here. I eventually thank Cristina Ferro for proofreading drafts and for bearing with me for the past four years.

Contents

Abstract	i
Acknowledgements	iii
List of Symbols	ix
1 Introduction	1
1.1 Motivation	1
1.2 Outline	2
1.3 The Inverse Problem	3
1.4 Seismic Data Inversion	3
1.5 Bayesian Inference	6
1.6 State of the Art in Seismic Amplitude Inversion	7
1.7 Factors Affecting Seismic Amplitudes	9
1.8 Controlled-amplitude processing	11
1.8.1 Amplitude Variability in Real Case Scenarios	12
1.8.2 Reference Amplitude	14
2 Deconvolution and Trace Reconstruction	17
2.1 Introduction	17
2.2 The Convolutional model of the seismic trace	17
2.3 Spectral Extension of Band-limited Time Series	18
2.4 Reconstruction of Sparse Time series	19
2.4.1 Linear Programming	19
2.4.2 LASSO	20
2.4.3 Minimum Entropy Deconvolution	21
2.4.4 Total Variation Regularisation	21
2.5 Harmonic interpolation	22
2.5.1 Spectral Estimation	22
2.5.2 The Low-frequency Interpolation Procedure	32
2.5.3 Low-frequency Interpolation Varying the Norm of the Prediction Error	34
2.5.4 Constraints on Impedance at Depth	36
2.5.5 High-frequency Reconstruction by Minimum Entropy Deconvolution	39
2.5.6 Comparison between AR Reconstruction and Sparse-Spike Solution	45
2.5.7 Residual Wavelet Effects	50
2.6 Envelope Inversion	52
2.7 Bayesian Approach to Sparse Inversion	53

3	Acoustic Impedance Estimation from Combined Harmonic Interpolation and Interval Velocity	55
3.1	Introduction	55
3.2	Theory	56
3.3	CARV Method	60
3.3.1	ARMA Models for Noisy Data	60
3.3.2	AR Low Frequency Reconstruction	61
3.3.3	Interval Velocity Field	62
3.3.4	A priori Geologic Constraints	63
3.3.5	Inversion Formulation	64
3.3.6	Inversion with Lateral Continuity	65
3.3.7	Amending the Cost Function with a Lateral Smoothing Term on AI	66
3.3.8	Amending the Cost Function with a Lateral Smoothing Term on the Reflectivity	67
3.3.9	Reflectivity Extension to High Frequency	68
3.4	Results of the CARV inversion	68
3.4.1	Synthetic Examples	69
3.4.2	Real Data	76
3.4.3	Lateral Continuity Enhancement on Real Data	87
3.5	Discussion and Conclusions	89
4	Sparsity-based Approach to Pre-stack Inversion	93
4.1	Introduction	93
4.2	Offset to Angle Mapping	94
4.2.1	Interpolation Solution	95
4.2.2	Stack Solution	95
4.2.3	Weighted Stack Solution	96
4.2.4	Mapping of Synthetic and Real Data	96
4.3	Autoregressive Recovery of Elastic Parameters	100
4.4	Mapping between Constraints on V_p V_s and Density into Constraints on EI	103
4.5	Synthetic Example	104
4.6	Discussion	105
5	Stabilising Effects of Rock Physics Relationships for the Linear AVA Inversion	107
5.1	Introduction	107
5.2	Theory	108
5.3	Method	110
5.4	Results	112
5.5	Discussion and Conclusions	116
6	Acoustic and Elastic Inversion on a Test Land Dataset	119
6.1	Introduction	119
6.2	Seismic Data Pre-conditioning	123
6.3	Post-stack Inversion	131

6.3.1	2D Section	131
6.3.2	3D Inline	134
6.4	Pre-stack Inversion	137
6.5	Discussion	144
7	Acoustic and Elastic Inversion on a Test Marine Dataset	147
7.1	Introduction	147
7.2	Post-stack inversion	151
7.3	Pre-stack inversion	153
7.4	Discussion	158
8	Sparsity-based Inversion of Ground Penetrating Radar Data	161
8.1	Introduction	161
8.2	Work-flow for GPR Data Inversion	162
8.3	Case study: Boulder Clay Glacier	163
8.4	Amplitude Inversion: Work-flow 1	169
8.5	Amplitude Inversion: Work-flow 2	172
8.6	Discussion	173
9	Conclusions	177
9.1	Summary of the Results	177
9.2	Future Work	178
A	Matlab code - Combined AR-velocity inversion of AI	181
A.1	181
	References	189

List of Symbols

<i>AI</i>	Acoustic Impedance
<i>AIC</i>	Akaike Information Criterion
<i>AR</i>	Autoregressive
<i>ARMA</i>	Autoregressive Moving Average
<i>AVA</i>	Amplitude versus Angle
<i>AVO</i>	Amplitude versus Offset
<i>CARV</i>	Combined Autoregressive - Velocity
<i>CAT</i>	Criterion of Autoregressive Transfer
<i>CDP</i>	Common Depth Point
<i>CIG</i>	Common Image Gather
<i>EI</i>	Elastic Impedance
<i>EM</i>	Electromagnetic
<i>FISTA</i>	Fast Iterative Shrinkage-Thresholding Algorithm
<i>FPE</i>	Final Prediction Error
<i>GPR</i>	Ground Penetrating Radar
<i>IRLS</i>	Iterative Reweighted Least Squares
<i>LASSO</i>	Least Absolute Shrinkage and Selection Operator
<i>MA</i>	Moving Average
<i>MUSIC</i>	MULTiple Signal Classification algorithm
<i>NMO</i>	Normal Moveout
<i>PEO</i>	Prediction Error Operator
<i>PSTM</i>	Pre-stack time migration
<i>RMO</i>	Residual Moveout
<i>RMS</i>	Root-Mean-Square
<i>SVD</i>	Singular Value Decomposition
<i>S/N</i>	Signal-to-Noise ratio
$t - x$	Traveltime - offset
<i>TOC</i>	Total Organic Carbon
<i>TWT</i>	Two-way travel time
$\tau - q$	Intercept time - curvature

Chapter 1

Introduction

1.1 Motivation

The estimation of the subsurface elastic parameters with high spatial and temporal resolution over large areas is a problem that can hardly find a direct solution due to the limited nature of the data collected during geophysical surveys. It is a problem of paramount importance for oil and gas exploration as well as for scientific purposes, because it would provide both the trend and a certain degree of detail on the distribution of physical properties in the subsurface. Inverse modelling tries to answer to this problem by proposing acceptable explanations for the distribution of the recorded data. One of the most emblematic examples in this sense is the estimation of acoustic impedance (AI) at depth. AI could be linked to the presence of organic carbon in source rocks (see Figure 1.1) and for this reason it plays an important role in oil and gas exploration. Contrasts of AI are exactly what is needed to generate seismic reflection records but the AI at depth is something which is not currently estimated from seismic data alone. Although there are recent attempts to move seismic acquisition toward low frequencies (Wehner and Landrø, 2017), the trend of elastic parameters is something which has never been measured with the desired accuracy. In fact, the subsurface truth in this context is only known by the sparse spatial sampling due to the presence of well logs or by the low resolution investigation brought about by the natural occurrence of earthquakes. A partial exception is represented by the travel-time tomography which allows to obtain relatively higher resolution estimates of the wave-field propagation velocity in the subsurface (i.e. see Figure 1.3).

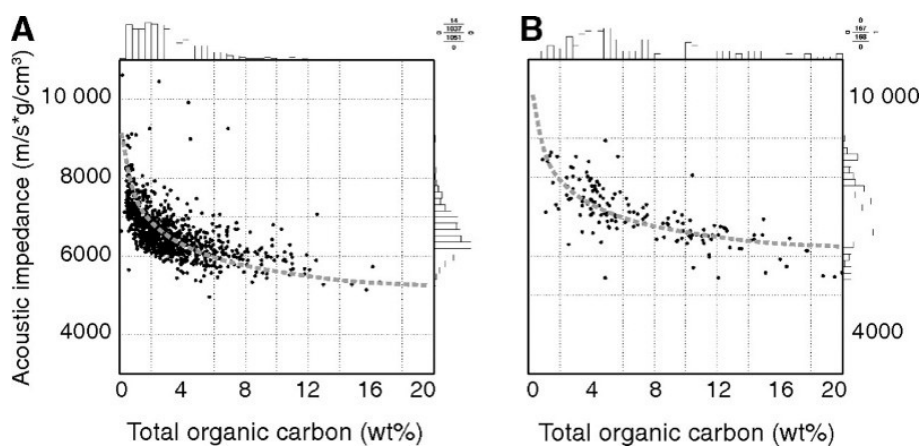


FIGURE 1.1: Examples from Kimmeridge Clay and Ekkingen Formation well data showing the correlation between the acoustic impedance and the total organic carbon (TOC) in source rocks (from Loseth et al. (2011)).

A large number of reconstruction algorithms exist to date to estimate the subsurface elastic properties, but very few of them use only the information collected at the surface (reflection seismic data only) because the problem is poorly posed and the seismic amplitudes are not always reliable indicators of the acoustic reflectivity. Although using only the data collected on the surface appears a daunting task, the thesis will review the methods developed to date for this purpose, it will discuss the issue of amplitude inversion on seismic and Ground Penetrating Radar data, and it will provide new insights for estimating

- the acoustic impedance,
- the p-wave velocity, the s-wave velocity and the bulk density,
- the electromagnetic permittivity

of the subsurface from properly conditioning the recorded time series. The final aim of the work is to develop reconstruction approaches that lead to sensible estimates of the subsurface interval properties from wavefield recorded at the earth surface.

1.2 Outline

The thesis first introduces the problem of amplitude inversion of wavefield-based geophysical data from discrete time-series (reflection seismics and Ground Penetrating Radar). Once the problem is posed with adequate detail in Chapter 1, I describe some theoretical aspects about spectral estimation, regularization and reconstruction with sparsity constraints that are used throughout the research (Chapter 2). In Chapter 2, elements of novelty with respect to the existing literature are related to the comparison between harmonic and sparse-spike reconstructions as well as to the comparison among different spectral estimators that are used for the harmonic reconstruction.

Three main topics are then discussed in the thesis.

I detail in Chapter 3 a novel approach to harmonic interpolation on post-stack seismic traces, which I call Combined Autoregressive-Velocity (CARV) method, giving application to both synthetic examples and real data.

I then approach the elastic information contained on multichannel seismic data. I first describe the issues related to data pre-conditioning, with particular reference to the issue of offset-to-angle mapping, and then I use harmonic extrapolation and sparsity constraints to obtain an estimate of the elastic parameters at depth in Chapter 4. The results of such approach are presented on synthetic scenarios first, and then, together with the CARV method, on a marine and a land seismic dataset in Chapter 6 and 7 respectively.

The elastic parameter estimation from pre-stack gathers opens another main topic addressed by this research, namely the stability of the amplitude versus angle (AVA) inversion problem. I perform an analysis of the effects of Rock Physics regularisation on the three-terms linearised AVA problem in Chapter 5.

The post-stack approaches are eventually attempted on Ground Penetrating Radar (GPR) data and the reconstruction on a low-dispersion medium is discussed with reference to a case-study on an Antarctica glacier (Chapter 8). The MATLAB code of the post-stack harmonic interpolation inversion method concludes the dissertation.

TABLE 1.1: Summary of the topics discussed in the thesis with a brief description for each Chapter.

Chapter	Description of the Research
Chapter 1	Introduction of the research problem.
Chapter 2	Review of autoregressive and sparsity-based methods for seismic trace reconstruction.
Chapter 3	Description and test of the CARV reconstruction method.
Chapter 4	Description and test of the pre-stack AR and sparse-spike reconstruction of seismic data.
Chapter 5	Analysis of the stability of the linearised AVA inversion.
Chapter 6	Test of the CARV and pre-stack inversion methods on a seismic land dataset.
Chapter 7	Test of the CARV and pre-stack inversion methods on a seismic marine dataset.
Chapter 8	Test of sparsity-based methods for GPR data inversion.
Chapter 9	Conclusions and discussion on the work ahead.

1.3 The Inverse Problem

The main concern of this thesis is the development of methods that allow to infer information on the physical properties of media from records of various wave-fields (seismic and GPR data) propagating through them. The mathematical theory of inverse problems for geophysical application is beyond the scope of this work as many influential authors (i.e. Tarantola (1984), Scales (1985)) have already discussed the topic in detail. Nonetheless, it is worth defining the vocabulary that is used later in the text.

Following Tarantola (2005), the forward problem consists on the simulation of the records when the model and the physical laws that relate the model to the records are assumed to be known. The inverse problem, on the other hand, is the process of model estimation from recorded data. This is indeed a prediction problem because the recorded data are affected by noise and the adopted physical governing law is also valid up to a certain degree of approximation. Geophysical data provide the input for discrete inverse problems with a finite number of observations and a finite number of model parameters to be estimated. Despite this apparent limitation, the resulting inverse problem has infinite solutions because the data partially describe the features of interest and they are always affected by noise. The latter fact prevents from obtaining an exact solution even when the illumination of the target is adequate. In this case, infinite approximate solutions can be devised (Menke, 1989).

1.4 Seismic Data Inversion

Seismic reflection data, in the context of this thesis, are thought as the record of the particle velocity or displacement (u) at a limited number of point locations of a wave propagating in an elastic medium. From this assumption it is straightforward to think about the underlying model that explains the data in terms of the Lamé parameters (λ, μ), and the bulk density (ρ). The wave-field propagation in an isotropic medium is described by the partial differential equation

$$\rho \frac{\partial^2 u(t, x, y, z)}{\partial t^2} = (\lambda + \mu) \nabla (\nabla \cdot u(t, x, y, z)) + \mu \nabla^2 u(t, x, y, z) + s(t, x, y, z). \quad (1.1)$$

In equation 1.1, t represents the time, and $s(t, x, y, z)$ the source perturbation at the location described by the coordinates x , y , and z . Tarantola (1984) provides a mean to fully invert the acoustic approximation of equation 1.1 for the p-wave velocity ($\sqrt{\frac{\lambda+2\mu}{\rho}}$) and the density. I focus throughout this thesis on a simpler problem: that of inverting the amplitudes of plane waves at elastic interfaces as described by the Zoeppritz (1919) equations. Although not discussed in the thesis, seismic inversion may also mean to infer a vast number of petrophysical parameters other than the elastic ones from seismic data and well logs. It is worth noting that this process involves two different kinds of inversion even when it is performed in one-stage only. Mechanical parameters of the subsurface are firstly estimated from seismic data through wave equation modelling. A further inversion, which is governed by Rock Physics relationships derived from upscaling well log information, allows to estimate petrophysical properties such as porosity, water saturation, or permeability, from the mechanical parameters and the a priori geologic knowledge of the target of interest.

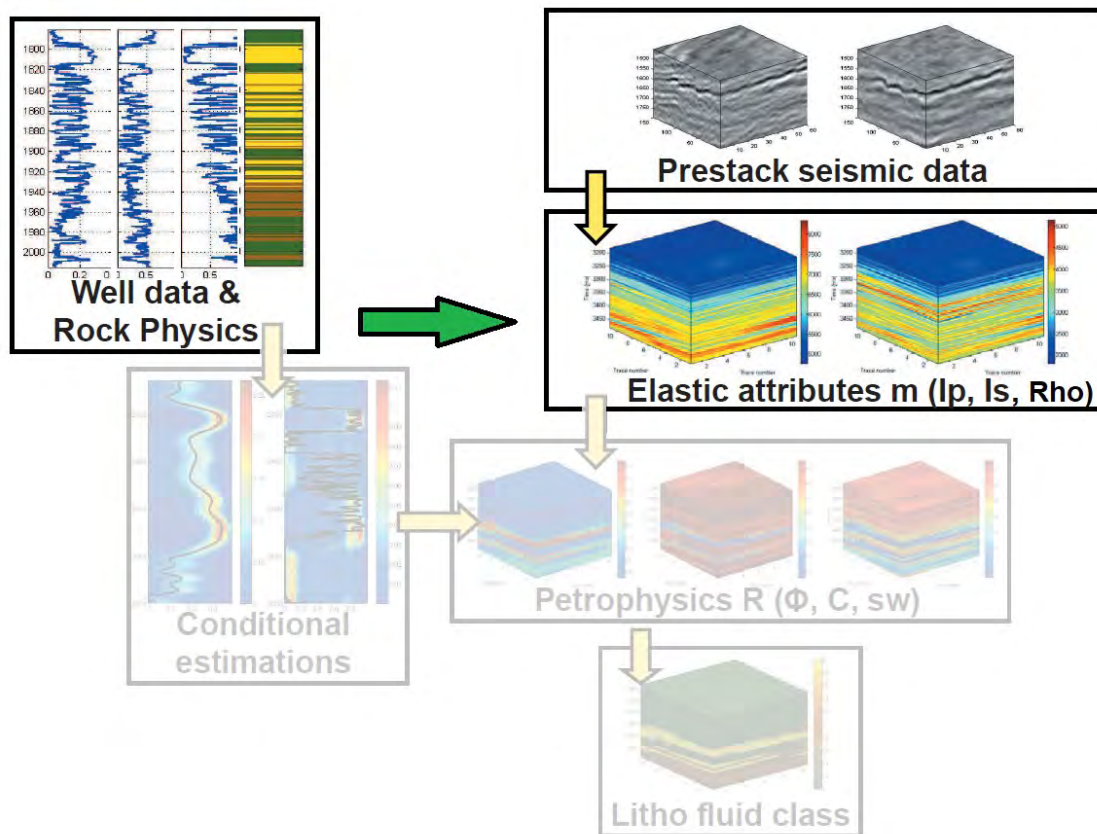


FIGURE 1.2: *Seismic data inversion conceptual scheme. Modified from Grana and Della Rossa (2010). The present work focuses on the recovery of elastic properties of the subsurface, which, in turn, prompt to infer petrophysical properties. Rock-physics relationships together with borehole logs can be used as ancillary information to estimate the elastic attributes and to calibrate the petrophysical property model.*

A first classification of the different kinds of seismic inversion may account for the data domain in which the inversion is performed:

- Pre-Stack inversion
- Post-Stack inversion.

In the pre-stack case, data are available at multiple incidence angles and this allows to estimate a model that includes elastic parameters, density, and, potentially, anisotropic features. In the post-stack domain (normal incidence reflectivity), the experiment allows to estimate the property of acoustic impedance.

Seismic inversion can also be categorized by the wave equation approximation adopted. The approaches in this case are the:

- Inversion focused on the kinematic aspect of seismic data
- Inversion focused on the dynamic aspect of seismic data
- Full-waveform inversion

The kinematic aspect refers to the arrival time of seismic wavefronts in a low-dispersive medium (phase information is picked and inverted to recover the propagation velocity). The kinematic approach is based on the Eikonal equation and it is commonly known as travel-time inversion or tomography. The present thesis focuses on the dynamic aspect of the data, in other words, on the inversion of seismic waveform amplitudes to obtain the model of the elastic parameters that may describe the data. The intrinsic attenuation of the materials investigated by the wave-field is the additional information that could be recovered by the dynamic aspect of the seismograms, but this additional piece of information has not been considered in the thesis. The kinematic and the dynamic aspects of data are associated with two different spectral characteristics of the seismic data: the phase information (kinematics) allows to reconstruct low frequency estimates, while the amplitude information (dynamics) allows to reconstruct a much higher frequency content (see Figure 1.3). Those two approaches are separated by a spectral range that is often difficult to extract from the data.

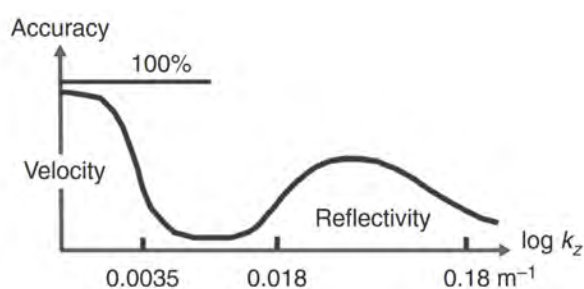


FIGURE 1.3: Extraction percentage of vertical model variation as a function of the vertical component of the seismic wavenumber vector. Figure taken from Virieux et al. (2017) after Claerbout (1985).

Finally, for the importance it has assumed in the past decade, it is worth hinting at the full-waveform inversion methods, which try to bridge the gap between the two above mentioned approaches. They consider the full seismic traces (not only picks or deconvolved amplitudes) trying to maximise the information extracted from seismic records. They basically compare the seismic response of a modelled subsurface to the recorded data. By minimising the misfit between the modelled and the recorded data, the subsurface elastic properties are then estimate. The drawback in this case is the computational cost and the non linearity of the optimisation process, which could lead to a local minimum solution. Low-frequency components are noisy

on the observed data of a reflection experiment, such that the method requires a starting background model to converge towards a global optimum solution. The actual meaning of ‘low-frequency components’ depends on the dataset analysed and on the purposes of the inversion. The low-frequencies represent the components of the spectrum that show a poor S/N such as they cannot be taken into account for the inversion because they only degrade the result. This general definition of low-frequency is used throughout the thesis, while dataset-specific ranges are provided where relevant. It is also worth noting the angle-dependency on the spatial low-wavenumber components of the data when a non-zero offset survey is performed (Virieux and Operto, 2009). This dependency is summarised in equation 1.2, where \mathbf{k} represents the vector of spatial wavenumber, f represents the frequency bandwidth of the signal, c represents the propagation velocity, θ represents the incidence angle and \mathbf{n} is a versor in the direction of the wave propagation:

$$\mathbf{k} = \frac{2f}{c} \cos\left(\frac{\theta}{2}\right) \mathbf{n}. \quad (1.2)$$

Equation 1.2 indicates that a transmission experiment ($\theta = 180^\circ$) theoretically contains the information on the DC component ($\mathbf{k} = 0$) of the object of interest, while a normal-incidence reflection experiment ($\theta = 0^\circ$) only investigates the medium within the source bandwidth.

Another relevant difference among the inversion methods lies in the nature of the results that they provide. In this respect it is possible to distinguish between:

- Deterministic inversion
- Probabilistic inversion.

In the first case the lack of information available from the data is filled in such a way that a unique model is extracted from the data. This is only one of the infinite models that are compatible with the data and the solution may be useful as long as all the assumptions suit the subsurface truth and the user is aware of the assumptions role. On the contrary, the probabilistic inversion produces a probability distribution in the space of the feasible inverted models, it therefore provides a way to assess the uncertainty of the result. The latter approach appears desirable as it provides an estimation of the risk associated with the model prediction, but it is more computationally expensive (i.e. the current literature about Full Waveform Inversion deals with deterministic results only). One must also be aware that the risk associated with one estimate always holds a dependency on the a priori assumptions which are required to obtain the estimate itself.

1.5 Bayesian Inference

Bayes’ theory of probability provides a framework for probabilistic inversion and it is commonly adopted for geophysical problems (Ulrych, Sacchi, and Woodbury, 2001). In this context, the probability of a model given the recorded data is related to the likelihood of the data to the model $p(d|m)$ and to the a priori model $p(m)$:

$$p(m|d) = \frac{p(d|m)p(m)}{p(d)} \propto p(d|m)p(m). \quad (1.3)$$

Ulrych, Sacchi, and Woodbury (2001) point out that the a priori model must be less informative as possible in order to limit the bias introduced by discretionary assumptions. Gaussian priors, based on the central limit theorem, are often used because they allow an analytical linear solution for the distribution of the inverse models (most probable model expressed by the mean model and uncertainty expressed by the covariance matrix). Other priors may be used to better describe the state of knowledge on the physical process, to obtain sparser (i.e. Cauchy distribution (Sacchi, 1997)), or other favourite features in the inverted model. The posterior distribution of the model given the data can be estimated by Montecarlo sampling in these cases.

1.6 State of the Art in Seismic Amplitude Inversion

I follow the works of Veeken and Da Silva (2004) and Russell (1988) to describe some of the best practices developed for the purpose of seismic data inversion. The classification of seismic inversion methods provided by Russell (1988) distinguishes among:

- Recursive inversion
- Model-based inversion
- Sparse-spike inversion
- Amplitude versus offset inversion
- Travel-time inversion
- Migration

While the last two topics are broad subjects by themselves and they are not discussed here, the first four points can be grouped under the umbrella term of *amplitude-based inversion* and they will be the focus of the thesis.

The recursive inversion, based on the weak contrast approximation introduced by Peterson, Phillipone, and Coker (1955), integrates the interface property of reflectivity (r_i) into the acoustic impedance $AI(t)$ for a continuous earth model and normal incidence:

$$AI(t) = AI(t_0)e^{2\sum_{i=1}^t r_i}. \quad (1.4)$$

The knowledge of a reference value $AI(t_0)$ at time t_0 , and the summation proposed in equation 1.4 on properly conditioned seismic data leads to a band-limited version of the AI (or of any other elastic parameter of interest). This method requires a background model to estimate the absolute value of the AI. The background model may be derived by spatially extending well log information along selected horizons (Morozov and Ma, 2009).

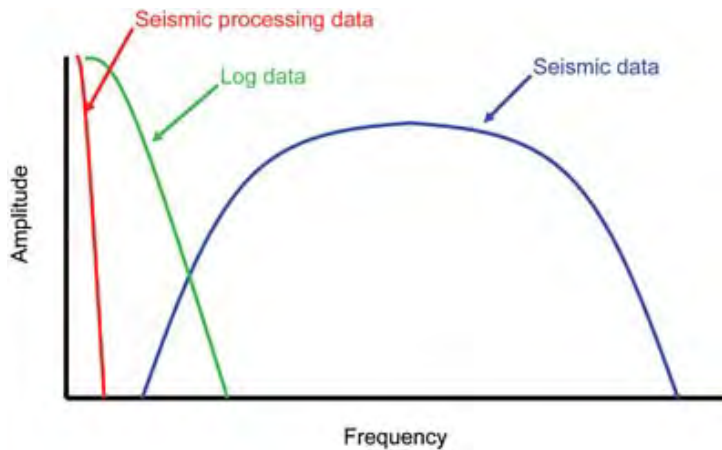


FIGURE 1.4: Typical spectral distribution of the information available to build a subsurface elastic model. Seismic processing data provide info on the largest scale features of the subsurface investigated through velocity analysis. Figure taken from Cerney and Bartel (2007).

The early attempts of seismic data inversion (Lindseth, 1979) tried to add the acoustic impedance trend to the recursive inversion by using the information contained in the sonic logs together with an assumption on the bulk density at depth. Following Veeken and Da Silva (2004) five steps may be singled out for the typical recursive inversion:

- Pre-conditioning the input data
- Seismic to well tie
- Zero-phasing on the target area and extraction of the seismic wavelet
- Running the inversion algorithm (by accounting for the low frequency if a full-band estimate is sought)
- Interpretation of the results and, in unsatisfactory cases, re-considering the parameters adopted during the process.

The model-based inversion assumes to know the mathematical relationship between the model and the data and, by an updating criterion, it minimises the differences between the forward modelled seismic section and the recorded data. The generalized linear inversion (GLI) method proposed by Cooke and Schneider (1983) allows to iteratively find an optimum solution, but the model thus obtained is accurate only if the initial model is close enough to the subsurface truth. A way to overcome the limitations imposed by the linear approach is provided by Veeken et al. (2009). They proposed a non-linear multi-trace inverse approach for obtaining the acoustic impedance and other elastic properties based on a genetic algorithm. The algorithm is first trained on seismic data that have a well log control and then it predicts the elastic property across a seismic volume. Local minima may be overcome by introducing a mutation step. This method also requires the extension of a low-frequency model calibrated on well logs to the whole volume investigated by the seismic experiment.

Sparse-spike and harmonic inversion are the methods that are more extensively considered in this thesis and a review of several approaches based on sparseness of the reflectivity is presented in Chapter 2. By assuming that the seismic reflectivity is sparse in time domain, a full

bandwidth AI model can be reconstructed even from band-limited data. The resulting models show a limited number of layers, consistently with the recorded data. O'Doerthy and Anstey (1974) observed that the sparse-spike method requires all the reflection coefficient magnitudes to be correct in order to obtain sensible estimates at depth when no further constraints are set. Lancaster and Whitcombe (2005) developed a further approach to amplitude inversion that they called *Coloured Inversion*. Their method makes use of a convolutional filter obtained from matching the amplitude and phase spectra of the reflectivity derived from well logs to the amplitude and the phase of the average seismic records around well location. The convolutional filter is limited in band to the frequencies pertaining to the seismic signal in order to avoid noise boosting. For this reason the result does not represent a full-bandwidth estimate of the elastic parameters and it is rather a mean to perform a band-limited deconvolution. The relevance of the method lays in the calibration of the seismic (no seismic wavelet estimation is required) to the log information and in its reduced computational cost.

Amplitude versus Offset (AVO) and Amplitude versus Angle (AVA) inversion are also considered in the present thesis (see Chapter 4). Those two methods allow to qualitatively single out the presence of anomalies related to possible hydrocarbon accumulations in the first case, and to infer the elastic properties of the subsurface in the second case (Sun et al., 2015).

Whilst the description of the practices typically adopted for inversion in the seismic industry does not add much scientific insight to the elastic property estimation problem, it provides a starting point for the analysis developed in the following chapters and a benchmark to evaluate the benefits and the drawbacks of the methods studied against the solutions currently adopted. The sources for this description consist on the UK Oil and Gas report for the reprocessing of several 2D lines in the Rockall Through area (see Chapter 3) and on the user guide of the OpendTect and Hampson-Russell Software. The more common approach to acoustic and elastic parameter inversion is the model-based inversion. Processed seismic data are typically matched to the reflectivity that can be obtained from an edited version of the available well logs. This process extracts a seismic wavelet by iteratively editing well logs and by stretching and squeezing a statistically extracted wavelet. Missing parts of density and shear logs are often reconstructed from sonic and background geologic information. Seismic inversion is then performed within two user-defined frequency ranges. The ranges are iteratively selected by looking at log matches at well locations. A low-frequency model is adopted to obtain an estimate of the absolute value of the elastic property. This model is extracted from well logs and extended in between well locations following user-picked horizons. Finally a matching filter merges the low frequency model and the band-limited inversion. Lateral continuity may also be enhanced in the inversion: this is done by re-scaling the trace amplitudes or by other multichannel filters at the expenses of increasing the data misfit. In the case of three-terms pre-stack inversion, a rock physics term estimated from well logs, is often introduced to solve the ambiguity between the inverted elastic parameters.

1.7 Factors Affecting Seismic Amplitudes

Before describing the inversion techniques studied in the thesis in more detail, I briefly review the factors affecting the seismic amplitude. For a more detailed analysis on the amplitude

characteristics of the GPR dataset the reader is referred to Chapter 8.

Many different physical phenomena influence the amplitude of the time series that constitute the seismic traces. A partial list of them can be found in Muerdter and Ratcliff (2001) or in Sheriff (1975) and it can be further expanded to include:

- Geometrical spreading
- Transmission losses
- Viscoelastic attenuation
- Scattering
- Interface geometry (focusing / illumination problems)
- Interference
- Multiple energy
- Source-receiver directionality
- Dip of the reflectors
- Environmental and instrumental noise
- Seismic data processing artefacts
- Mode conversion
- Anisotropy
- Contrast of elastic and density properties at plane interfaces.

All these aspects affect the amplitudes of the seismic trace, but only the latter one, namely the contrast of elastic and density properties at plane interfaces is what the physical relationships for the inverse modelling look after, in the present thesis. The other factors should be accounted for in the pre-processing steps and removed, minimised, or compensated when possible. Some effects such as anisotropy and mode conversion are neglected in this thesis as they often produce minor effects on seismic amplitudes.

The issue of source directionality is more concerning for land seismic surveys rather than for marine datasets in which a far-field wavelet can be easily recorded at different spatial positions, but the current practice to use arrays of sources and receivers in land seismic surveys allows to attenuate this problem to a great extent.

Illumination is a relevant issue in terms of determining the amplitude of the seismic events, being the dips of the event and the overlying heterogeneities the most important factors to cause amplitude variations. Below salt lenses or gas reservoirs the amplitudes of the events are strongly influenced by focusing and de-focusing of ray-paths (Sheriff, 1975). Events which are particularly steep are sampled with less reflection points per unit of length so they appear weaker with respect to sub-horizontal ones because the source and the receiver lay on a near horizontal plane.

Balancing transmission losses, viscoelastic attenuation, energy losses due to scattering, geometrical spreading and interference is the aim of seismic processing.

1.8 Controlled-amplitude processing

Field seismic data must undergo a controlled-amplitude processing sequence before any inversion attempt could be approached. The term *controlled-amplitude processing* was introduced by Yu (1985): it represents a category of seismic processing workflows rather than a well-defined series of steps to obtain the best dataset for seismic inversion. This is because each of the inversion methods described in section 1.6 requires different care during data pre-conditioning and imaging. The typical controlled-amplitude workflow includes

- trace editing,
- spherical correction,
- band-pass filtering and coherent noise attenuation,
- statics,
- wavel de-signature,
- velocity analysis,
- multiple energy suppression,
- migration,
- attenuation compensation and offset balancing,

but it should not include window-dependent scalars, multi-trace equalisation processes that are not surface consistent, and migration algorithms that are not formulated in an amplitude-preserving fashion. Depending on whether land or marine seismic data are considered, differences arise. In the land case, array directivity correction (Mazzotti and Ravagnan, 1995) must be considered, while for marine data the attenuation of residual moveout energy is of paramount importance. Processing assumptions lead to a certain degree of inaccuracy, especially regarding the time-depth conversion for the subsequent geometrical spreading correction. For this reason such correction is often performed by applying a theoretically sound scaling factor proportional to the square power of the TWT (Yilmaz, 2001). The compensation of seismic attenuation and dispersion is also a critical step, being the overburden characteristics not accurately available. Any controlled-amplitude processing sequence must pay particular attention to the migration algorithm: pre-stack migration is required to correctly place seismic events, but it should also preserve the amplitude content of the seismic events. The details of the migration implementation play the most important role in achieving both objectives (Simm and Bacon, 2014). For AVA analysis $f - x$ deconvolution (e.g. Mazzotti and Ravagnan (1995)) and incoherent noise attenuation via rank reduction in common offset domain could be used to improve the S/N of the pre-stack gathers. Spectral equalisation to attenuate the moveout stretching, and data registration are routinely performed. When well log data are available, offset balancing based on a modelled response of the subsurface interface is also performed on seismic data.

1.8.1 Amplitude Variability in Real Case Scenarios

In order to provide a measure of the amount of amplitude variability across seismic traces I present some statistics on two different seismic data-set that have undergone a processing sequence. A similar quality control test is proposed on GPR data in Chapter 8. The first case of study is a pre-stack inline of a 3-D land data-set provided by Eni. Data have been processed for the purposes of AVO analysis as detailed in Chapter 6. The quality control on amplitudes is performed on 1000 traces and it shows a standard deviation of the amplitudes after a polynomial trend removal (bottom panel of Figure 1.5) of the order of 10% of the average amplitude. This result is compatible with high spatial frequency heterogeneities of geologic relevance across the selected event. Of course, the geologic setting should also be carefully considered when assessing how genuine the seismic amplitudes are: an interface between a shale and a highly fractured carbonate is expected to show higher lateral amplitude variation than an interface between the same shale and a tighter carbonate. More problematic appears the channel to channel variability presented in Figure 1.6 for the pre-stack inversion. Near channels record less energy and some unrealistically high amplitude channels are visible across the inline selection.

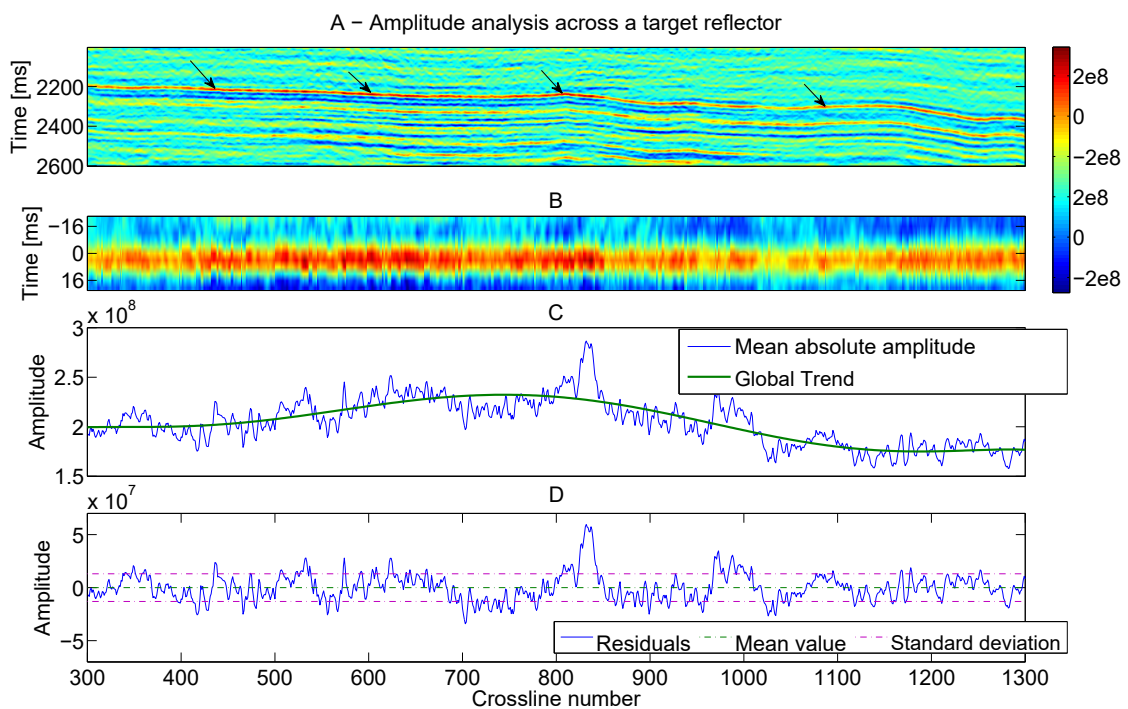


FIGURE 1.5: Analysis of the amplitude variability on Eni land data. Post-stack amplitude analysis across the event evidenced by the black arrows in panel A. A 40 ms window centred on the peak of the event is displayed in panel B, while in panel C the peak amplitude and a low frequency trend is displayed across traces. Panel D shows the amplitude residuals of panel C after the trend removal with a measure of their variability provided by the sample standard deviation in purple.

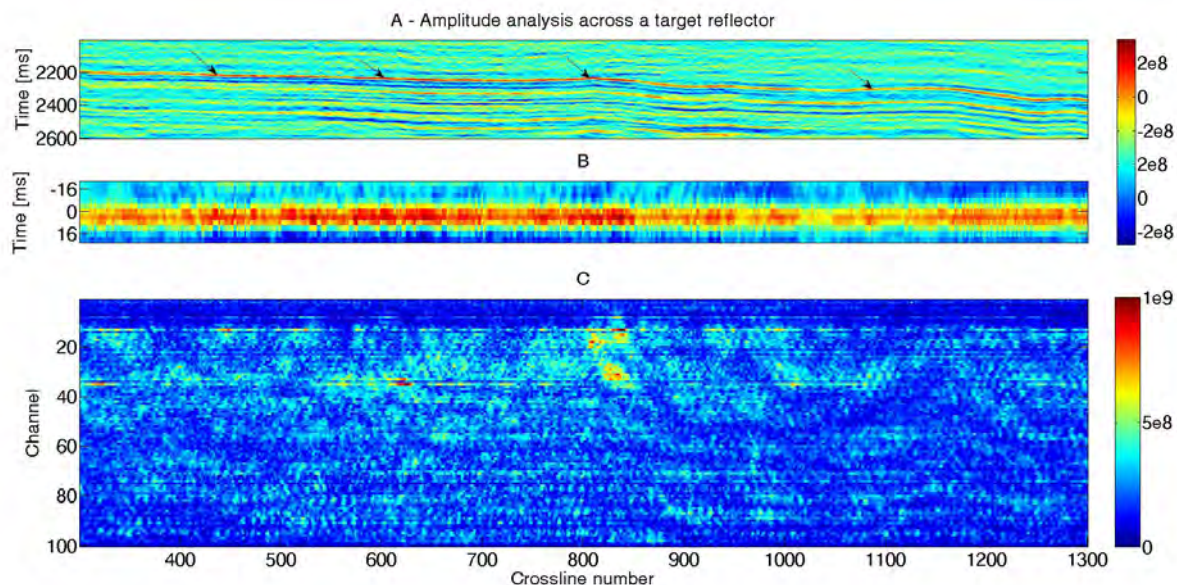


FIGURE 1.6: *Analysis of the amplitude variability on Eni land data. Multi-offset amplitude analysis across the event evidenced by the black arrows in the stack of panel A. A 40 ms time window is displayed around the main reflector in panel B. Strong amplitude variability from channel to channel on the sum of the envelope in the 40 ms across the target reflector is evidenced in panel C.*

In case an amplitude versus angle (AVA) analysis has to be performed on the dataset, a near channel mute and some kind of equalization across common image gathers appears highly desirable before running any inversion algorithm on the data, even if AVA inversion is robust to the random presence of outliers.

The second dataset analysed is a portion of a 2-D marine line from the UK Oil and Gas Authority in the Rockall Trough area. Data are processed for the specific purpose of AI inversion. Details on the dataset can be found in Chapter 3. The amplitude variation, represented by the standard deviation of the residuals of a low-frequency trend (Panel D in Figure 1.7) reaches the 20% in this case, with a maximum amplitude of the traces ranging from 5000 to 2000 in a hundred trace length. This amount of amplitude variability appears of difficult explanation on a geological basis only, unless the presence of thin volcanic lenses is invoked.

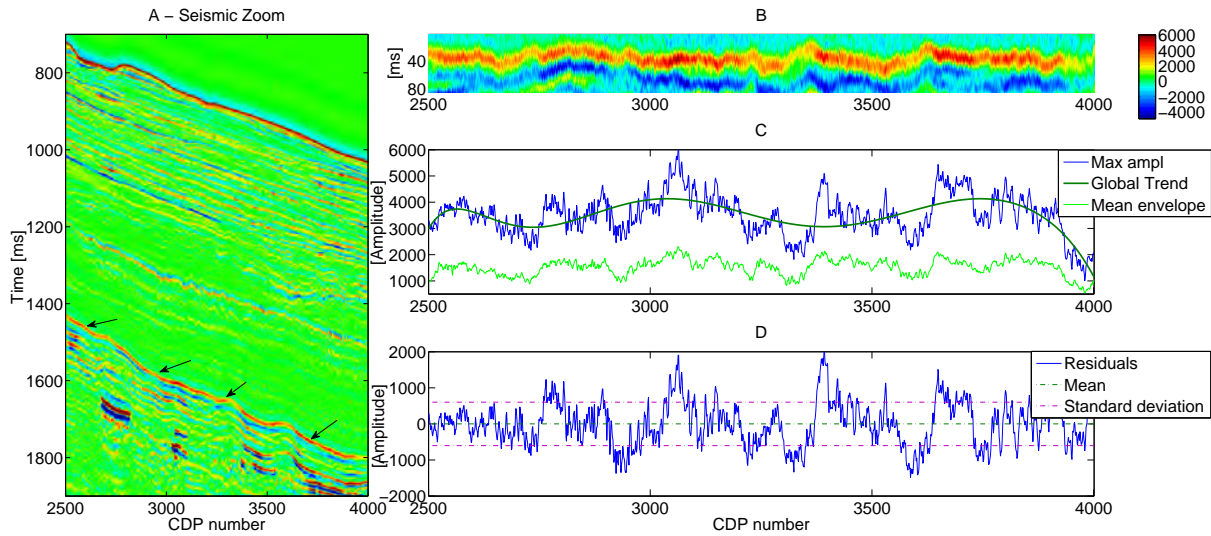


FIGURE 1.7: Amplitude analysis across the target reflector highlighted by the black arrows in panel A. A 21-samples interval across the picked horizon is displayed in panel B, while panels C and D provide a measure of the lateral variability of the peak amplitude. The envelope peak amplitude is smoother than the positive peak amplitude, possibly indicating a differential phase rotation across traces.

1.8.2 Reference Amplitude

I finally describe a typical problem that a seismic inversion process deals with. Seismic records are measurements of particle displacement, velocity or acceleration and they are not direct measurements of reflectivity. For this reason amplitudes after processing can be considered at best a scaled version of the subsurface reflectivity and they need calibration to represent actual reflectivity values. The traditional approach to calibration consists on obtaining a seismic wavelet from well logs. Tying seismic data to well logs can be performed best when a checkshot is available. If the checkshot is not available, the sonic log can be used for the time-to depth conversion of the seismic data. Sonic and density logs can be combined to generate an AI time series. Editing this time series is crucial before matching the seismic data to it. Blocking the well logs by assigning a single value to the depth interval that displays even features in the log is a common practice to reduce high frequency noise and outliers. A blocking interval closer to seismic data sampling interval is usually selected (Herron, 2014). Well logs are then transformed into reflectivity by a differentiation operation, and convolved with the seismic wavelet extracted at specific events. After such processing, log data are ready to be compared with seismic amplitudes and hence used to calibrate the amplitudes of the seismic survey. Sometimes local scalars for single traces are subsequently used to adjust for source, receiver or offset bias (trace balance). Surface consistent deconvolution (Levin, 1989) and the adoption of different wavelets for different angles stacks are the most popular choices for performing such adjustments.

An alternative and rough calibration can be performed on a statistical basis if the impedance at two different depths is known or estimated across a large number of traces. This requires the source and the receiver signature knowledge. Even if the preliminary data processing applied is controlled-amplitude, inaccurate spherical divergence correction and incorrect recovery of

attenuation for transmission losses and dispersion may lead to biased amplitudes. For these reasons the statistical estimation of a global scalar can only be considered as a last resort method to transform records into a bandlimited estimate of the reflectivity.

Chapter 2

Deconvolution and Trace Reconstruction

2.1 Introduction

An overview of the methods for the bandwidth extension of seismic and GPR data is provided in this Chapter. The convolutional model of the seismic trace at the basis of all the discussed methods is first presented, then a review of the sparsity-based methods available in the relevant literature is proposed. The harmonic interpolation method is discussed with particular detail as elements of novelty with respect to the published works on the topic are presented. In particular the model order selection, the signal bandwidth selection, the spectral technique selection, and the regularisation approach to introduce constraints in the harmonic reconstruction represent elements of novelty. Section 2.4.3 and 2.5 are at the basis of the discussion of Chapter 3, while section 2.4.2 is also of paramount importance for the methods proposed in Chapters 4 and 8. This Chapter concludes with an overview on the probabilistic approach to sparsity-based trace reconstruction.

2.2 The Convulsive model of the seismic trace

The convolutional model of the seismic trace (Robinson, 1954) provides the means for a relevant 1-D simplification of the physical law that relates the subsurface model parameters to the recorded data (Sayers and Chopra, 2009). In case of small lateral variations and of weak contrast approximation, the convolutional model can still provide sensible results and it greatly reduces the computational cost of any analysis with respect of considering the full wave equation 1.1. The convolutional model assumes that the processed seismic trace d_t can be expressed as:

$$d_t = w_t * r_t + n_t \quad (2.1)$$

where w_t is a stationary seismic wavelet, r_t is the reflectivity series providing information on the subsurface features of interest, and n_t is the additive noise which includes all the features of the data that cannot be ascribed to the previous two terms. Seismic data need to undergo a de-convolution process to provide an estimate of the band-limited version of the reflectivity that could be used for the bandwidth extension methods discussed by the thesis. There are two different approaches to deconvolution depending on the data availability:

- Deterministic deconvolution: an estimate of the wavelet is available (calibrated well logs are needed for accurate estimates)
- Blind deconvolution: the wavelet is statistically estimated from the data

I do not discuss in the present thesis the topic of seismic to well tie, although some hints regarding coloured inversion and the reference amplitude are given in Chapter 1. The focus of my investigation are the inversion methods based on surface seismic records only. Blind deconvolution methods will be used for spectral balancing and they will be investigated for frequency interpolation. If the time-domain representation of the reflectivity can be considered random (Walden and Hosken, 1985), the amplitude spectrum of the signal should be a scaled version of the amplitude spectrum of the wavelet. Random reflectivity, together with the knowledge or estimate of the noise variance and an assumption on the wavelet phase, are at the basis of Wiener filters applied in both spiking and predictive deconvolution. Those are blind deconvolution processes, however, they should not be used for reconstructing the low and high frequency part of the spectrum because of the unavoidable boosting of the frequency components with poor S/N when the spectral whitening is performed. Only methods that fit a model on the frequency band where the S/N is more favourable and then extend the model to spectral components with a poorer S/N may succeed in providing quantitatively sound estimates of the full-bandwidth of reflectivity.

Wiggins (1978) was the first to propose a blind deconvolution algorithm based on the minimisation of the entropy of the data. The entropy, in the context of signal processing, is a measure of the simplicity of the recorded time-series, which can be implemented by the minimisation of an adequate norm. He chose, as norm, the sum of the second power of the data normalised by their variance. Ooe and Ulrych (1979) introduced an exponential transform to the data before calculating the norm, aiming at enhancing the sparsity of the reconstructed reflectivity. Blind deconvolution can also be obtained via a principal component analysis approach (Kaplan, 2002) or via the analysis of different order statistics to estimate the amplitude and the phase of the reflectivity (Van der Baan and Pham, 2008). Within the convolutional model, as Russell (1988) pointed out, the deconvolution and inversion norm that provides the best results in terms of subsurface truth further depends on the properties of the reflectivity and those of the wavelet.

The wavelet is assumed to be stationary throughout the thesis: a short enough time and spatial data window may always meet the hypothesis of stationarity when the wave-field travels through a low-dispersion medium.

2.3 Spectral Extension of Band-limited Time Series

In the following sections I discuss several methods that have been proposed for extending the spectral content of recorded seismic time-series. It is worth stressing the point that if no information outside the signal bandwidth is available, infinite reconstructions are potentially acceptable. Even though I restrict my research to reconstructions that have a definite structure, the reader must be aware that unpredictable components of the signal outside the recorded

bandwidth may be present or even dominant in the actual subsurface but not in the reconstruction. The convolutional model suggests a way to single out the effects of the earth reflectivity from those related to the wavelet on the recorded data. Oldenburg, Scheuer, and Levy (1983) discuss another characteristic of the reflectivity within this model, stating that the earth can be adequately represented by a sequence of homogeneous layers in specific geological settings. This leads to the assumption that the reflectivity is sparse in time domain. Sparsity, or similarly the assumption that the relevant reflectors are limited in number, leads to the reconstruction variants that are discussed in this thesis such as:

- Sparse-spike reconstruction of the reflectivity
- Minimum entropy deconvolution
- Minimisation of the total variation of impedance
- Harmonic interpolation
- Envelope inversion

A brief description of the above mentioned methods is provided in the following sections. The overview on the reconstruction methods is completed by the reflectivity reconstruction on a benchmark synthetic trace representing a band-limited zero-offset sparse reflectivity immersed in white noise (S/N 34 dB in terms of maximum amplitudes). The model of AI at the basis of the synthetic example is named MODEL A.

2.4 Reconstruction of Sparse Time series

Solving the convolutive problem 2.1 in a least square sense (minimum L2 norm) as

$$\min_{\mathbf{r}} \|\mathbf{W}\mathbf{r} - \mathbf{d}\|_2^2. \quad (2.2)$$

where \mathbf{d} are the recorded data, \mathbf{r} the reflectivity, and \mathbf{W} the convolution matrix of the wavelet, produces a result that is limited in the range of frequencies of the input data. On the contrary, the minimum L-1 solution

$$\min_{\mathbf{r}} \|\mathbf{W}\mathbf{r} - \mathbf{d}\|_1, \quad (2.3)$$

allows to extend the reconstruction of the reflectivity from the DC component up the Nyquist frequency, because of the information contained in the assumption that the seismic reflectivity is made up of only few strong reflectors (Zala, Barrodale, and Kennedy, 1987). The aim of the sparse-spike methods is to minimise the sum of the absolute values of the reflectivity, provided that the recorded data are honoured up to a certain degree of confidence. Different methods have been specifically implemented to obtain this result.

2.4.1 Linear Programming

One of the oldest papers on sparse-spike seismic reconstruction (Oldenburg, Scheuer, and Levy, 1983) delineates the linear programming approach to reflectivity reconstruction. Those

authors proposed to obtain a full-bandwidth estimate of the reflectivity by minimising:

$$\sum_{i=1}^N |r_i| \quad s.t. \quad \begin{cases} \text{Re}(R_j) - \delta \leq \sum_{i=1}^N r_i \cos(\frac{2\pi ij}{N}) \leq \text{Re}(R_j) + \delta \\ \text{Im}(R_j) - \delta \leq \sum_{i=1}^N r_i \sin(\frac{2\pi ij}{N}) \leq \text{Im}(R_j) + \delta \end{cases} \quad (2.4)$$

for all the R_j in the signal bandwidth. In equation 2.4, r represents the reflectivity sampled at discrete time intervals i , R_j represents the Fourier components of the reflectivity in the signal bandwidth, and δ stands for the uncertainty on the data which can be an empirically or a statistically derived quantity (Levy and Fullagar, 1981). Equation 2.4 describes a constrained linear programming problem, that can be solved, for example, with the simplex algorithm.

2.4.2 LASSO

A minimum-L1 norm reflectivity solution can be obtained by a Least Absolute Shrinkage and Selection Operator (LASSO). The approach is slightly different than the one proposed in equation 2.4 in this case. The problem becomes a simultaneous minimisation of an L-1 and L-2 norm quantity. Under the hypothesis of Gaussian errors on the data it is sensible to minimise the norm-2 of the data misfit, while the minimisation of the norm-1 of the reflectivity model (\mathbf{r}) is required to obtain the desired sparse structure:

$$J(r) = \|\mathbf{W}\mathbf{r} - \mathbf{d}\|_2^2 + \lambda^2 \|\mathbf{r}\|_1 \quad (2.5)$$

In the cost function 2.5, \mathbf{W} represents the relationship between the model and the data (\mathbf{d}): it is the convolution matrix of a stationary wavelet. The iterative re-weighted least squares (Daubechies, 1992) method or FISTA (Beck and Teboulle, 2009) can be used to obtain a fast solution of the problem in equation 2.5.

The formulation of the problem 2.5 can be modified into the constrained version:

$$J(r) = \|\mathbf{W}\mathbf{r} - \mathbf{d}\|_2^2 \quad s.t. \quad \|\mathbf{r}\|_1 \leq c^2 \quad (2.6)$$

The parameter c^2 in equation 2.6 plays a similar role to λ^2 in equation 2.5. A variety of modifications to the problem 2.5 has been proposed in the context of seismic data inversion. Pereg, Cohen, and Vassiliou (2017) suggest an additional term in the cost function to account for the lateral continuity of the solution. Perez, Velis, and Sacchi (2017) adopt a weighted L1/L-2 norm to solve the pre-stack inversion for a blocky structure of elastic parameters. A sparse-spike reconstruction of the full-bandwidth of the reflectivity with the subsequent AI estimation is presented in Figure 2.1.

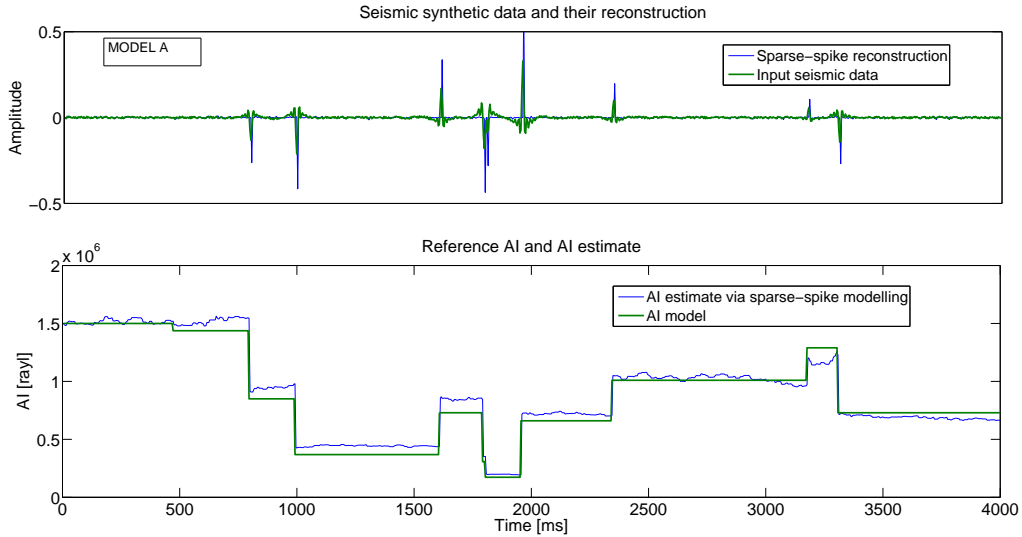


FIGURE 2.1: *Sparse-spike reconstruction of the full-bandwidth of the reflectivity and subsequent AI estimate from the bandlimited synthetic model named MODEL A. $S/N = 34$ dB in terms of maximum amplitudes. The reconstruction has been obtained with $\lambda^2 = 0.001$ in equation 2.5.*

2.4.3 Minimum Entropy Deconvolution

The initial approach to the minimum entropy deconvolution of Wiggins (1978) was re-adapted by Sacchi, Velis, and Cominguez (1994) to perform the bandwidth extrapolation while being consistent with the information contained in a user-defined signal bandwidth. Those authors make use of the orthogonality among the Fourier components to keep the signal bandwidth unvaried while conditioning the remaining components to be consistent to the smaller variation of a logarithmic norm of the reflectivity. This choice aims at obtaining a solution that enhances the presence of few strong events. One of the variational norm adopted by those authors is

$$V = \frac{\sum_i \frac{Nr_i^2}{\sum_i r_i^2} \ln\left(\frac{Nr_i^2}{\sum_i r_i^2}\right)}{N \ln(N)} \quad (2.7)$$

where N is the number of samples of the seismic trace, and r_i the reconstructed reflectivity. This norm is applied to Chapter 3 and 4 for improving the high-frequency content of the estimated reflectivity and for reducing the ringing in the estimated elastic interval properties.

2.4.4 Total Variation Regularisation

The low frequency components of the subsurface impedance can be constrained by minimizing their total variation. A number of authors (i.e. Gholami (2015)) have worked on this strategy to enhance the vertical and lateral homogeneity of the reconstructed property of interest. This method works in impedance domain and it accounts for a weighting term that imposes parsimony on the number of variations of impedance. When the method is performed in one dimension only, it corresponds with the sparse reconstruction of reflectivity in time domain.

The minimisation of the cost function

$$J = \|\mathbf{X}\|_{TV} \quad s.t. \quad \|\mathbf{DX} - \mathbf{R}\|_F^2 < \epsilon \quad (2.8)$$

with respect to the quantity $\mathbf{X} = \frac{1}{2} \log(\mathbf{AI})$, provides the result with the smallest variation on impedance compatible with the data misfit that is imposed. The matrix \mathbf{D} in equation 2.8 represents a discrete version of the derivative operator, and \mathbf{R} is the vector of the recorded data. The Frobenius norm minimisation, together with the constraint on data misfit, produces an impedance that honours the recorded data up to a certain level of confidence given by ϵ . The total-variation norm in one dimension corresponds to

$$\|\mathbf{X}\|_{TV} = \sqrt{\sum_i [\mathbf{DX}]_i^2}. \quad (2.9)$$

The one-dimensional case is not much significant as it reduces to the same formulation provided by equation 2.6, with the only difference being the vector that is minimised. In fact, rather than obtaining a solution in terms of reflectivity as in the LASSO case, the solution is in terms of the logarithm of impedance (\mathbf{X}). For this reason no total variation reconstruction is presented on the synthetic examples and the reader is referred to the results of Figure 2.1.

2.5 Harmonic interpolation

Harmonic interpolation is a method that under the hypothesis of a limited number of events in the recorded time-series may lead to the band-width continuation. Liang, Castagna, and Torres (2017) underline the physical validity of the method when the number of events is less than the number of sampled frequencies in the signal band-width.

In the case of real time-series, an harmonic model aims at finding the spectral peaks in the amplitude spectrum, while I use the conjugate property of finding the peaks (events) of the time series which is known in terms of its Fourier spectrum. For this reason, this section deals with complex-value stationary series that are the ideal description of a part of the Fourier spectrum of the processed seismic traces. Seismic complex-value series have a finite length, therefore different harmonic interpolation estimators exist for modelling the signal behaviour within the signal bandwidth and to extend it outside the recorded interval. Most of the approaches investigated in the thesis are based on power spectral estimation. In the following subsection I briefly review the strengths and weaknesses of the spectral estimation methods.

2.5.1 Spectral Estimation

Spectral estimation aims at describing the periodic components of a signal from a discrete set of observations over a limited number of samples. Proakis et al. (1992) point out that the length of the observation window, or alternatively the wavelength in which a non-stationary time-series may be considered stationary, is the most important factor in determining the resolution of the spectral estimation. Kay and Marple (1981) provide a summary of different methods for power spectral estimation. They make a classification of the methods that distinguishes between:

- Parametric methods

- Non parametric methods.

The non parametric methods are based on the Periodogram (Schuster, 1898): the Periodogram only assumes that the data generation process is periodic outside the observation window. The periodogram estimates the power spectrum at a given sampling frequency via the Discrete Fourier Transform on the sample-autocorrelation estimate that can be obtained from the data. The autocorrelation may be tapered at late lags to reduce spectral leakage. Non parametric methods suffer in resolution for short observation windows. Parametric methods, on the contrary, may resolve two close spectral components even in short time series by making further assumptions on the process that generated the data. As far as it concerns the parametric methods I only deal with linear-time-invariant processes, whose transfer function can be represented by

$$H(z) = \frac{B(z)}{A(z)} = \frac{\sum_{k=0}^q b_k z^{-k}}{1 + \sum_{k=1}^p a_k z^{-k}}. \quad (2.10)$$

The process described by equation 2.10 in the z -domain ($z = e^{-i2\pi\tau}$) is called autoregressive-moving average (ARMA). Moving Average (MA) models in which $p = 0$ describe a signal which is the convolution between the model coefficients b_k and the input series. On the contrary, autoregressive (AR) models, in which $q = 0$, describe a signal with a feedback whose value at present frequency is a linear combination of the values at previous (or future) frequencies (together with an innovation term). AR models of coefficients a_k describe a limited number of cyclic components in the recorded data, while ARMA models with the same coefficients for the AR and the MA parts, account for the presence of random noise into the former model.

Model Order Selection The ARMA model order (p, q) selection is a research topic by itself and several authors propose different statistical criteria for addressing this problem. Too low the order, too simplistic the model thus making impossible to capture all the features of the reflectivity that are present in the data. Too high the model order, too much noise is considered as part of the signal. As far as it concerns the AR family of models, Akaike (1992) provides the final prediction error (FPE) as an unbiased expectation of the prediction error of the model. The model order p that produces the minimum FPE

$$FPE_p = \frac{N + p + 1}{N - p - 1} \|\mathbf{y} - \mathbf{y}'_p\|_2^2 \quad (2.11)$$

becomes the model order of choice under this statistic criterion. In equation 2.11 N is the number of data samples, p the model order, \mathbf{y} the actual data and \mathbf{y}'_p their estimates via the order p AR model. Low prediction error ($\|\mathbf{y} - \mathbf{y}'_p\|_2^2$) together with parsimony in the model order produce a low FPE value.

Akaike (1992) also suggests another criterion for AR model order selection. The minimisation of the information lost due to the approximation of the data with an AR process is obtained when

$$AIC_p = \ln(\|\mathbf{y} - \mathbf{y}'_p\|_2^2) + \frac{2(p + 1)}{N} \quad (2.12)$$

is minimum (Kay and Marple, 1981). The formulation of equation 2.12 is valid under the hypothesis that the data (\mathbf{y}) are Gaussian. If this hypothesis is not met, the expression $\|\mathbf{y} - \mathbf{y}'_p\|_2^2$

must be replaced in equation 2.12 by the maximum likelihood of the AR model of order p , given the recorded series. Parzen (1974) introduces a further criterion for the AR model selection: the criterion of autoregressive transfer (CAT) which is expressed by:

$$CAT_p = \frac{1}{N} \sum_{k=1}^p \frac{N-k}{N \|\mathbf{y} - \mathbf{y}'_k\|_2^2} - \frac{1}{\|\mathbf{y} - \mathbf{y}'_p\|_2^2}. \quad (2.13)$$

In this case, the difference between a measure related to the average of the prediction error up to the order p , and a measure related to the prediction error at order p , becomes the criterion to identify the order of the model. Ulrych and Bishop (1975) reviewed the above mentioned statistical criteria for AR model order selection, with respect to the problem of the spectral estimation of the normal modes of the earth. Ulrych and Clayton (1976) recommend using longer model orders than those identified by the statistic criteria and they propose $\frac{N}{2}$ to $\frac{N}{3}$ as reference values (N being the number of samples available). As far as it concerns the spectral analysis of seismic traces, Walker and Ulrych (1983) support the latter choice and recommend using 0.7 of the signal bandwidth length (considering only half of the Fourier Spectrum). This seems to be a trade-off between the necessity to use long AR models to approximate ARMA models in presence of noise, and the necessity to limit the uncertainty determined by the poor estimation of the later lags of the autocorrelation (in the Toeplitz matrix within equation 2.23).

I show, here below, the above mentioned AR model order selection criteria on a synthetic complex-value series. This choice is consistent to the harmonic modelling of seismic spectra, which is performed in the Fourier domain (see section 2.5.2). Two synthetic models (MODEL A and MODEL B) with a limited number of events and additive white noise are used to this end. Figure 2.2 compare the reconstruction of AI with the AR model order selected via the AIC and with the AR model order selected via the $\frac{N}{3}$ recommendation of Ulrych and Clayton (1976). The two panels of Figure 2.2 show that the structure of AI is quite insensitive to this value (Schwetlick, Miyashita, and Schickert (1987) pointed out a similar experience with reference to the problem of super-resolution estimates for holographic imaging). Further details on the reconstruction algorithm could be found in section 2.5.2. Figure 2.3 shows the actual values of the three different statistic criteria for model order choice. Although the absolute value of the statistics is different across the test performed, all the panels of Figure 2.3 show a sharp decrease of the modelling error as soon as the AR order increases, a minimum of this error, and then an increase due to the penalty term related to the risk of over-fitting a too complex model on the available dataset.

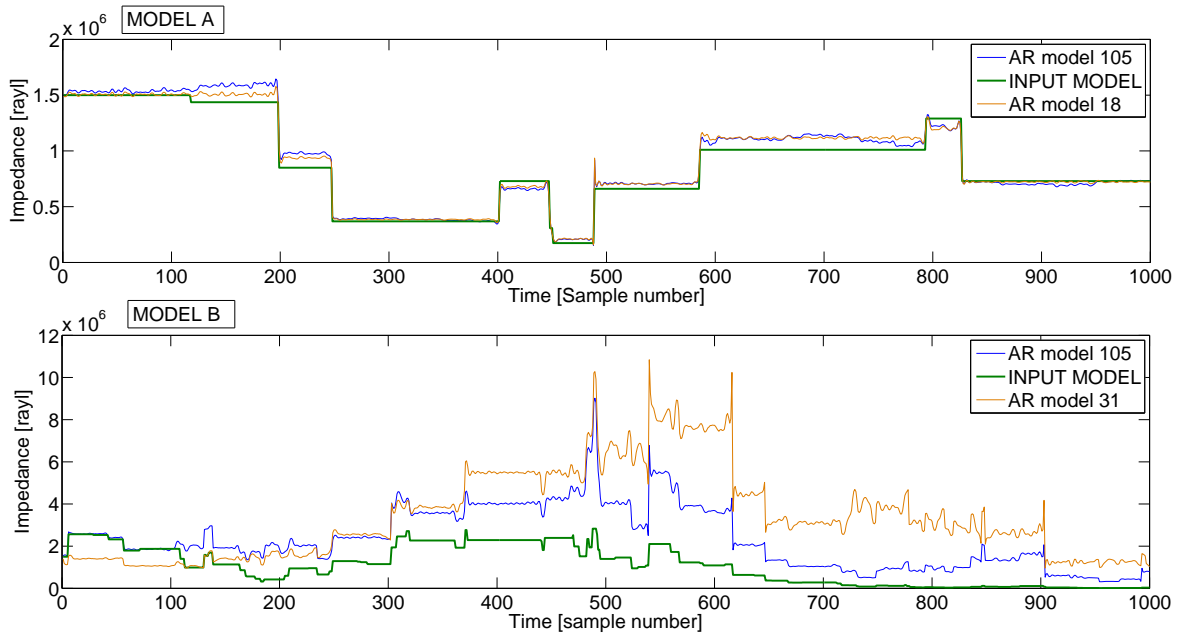


FIGURE 2.2: Reconstruction of the full-bandwidth of the AI derived from zero-offset synthetic seismogram with the AR model that best matches the $N/3$ criterion (105 both for the top and the bottom panel), and with the model order that minimises AIC (18 for the top panel and 31 for the bottom panel). $S/N = 34$ dB in terms of maximum amplitudes. The main differences, between the blue and the orange lines consists in the complexity of the response, which is lower when the model order is lower.

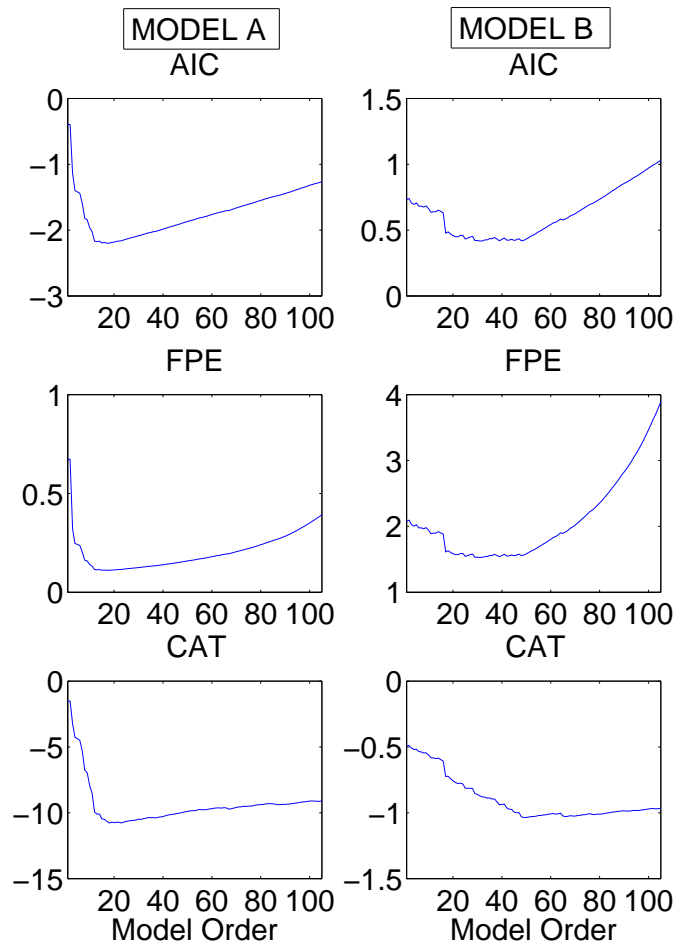


FIGURE 2.3: Comparison between different statistical criteria for the AR model selection on the synthetic example of Figure 2.2. Input data consists on the complex-value series of the Fourier components corresponding to the signal bandwidth of the synthetic trace derived from the MODEL A and MODEL B in Figure 2.2. All the three criteria suggest 18 in the panels on the left referring to the synthetic MODEL A. The three criteria provide different model order choices: 35 (AIC), 22 (FPE) and 44 (CAT) on the panels on the right referring to MODEL B. The absolute value of each statistic is not significant as it varies with the criterion adopted and with the dataset complexity.

Signal Bandwidth Selection Once the order is selected, the method for estimating the AR-ARMA coefficients a_k and b_k must be evaluated on the data available. It is worth removing the noisiest components (typically at the beginning and at the end of the complex-value series) before modelling, for obtaining a more sensible result. The influence of the low and the high-cut frequency limits used for AR-ARMA model fitting on the bandwidth extension result are shown in Figure 2.4 for the MODEL A synthetic example. The complex-value series of the Fourier spectral components must be stationary for autoregressive modelling and long enough to detect all the corresponding temporal peaks (Hendrick and Hearn, 1993). Those two objectives are at odds, and a possible trade-off criterium on seismic data may be represented by identifying the signal bandwidth within the spectral band whose amplitudes are larger than -6 dB with respect to the spectral peak amplitude. This choice is more extensively discussed in Chapter 3.

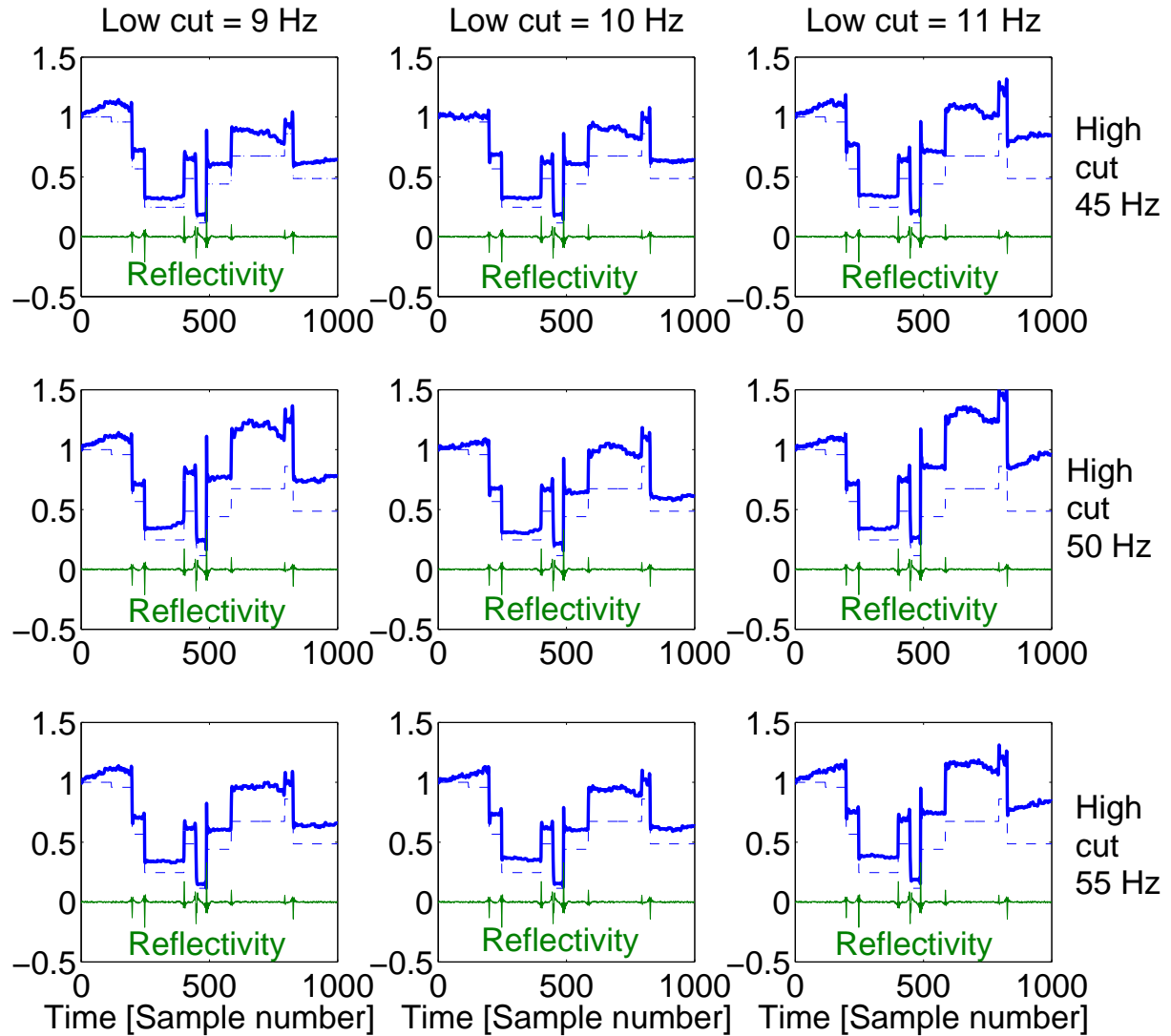


FIGURE 2.4: AR reconstruction of the AI from zero-offset band-limited (8-70 Hz cut-off frequencies) synthetic trace, referring to MODEL A (reported in green for reference - S/N = 34 dB). Nine different panels show the effects of varying the bandwidth in which the AR model is estimated. The reconstructed AI, normalised by the AI of the first sample, is reported in blue. The low-cut frequency increases from panels on the left to panels on the right, while the high-cut frequency increases from panels in the top row to panels in the bottom row. The AI of MODEL A, normalised by the AI of the first sample, is reported with a dotted blue line for reference in all the panels. Significant differences are visible across the panels even though the cut-off frequencies remain within the flat part of the spectrum.

ARMA Coefficient Estimation For a limited number of sinusoids in additive white noise, the ARMA representation with the same coefficients for the AR and the MA parts correctly models the data (Ulrych and Clayton, 1976) and it leads to the eigenvalue-eigenvector problem

$$\mathbf{A}\mathbf{g} = \sigma^2\mathbf{g}. \quad (2.14)$$

In equation 2.14, $\mathbf{g} = 1 - \mathbf{a}$ is the vector of the AR prediction error coefficients, \mathbf{A} represents the data autocovariance matrix, and σ^2 represents the noise variance. The relationship between

the data autocorrelation and the coefficients of the ARMA model is derived by taking the expectation of the prediction error multiplied by the signal. In fact, the band-limited and scaled seismic trace

$$D_f = R_f + N_f \quad (2.15)$$

has the reflectivity components of the spectrum (R_f) fully described by the linear combination of M harmonics:

$$R_f = \sum_{k=1}^M a_k R_{f-k}. \quad (2.16)$$

In equation 2.15 N_f represents the Fourier spectrum of the noise. Substituting equation 2.15 into equation 2.16 leads to:

$$D_f - N_f = R_f = \sum_{k=1}^M a_k R_{f-k} = \sum_{k=1}^M a_k (D_{f-k} - N_{f-k}). \quad (2.17)$$

Taking the leftmost and the rightmost terms in equation 2.17 and substituting $\mathbf{g} = 1 - \mathbf{a}$ it is possible to write

$$\sum_{k=0}^M g_k D_{f-k} = \sum_{k=0}^M g_k N_{f-k}. \quad (2.18)$$

In case the signal is uncorrelated to the noise such as $(R_f + N_f)N_f = N_f^2$, multiplying equation 2.18 by the data itself and taking the expectations leads to

$$\mathbf{A}\mathbf{g} = E\left[\sum_{k=0}^M g_k D_{f-k}^2\right] = E[g_k N_{f-k}^2] = \sigma^2 \mathbf{g}, \quad (2.19)$$

which is exactly the eigen-system described in equation 2.14. There is a large variety of approaches to ARMA coefficient estimation, from the least-squares modified Yule-Walker method (Cadzow, 1982) to algorithms that aim at separating the noise from the signal subspace in the data autocorrelation matrix such as:

- Pisarenko spectral estimation
- MUSIC.

Linear programming is a further approach to autoregressive coefficient estimation (Levy et al., 1982). This method defines the smallest number of spectral components in the power spectrum compatible with the autocorrelation estimate.

Pisarenko spectral estimation for ARMA modelling. In problem 2.14 the Pisarenko spectral estimation technique assumes that the variance of the background white noise has dimension one in an orthogonal basis that describes the autocovariance \mathbf{A} transform. This assumption is realistic if the model order corresponds to the number of harmonic components described in the data plus one. Pisarenko (1972) determines the components of \mathbf{g} as the eigenvector associated with the minimum eigenvalue of the matrix \mathbf{A} . The minimum eigenvalue represents the noise variance and it can be estimated once a method for obtaining \mathbf{A} from the data is selected (see for example equation 2.24 or the recursion presented in section 2.5.1). The Pisarenko method can be

extended to model orders (p) that are larger than the number of harmonic components plus one. If there are M harmonic components in the signal, and those harmonics show an energy larger than the background noise, the autocovariance of the signal spans a M -dimensional space in \mathbf{A} . This subspace is described by the eigenvectors corresponding to the largest M eigenvalues of the data autocovariance \mathbf{A} . The remaining, smaller eigenvectors, span the noise subspace. Once the harmonic components are separated from the noise, the ARMA coefficients can be estimated by averaging the smallest eigenvalues to obtain an estimate of the noise variance. A particular case of subspace decomposition method for obtaining the noise subspace is the MUSIC algorithm (Schmidt, 1986).

AR Coefficient Estimation If noise had not been present in the data, $D_f = R_f$ (from equation 2.15). A limited number (M) of events in a recorded time series is represented in the Fourier domain (R_f) by a sum of a limited number of complex sinusoids

$$R_f = \sum_{k=1}^M r_k e^{-i2\pi f \tau_k}. \quad (2.20)$$

In equation 2.20 τ_k represents the travel-time of the events r_k . A limited number of sinusoids are fully described by a linear combination of M discrete Fourier components

$$R_f = \sum_{k=1}^M R_{f-k} e^{-i2\pi k \tau_k}. \quad (2.21)$$

Equation 2.21 can be interpreted as perfectly predictable AR process of coefficients g_k and innovation equal to 0:

$$R_f = \sum_{k=1}^M g_k R_{f-k}. \quad (2.22)$$

Multiplying equation 2.22 by R_f and taking expectations, equation 2.14 becomes (Walker and Ulrych, 1983)

$$\mathbf{A} \mathbf{g} = \sigma^2 \mathbf{i} \quad (2.23)$$

and it leads to the estimation of the AR coefficients. In equation 2.23, \mathbf{i} represents a unitary spike at zero lag and σ^2 accounts for the variance of the prediction error. Among the different methods for solving equation 2.23 I have analysed the:

- Yule-Walker method
- Burg method
- Unconstrained least-squares method.

Yule-Walker spectral estimation for AR modelling. In equation 2.23 the Toeplitz autocovariance matrix \mathbf{A} can be estimated by a discrete sampling of the autocorrelation function of the data:

$$\mathbf{A}_{\text{dd}}(i) = \frac{1}{N} \sum_{j=0}^{N-p} d_i d_{i+j}^H \quad (2.24)$$

In equation 2.24 $\mathbf{A}_{dd}(i)$ represents the coefficients of the autocorrelation function at lag (i) , N is the number of samples of the complex-value series, and p is the model order. The solution of equation 2.23 exploits the Levinson recursion scheme starting from the coefficients of the model of order 1:

$$\begin{aligned} g_1(1) &= -\frac{\mathbf{A}_{dd}(1)^H}{\mathbf{A}_{dd}(0)} \\ \sigma_1^2 &= \mathbf{A}_{dd}(0)(1 - g_1(1)g_1(1)^H) \end{aligned} \quad (2.25)$$

where the $g_i(k)$ represent the component i of the vector of AR coefficients of order k , such as $g_3(2)$ represents the second coefficient of the AR model of order 3. The recursion (which is detailed in Ulrych and Sacchi (2005)) proceeds for each i up to the desired order p by computing:

$$\mathbf{G}_i = \begin{bmatrix} 1 \\ g_{i-1}(1) \\ \dots \\ g_{i-1}(i-1) \\ 0 \end{bmatrix}, \quad (2.26)$$

$$\mathbf{A}_i = \begin{bmatrix} A_{dd}(i+1)^H & A_{dd}(i)^H & \dots & A_{dd}(0) \end{bmatrix}, \quad (2.27)$$

$$\Delta_{i-1} = \mathbf{A}_i \mathbf{G}_i. \quad (2.28)$$

The estimation of the last coefficient of the AR model of order i is

$$g_i(i) = -\frac{\Delta_{i-1}}{\sigma_{i-1}^2}. \quad (2.29)$$

The variance of the noise is estimated as:

$$\sigma_i^2 = \sigma_{i-1}^2(1 - g_i(i)g_i(i)^H). \quad (2.30)$$

Finally the estimation of the remaining coefficients of the AR model of order i is obtained by:

$$\begin{aligned} g_i(1) &= g_{i-1}(1) + g_i(i)g_{i-1}(i-1)^H \\ &\dots \\ g_i(i-1) &= g_{i-1}(i-1) + g_i(i)g_{i-1}(1)^H. \end{aligned} \quad (2.31)$$

A so called Multi-step Yule Walker estimator has been proposed by Tingyan (2010) to improve the estimation of the AR model. He considers, in the estimation of the AR coefficients, the lags of the autocorrelation longer than the model order that are related to the information present in the whole series and not only in the proximity of the frequencies to be reconstructed. This method appears particularly useful when the model order is much shorter than the series into which the AR model is fitted.

Burg spectral estimation for AR modelling. The Burg procedure for AR coefficients estimation (Burg, 1975) minimises the sum of the squared forward and backward prediction error

$$\sum_{n=p}^{N-p} [e_{fwd}(n)^2 + e_{bwd}(n)^2] = \sum_{n=p}^{N-p} [(d_n - \sum_{j=1}^p a_j d_{n-j})^2 + (d_{n-m} - \sum_{j=1}^p a_j^H d_{n+j-p})^2] \quad (2.32)$$

and it obtains the (i) -th AR coefficient of the AR model of order i as:

$$a_i(i) = \frac{-2 \sum_{n=i}^{N-1} (-\sum_{j=0}^{i-1} a_{i-1}(j) d(n-j)) (-\sum_{j=0}^{i-1} a_{i-1}^H d(n+j-i-1))}{\sum_{n=i}^{N-1} [(-\sum_{j=0}^{i-1} a_{i-1}(j)^2 d(n-j)^2) + (-\sum_{j=0}^{i-1} a_{i-1}^H)^2 d(n+j-i-1)^2]}. \quad (2.33)$$

The term on the right hand-side is known once the solution for order $i-1$ has been obtained. In equation 2.32 N is the trace length and p is the model order. The Burg method extracts the AR coefficients directly from the Levinson recursion (Claerbout, 1976) such as no sample-autocorrelation estimator (equation 2.24) is required. This implies that the AR coefficients (k) of all orders i must satisfy:

$$a_i(k) = a_{i-1}(k) + a_i(i) a_{i-1}(i-k) \quad (2.34)$$

The knowledge of the solution at order $i-1$ together with the AR coefficient $a_i(i)$ from equation 2.34 provides enough information for estimating all the $a_i(k)$ AR coefficients of order i . Proakis et al. (1992) and Kay and Marple (1981) discuss the topic further. Walker and Ulrych (1983) found the Yule-Walker method more robust to variations in model order than the Burg approach as far as it concerns the modelling of seismic spectra.

Unconstrained least squares spectral estimation for AR modelling. The unconstrained least squares approach to the AR coefficients estimation minimises the squared prediction errors (equation 2.32) without making use of the Levinson recursion. Minimising equation 2.32 for a number of observed samples (N) larger than the model order (p) leads to an overdetermined system that is solved via least squares as:

$$\mathbf{g} = -(\mathbf{D}^H \mathbf{D})^{-1} \mathbf{D}^H \mathbf{d}. \quad (2.35)$$

In equation 2.35, \mathbf{D} represents the convolution matrix of the data (\mathbf{d}). Kay and Marple (1981) report that, for short time series, the resolution of the least squares method are superior to those of the Yule-Walker and Burg estimates.

Here below we report for reference the reconstruction of MODEL A with the three different estimators of the autocovariance coefficients discussed above. None of them can be considered superior to the others on the synthetic example tested.

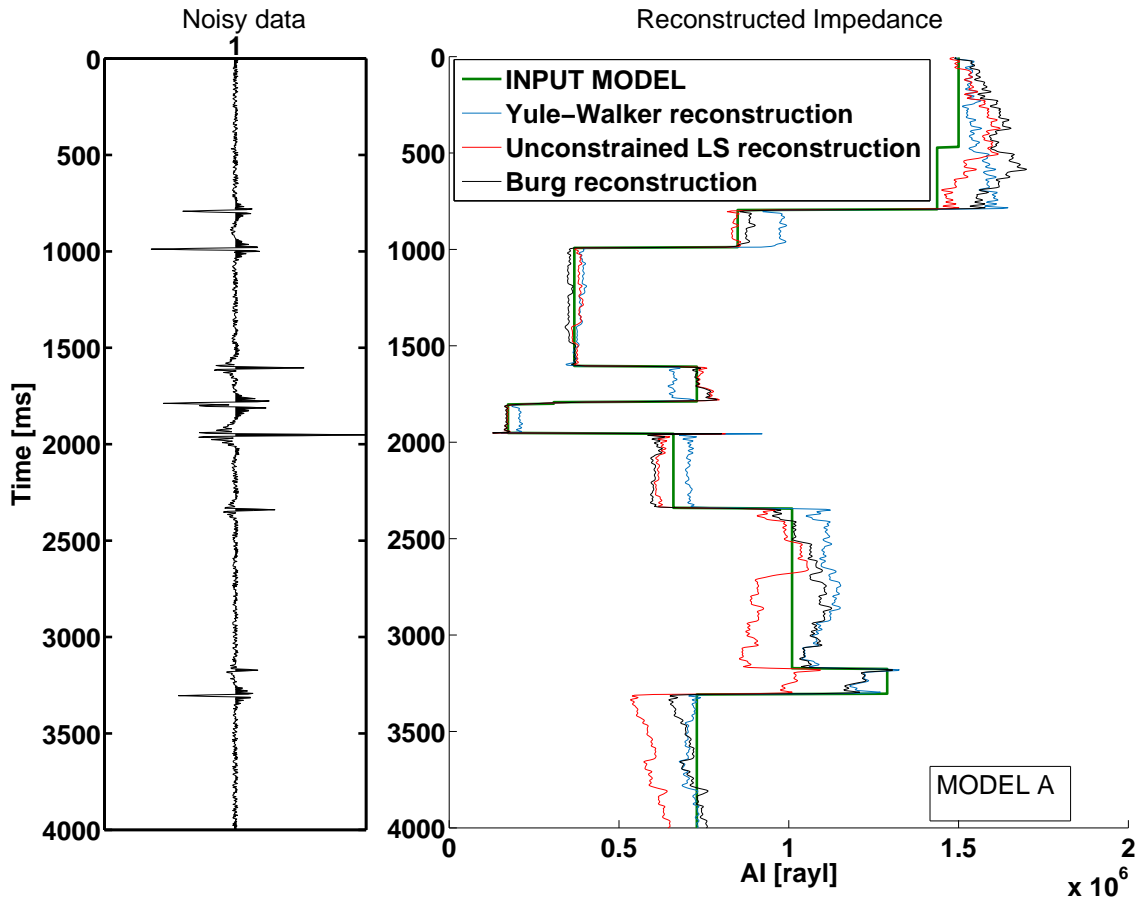


FIGURE 2.5: Comparison of different AR model coefficient estimators in terms of estimated AI. The input data consists of the bandlimited (8-70 Hz zero-phase Butterworth filter) trace derived from MODEL A (with $S/N=34$ dB in terms of maximum amplitudes). The absolute value of the AI estimation differs from estimator to estimator, but all the methods are adequate to detect the main blocks of the AI.

2.5.2 The Low-frequency Interpolation Procedure

The harmonic interpolation method that is widely used in this thesis as a tool for bandwidth extension is derived from Walker and Ulrych (1983) and it is briefly summarized here for completeness. Those authors proposed to:

- Fit an AR model to the frequency bandwidth (complex-value series) that shows good S/N
- Obtain the low-frequency completion by minimisation of the sum of the squared forward and backward prediction error
- Compute the AR filter in the signal bandwidth plus the low frequency reconstruction obtained in the previous step
- Extend the bandwidth of the reflectivity to higher frequencies via minimum entropy (if feasible).

A variety of AR model fitting procedures has been discussed in the previous section for accomplishing the first point of the process. In this section I describe the second and the third points in the list while the high frequency extension is discussed in section 2.5.5. The minimisation of the sum of the squared forward and backward prediction errors is the criterion adopted for bandwidth extension (Walker and Ulrych, 1983). The sum of the squared forward and backward prediction error can be expressed as

$$S = \sum_{j=-K}^{K+p} |E_j^f|^2 + |E_j^b|^2 = \sum_{j=-K}^{K+p} \left| \sum_{i=0}^p g_i R_{i-j} \right|^2 + \sum_{j=-K-p}^K \left| \sum_{i=0}^p g_i^H R_{i+j} \right|^2 \quad (2.36)$$

where K is the low cut frequency that discriminates between the signal bandwidth and the lower frequencies. The minimisation is performed with respect to positive and negative conjugate low-frequencies in the interval from $-K$ to K , producing a set of $2K + 1$ equations in $2K + 1$ unknowns. In fact,

$$\frac{\partial \mathbf{S}}{\partial R_k} = \begin{bmatrix} \frac{\partial \mathbf{S}}{\partial R_{-K}} \\ \dots \\ \frac{\partial \mathbf{S}}{\partial R_k} \end{bmatrix} = \begin{bmatrix} 0 \\ \dots \\ 0 \end{bmatrix} = \begin{bmatrix} 2 \left| \sum_{i=0}^p \sum_{j=0}^{p-i} g_j g_{i+j}^H R_{-K-i} \right| + 2 \left| \sum_{i=0}^p \sum_{j=0}^{p-i} g_j g_{i-j}^H R_{-K+i} \right| \\ \dots \\ 2 \left| \sum_{i=0}^p \sum_{j=0}^{p-i} g_j g_{i+j}^H R_{K-i} \right| + 2 \left| \sum_{i=0}^p \sum_{j=0}^{p-i} g_j g_{i-j}^H R_{K+i} \right| \end{bmatrix}. \quad (2.37)$$

For symmetry, only one between the forward and backward prediction error is required for each row of the rightmost matrix in equation 2.37 (Walker and Ulrych, 1983). I keep the backward term and I substitute the sample-autocorrelation of the AR coefficients

$$\begin{bmatrix} 2 \left| \sum_{k=-p}^p g_k g_k^H R_{f+k} \right| \\ \dots \\ 2 \left| \sum_{k=-p}^p g_k g_k^H R_{-f+k} \right| \end{bmatrix} = \begin{bmatrix} 0 \\ \dots \\ 0 \end{bmatrix}, \quad (2.38)$$

$$\mathbf{AC}(-i) = \mathbf{AC}^H(i) = \sum_{j=0}^{p-i} g_j g_{j+i}^H. \quad (2.39)$$

The system of equation 2.38 has been re-written by Walker and Ulrych (1983) as

$$\mathbf{GR} = \mathbf{B}. \quad (2.40)$$

The vector \mathbf{B} results from the convolution of the autocorrelation of the AR coefficients with the known spectral terms $R_f < R_{-K}$ or $R_f > R_K$. Matrix \mathbf{G} is Toeplitz with the autocorrelation of the AR coefficients at zero lag on its main diagonal. For instance an AR model order 3 that fills a $K=1$ low frequency gap is cast in the form:

$$\begin{aligned} AC_{-3}R_{-4} + AC_{-2}R_{-3} + AC_{-1}R_{-2} + AC_0\mathbf{R}_{-1} + AC_1\mathbf{R}_0 + AC_2\mathbf{R}_1 + AC_3R_2 &= 0 \\ AC_{-3}R_{-3} + AC_{-2}R_{-2} + AC_{-1}\mathbf{R}_{-1} + AC_0\mathbf{R}_0 + AC_1\mathbf{R}_1 + AC_2R_2 + AC_3R_3 &= 0 \\ AC_{-3}R_{-2} + AC_{-2}\mathbf{R}_{-1} + AC_{-1}\mathbf{R}_0 + AC_0\mathbf{R}_1 + AC_1R_2 + AC_2R_3 + AC_3R_4 &= 0. \end{aligned} \quad (2.41)$$

The bold terms in the system of equation 2.41, are the components of the unknown vector \mathbf{R} of low frequency components. Given the general nature of the seismic trace autocorrelation function, matrix \mathbf{G} is usually well conditioned, such that \mathbf{R} can be obtained by direct inversion

of the system 2.40. When the matrix \mathbf{G} is ill-conditioned \mathbf{R} can be obtained via ridge-regression, by solving the regularised inverse problem

$$\min_{\mathbf{R}} \|\mathbf{C}\mathbf{R} - \mathbf{b}\|_2^2 + \lambda^2 \|\mathbf{I}\mathbf{R}\|_2^2 \quad (2.42)$$

in which $\mathbf{C}^t\mathbf{C} = \mathbf{G}$, $\mathbf{C}^t\mathbf{b} = \mathbf{B}$, and \mathbf{I} is the identity matrix. After the low frequency gap is filled with the vector \mathbf{R} , Walker and Ulrych (1983) recommend fitting a new AR model to the extended complex-value series. This is to exploit a longer series to better estimate the later lags of the autocorrelation that are particularly relevant for the estimation of the AR coefficients when the order of the AR model is close to the length of the spectral pass-band. This choice is justified by those authors as a mean to reduce the prediction error, and the synthetic example presented in Figure 2.6 supports this statement.

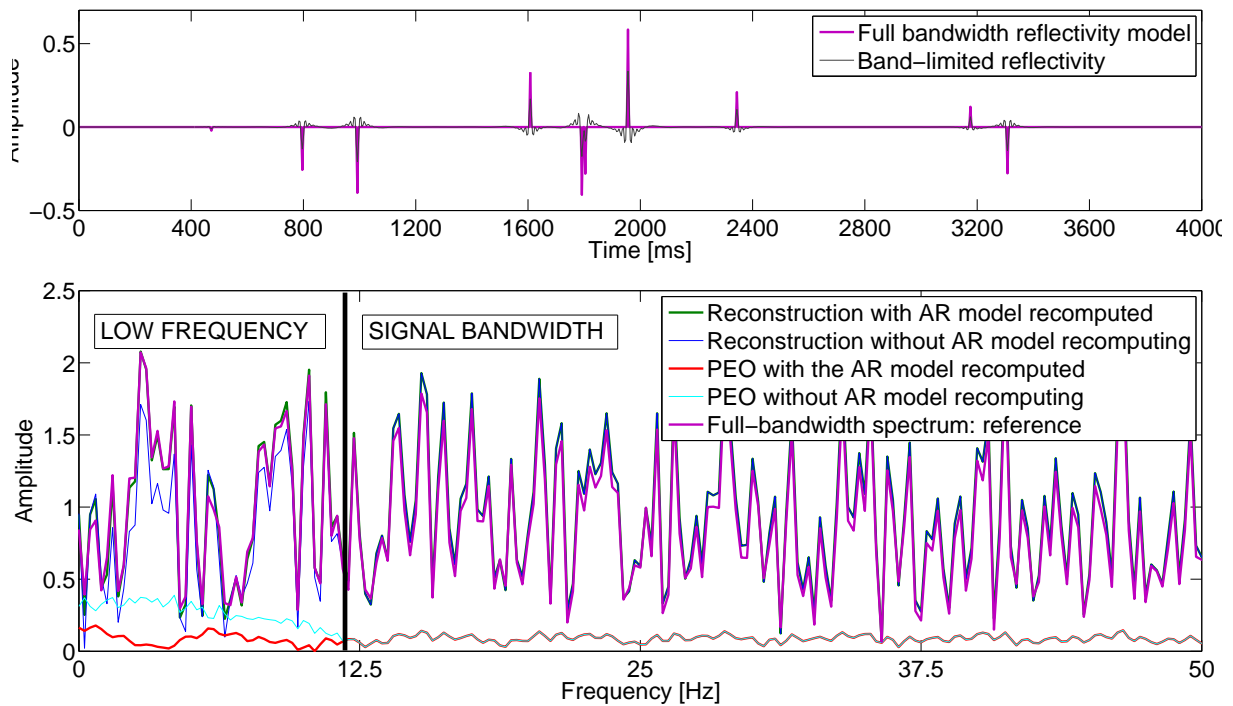


FIGURE 2.6: Evaluation of the prediction operator error of the AR reconstruction in case the AR model is directly obtained from the signal bandwidth (cyan curve) or recomputed after the gap filling (red curve). The top panel shows the temporal behaviour of the reference reflectivity (purple) and the input band-limited data (grey). The panel on the bottom shows the lowest part of the amplitude spectrum of the reference model (purple) and that of the low frequency reconstruction without recomputing the AR filter (blue) and with the recalculated filter (green). In absence of noise the green line overlaps fairly well the reference spectrum at the low frequency leading to a lower PEO (red) than the solution without the AR recomputing (cyan).

2.5.3 Low-frequency Interpolation Varying the Norm of the Prediction Error

In the previous subsection the L-2 norm was adopted to obtain the Prediction Error filter that reconstructs the low frequency components of the reflectivity. A norm different from 2, with a different statistical assumption for the errors on the data can also be assumed. This leads to

rewrite equation 2.36 as

$$S = \sum_{j=-K}^{K+p} |E_j^f|^q + \sum_{j=-K-p}^K |E_j^b|^q, \quad (2.43)$$

where q is a non-negative real number. Levy et al. (1982) adopted a linear programming approach for the minimisation of the prediction error in order to obtain a more robust reconstruction of the low frequencies of reflectivity. A particular case of equation 2.43 is

$$S = \sum_{j=-K}^{K+p} \left| \sum_{i=0}^p g_i R_{i-j} \right|^1 + \sum_{j=-K-p}^K \left| \sum_{i=0}^p g_i^H R_{i+j} \right|^1. \quad (2.44)$$

With this choice, the minimisation of the forward prediction error provides, for instance:

$$\min_{R_{-K:K}} \left\| \begin{bmatrix} g_0 & 0 & \dots & 0 \\ g_1 & g_0 & \dots & 0 \\ \dots & \dots & \dots & \dots \\ \dots & \dots & g_1 & g_0 \\ \dots & \dots & \dots & \dots \\ 0 & \dots & g_p & g_{p-1} \\ 0 & \dots & 0 & g_p \end{bmatrix} \begin{bmatrix} R_{-K} \\ \dots \\ R_0 \\ \dots \\ R_K \end{bmatrix} + \begin{bmatrix} (g_{1:end}) * (R_{-K-p:-K-1}) \\ (g_{2:end}) * (R_{-K-p+1:-K-1}) \\ \dots \\ \dots \\ (g_{1:end-2}) * (R_{K+1:K+p-1}) \\ (g_{1:end-1}) * (R_{K+1:K+p}) \end{bmatrix} \right\|. \quad (2.45)$$

In the sum, the matrix on the left is the convolution matrix of the AR coefficients and the right-most matrix contains the terms derived from the convolution of the AR coefficients and the known part of the spectrum. The solution of the problem can be approximated by an IRLS routine to obtain the minimisation of the L-1 norm of the forward prediction error. Analogously, the solution for the backward prediction error produces a conjugate solution. When minimising the expression 2.43 with a norm different from 2, the reconstruction of the interval property of AI varies (see Figure 2.7) but no norm provides a conclusive improvement.

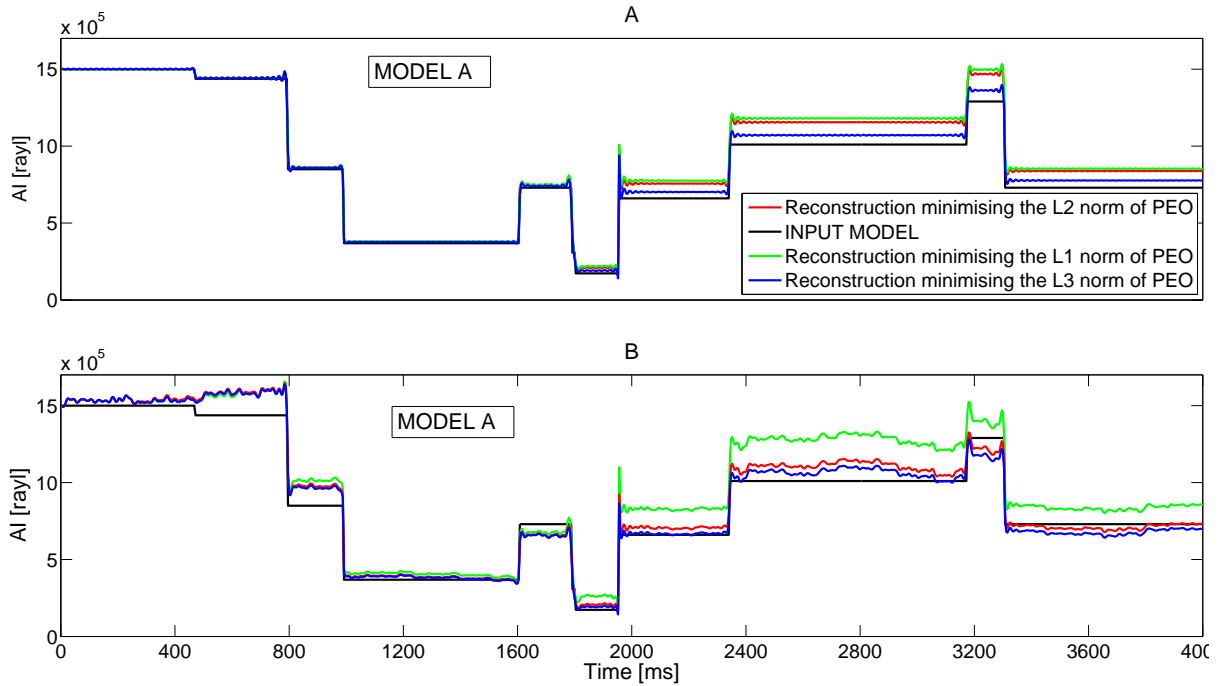


FIGURE 2.7: Reconstruction of the low frequency components of reflectivity by minimising the norm 1, 2 and 3 of the PEO in equation 2.43. The results obtained for the synthetic trace derived from MODEL A are similar in terms of structure both in the absence (panel A) and in the presence (panel B) of noise ($S/N = 34$ dB). No conclusive improvement is seen when the norm adopted to minimise the prediction error varies.

2.5.4 Constraints on Impedance at Depth

The linear relationship between the logarithm of the AI and the sum of the reflectivity (see equation 1.4) has been exploited by Ulrych and Walker (1984) to constrain the reconstruction problem with little computational cost. In fact, errors on the estimated reflectivity cumulate with depth when the reconstructed reflectivity is integrated to obtain an estimate of the interval elastic property. Ulrych and Walker (1984) approached this issue by introducing equality constraints to guide the elastic property toward sensible values at depth (see equation (2.46)). In section 3.3.4, I also extend the relationship provided by Ulrych and Walker (1984) for introducing soft constraints. Here below I analyse possible strategies for introducing the constraints in the estimate in order to avoid instabilities.

Regularisation Strategies for Introducing the Constraints The word regularisation is intended here as “the selection of a well behaved model from the infinite set of models that satisfy the data” (Parker, 1994). Different strategies has been studied for obtaining geologic sensible models from the AR reconstruction of low frequencies. The unconstrained AR reconstruction produces unrealistic outputs on real data: even when very few constraints on AI are enforced (see Chapters 6 and 7) results with unrealistic trace-to-trace variability and biased absolute value of the AI are obtained.

I first considered the presence of hard constraints on AI at depth. Ulrych and Walker (1984) provide a relationship to tie the low frequency components of the reflectivity (R_L^f) to the values

of impedance at depth:

$$\begin{aligned} \log \frac{AI(t)}{AI(0)} - 2 \int_{t_0}^{t_k} r^H(u) du &= 2 \int_{t_0}^{t_k} r^L(u) du = 2 \int_{t_0}^{t_k} \sum_{f=-F_{min}}^{F_{max}} R_L^f e^{-i2\pi fu} du = \\ &= \sum_{f=-F_{min}}^{F_{max}} R_L^f 2 \int_{t_0}^{t_k} e^{-i2\pi fu} du. \end{aligned} \quad (2.46)$$

$(r^H(u))$ is a known term that describes the time-domain reflectivity components within the passband. t_k is the time corresponding to the k -th AI constraint. If the constraints of equation 2.46 are incorporated via Lagrange multipliers (equation 2.47), such as in the Ulrych and Walker (1984) paper, the resulting impedance is prone to show instabilities in the form of unrealistic peaks in the impedance reconstruction. This is due to the incompatibility between the constraints and the unconstrained AR reconstruction. The presence of a large number of constraints, or the absence of noise in synthetic scenarios exacerbates this behaviour (see the bottom panel in Figure 2.8). Ulrych and Walker (1984) proposed the Golub (1965) method to relax the constraints. The system

$$\begin{pmatrix} \mathbf{G} & \mathbf{H} \\ \mathbf{H}^H & \mathbf{0} \end{pmatrix} \begin{pmatrix} \mathbf{R} \\ \lambda \end{pmatrix} = \begin{pmatrix} \mathbf{B} \\ \beta \end{pmatrix} \quad (2.47)$$

is solved by first obtaining the unconstrained solution

$$\mathbf{Z} = \mathbf{G}^{-1} \mathbf{B}, \quad (2.48)$$

and by subsequently calculating the constrained solution as

$$\mathbf{R} = \mathbf{G}^{-H} [\mathbf{B} - \mathbf{H}(\mathbf{H}^H \mathbf{G}^{-H} \mathbf{H})^{-1} (\mathbf{H}^H \mathbf{Z} - \beta)]. \quad (2.49)$$

In the system of equations 2.47, the part $\mathbf{H}\mathbf{R} = \beta$ is the matrix notation of equation 2.44, and λ is the Lagrange multiplier. During the second step described by equation 2.49, a rank reduction (via SVD) of the matrix $(\mathbf{H}^H \mathbf{G}^{-H} \mathbf{H})$ is beneficial to reduce the instabilities. The drawback of the rank-reduction approach is that the constraint relaxation thus obtained, can hardly be related to the a priori geologic knowledge. The solution in this case, may completely ignore one of the constraints in the attempt to fit the other constraints. In order to relax the constraints on impedance in adherence to the geologic knowledge, the AR reconstruction problem can be modified as:

$$\min_{\mathbf{R}} \|\mathbf{G}\mathbf{R} - \mathbf{B}\|_2^2 \quad s.t. \quad \|\mathbf{H}(\mathbf{R} - \mathbf{R}_0)\|_2^2 = N \sum_{j=1}^N \sigma_j^2. \quad (2.50)$$

In equation (2.50) Ulrych and Walker (1984) make the assumption that the uncertainties on each constraint have a Gaussian distribution described by the mean value $(\mathbf{H}\mathbf{R}_0)$ and by the variance σ_j^2 . Assuming the uncertainties to be independent, their sum has a χ^2 distribution of mean equal to the number of constraints (N). This justifies the formulation of equation (2.50), that imposes only a global constraint in the reconstruction. The reconstruction obtained in this case is not exactly the AR reconstruction but it is the closest (least-squares) reconstruction that meets, in a statistical sense, the presence of constraints on AI. In case there is the availability of many constraints at given depth, this formulation tends to smear the uncertainty information on the single constraint and some constraints tend to be relaxed much more than others. A

more punctual approach to the introduction of constraints at given depth can be that of solving a minimisation problem by setting twice as many constraints as the number of known AI values at depth. The impedance can be bounded at each depth between two values, and the resulting reconstruction becomes the closest (norm-2) reconstruction to the AR model that meets the constraints:

$$J = \|\mathbf{CR} - \mathbf{b}\|_2^2 \quad s.t. \quad \begin{cases} \mathbf{HR} \leq \boldsymbol{\beta} + \Delta\boldsymbol{\beta} \\ -\mathbf{HR} \leq -\boldsymbol{\beta} + \Delta\boldsymbol{\beta} \end{cases} \quad (2.51)$$

An alternative approach to the formulation of equation 2.51 consists of solving a weighted least-squares problem with a weighting matrix (\mathbf{W}) that contains the uncertainties on the constraints on its diagonal. Rather than minimise the error $\mathbf{e}^t\mathbf{e} = \|\mathbf{CR} - \mathbf{b}\|_2^2$, the minimisation of the error $\mathbf{e}^t\mathbf{W}\mathbf{e}$, produces a very similar result of the minimisation of the cost function in equation 2.51. This is well known (e.g. (Menke, 1989)), but in particular conditions, the inadequate weighting of the matrix \mathbf{W} could lead to unstable AI estimates. Lagrange multipliers and the weighted least-squares approaches are not adequate in the situation described by the bottom panel of Figure 2.8, while the Golub solution does not meet all the constraints at depth. To avoid introducing instabilities while meeting all the constraints at depth, the constrained least squares approach is adopted throughout the research. Further development on the topic of constraining the reconstruction is reported in section 3.3.4.

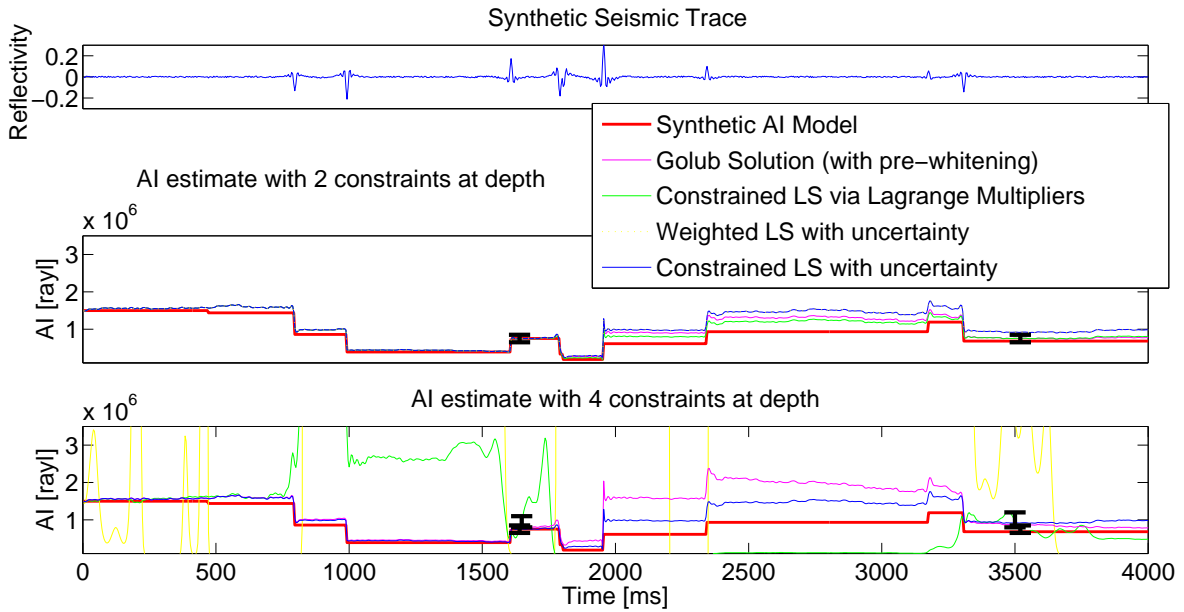


FIGURE 2.8: Effects of the different types of regularisation on the problem of AR AI estimation with constraints at depth. The top panel represents the input synthetic trace. The middle panel shows that when the constraints are not influencing much the AR low frequency reconstruction any regularisation method produces similar results. In the bottom panel, two additional constraints are set very close to the timings of the previous constraints, producing an unstable solution for the Lagrange multipliers and weighted least-squares methods.

2.5.5 High-frequency Reconstruction by Minimum Entropy Deconvolution

The final step for the full-bandwidth extension proposed in the Walker and Ulrych (1983) work, consisted in a blind deconvolution process. The process seeks to obtain the high frequency components of the reflectivity which are compatible with the signal band-width and the completed low-frequencies. The compatibility lies in the fact that both the AR reconstruction and the blind deconvolution methods aim at minimising the number of the events that are sufficient to describe the data. This step makes use, in the paper of Walker and Ulrych (1983), of the Ooe and Ulrych (1979) entropy norm ($V(z)$) to enhance the sparsity:

$$V(z) = \frac{\sum_t z_t^2}{(\sum_t z_t)^2}, \quad (2.52)$$

where $z_t = 1 - e^{-a^2 r_t^2}$. r_t is the time-domain representation of the seismic trace, and a is a scalar which serves as normalisation factor. Walker and Ulrych (1983) maximise the norm $V(z)$ with respect to the unknown high frequency components of the reconstructed trace (R_k). I report the derivation of their algorithm because I found some misprint in the original paper. Given the definition of the discrete Fourier Transform:

$$R_j = \sum_{t=1}^N r_t e^{-\frac{2i\pi kt}{N}}, \quad (2.53)$$

the maximisation of the entropy norm can be imposed by

$$\frac{\partial V}{\partial R_k} = \frac{\partial \frac{\sum_t 1 - e^{-a^2 \sum_{j=-F_N}^{F_N} R_j e^{\frac{2i\pi jt}{N}}}}{(\sum_t 1 - e^{-a^2 \sum_{j=-F_N}^{F_N} R_j e^{\frac{2i\pi jt}{N}}})^2}}{\partial R_k} = 0. \quad (2.54)$$

Analytically solving equation 2.54 for each high frequency component k leads to

$$R_k = \sum_t \left(1 + \frac{1 - z_t}{V \sum_p z_p}\right) z_t r_t e^{-\frac{2i\pi kt}{N}}. \quad (2.55)$$

The system is valid for all the Fourier components, however Walker and Ulrych (1983) calculate R_k only at high frequencies and they constrain the low-mid band to the reconstruction they found via AR modelling. This fact limits the effectiveness of the minimum entropy algorithm in terms of sharpening the spiky features of the time-domain reconstruction of the seismic traces. Figures 2.9 and 2.10 provide a comparison of the results that can be achieved with the constrained procedure and the unconstrained one for the synthetic example of MODEL B. The first approach corresponds to an high frequency completion while the latter corresponds to a full bandwidth minimum entropy deconvolution. Figure 2.11 shows the effects of recursively minimising the entropy norm: only minor changes are visible between this results and the one pass reconstruction of Figure 2.9. The Sacchi, Velis, and Cominguez (1994) norm introduced in section 2.4.3 produces a more stable high frequency reconstruction compared to the original results of Walker and Ulrych (1983). This is particularly evident in the time domain representation of the reconstructed trace of Figure 2.12 that shows a spiky behaviour without the high

frequency artefacts that appear in Figure 2.11 or 2.9.

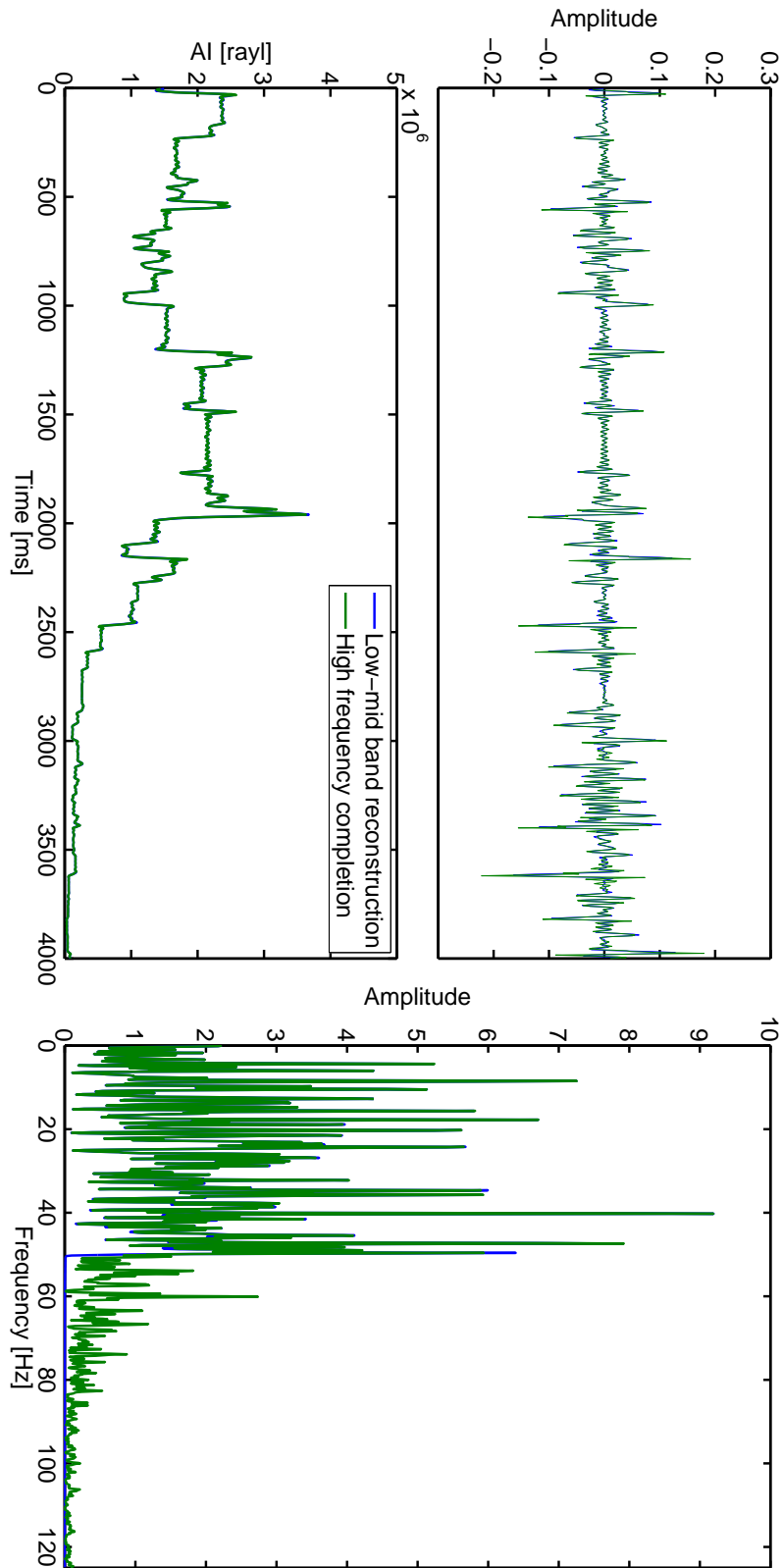


FIGURE 2.9: Reconstruction of the high frequencies of the reflectivity on the synthetic input trace named MODEL B in Figure 2.2. $S/N = 34$ dB in terms of maximum amplitudes. One pass of the original Walker and Ulrych (1983) algorithm applied to high-frequency only. $a=4$ in equation 2.52. The panels on the top show the time-domain representation of the input (blue) and the reconstructed (green) trace in terms of reflectivity and of the interval property of AI. The bottom panel shows the amplitude spectrum of the input (blue) and the reconstructed trace (green).

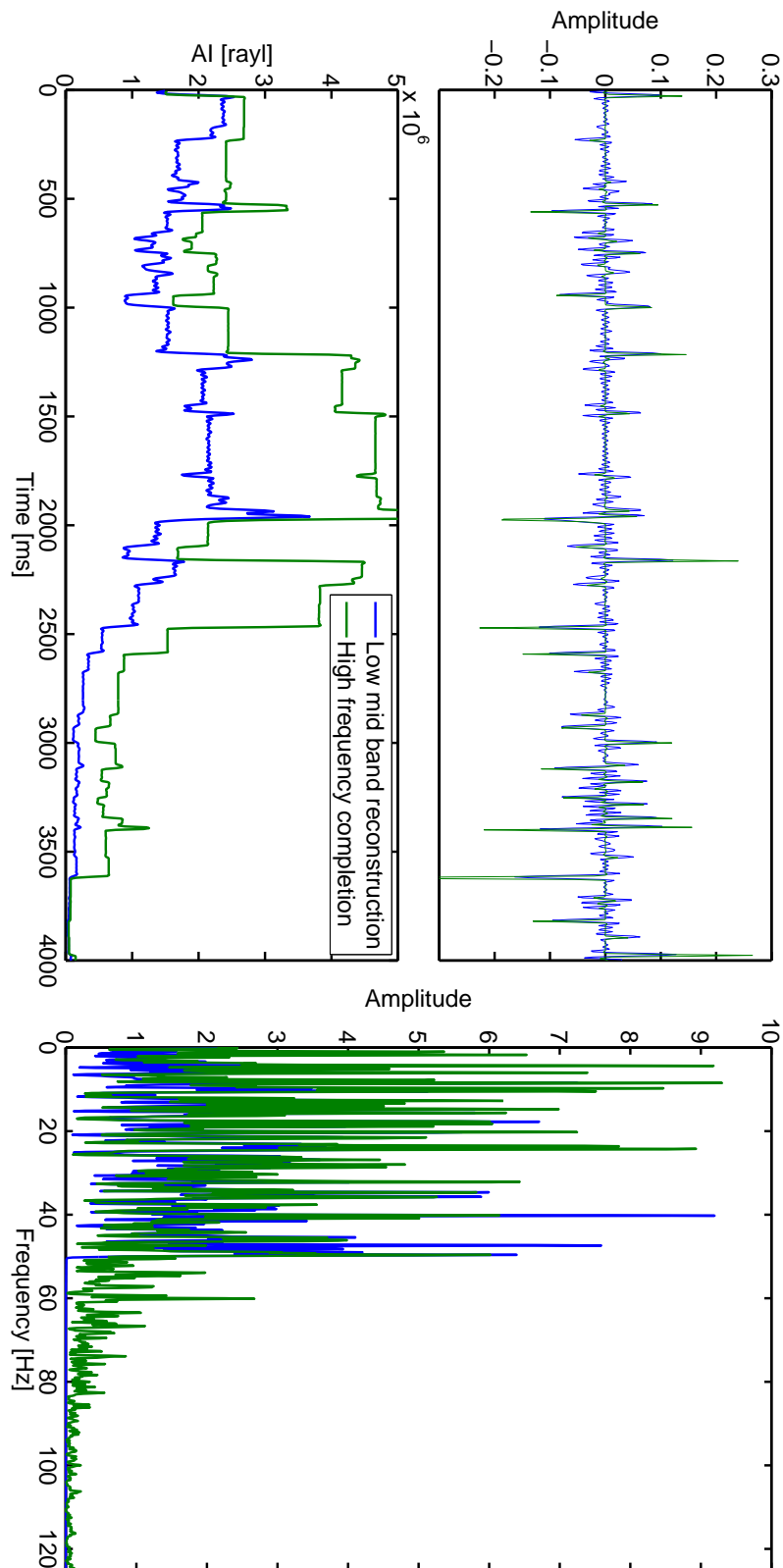


FIGURE 2.10: Reconstruction of the minimum entropy reflectivity on the synthetic input trace named MODEL B in Figure 2.2. $S/N = 34$ dB in terms of maximum amplitudes. One pass of the Ooe and Ulrych (1979) algorithm applied to all the frequencies. $a=4$ in equation 2.52. The panels on the top show the time-domain representation of the input (blue) and the reconstructed (green) trace in terms of reflectivity and the interval property of AI. The bottom panel shows the amplitude spectrum of the input (blue) and the reconstructed trace (green).

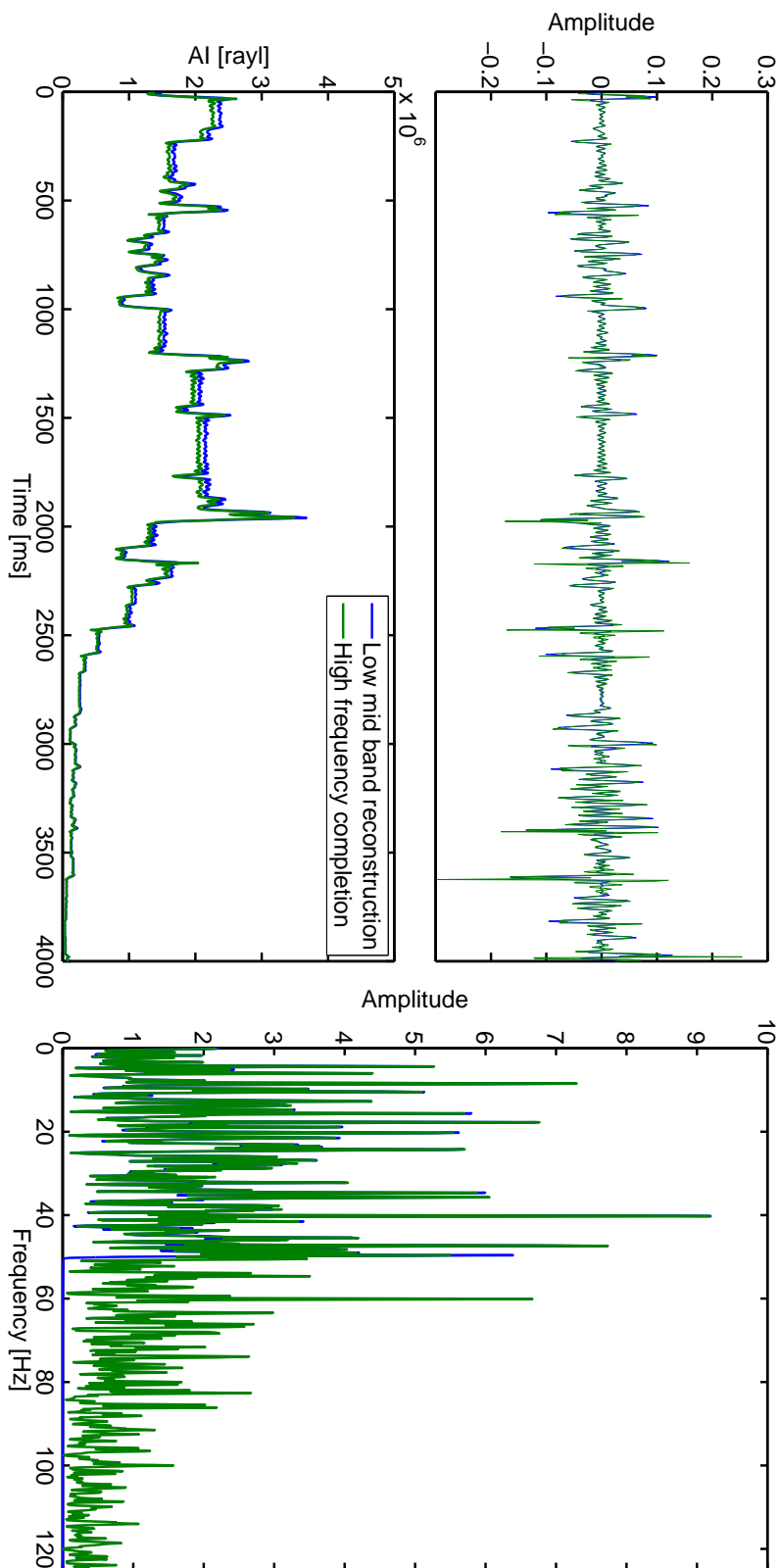


FIGURE 2.11: Reconstruction of the high frequencies of the reflectivity on the synthetic input trace named MODEL B in Figure 2.2. $S/N = 34$ dB in terms of maximum amplitudes. Walker and Ulych (1983) algorithm has been applied recursively until a maximum value in the variational norm (equation 2.52) is found. $a=4$ in equation 2.52. The panels on the top show the time-domain representation of the input (blue) and the reconstructed (green) trace in terms of reflectivity and the interval property of AI. The bottom panel shows the amplitude spectrum of the input trace (blue) and the reconstructed spectrum (green).

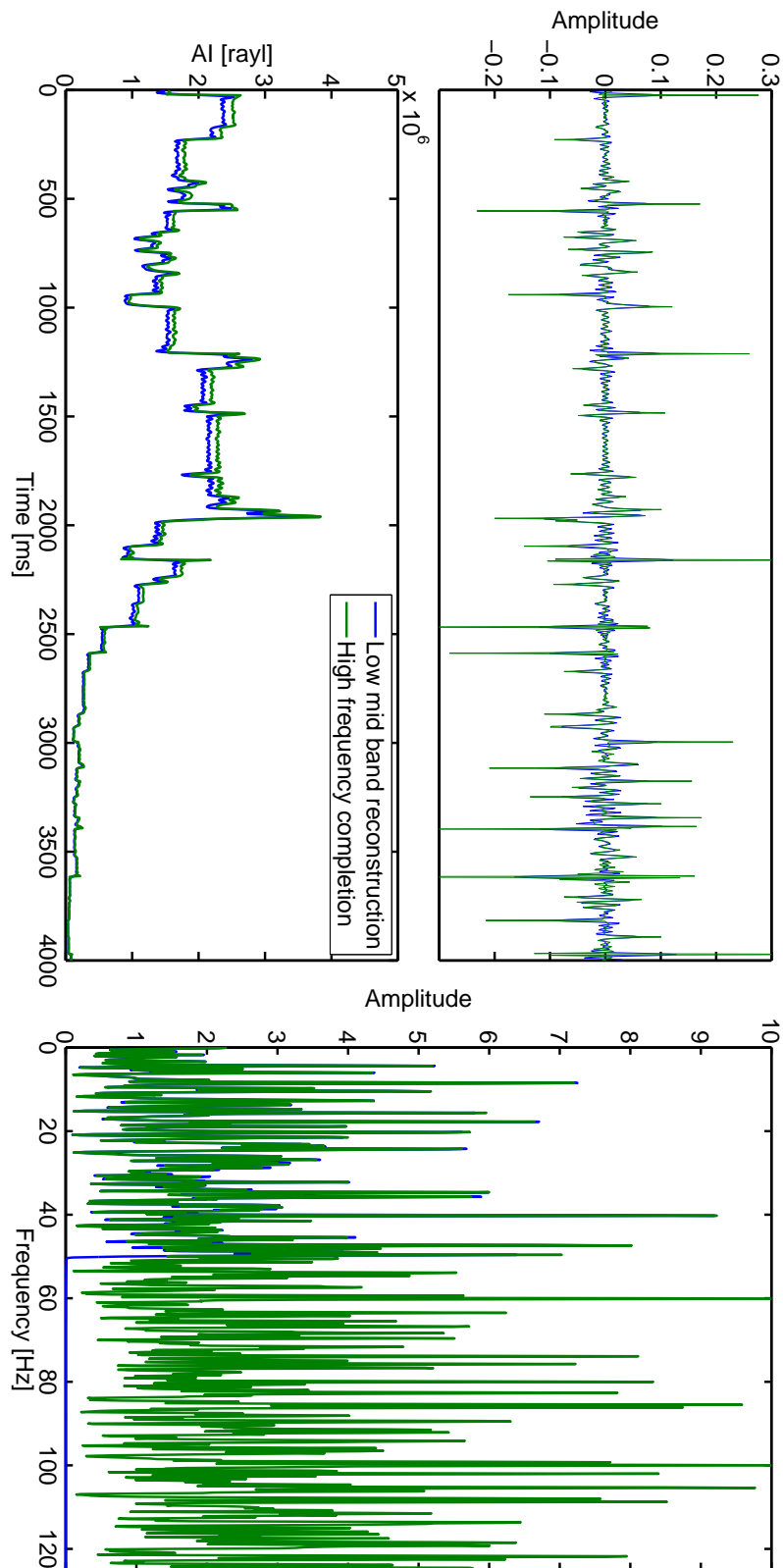


FIGURE 2.12: Reconstruction of the high frequencies of the reflectivity on the synthetic input trace named MODEL B in Figure 2.2. $S/N = 34$ dB in terms of maximum amplitudes. Sacchi, Velis, and Cominguez (1994) algorithm has been applied recursively to high frequencies as described in section 2.4.3. The panels on the top show the time-domain representation of the input (blue) and the reconstructed (green) trace in terms of reflectivity and the interval property of AI. The bottom panel shows the amplitude spectrum of the input trace (blue) and the reconstructed spectrum (green).

2.5.6 Comparison between AR Reconstruction and Sparse-Spike Solution

I briefly discuss a possible implementation of the sparse-spike reconstruction for acoustic impedance estimation in order to compare the results of the AR reconstruction to the well-established results of the sparse-spike family of methods (Russell, 1988). One of the computationally cheapest way to implement the sparse-spike reconstruction is by solving a problem very similar to that of equation (2.5), in which the minimisation of the part $\|\mathbf{W}\mathbf{r} - \mathbf{d}\|_2^2$ simulates the presence of the constraints coming both from the data in the seismic bandwidth, and the impedance values at depth. The solution could be achieved via an IRLS algorithm. The minimisation of the cost function

$$J = \min_{\mathbf{r}} \|(\mathbf{W} + \lambda\mathbf{Q})\mathbf{r} - \mathbf{d}\|_2^2, \quad (2.56)$$

with λ the same hyperparameter of equation 2.5, leads to a very close approximation of the sparse-spike solution. The matrix \mathbf{Q} is set to the identity matrix in the first iteration of the re-weighted least squares routine, and it is then modified as

$$\mathbf{Q} = \begin{bmatrix} \frac{1}{|r_1|+\epsilon} & 0 & 0 \\ 0 & \dots & 0 \\ 0 & 0 & \frac{1}{|r_n|+\epsilon} \end{bmatrix}, \quad (2.57)$$

where ϵ is a positive small value. When the result little changes from the previous iteration or when the maximum number of iterations has been reached, the algorithm terminates. I report, here below, a comparison between the AR estimation of AI from normal incidence seismograms, and the sparse-spike estimation for the case of a synthetic seismic trace and a real marine 2D section from the Rockall Trough area. A description of the marine dataset is available in Chapter 3. The synthetic example refers to a sparse reflectivity with S/N set at the two levels of 60 dB (Figure 2.13) and 20 dB (Figure 2.14). The sparse-spike (minimum L1 norm solution) and the AR solutions show similar results. Late traveltimes show a biased reconstruction of AI, but none of the solutions could be considered better than the other, the only difference being the more blocky behaviour of the sparse-spike result.

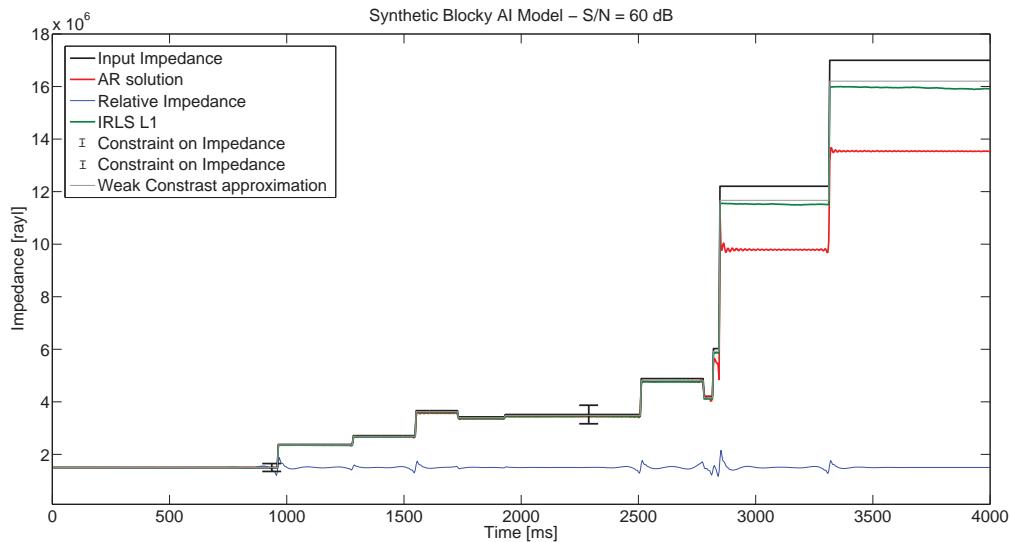


FIGURE 2.13: Reconstruction of the AI of a sparse time series corresponding to a normal incidence seismogram with additional white noise ($S/N = 60$ dB in terms of maximum amplitudes). The reconstruction has been performed via the AR method (red curve) and via a minimum L1 norm solution (green curve) for comparison.

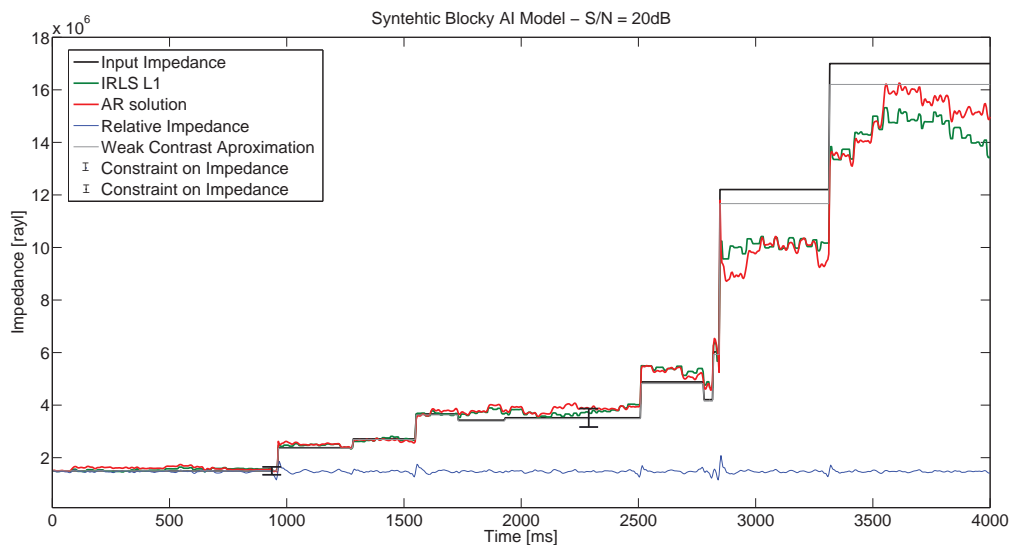


FIGURE 2.14: Reconstruction of the AI of a sparse time series corresponding to a normal incidence seismogram with additional white noise ($S/N = 20$ dB in terms of maximum amplitudes). The reconstruction has been performed via the AR method (red curve) and via a minimum L1 norm solution (green curve) for comparison.

The sparse-spike solution is very sensitive to the value of the trade-off parameter between sparseness and data fitting λ . Figure 2.15 reports the AI estimations that could be achieved when increasing λ by two orders of magnitude with respect to the result of Figure 2.13. When the regularisation term that governs the sparseness of the solution is too high, less layers than the actual number of events in the synthetic seismic trace are identified.

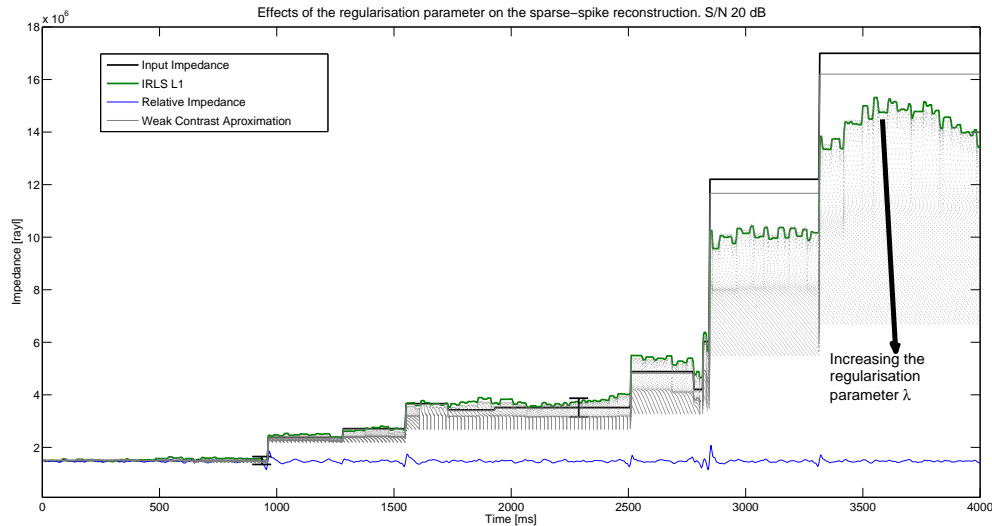


FIGURE 2.15: Reconstruction of the AI of a sparse time series ($S/N = 20$ dB in terms of maximum amplitudes) corresponding to a normal incidence seismogram. The reconstruction has been performed for 100 different minimum L1 norm solutions with λ varying from the level of Figure 2.14 (green) to hundredth times this level.

The tuning of the parameters of the sparse-spike algorithm has been more demanding than the tuning of the AR algorithm. Overall the two approaches, when constrained at two different depths, produce similar results on the AI, and also on the reflectivity. This is also true for the case of the section of Figure 2.16, a seismic line from the Rockall Trough marine dataset. In the real case scenario assumed for comparison, the AR and the sparse-spike reflectivities evidence the same events. The events are probably more resolved by the sparse-spike solution (2.17) than they are by the AR solution (Figure 2.18), and this is particularly evident when comparing the zoom section of Figure 2.21 to the zoom section of Figure 2.22.

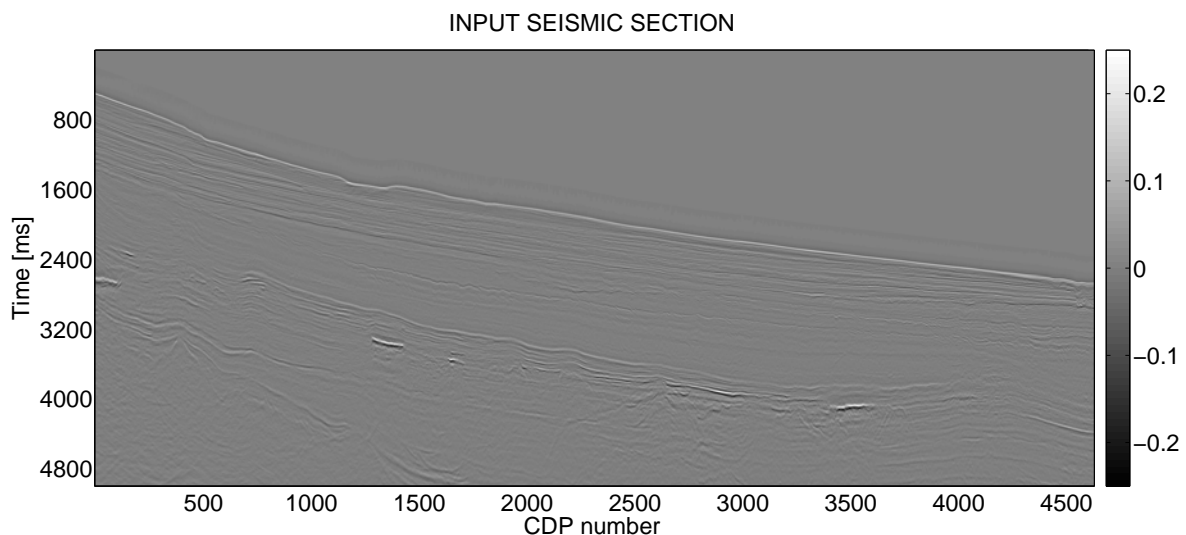


FIGURE 2.16: Input seismic section from the Rockall Trough area adopted for comparing the AR and the sparse-spike solution.

The amplitudes of the reference 2-D seismic section have been scaled to amplitudes pertaining to the reflectivity before the reconstruction. The aspect of scaling the seismic data is discussed

in Chapter 3. The AI estimation reported in Figure 2.18 uses the same parametrisation of Figure 3.12B (other than lacking a lateral smoothing weight): this choice allows for a comparison between the sparse-spike inversion and the results of Chapter 3. Figures 2.17 and 2.18 show the AI estimation obtained via sparse-spike reconstruction of the seismic traces and via the AR modelling respectively.

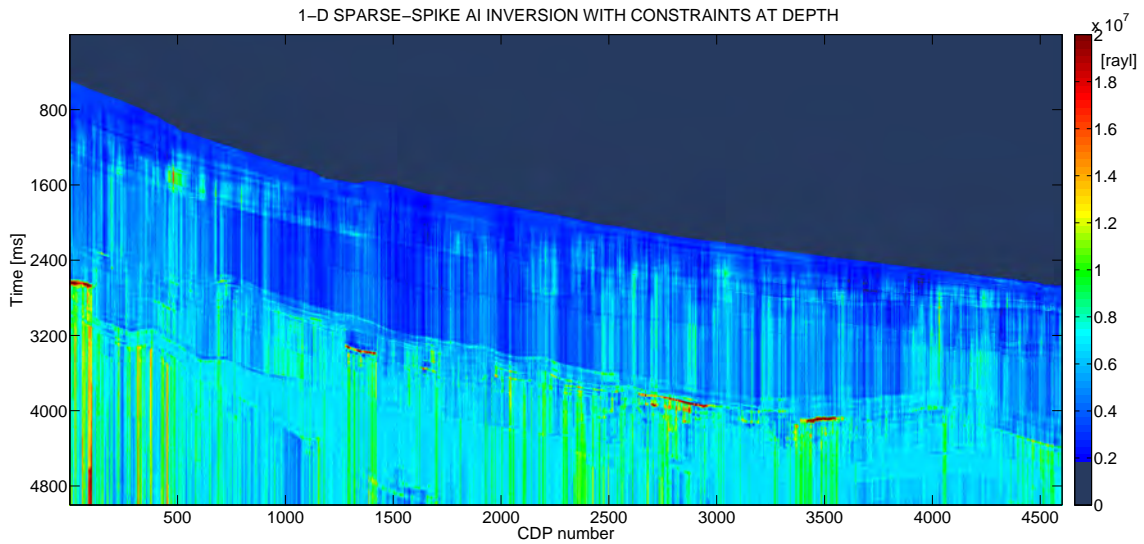


FIGURE 2.17: *Absolute AI estimation [rayl] after the sparse-spike reconstruction of the reflectivity.*

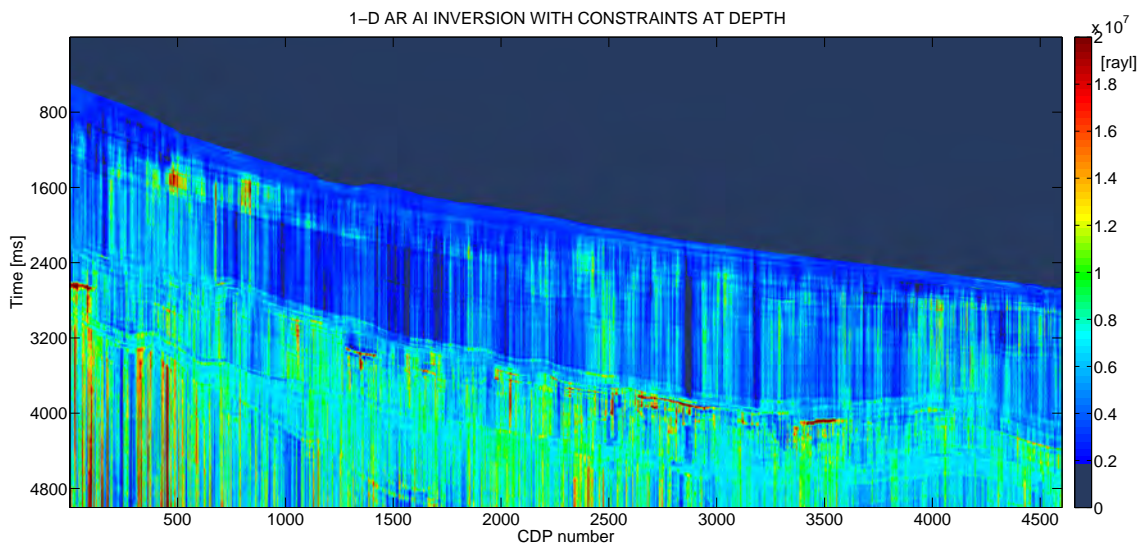


FIGURE 2.18: *Absolute AI estimation [rayl] after the AR reconstruction of the reflectivity.*

The estimation of AI show very similar patterns in Figure 2.17 and Figure 2.18. The similarity may indicate that both methods are valid on real data as long as the convolutive model at their basis holds true.

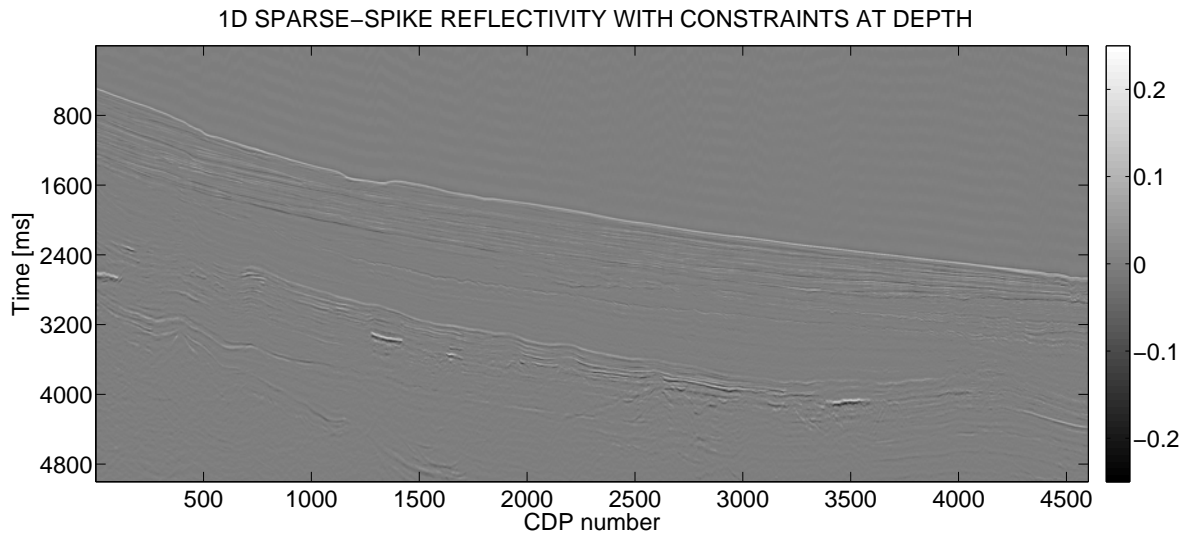


FIGURE 2.19: *Reconstruction of the reflectivity via the sparse-spike method from a full-stack seismic section.*

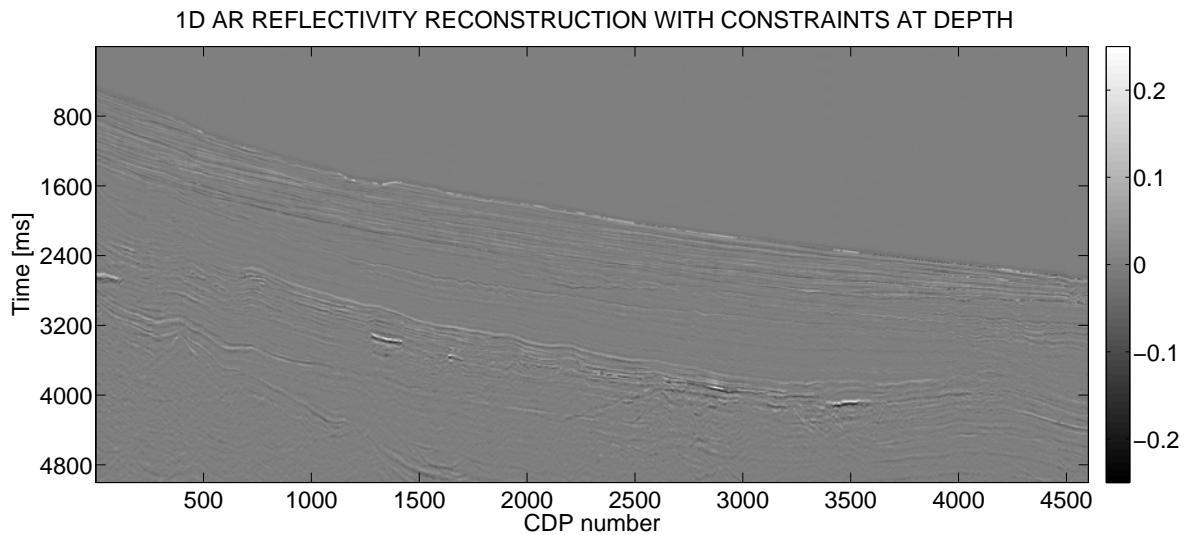


FIGURE 2.20: *Reconstruction of the reflectivity via the AR method from a full-stack seismic section.*

The reconstructed reflectivity appears sharper in the sparse-spike method than in the AR one, a zoom section in the travel-time range 1000-3000 ms is provided in Figure 2.21 and 2.22 to better appreciate this aspect.

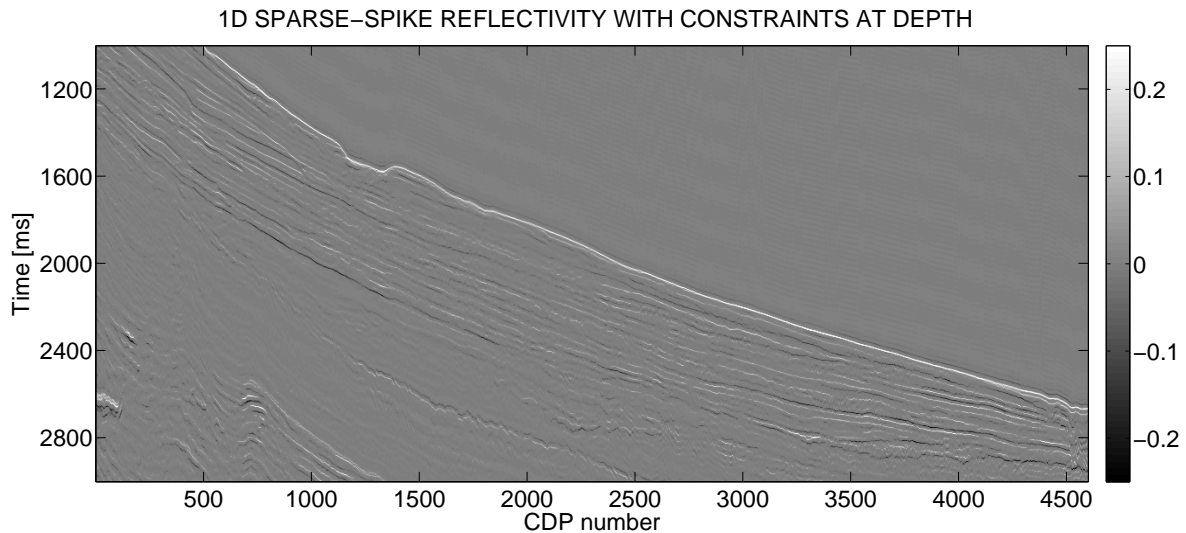


FIGURE 2.21: Reconstruction of the reflectivity via the sparse-spike method from a full-stack seismic section. Zoom in the TWT range 1000-3000 ms.

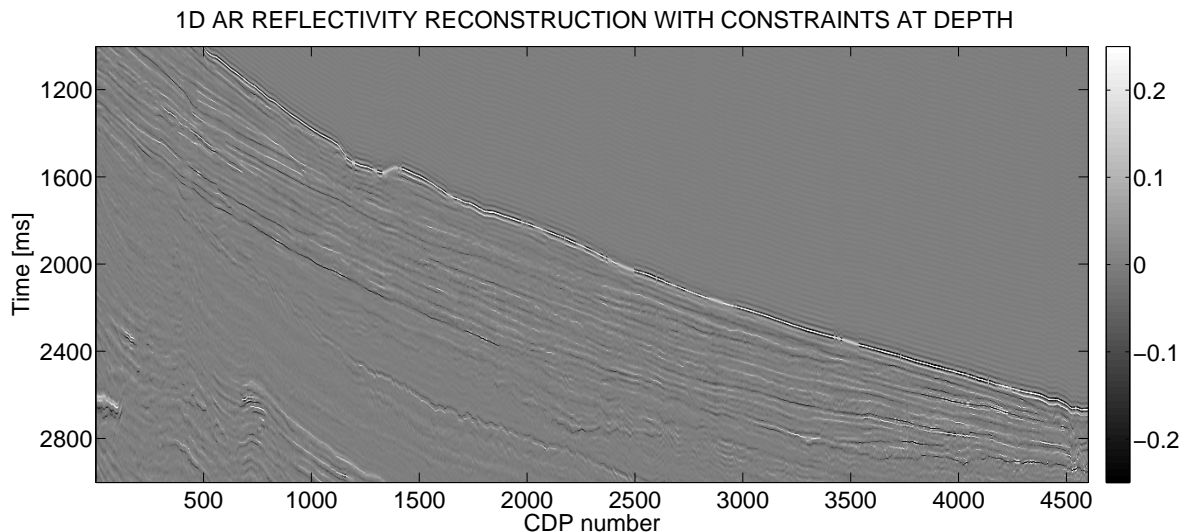


FIGURE 2.22: Reconstruction of the reflectivity via the AR method from a full-stack seismic section. Zoom in the TWT range 1000-3000 ms.

2.5.7 Residual Wavelet Effects

The following section is edited from the appendix A of the paper “Acoustic impedance estimation from combined harmonic reconstruction and interval velocity” (Bianchin, Forte, and Pipan, 2019). One of the hypothesis at the basis of the AR modelling for low frequency interpolation is that the seismic data represent a bandlimited version of reflectivity before fitting the AR model. However, on real seismic data, it is not possible to completely remove all the wavelet effects. This leads to incorrectly assume that equation 2.1 actually describes the recorded data. The consequences of fitting an order 1 AR model to a non-stationary complex-series is presented for the particular case where $w(t)$ is described by a Ricker wavelet with a

given dominant frequency (f_d). This wavelet has the following time-domain analytic formulation:

$$w(t) = (1 - \pi f_d^2 t^2) e^{i2\pi^2 f_d^2 t^2} \quad (2.58)$$

which leads to an amplitude spectrum:

$$W(f) = \frac{2f^2}{\sqrt{\pi} f_d^3} e^{-\frac{f^2}{f_d^2}}. \quad (2.59)$$

In the absence of noise and for a single event r_1 in the data, equation 2.58 can be rewritten as

$$d(t) = [(1 - \pi f_d^2 t^2) e^{i2\pi^2 f_d^2 t^2}] * [r_1 \delta(t - \tau_1)]. \quad (2.60)$$

Equation 2.60 has the following representation in the Fourier domain

$$D(f) = \frac{2f^2}{\sqrt{\pi} f_d^3} e^{-\frac{f^2}{f_d^2}} r_1 e^{-i2\pi f \tau_1}. \quad (2.61)$$

In case I model equation 2.61 as an AR process of order 1, the resulting AR coefficients would depend on a frequency term:

$$D(f) = \frac{2(f-1)^2}{\sqrt{\pi} f_d^3} e^{-\frac{(f-1)^2}{f_d^2}} r_1 e^{-i2\pi(f-1)\tau_1} \frac{f^2}{(f-1)^2} e^{-\frac{f^2}{(f-1)^2}} e^{-i2\pi\tau_1}. \quad (2.62)$$

If I name $r_1 e^{-i2\pi\tau_1}$ as α_1

$$D(f) = D(f-1) \alpha_1 \frac{f^2}{(f-1)^2} e^{-\frac{f^2}{(f-1)^2}}. \quad (2.63)$$

Recursively

$$D(f) = D(f-k) \alpha_1^k \frac{f^2}{(f-k)^2} e^{-\sum_{j=1}^k \frac{(f-j+1)^2}{(f-j)^2}}. \quad (2.64)$$

The extension to longer AR models depends on the spectral estimator used and it is not analytically derived here. In any case, modelling the complex time-series as a stationary AR process neglects the presence of the wavelet: if the signal shows a decaying amplitude with frequency in the pass-band, the AR model coefficients are biased by that decay and the subsequent frequency content interpolated outside the band-pass region is biased. The bias is higher when the spectral distance between the known frequencies adopted to fit the AR model to the data and the frequency to be predicted increases. For AR models of order 1, this is due to the term

$$\frac{f^2}{(f-k)^2} e^{\sum_{j=1}^k -\frac{(f-j+1)^2}{(f-j)^2}} \quad (2.65)$$

from equation 2.64, which increases as the distance between the frequency to be predicted (f) and the known spectral component ($f-k$) increases. The issue may find a solution by modelling the Fourier representation of the seismic trace as a time-variant AR process (Rao, 1970), but a larger number of parameters is required.

2.6 Envelope Inversion

A different approach for extracting the low frequency information encoded in the seismogram is the envelope inversion. There are cases (i.e. Vibroseis data) in which the seismic data can be thought as a modulated reflectivity signal on a low frequency carrier which is related to inelastic attenuation and to the long wavelength impedance structure. Wu, Luo, and Wu (2014) propose a method for extracting the low frequency carrier out of the seismic envelope. Envelope inversion is more promising when the signal is monochromatic or very narrow band, which is at odds with the assumptions at the basis of the sparse-spike reconstruction. It is still valid on synthetic examples that mimic traditional seismic data. No application on real data has been demonstrated to date, possibly because the assumptions of the method are too strong with respect to the seismic data quality. According to the sampling theorem, long sweeps provide information on the low frequency content of the data (as shown in Figure 2.23). The amplitude of the envelope over time is closely related to the AI. In fact the amplitude spectrum of the envelope of each monochromatic signal is a Dirac delta centred at the DC component. Convolution of the full-bandwidth reflectivity of the earth with the envelope of a monochromatic signal provides an output with the energy mainly distributed at the low frequencies. As soon as the input source contains more than one frequency, the envelope information drifts from the Dirac delta, thus leading to a degraded reconstruction of interval properties at depth. The envelope inversion by itself does not provide information on the polarity of the interval property estimated, but Chen et al. (2018) propose a solution to this end by incorporating in the inversion a phase detection algorithm. The main concern on the application of the methodology to real data is that the carrier cannot be easily separated from the other frequency components pertaining to the source wavelet. Other issues for the application of the method are related to attenuation, dispersion and to the problems related to transmitting a sweep of constant frequency into the subsurface. Moreover, the interference due to thin layers disrupts the reconstruction analogously to the case of the sparse-spike and AR inversion (e.g. Figure 3.1).

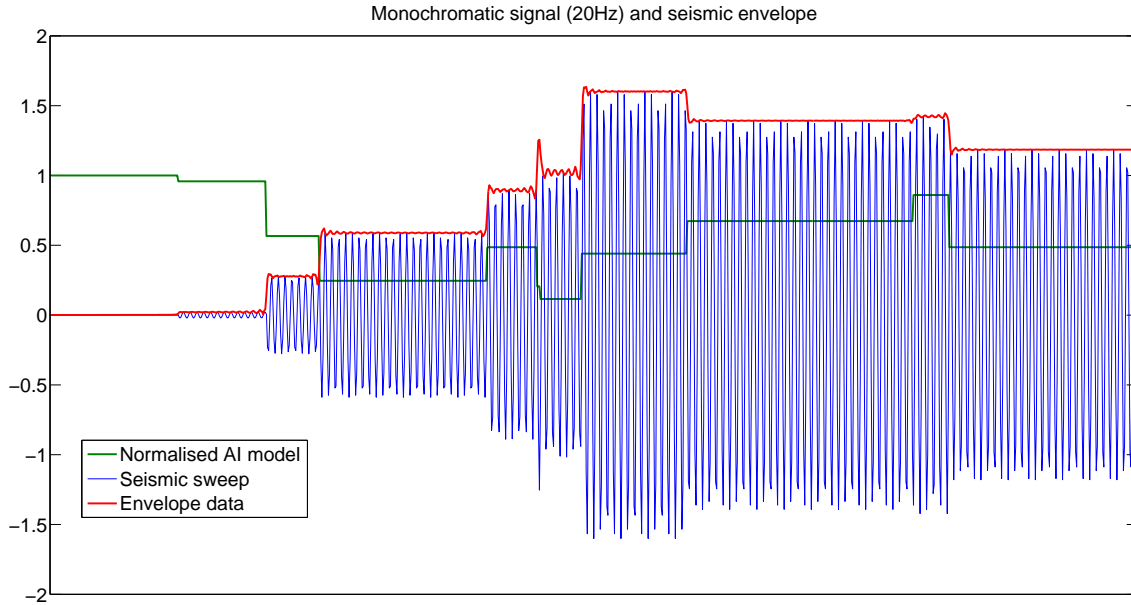


FIGURE 2.23: Effects of adopting as seismic source a monochromatic sweep (20 Hz) on the MODEL A AI structure. Some indications on the magnitude of the impedance contrast can be obtained by evaluating the envelope data (red curve), but they do not include polarity.

2.7 Bayesian Approach to Sparse Inversion

If a priori knowledge on the model of low-frequencies of the acoustic impedance is available with a given degree of confidence, this piece of information can be added to the band-limited knowledge brought about by the seismic data. The deterministic merge of the two sources of information can be achieved by selecting a range of frequencies pertaining to the data and a range of frequencies pertaining to the model (mutually orthogonal) and then summing the inversion result based on the data, with the a priori model. A probabilistic reconstruction can be based on the Bayes' rule for obtaining the posterior probability of the model given the data (see section 1.5). The probabilistic approach has the advantage that it provides a measure of the uncertainty related to the most likely model. Adequate information must be provided to fill the indeterminacy of the problem even in this case and, provided that no useful information is available on the seismic data below a given frequency, the probability distribution of the posterior model is the same of the prior model in the low frequency band. If the a priori model is described by a (multivariate) Gaussian distribution of known mean ($\mathbf{m}_{\text{prior}}$) and covariance ($\mathbf{\Sigma}$):

$$p(\mathbf{m}) = \frac{e^{(\mathbf{m}-\mathbf{m}_{\text{prior}})^t \mathbf{\Sigma}^{-1} (\mathbf{m}-\mathbf{m}_{\text{prior}})}}{2\pi^{N/2} \det(\mathbf{\Sigma}^{-1})} \quad (2.66)$$

and the data errors ($\mathbf{A}\mathbf{m} - \mathbf{d}$) are also assumed Gaussian, with data covariance matrix \mathbf{C}_d , the maximum a posteriori solution is

$$\mathbf{m} = (\mathbf{A}^t \mathbf{C}_d \mathbf{A} + \mathbf{\Sigma}^{-1})^{-1} (\mathbf{A}^t \mathbf{d} + \mathbf{\Sigma}^{-1} \mathbf{m}_{\text{prior}}). \quad (2.67)$$

Instead of introducing information on the low frequency distribution of the AI, it is possible to introduce a priori information on the statistical properties of reflectivity and later integrate the reconstructed reflectivity into impedance. When the distribution of the reflectivity coefficients is Gaussian and the data errors are random (Gaussian likelihood), equation (2.67) can be adopted to obtain the maximum a posteriori model. In this case no bandwidth extension is obtained. Sacchi (1997) discusses a way to introduce longer tailed a priori distributions for the estimate of the full-bandwidth of reflectivity from band-limited seismic data. One of the approaches he proposes is based on the Cauchy a priori distribution which approximates a sparsity-based model in the explanation of the seismic data:

$$p(\mathbf{m}) \propto \prod_{i=1}^N \frac{1}{1 + \frac{m_{0i}^2}{2\sigma_i^2}}, \quad (2.68)$$

where m_0 represents the expected value, and σ_0 represents the half-width of the Cauchy distribution. The maximum a posteriori becomes in this case:

$$p(\mathbf{m}|\mathbf{d}) \propto e^{-\sum_{i=1}^N \frac{(A_i \mathbf{d} - m_i)^2}{2\sigma_i^2}} \prod_{i=1}^N \frac{1}{1 + \frac{m_i^2}{2\sigma_i^2}} \quad (2.69)$$

or in an alternative form (Sacchi, 1997):

$$p(\mathbf{m}|\mathbf{d}) \propto e^{-\sum_{i=1}^N \frac{(A_i \mathbf{d} - m_i)^2}{2\sigma_i^2}} e^{-\sum_{i=1}^N \log(1 + \frac{m_i^2}{2\sigma_i^2})} = ae^{(\mathbf{A}\mathbf{m} - \mathbf{d})^t \Sigma_d^{-1} (\mathbf{A}\mathbf{m} - \mathbf{d}) - \log(1 + \mathbf{m}^t \Sigma_m^{-1} \mathbf{m})}. \quad (2.70)$$

The maximisation of the posterior distribution in this case leads to a re-weighted least squares problem:

$$\mathbf{A}^t \Sigma_d^{-1} \mathbf{A} \mathbf{m} - \left(\frac{\Sigma_m^{-1} \mathbf{m}}{1 + \mathbf{m}^t \Sigma_m^{-1} \mathbf{m}} \right) = \mathbf{A}^t \Sigma_d^{-1} \mathbf{d}. \quad (2.71)$$

The reweighting term in the least squares problem is $\frac{\Sigma_m^{-1}}{1 + \mathbf{m}^t \Sigma_m^{-1} \mathbf{m}}$. The solution via iterative schemes (i.e. IRLS) determines the expected value of the posterior model (\mathbf{m}). The Variance of the posterior model must be numerically estimated.

Chapter 3

Acoustic Impedance Estimation from Combined Harmonic Interpolation and Interval Velocity

3.1 Introduction

This Chapter introduces a post-stack low-frequency reconstruction methodology that aims at inferring the absolute value of the acoustic impedance of the subsurface from amplitudes of seismic records and ancillary information that may be available in the aftermath of a seismic survey. The method is based on the incorporation of the velocity field in the AR approach detailed by Walker and Ulrych (1983) and further discussed in Chapter 2. Most of the contents of this Chapter could be found in Bianchin, Forte, and Pipan (2019). The 1-D trace-by-trace approach discussed here implies a computationally inexpensive algorithm that can be useful for an initial assessment of the subsurface acoustic properties in an inversion project. The subsurface AI model is reconstructed by assuming an acoustic propagation medium that is made up of a limited number of isotropic layers. Low frequencies of this model are ill-conditioned components of the solution because of the poor S/N that active-source seismic data exhibit at those frequencies. Typically, when dealing with seismic data for oil and gas exploration, frequencies below 5-10 Hz are strongly affected by acquisition and environmental noise due to the limited amount of energy produced by the seismic sources in that spectral range (e.g. Lesage et al., 2015). Broadband seismic data acquired in recent years, show a good S/N starting from frequencies as low as 2.5 Hz (Soubaras and Lafet, 2011). In any case, the proposed method remains useful for conventional, as well as for higher resolution seismic data. Several inversion methods for the recovery of noisy low frequencies exist (Veeken and Da Silva, 2004). The novelty of the proposed method consists on modifying the autoregressive (AR) approach of (Walker and Ulrych, 1983) by constraining the AR inversion using a seismic-based velocity field. I call this approach combined AR-velocity (CARV) method. The AR low frequency interpolation method was proposed together with the minimum L1-norm solution (Oldenburg, Scheuer, and Levy, 1983) in the 1980's. The latter solution found larger success by the advent of fast algorithms (i.e. Iterative Reweighted Least Squares) in the field of linear programming. Minimum L1 or L1/L2 norm solutions do not require a spectral estimation with its associated sources of error. They make a different a priori assumption: the reflectivity has a sparse time-domain representation (Walden and Hosken, 1985). In this respect, they single out different AI

models than the ones identified by the AR reconstruction. More recently, Gholami and Sacchi (2013) achieved a sparse solution by minimizing the total variation of AI rather than performing the reconstruction in reflectivity domain. Many other methods for bandwidth extension have been proposed to date but I limit my analysis to the harmonic interpolation methods for a physically valid quantitative reconstruction of the acoustic properties (Liang, Castagna, and Torres, 2017).

The AR method for AI inversion (section 2.5) is a model-based method. It predicts the low frequency components of each seismic trace by fitting an AR model to the frequency components that show an adequate S/N. The AR model assumes the signal to be composed of a limited number of events in time domain. A limited number of events in time domain corresponds to a limited number of complex sinusoids in the Fourier domain and in turn to a blocky AI. By assuming that the trace is made up of a limited number of reflections, ill-conditioned low frequency components of reflectivity are univocally reconstructed to be consistent to the components measured in the bandwidth where the S/N is higher. The reconstruction is based on the extension of few sinusoids estimated from the data, hence the term harmonic. The reconstruction makes use of the conjugate symmetry of real signals in the Fourier domain, hence the term interpolation. The reconstruction is deterministic because the inverted output consists only of a single model among many that fit the data. The deterministic nature of the proposed estimates does not prevent to carry out a sensitivity analysis on the adopted parametrization, in order to assess the confidence on the estimates. The most relevant parameters to consider are the impact of the interval velocity field in the estimate, the number of reflection events to be modelled, and the frequency band in which the AR model is estimated.

3.2 Theory

In order to obtain a sensible absolute AI inversion, the input seismic trace must be properly processed to include only primary energy. Effects of source and receiver signatures must be accounted for and removed during processing. Accurate imaging is required in order to place seismic events at their true subsurface locations before inversion. The inversion algorithm proposed here does not account for non-zero incidence angles; therefore the input post-stack data should ideally be a near-angle partial stack. The choice of angles has to be a trade-off between data quality, which is related to stacking fold, and the offset required to achieve such fold. Alternatively, the AVO intercept section could be used as input for the reconstruction. This implies that the AVO behaviour of the data is properly modelled, which could be problematic when strong anisotropic or higher order effects are present in the records. Relative amplitudes of the events must be preserved throughout processing. Since often the relative amplitude is preserved but the processing is not actually “true amplitude”, I invoke a global scalar for the whole seismic section. In absence of accurate well log ties, the scalar can be approximately determined from the a priori knowledge of AI at two different depths and applied to the data before inversion.

The convolutional model of equation 2.1 is at the root of the impedance inversion method

proposed in this Chapter. Dispersion and attenuation are not taken into account by the convolutional model as well as by the proposed algorithm. In order to uniquely single out the interfaces between layers of contrasting AI, I make three assumptions: weak dispersion, sparsity of reflectivity (Oldenburg, Scheuer, and Levy, 1983) (and more recently Hargreaves, Treitel, and Smith (2013)), and high frequency approximation (i.e. Bleistein, Cohen, and Stockwell (2001) pp. 5-6). The high frequency approximation assumes that the rock property variations have much longer wavelength than the longest wavelength of the seismic source. In the presence of thin layers the AR method is expected to fail and the absolute value of the predicted AI to be biased below those features (see Figure 3.1 at about traces 2-10 for reference). As presented in section 2.5.7, the absolute value of the AI is also sensitive to the presence of residual wavelet effects (see Figure 3.2). A phase shift larger than about 30° produces a bias in the estimate that cannot be neglected (Simm and Bacon, 2014). This behaviour is well known (Ulrych and Walker, 1984) and additional information (interval velocity and a priori geologic constraints) is required to increase the robustness of the inversion to the violation of the model assumptions in real case scenarios.

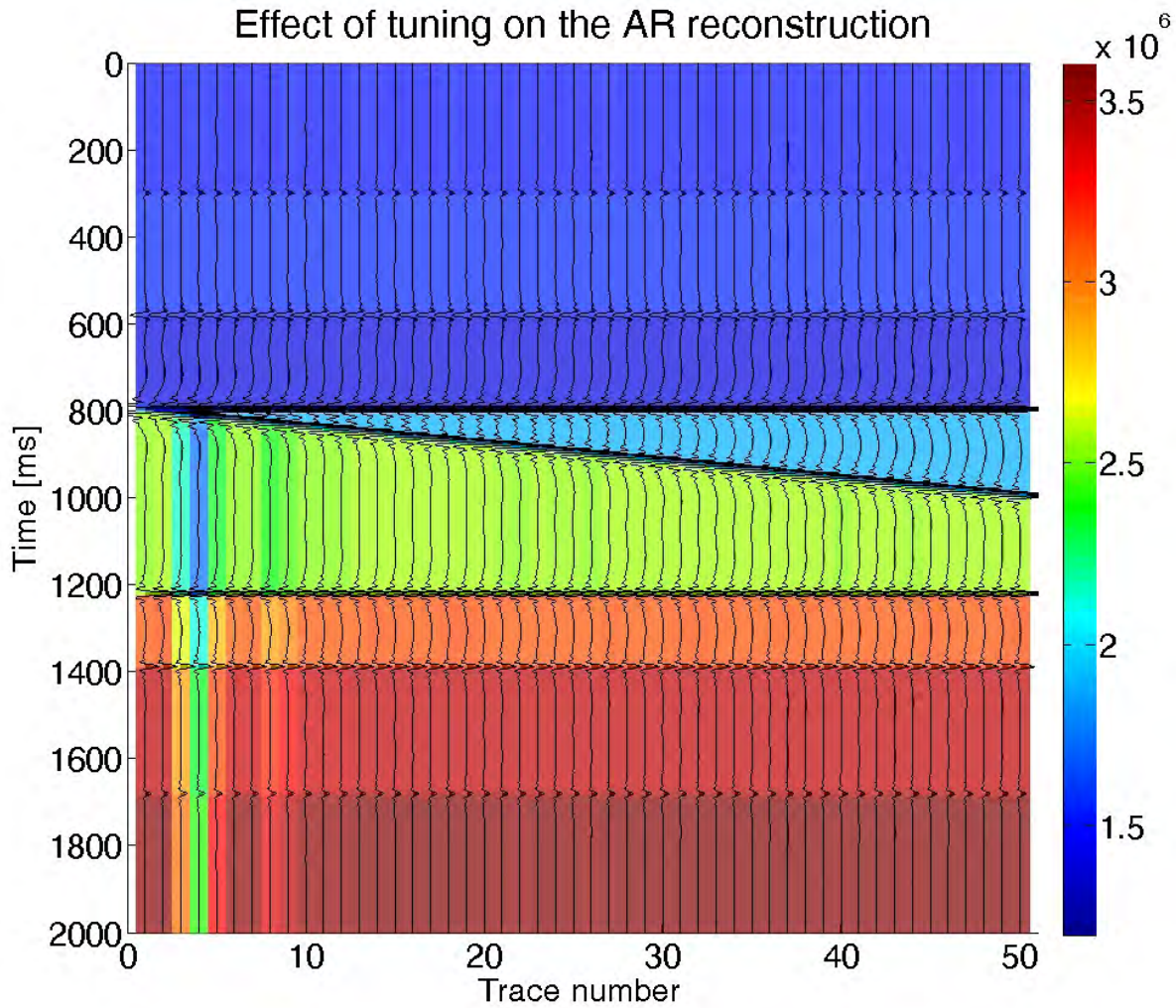


FIGURE 3.1: Synthetic wedge model that shows the effects of thin beds in the AR reconstruction of AI. Reconstructed AI is displayed in colours on top of the synthetic seismic input (wiggles). Input data are band-limited by a Butterworth zero phase filter with 7-80 Hz cut-off frequency, while the frequency band 12-50 Hz has been used for the AR modelling.

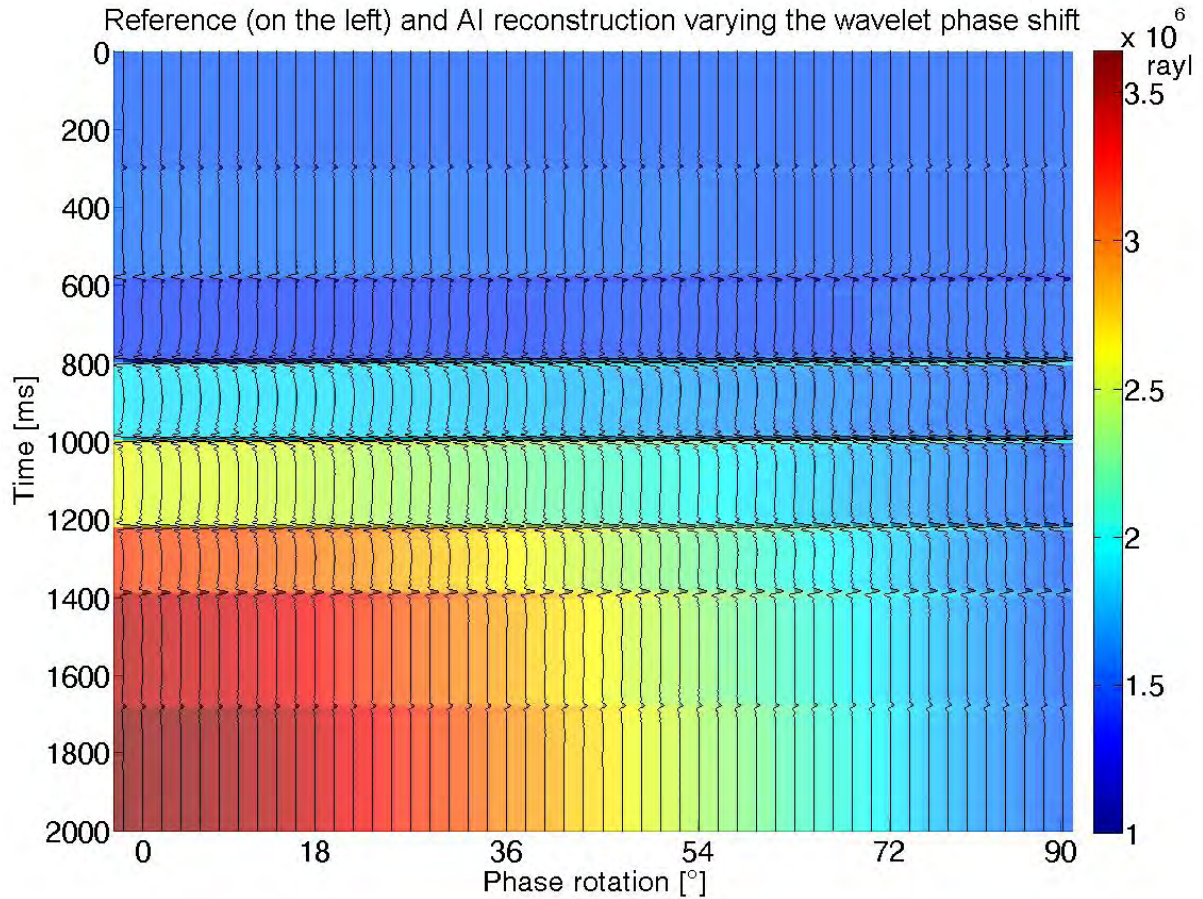


FIGURE 3.2: Reconstruction of the AI for a phase shifted version of trace 50 of Figure 3.1. Results evaluate the impact of phase shifts on the reconstruction of the AI.

The seismic traces that meet the assumptions described above, having been band-pass filtered to reject the noisier spectral components (including the low frequencies), can be modelled as:

$$d'(t) = sr'(t) + n'(t), \quad (3.1)$$

where $d'(t)$ is the band-limited seismogram, s is a scalar, $r'(t)$ is a band-limited version of reflectivity and $n'(t)$ represents the band-limited component of noise. After such processing, the seismic traces represent a scaled and noisy band-limited reflectivity series. Data must be processed to zero phase in order to place the interfaces between adjacent layers at their correct temporal position. Approximate results can also be obtained without properly removing the wavelet effects. However, the result departs from the theoretic reconstruction in such a way that the resulting very low frequencies are completely unreliable if no accurate constraints at depth are imposed during the inversion (see section 2.5.7). A time variant AR process (Rao, 1970) may model the complex-value non stationary series in this case. (Tary, Herrera, and Van der Baan, 2014) provide a detailed description on the topic of fitting time variant AR models on seismic time series, but such models have not been considered in this thesis. Provided that equation 3.1 is valid and as long as the scalar s is properly estimated and noise taken into account, it is equivalent to input $d'(t)$ or $r'(t)$ in the reconstruction. The reconstruction performed in the data domain is proportional to the reconstruction performed in the reflectivity

domain. In what follows, the data in the band-pass window will be modelled by equation 3.1 which provides a straightforward mean to estimate $r'(t)$ from the data. The reflectivity thus obtained becomes the input to the inversion process. I follow the weak contrast approximation introduced by Peterson, Fillipone, and Coker (1955) to relate the AI to the interface property of reflectivity (r_i) for a continuous earth model and normal incidence as per equation 1.4. If the reference impedance is known or estimated at a certain depth $AI(t_{ref})$ rather than near the surface ($AI(t_0)$), the AI reconstruction above the reference level is obtained by rewriting equation 1.4 as:

$$AI(t) = \frac{AI(t_{ref})}{e^{2\sum_{i=t_0}^t r_i}}. \quad (3.2)$$

In case the absolute value of reflectivity is smaller than 0.4, the difference between the results of equation 1.4 and the formulation of impedance for a discrete layered earth

$$AI(t) = AI(t_0) \sum_{i=t_0}^t \frac{1+r_i}{1-r_i} \quad (3.3)$$

is negligible for a single interface (Bertheussen and Ursin, 1993), but the difference accumulates for increasing depths proportionally to the sum of the cubic power of the amplitudes of each event. All the frequency components of the reflectivity must be available to invert for the absolute AI by using equation 1.4 or 3.2. In particular, the low frequency components of reflectivity play the most relevant role in describing the features of AI because of the low frequency boosting due to the summation operator in equation 1.4 or 3.2.

3.3 CARV Method

The combined AR-velocity method proposed here estimates the absolute AI value by considering the spectrum of each post-stack seismic trace as a gapped complex signal. The gap refers to the low frequency part of the recorded data that is bounded by the negative and positive signal spectral components. The idea of filling the gap was initially proposed by Fahlman and Ulrych (1982) in the context of power spectral estimation and developed by Walker and Ulrych (1983) for the case of seismic inversion. The novelty of the proposed approach consists of including, during the gap filling process, information from interval velocity together with geologic knowledge on impedance and its uncertainty. The harmonic AR modelling is fully detailed in Walker and Ulrych (1983) with few extensions discussed in Chapter 2. I only outline here the salient points that may be useful for the new aspects of the implemented inversion.

3.3.1 ARMA Models for Noisy Data

In the presence of noise (N_f) that is uncorrelated to signal (R_f) in the recorded data (D_f), an autoregressive moving average (ARMA) process with the same coefficients for the AR and moving average part is the correct representation of the signal (Ulrych and Clayton, 1976). This is theoretically described in the derivation of equation 2.18. The spectral estimator of Pisarenko (1972) can be used to fit an ARMA model to the data. However, this method is very sensitive to the model order (see subsection 2.5.1), which must be chosen to be equal to the number of the

reflections plus one: this piece of information is not available a priori in real case scenarios. A modification of the Pisarenko method that makes use of projection filters (Soubaras, 2005) has been proposed by Sacchi and Kuehl (2005). This approach provides an estimate of all the R_f in equation 2.17 as

$$\mathbf{R} = (\mathbf{Id} - (\mathbf{G}^H \mathbf{G} + \psi \mathbf{Id})^{-1} \mathbf{G}^H \mathbf{G}) \mathbf{X}, \quad (3.4)$$

where \mathbf{G} is the convolution matrix of the coefficients of the Prediction Error Operator ($\mathbf{g}^H \mathbf{g}$ as per equation 2.40) and ψ is a regularization parameter to account for the magnitude of the noise variance when its distribution is assumed to be Gaussian (Chen and Sacchi, 2014). The vector \mathbf{R} estimated from equation 3.4 is in theory the noise-free spectral representation of a limited number of events in the time representation of the seismic trace (Sacchi and Ulrych, 2005). The noise-free estimate can be used as input for the AR reconstruction of low frequencies.

3.3.2 AR Low Frequency Reconstruction

AR models of order much longer than the number of complex sinusoids in the data mimic the ARMA behaviour and can be adopted to reduce the sensitivity of the results to the model order in the presence of noise (Walker and Ulrych, 1983). Figure 3.4 illustrates the robustness of the AR models in comparison to the ARMA models in the reconstruction of the full bandwidth of a synthetic sparse time series. In order to fill the low frequency gap with an AR model, Walker and Ulrych (1983) minimize the AR forward and backward prediction error in the cost function

$$\min_{\mathbf{R}, \mathbf{L}_f} \left\| \sum_{k=0}^M g_k R_{f-k} \right\|_2^2 + \left\| \sum_{k=0}^M g_k^H R_{f+k} \right\|_2^2 = \min_{\mathbf{R}} \|\mathbf{C}\mathbf{R} - \mathbf{b}\|_2^2. \quad (3.5)$$

The vector \mathbf{R} contains the low frequency components of the reflectivity spectrum, the matrix \mathbf{C} contains the convolution of the AR coefficients, and the vector \mathbf{b} describes the known terms resulting from the multiplication of the AR coefficients and the known Fourier components of the spectrum at higher frequencies (see for further reference the description that leads to equation 2.38 in Chapter 2). The minimization of equation 3.5 is a two-stage process: the AR filter coefficients (g_k) are initially estimated from a spectral window where the wavelet effects are properly removed and, after the gap of low frequencies is filled, a new AR model is fitted to the original spectral window plus the low frequency band to return an updated version of the low frequency reconstruction. This procedure reduces the prediction error (Fahlman and Ulrych, 1982) as also discussed in section 2.5.2.

Different spectral estimators lead to different reconstructions of the AR coefficients. This is particularly relevant in presence of a large number of reflectors and interference features. In this Chapter the Yule-Walker method has been adopted, providing more stable results when applied to both complex synthetic scenarios and real seismic data.

The spectral components that show a poor S/N are not suitable for quantitative inversion in the framework of AR models (Kay and Marple, 1981). Following the work of Walker and Ulrych (1983) I define a frequency band where S/N is adequate for inversion. The average amplitude spectrum of the input seismic section can be used to estimate reasonable cut-off frequencies. The choice is a trade-off between neglecting part of the information present in the data, and estimating the model on a flat part of the spectrum, where the signal prevails over the noise.

The choice of low- and high-cut frequencies (pass-band length) also influences the order of the AR model that best describes the data. Walker and Ulrych (1983) recommend an AR model order which is 0.7 times the passband length (in units of sampled frequencies) on the real data tested. The same length is recommended by the present research for the AR part of the CARV method. Such recommendation implies that as the passband length shortens, the AR model also shortens, and therefore fewer features of impedance variation can be accurately obtained by the model (Hendrick and Hearn, 1993). To overcome the incorrect predictions due to the AR reconstruction only, I introduce the information coming from the interval velocity field in the CARV algorithm.

3.3.3 Interval Velocity Field

I do not discuss here all the various methods to obtain an accurate seismic-based interval velocity field, since this is a very wide and deeply studied topic which is outside from the scope of my research. I only consider the velocity field as an input for the CARV algorithm. In order to tie the reconstruction of AI to the velocity field, a rock physics relationship for the density term has to be assumed. Gardner (Gardner, Gardner, and Gregory, 1974) or other empirical relationships could be adopted. With the first choice

$$\rho(t) = C\alpha(t)^b \quad (3.6)$$

where $\rho(t)$ is the bulk density, $\alpha(t)$ the p-wave velocity, C and b are two scalars. The AI can consequently be estimated by the following expression:

$$AI(t) = C\alpha(t)^{1+b}. \quad (3.7)$$

The coefficient b is typically much smaller than 1, leading to a quasi-linear propagation of the error from the interval velocity field to the AI obtained from equation 3.7.

Many prospects of interest for oil and gas exploration show anomalous deviations from Gardner's trend. Loseth et al. (2011) describe this issue with particular emphasis on the amount of organic content in source rocks. In the CARV method the velocity field information is not incorporated as a constraint (Oldenburg, Levy, and Stinson, 1984), but rather as a weighting factor in the inverse problem. The use of the weights provides more flexibility to the solution and the possibility to evidence anomalies on Gardner's trend. The interval velocities from move-out or travel-time tomography contain most of their informative content at very-low-frequency. Conventional seismic tomography, for instance, show significant spectral content typically up to 2 Hz (ten Kroode et al., 2013), but factors related to target depth, offset length and velocity variations may imply a higher resolution. I chose to sample the velocity field at the sampling rate corresponding to the low frequency cut-off chosen for the seismic passband. This choice is generally safe with respect to the spectral content of the velocity field and, providing there is no aliased energy, larger sampling intervals can be chosen to improve the algorithm performance. Each of the re-sampled values of the velocity field is transformed into AI by using equation 3.7. The continuous approximation of the reflectivity integral for a discrete time series allows

the analytic solution of equation 2.46 as

$$\log \frac{AI(t)}{AI(0)} - 2 \int_{t_0}^{t_k} r^H(u) du = \sum_{f=-F_{min}}^{F_{max}} R_L^f \left(2 \frac{e^{i2\pi f t_k}}{i2\pi f} - 2 \frac{e^{i2\pi f t_0}}{i2\pi f} \right). \quad (3.8)$$

The unknowns of equation 3.8 are R_L^f , where $(r^H(u))$ is a known term that describes the time-domain reflectivity components within the passband. t_k is the time corresponding to the k-th velocity-derived recommendation for the AI. All the equations described in the system 3.8 are linear with respect to the unknowns R_L^f and can be rewritten in matrix notation as

$$\gamma = \mathbf{LR}. \quad (3.9)$$

In equation 3.9, γ describes the known terms and \mathbf{R} is the vector of low-frequency reflectivity. The smaller is the Euclidean norm of the residual $\|\mathbf{LR} - \gamma\|_2^2$, the closer is the estimated reflectivity to the information provided by the velocity field.

3.3.4 A priori Geologic Constraints

Seismic data acquisition normally follows a preliminary geologic assessment of the region of interest from direct observations on the field, or on nearby wells. Sometimes magnetic or gravimetric surveys might be available together with the seismic post-stack volumes. It is therefore natural to consider the availability of constraints for AI at different depths on a geologic basis. The accuracy of such constraints depends on the degree of knowledge of the surveyed area. Equation 2.46 describes a way to introduce equality constraints on AI to the AR solution. To account not only for the value of impedance at depth but also for its uncertainty, “soft constraints” are proposed for application to each trace of a 2D section or a 3D seismic volume. By soft constraints I refer to constraints that provide an upper and a lower bound to the AI inversion at selected depths. When the unconstrained AR reconstruction produces an AI inversion that does not fit within the impedance constraint limits, the AR method is modified such as the vector \mathbf{R} from equation 3.5 is no longer the one that minimizes the AR prediction error, but it is the one that minimizes the AR prediction error among those that fit the impedance constraint limits. In a probabilistic framework, the approach taken here imposes a uniform a priori probability distribution for the AI at selected depths within two bounds. This condition was not extensively explained in the original Ulrych and Walker (1984) publication. The uncertainty can both be in time and in the value of the AI. Small errors in defining the time of the constraints (of the order of tenths of temporal samples) can be tackled by evaluating the cost function proposed in equation 3.13 for the different combinations of the travel-times admitted by the timing uncertainty. The timings of the constraints that produce the minimum value of the cost function are then adopted. The use of large time uncertainties makes the constraints ineffective. On the other hand, to account for the uncertainty on the values of impedance constraints, equation 3.8 can be modified as follows:

$$\log \frac{AI(t) - \Delta AI(t)}{AI(0)} - 2 \int_0^t r^H(u) du \leq \sum_{f=-F_{min}}^{F_{max}} R_L^f \left(2 \frac{e^{i2\pi f t_k}}{i2\pi f} - 2 \frac{e^{i2\pi f t_0}}{i2\pi f} \right) \leq \log \frac{AI(t) + \Delta AI(t)}{AI(0)} - 2 \int_0^t r^H(u) du. \quad (3.10)$$

$\Delta AI(t)$ represents the uncertainty on the AI. In a more compact form, equation 3.10 can be written as:

$$\begin{cases} \mathbf{HR} \leq \beta + \Delta\beta \\ -\mathbf{HR} \leq -\beta + \Delta\beta. \end{cases} \quad (3.11)$$

Condition 3.11, introduced by the background geologic knowledge, can then be included in a constrained optimization problem as per equation 2.51.

3.3.5 Inversion Formulation

The CARV inversion method can be described in its general form by the minimization of the convex cost function:

$$J = \|\mathbf{CR} - \mathbf{b}\|_2^2 + \lambda \|\mathbf{LR} - \gamma\|_2^2 \quad s.t. \quad \begin{cases} \mathbf{HR} \leq \beta + \Delta\beta \\ -\mathbf{HR} \leq -\beta + \Delta\beta \end{cases} \quad (3.12)$$

with respect to the vector \mathbf{R} of low frequency components of reflectivity.

The condition $\min_{\mathbf{R}} \|\mathbf{CR} - \mathbf{b}\|_2^2$ comes from equation 3.5 and aims at minimizing the AR forward and backward prediction errors. The cost function includes the regularization term ($\|\mathbf{LR} - \gamma\|_2^2$) to make the resulting low-frequencies adhere to the AI estimated from the interval velocity field. The degree of adherence is controlled by the hyperparameter $\lambda \geq 0$.

Sensible values for λ may come from the ratio between the maximum eigenvalues of the matrix $\mathbf{C}^H\mathbf{C} = \mathbf{G}$ (in Walker and Ulrych (1983) original notation) and $\mathbf{L}^H\mathbf{L}$, but the final choice depends on the relative confidence on the velocity field with respect to the confidence on the seismic amplitudes. The velocity field is the regularization term and the soft constraints on impedance can be implemented by a constrained least squares algorithm (i.e. via a subspace trust-region method). Minimizing equation 3.12 is equivalent to solve a multi-objective optimization problem:

$$\min_{\mathbf{R}} \nabla J = \mathbf{GR} - \mathbf{B} + \lambda(\mathbf{L}^H\mathbf{LR} - \mathbf{L}^H\gamma) \quad s.t. \quad \begin{cases} \mathbf{HR} \leq \beta + \Delta\beta \\ -\mathbf{HR} \leq -\beta + \Delta\beta \end{cases} \quad (3.13)$$

where $\mathbf{B} = \mathbf{C}^H\mathbf{b}$. The regularization term pertaining to the velocity field $\mathbf{L}^H\mathbf{L}$ concentrates its information at the very low frequencies (around its main diagonal). This fact underlines the relevance of the velocity field term to weight the solution trend, while the AR term influence is stronger at the higher frequencies within the low frequency gap. There is no mathematical guarantee that the matrix to be inverted $\mathbf{G} + \lambda\mathbf{L}^H\mathbf{L}$ is well conditioned although no issue has been found during testing on synthetic and real data. This experimental statement finds an explanation by the decaying nature of the autocorrelation function of seismograms (e.g. Robinson (1954)) that leads to the Toeplitz matrix \mathbf{G} with largest values around its main diagonal. In case of instability during the inversion, additive white noise can be possibly introduced in the cost function 3.12 similarly to the approach of equation 2.42.

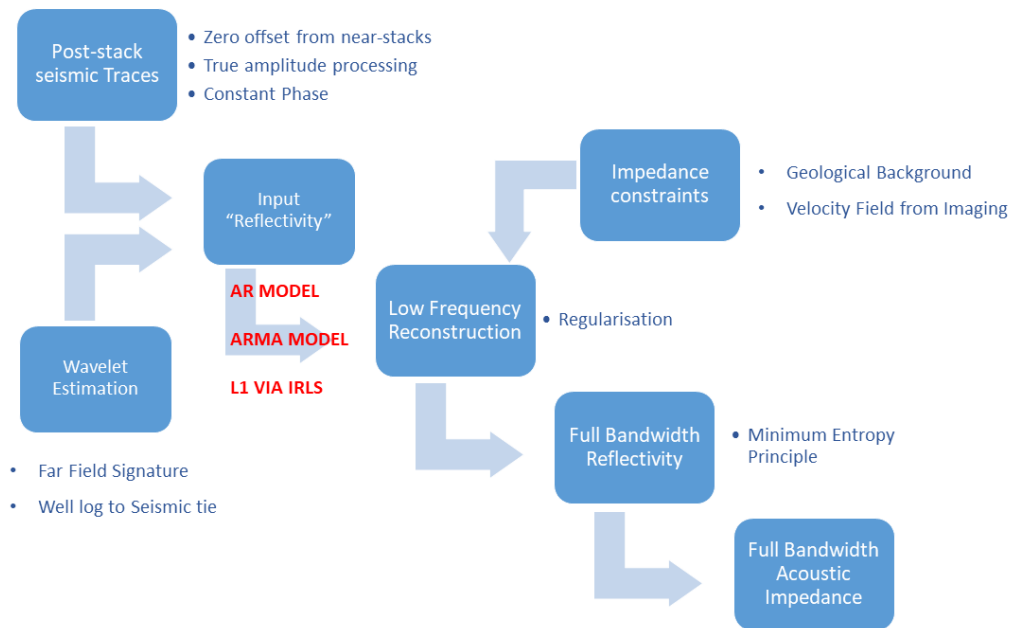


FIGURE 3.3: *Conceptual workflow of the CARV algorithm proposed for the estimation of the AI from post-stack seismic traces.*

3.3.6 Inversion with Lateral Continuity

An unwanted feature in the inversion of real data is the trace-to-trace variability of the results. A reason for the variability may be sought in the variability of the input data amplitude (see Chapter 1 for reference). Unfortunately, not all seismic amplitudes are related to reflectivity changes, as well as residual wavelet effects may vary from trace to trace. These features are further amplified in the inversion process. In fact, the integral operator that transforms reflectivities into AI magnifies the issue at the low-frequency end, leading to vertical stripes that degrade the interpretability of the inversion result. Ideally, I expect to find solutions that show nearly constant values of AI at nearby locations for the same travel-time. This is especially true for low-frequency components of AI, which are directly related to smooth spatial changes in geology. To reduce the instability in the inverted AI, three approaches have been analysed:

- Smoothing the seismic data before inversion
- Smoothing the inversion result
- Modifying the cost function.

The data may be smoothed before inversion with a processing that targets incoherent noise (see the result based on a rank-reduction technique in Figure 3.15). This approach becomes critical when strongly dipping events are present in the data. In this case, smoothing the dip-steered seismic dataset could be a possible solution in accordance to Hamid and Pidlisecky (2016). Seismic data could also undergo a targeted pre-processing step that enhances the lateral continuity of the events regardless of minimal damages on very steep features such as faults and channel banks. The amplitude of those features is already distorted because of their poor illumination, and they should not be considered as possible targets for the CARV inversion

(i.e. the fault zone of the Penobscot dataset - Figure 7.1). Alternatively, a spatial low-pass filter or a moving-average filter can be applied after inversion (see Figures 3.17, 3.16 for instance). Eventually, the cost function may be modified to promote the continuity of the solution. The lateral continuity could be either in terms of:

- Acoustic Impedance
- Reflectivity.

When the depositional sequence is sub-horizontal (the seismic events are gently dipping), elastic property estimates show nearly constant values at nearby locations (i). Similar to the work of Hamid and Pidlisecky (2015), such smooth estimates of the elastic parameters could be obtained by amending the cost function to include the relationship

$$AI_i(t) - AI_{(i+1)}(t) \cong 0 \quad \forall t, \quad \forall i, \quad (3.14)$$

or alternatively

$$r_i(t) - r_{(i+1)}(t) \cong 0 \quad \forall t, \quad \forall i \quad (3.15)$$

In equation 3.14 and 3.15 t is the index of a generic travel-time and r represents the reconstructed reflectivity.

3.3.7 Amending the Cost Function with a Lateral Smoothing Term on AI

Focusing only on the low frequency part of the AI estimation, and provided that the approximation of equation 1.4 is adequate, the smooth AI estimates could be obtained by rewriting equation 3.14 in terms of the Fourier components of the reflectivity(R_k) as:

$$e^{2\sum_{j=1}^t \sum_{k=-Fmin}^{Fmin} R_{k,i} e^{i2\pi k j}} - e^{2\sum_{j=1}^t \sum_{k=-Fmin}^{Fmin} R_{k,i+1} e^{i2\pi k j}} = e^{C(t)\mathcal{F}^{-1}R_{k,i}} - e^{C(t)\mathcal{F}^{-1}R_{k,i+1}} \approx 0. \quad (3.16)$$

Equation 3.16 allows to write for any couple of adjacent traces, n equations in the (four times the number of low frequency components plus two) unknowns ($R_{(k,i)}, R_{(k,i+1)}$). In equation 3.16, $C(t)$ is the linear summation operator, \mathcal{F}^{-1} represents the convolution matrix of the inverse Fourier transform, and k is the index of the low-frequency components. Equation 3.16 is non-linear. By exploiting the monotony of the exponential, minimizing the difference of equation 3.16 corresponds to minimizing

$$C(t)\mathcal{F}^{-1}R_{(k,i)} - C(t)\mathcal{F}^{-1}R_{(k,i+1)} \approx 0, \quad (3.17)$$

which is linear with respect to $R_{i,k}$. The cost function defined by equation 3.12 can easily incorporate the condition expressed by 3.17 when the inversion is performed simultaneously for all the traces in a patch of the seismic volume. This leads to the cost function:

$$J = \|CR - B\|_2^2 + \lambda \|LR - \gamma\|_2^2 + \mu \|DR\|_2^2 \quad s.t. \quad \begin{cases} HR \leq \beta + \Delta\beta \\ -HR \leq -\beta + \Delta\beta. \end{cases} \quad (3.18)$$

\mathbf{D} is a block diagonal matrix corresponding to the Kronecker product between matrices $\mathbf{C}(t)\mathcal{F}^{-1}$ and a discrete differentiator such as:

$$\mathbf{D} = \mathbf{C}(t)\mathcal{F}^{-1} \otimes \begin{pmatrix} 1 & -1 & 0 & \dots & \dots \\ 0 & 1 & -1 & 0 & \dots \\ \dots & \dots & \dots & \dots & \dots \\ \dots & \dots & 0 & 1 & -1 \end{pmatrix} \quad (3.19)$$

Local sliding windows of tenths of traces have been adopted in the implementation of the method. The longer the spatial window adopted, the larger the matrix \mathbf{D} and, therefore, the higher the computational cost of the inversion. Increasing the size of \mathbf{D} beyond tenths of traces does not dramatically improve the lateral smoothness of the solution, because the most stringent parameter that governs the character of the inversion becomes the amplitude of the non-negative hyperparameter μ in equation 3.18. The inversion result at a given trace is tied to the result at a far trace within the smoothing window by a cascade of constraints in such a way that the effects of the AI estimate at one trace is little influencing the AI estimates beyond few traces. A smoothed AI result obtained with this approach is presented in Figure 3.18.

3.3.8 Amending the Cost Function with a Lateral Smoothing Term on the Reflectivity

An additional approach to a laterally smooth inversion is the introduction, in the cost function, of a penalty term related to the trace-to-trace variability of the reflectivity reconstruction. Provided that the impedance of the first layer is constant for all the traces in the section and focusing only on the low frequency part of the reflectivity, I obtain a laterally smooth AI by solving for the lateral variation of the low frequency components of the reflectivity ($\Delta\mathbf{R}$) rather than for \mathbf{R} in equation 3.12. The cost function of equation 3.12 can be rewritten with an additive term $\mu\mathbf{Id}\Delta\mathbf{R}$ (where \mathbf{Id} represents the identity matrix):

$$J = \|\mathbf{C}\Delta\mathbf{R} + \mathbf{C}\mathbf{R}_0 - \mathbf{b}\|_2^2 + \lambda\|\mathbf{L}\Delta\mathbf{R} + \mathbf{L}\mathbf{R}_0 - \gamma\|_2^2 + \mu\|\mathbf{Id}\Delta\mathbf{R}\|_2^2 \quad s.t. \begin{cases} \mathbf{H}\Delta\mathbf{R} \leq \beta + \Delta\beta - \mathbf{H}\mathbf{R}_0 \\ -\mathbf{H}\Delta\mathbf{R} \leq -\beta + \Delta\beta - \mathbf{H}\mathbf{R}_0 \end{cases} \quad (3.20)$$

I call \mathbf{R}_0 the known term pertaining to the low frequency completion at the previous trace location. The additive term $\mu\mathbf{Id}\Delta\mathbf{R}$ controls the amount of trace-to-trace variability ($\mu \geq 0$). Once \mathbf{R}_0 is arbitrarily chosen at both ends of the line, the low frequency components of reflectivity \mathbf{R} can be iteratively obtained as $\mathbf{R} = \mathbf{R}_0 + \Delta\mathbf{R}$ at each trace location. I perform the summation from one end of the seismic line to the other, and in the opposite direction, then I adopt the average of the two results as a smoothed AI estimate.

The computational cost for solving the problem 3.18 is much higher than the cost required to solve the problem 3.20, because the matrix to be inverted is much smaller in the latter case.

The amendment of the cost function 3.12 proposed in this subsection could also be easily extended to any elastic property other than AI.

3.3.9 Reflectivity Extension to High Frequency

The high frequency components of the data are as unreliable as the very low frequencies, but it is worth noting that the high frequency content of reflectivity tends to be suppressed when recursively summed into the AI (see equation 1.4 or 3.2). Walker and Ulrych, 1983 proposed to minimize an entropy norm (Ooe and Ulrych, 1979) after the low frequency completion to reconstruct the full bandwidth of reflectivity from its low-mid frequency content. I adopt instead, a logarithmic entropy function with frequency domain constraints (Sacchi, Velis, and Cominguez, 1994) for the high-frequency completion of the CARV solution. Both norms aim at obtaining a sparse solution compatible with the input time series. This agrees with the initial assumption that the CARV algorithm recovers the full bandwidth of reflectivity given a limited number of events in the recorded traces. Minimizing an entropy norm as a final step of a constrained harmonic interpolation process might lead to instabilities (see subsection 2.5.5). Factors that may be accounted for this behaviour are the presence of noise, the presence of contrasting information from velocity field, geologic constraints, AR reconstruction, and, eventually, the parametrization of the minimum entropy deconvolution algorithm. The tolerance on the entropy norm increment at each algorithm iteration plays the most important role in determining the energy of the reconstructed high amplitudes. A threshold ratio equal to one between the energy of the high frequency components and the energy of the low-mid frequencies is adopted in all the CARV results presented in the thesis to terminate the iterative high frequency reconstruction process. The threshold choice has the purpose of limiting the high-frequency reconstruction impact on the inversion result. This is because I do not trust the quantitative outcome of the deconvolution process while using it only as a mean to enhance the sharpness of the stronger reflectors. In fact, the high frequency reconstruction may be considered a cosmetic step in the CARV work-flow for AI inversion. The application of this reconstruction step does not influence the validity of the low- and mid-frequency estimates of the AI.

3.4 Results of the CARV inversion

In this section I illustrate the novel aspects and the performance of the proposed inversion method, with emphasis on describing general outcomes rather than a data- or site-dependent behaviour which will be discussed more in detail in the case-studies of Chapter 6 and 7. For the sake of clarity, I summarize the various approaches to AI inversion that I discuss on synthetic examples and real data in Table 3.1. All the AI inversion results are expressed in *rayl*, corresponding to $kg/m^2/s$.

METHOD	DESCRIPTION AND REFERENCE
Classical ARMA approach	Method adopted when the exact number of events is known a priori. Pisarenko (1972)
Unconstrained AR approach	Method described in Walker and Ulrych (1983)
Classical AR approach	Method described in Ulrych and Walker (1984)
Model-based Inversion	Method that adds the a priori low-frequencies to the bandlimited inversion. Russell (1988)
Combined AR-velocity approach (CARV)	Method described in this paper.

TABLE 3.1: *Naming convention with short description of the AI inversion methods proposed in this Chapter.*

3.4.1 Synthetic Examples

I first generated 1-D time series that simulate seismic traces to assess the effectiveness of the four reconstruction methods described in Table 3.1. The fifth method, the model-based approach, is introduced in the inversion of a real seismic dataset for comparing the harmonic reconstruction methods with a different approach to seismic inversion. I assumed two input models, both characterized by a blocky impedance corresponding to a sparse time-domain reflectivity. Model 1, corresponding to MODEL A in Chapter 2, contains 10 vertically stacked AI blocks, while Model 2 contains 100 AI blocks. Both models are made up of 1000 temporal samples. The input synthetic trace in Figure 3.4A represents a bandlimited (8-70 Hz) version of the model reflectivity function with additional white noise (S/N=34 dB in terms of maximum amplitude). Figure 3.4 highlights the sensitivity of the unconstrained AR and ARMA reconstructions to the model order choice on the Model 1 synthetic example. No constraint at depth or velocity field regularization is required for obtaining reliable results on such a sparse and controlled synthetic example when the appropriate model order is chosen. The ARMA process that correctly models the data is of order 10, while I assume that the best AR approximation is obtained for a model order of 105 (in line with the recommendation of selecting the model order 0.7 times the passband length in units of sampled frequencies). Given a Nyquist frequency of 125 Hz, and a 12 to 50 Hz signal bandwidth choice, the number of sampled frequencies available for fitting the AR model is 152. When the ARMA model order is smaller than the actual number of events in the data (Figure 3.4B, model order 7), the reconstruction becomes unreliable because the low-frequencies are incorrectly modelled. The instability of the ARMA model appears hard to overcome because one needs to know exactly the number of reflectors before inverting the seismic data. Figures 3.4B and 3.4C show that the sensitivity of the impedance profile results is much lower for the AR than for the ARMA approach, despite the range of relative normalized order values being comparable between the two types of reconstruction. The comparison in Panel 3.4D between the two more accurate AR and ARMA solutions shows the good approximation, in presence of noise, of a long AR model to the appropriate ARMA model.

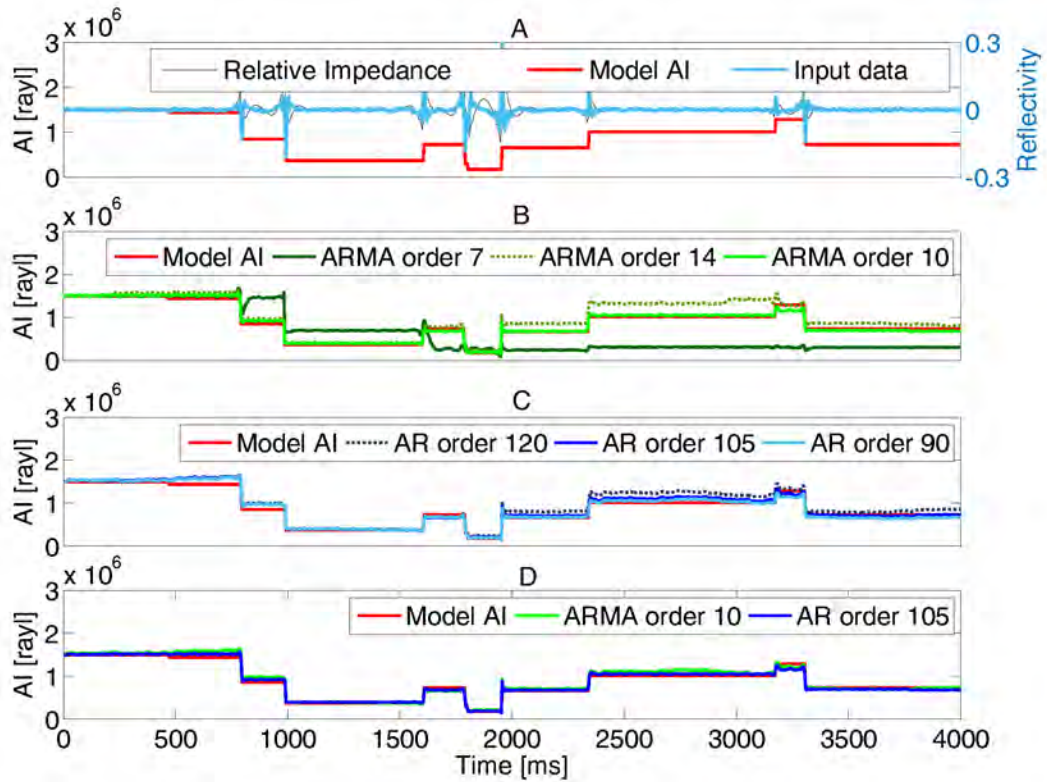


FIGURE 3.4: Results of low-frequency reconstruction with AR and ARMA models. Panel 3.4A shows the input AI Model 1 (red) and the derived synthetic trace (cyan) ($S/N = 34$ dB). Panel 3.4B: reconstruction via unconstrained ARMA modelling. Panel 3.4C displays the reconstruction via the unconstrained AR modelling. Panel 3.4D compares the results for the two more accurate solutions of panel 3.4B and 3.4C.

Synthetic Model 1 and Model 2 are compared in Figures 3.5, 3.6, and 3.7 to show the effectiveness of the CARV reconstruction with respect to the classical AR approach on a controlled input. In these Figures, panels A and B show the input synthetic data (7-80 Hz zero-phase Butterworth filter) on the Model 1 and Model 2 reflectivity with additional white noise ($S/N=34$ dB in terms of maximum amplitudes). Panels C and D are obtained after the low-frequency reconstruction and the subsequent AI inversion on the input trace of panels A and B, modified by the absence of additional white noise. Panels E and F are obtained from the reconstruction of the traces of panels A and B, respectively. I present, in panels G and H, the reconstruction results that can be obtained when the input trace is the convolution between the model reflectivity and a 30 Hz Ricker wavelet that bandlimits the data (no additive noise). Figure 3.5 shows the quality of the reconstruction that can be achieved with the unconstrained AR models, in comparison to the bias introduced by the weak contrast approximation. The weak-contrast approximation is not a relevant limitation for both Model 1 and Model 2 reconstructions: all panels of Figure 3.5 evidence the reduced bias of the unconstrained AR solution that can be imputed to this approximation. A bias in the reconstruction of the DC component of the AI is also clearly visible in Figures 3.5C to 3.5H. In fact, frequencies close to the DC component are generally the hardest to be successfully reconstructed by the AR model, as it has been reported since the work of Oldenburg, Scheuer, and Levy (1983). This behaviour can be clearly seen as

the AI drift, in particular for the more complex Model 2 (Figures 3.5D, 3.5F, and 3.5H). I include the two reconstructions of panels 3.5G and 3.5H to highlight the effects of not correcting for the wavelet shape before performing the reconstruction. The wavelet effects on the reconstruction are visible both in terms of high frequency undesired features and low frequency drift in Figures 3.5G and 3.5H.

Figure 3.6 shows the effects of the soft constraints on impedance at selected times (blue brackets) that aim at limiting the bias introduced by incorrect AR predictions. As reported in Table 3.2, the RMS error between the input Models (red curves) and the constrained AR reconstructions (black curves), is smaller or equal to the RMS error between the input Models and the unconstrained AR reconstructions (grey curves). The reconstructions in Panels 3.5H and 3.6H represent no exception, but the absence of constraints in the shallow layers has the side effect of producing a less accurate reconstruction in the shallow part of the constrained solution (Figure 3.6H) than in the shallow part of the unconstrained solution (Figure 3.5H). An explanation for this behaviour can be sought in the artefacts that are introduced when the wavelet shape is not removed before the low-frequency reconstruction. On the contrary, the drift from the input model is reduced in Panels 3.6D and 3.6F with respect to Panels 3.5D and 3.5F. Figures 3.4 to 3.6 do not make use of the velocity field information. The effects and artefacts of incorporating an interval velocity field which does not have the AI blocky structure are shown in Figure 3.7. The AI curve that plays the role of the velocity-derived AI field in Figures 3.7C, 3.7E and 3.7G is obtained by fitting, in a least squares sense, a polynomial of order 5 to the Model 1. The best fit polynomial of order 8 is used to derive the green AI curve for the most complex Model 2 in Figures 3.7D, 3.7F, and 3.7H. The trade-off parameter λ that governs the amount of velocity-field derived AI in the inversion, has been chosen as 0.5 times the ratio between the maximum eigenvalues of matrix \mathbf{G} and $\mathbf{L}^H\mathbf{L}$ for all the panels of Figure 3.7. In addition to the information coming from the velocity field, the constraints on impedance indicated by the blue brackets have been enforced in Figure 3.7. The CARV reconstruction of Model 2 still shows a relevant mis-tie with respect to the reference AI model in the shallowest part (panels 3.7D, 3.7F, 3.7H). Weighting in the solution the low frequency AI model that mimics an AI model derived from a velocity field reduces the reconstruction error with respect to the results of panels 3.6D, 3.6F and 3.6H. Note that the CARV reconstruction of panel 3.7C appears less blocky than the reconstruction 3.6C that does not account for the velocity field: this is an unrealistic case in which the extreme sparseness of the layer interfaces and the absence of noise lead to a CARV inversion that is less blocky than the classical AR inversion.

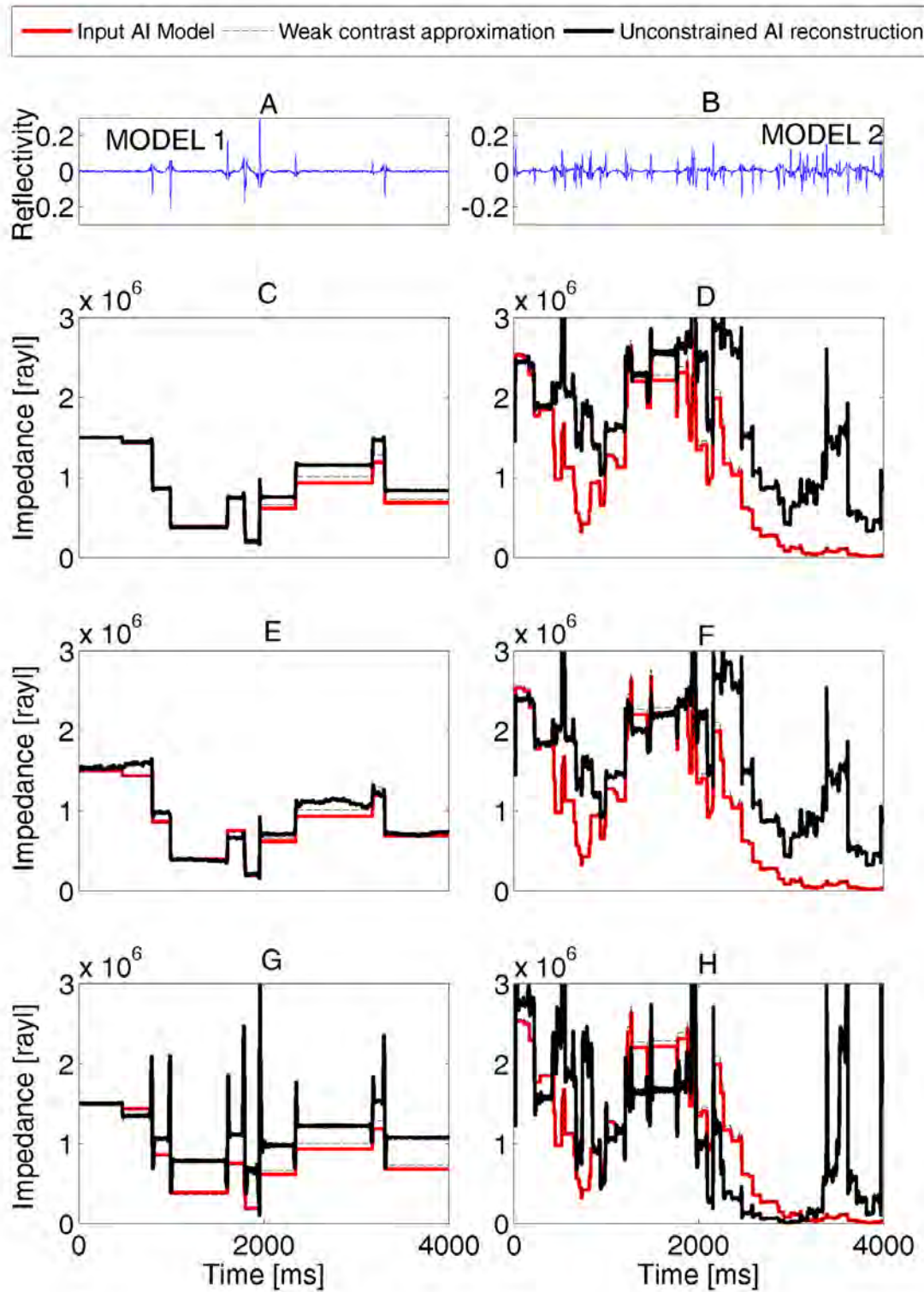


FIGURE 3.5: Effectiveness of the bandwidth extension via the unconstrained AR method. Panels 3.5A and 3.5B: input data ($S/N = 34$ dB). Panels 3.5C and 3.5D: reconstruction from band-limited input reflectivity (no noise). Panels 3.5E and 3.5F: reconstruction from input data of Panels 3.5A and 3.5B. Panels 3.5G and 3.5H: reconstruction from input reflectivity convolved with a Ricker wavelet.

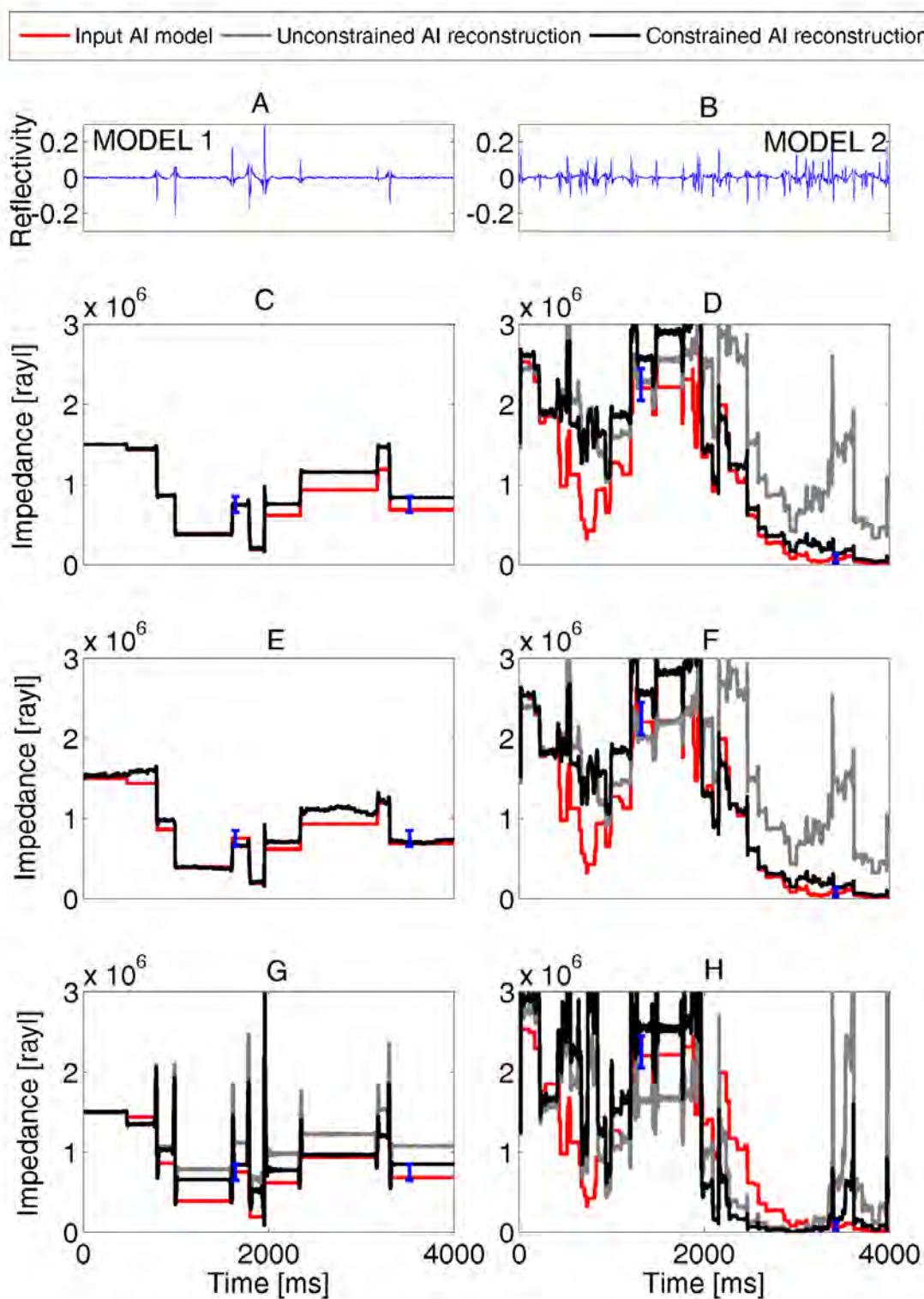


FIGURE 3.6: Effectiveness of the bandwidth extension in presence of impedance constraints at depth with a given uncertainty (in blue). Panel 3.6A and 3.6B: input data (S/N 34 dB). The unconstrained results from Figure 3.5 are reported in gray. Panels 3.6C and 3.6D: constrained reconstruction from band-limited input reflectivity (no noise). Panels 3.6E and 3.6F: constrained reconstruction from input data of Panels 3.6A and 3.6B. Panels 3.6G and 3.6H: constrained reconstruction from input reflectivity convolved with a Ricker wavelet.

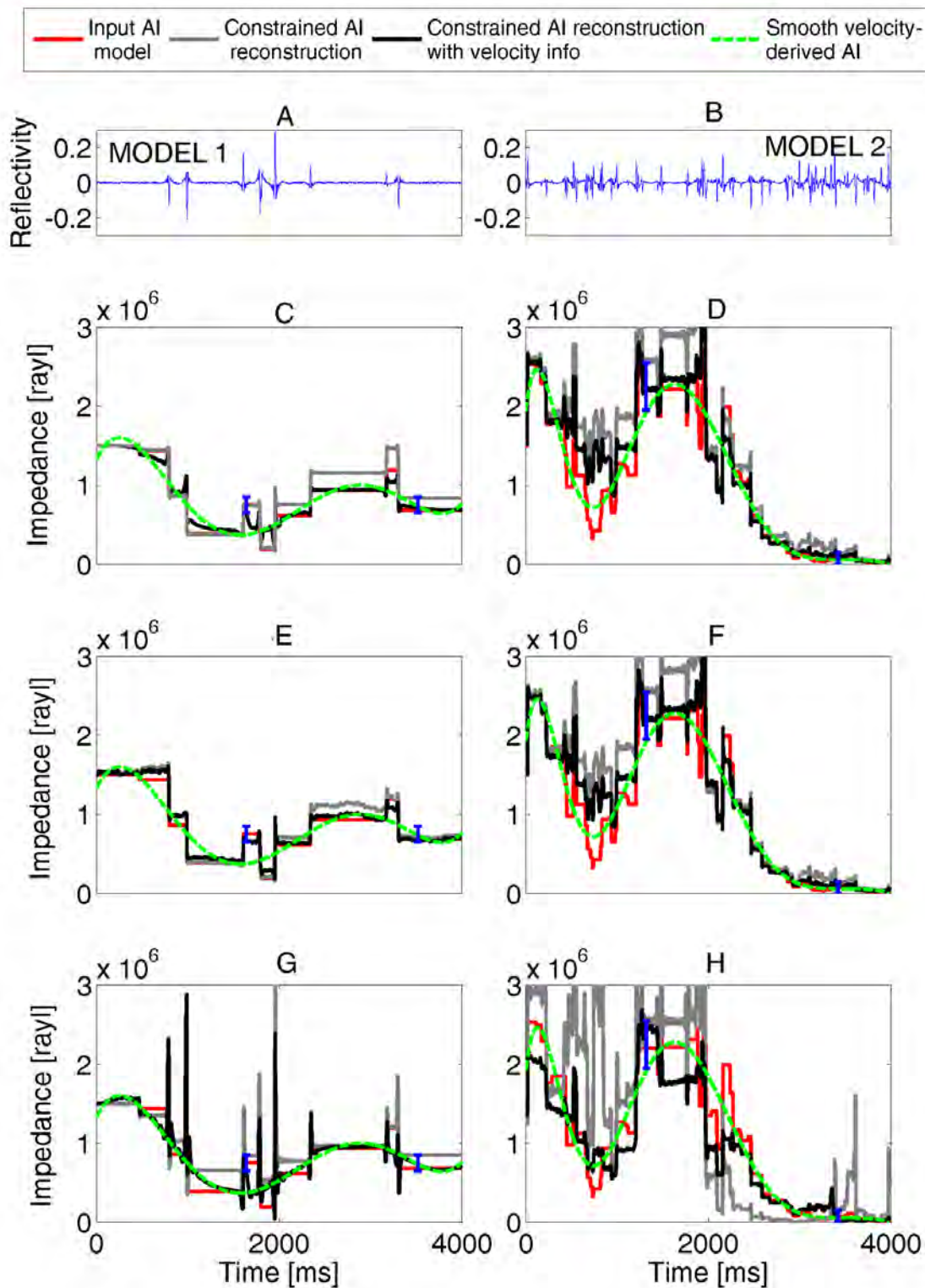


FIGURE 3.7: Results of the CARV reconstruction (black curves) and comparison with the constrained classic AR reconstruction reported in Figure 3.6 (gray curves). Panel 3.7A and 3.7B: input data (S/N = 34 dB). Panel 3.7C and 3.7D: CARV reconstruction from band-limited input reflectivity. Panel 3.7E and 3.7F: CARV reconstruction from input data of Panels 3.7A and 3.7B. Panel 3.7G and 3.7H: CARV reconstruction from input reflectivity convolved with a Ricker wavelet.

Figure	Reconstruction type	RMS error [rayl]	Figure	Reconstruction type	RMS error [rayl]
3.4B	ARMA order 7	$47.4 \cdot 10^4$	3.4C	AR order 90	$6.9 \cdot 10^4$
3.4B	ARMA order 10	$4.8 \cdot 10^4$	3.4C	AR order 105	$7.5 \cdot 10^4$
3.4B	ARMA order 14	$18.3 \cdot 10^4$	3.4C	AR order 120	$13.2 \cdot 10^4$
3.5C	Unconstrained AR	$10.1 \cdot 10^4$	3.5D	Unconstrained AR	$67.6 \cdot 10^4$
3.6C	Classic AR	$10.1 \cdot 10^4$	3.6D	Classic AR	$35.7 \cdot 10^4$
3.7C	CARV	$5.3 \cdot 10^4$	3.7D	CARV	$17.0 \cdot 10^4$
3.5E	Unconstrained AR	$7.9 \cdot 10^4$	3.5F	Unconstrained AR	$58.7 \cdot 10^4$
3.6E	Classic AR	$7.9 \cdot 10^4$	3.6F	Classic AR	$31.1 \cdot 10^4$
3.7E	CARV	$5.0 \cdot 10^4$	3.7F	CARV	$14.7 \cdot 10^4$
3.5G	Unconstrained AR	$30.9 \cdot 10^4$	3.5H	Unconstrained AR	$54.4 \cdot 10^4$
3.6G	Classic AR	$14.3 \cdot 10^4$	3.6H	Classic AR	$53.3 \cdot 10^4$
3.7G	CARV	$10.3 \cdot 10^4$	3.7H	CARV	$23.1 \cdot 10^4$

TABLE 3.2: RMS errors of the synthetic reconstructions.

Figure 3.8 shows the amplitude spectrum of the reconstructed reflectivity whose derived AI is shown in Figure 3.7F, in comparison to the amplitude spectrum of the Model 2 reflectivity. The match in the 12-50 Hz bandwidth, in which I fit the AR model is good. The relative error in this band is around the -34 dB, which can be attributed to the additive noise level that is present in the input data and not in Model 2. The relative error both in the low- and in the high-frequency reconstruction is much higher, around -20 dB. Although the spectral peaks of the input and the reconstructed reflectivity appear to be correlated, the two amplitude spectra assume very different values outside the signal bandwidth.

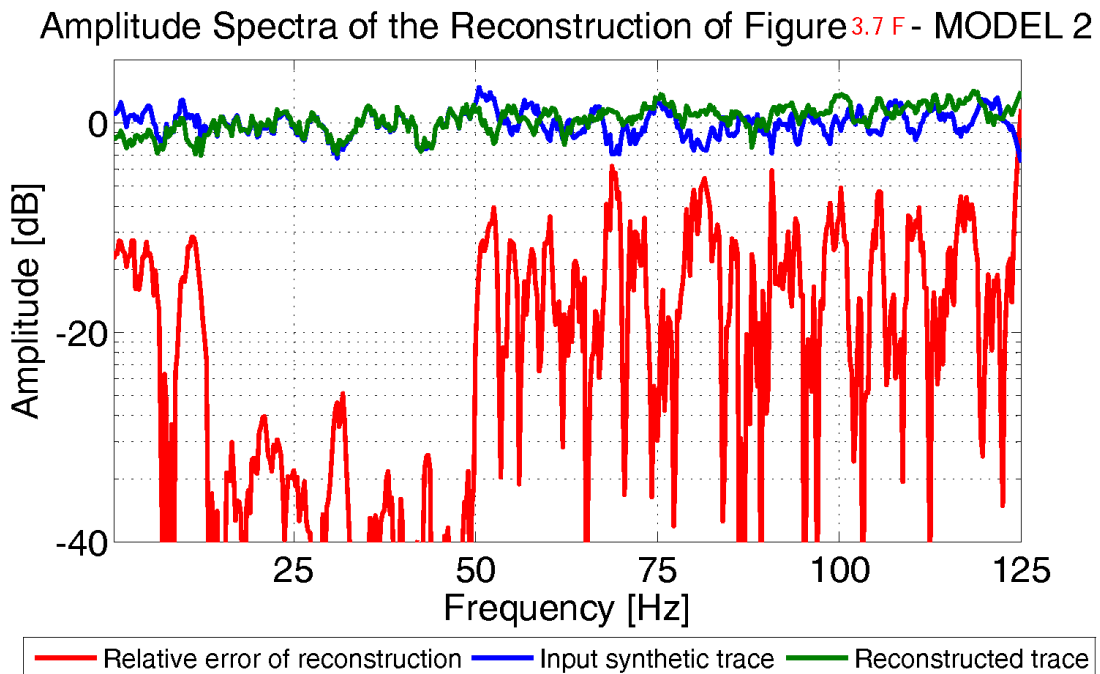


FIGURE 3.8: Amplitude Spectra of the relative error in the reconstruction of the reflectivity of the CARV reconstruction of Figure 3.7F. The relative error has been obtained by dividing the reconstruction misfit by the spectrum of the input reflectivity.

3.4.2 Real Data

I tested the AR and the CARV inversion on part of a marine profile from a 2015 towed-streamer seismic survey in the Rockall Trough area across the UK Atlantic margin. The PSTM full-angle stack (6° - 35°) seismic section is shown in Figure 3.9A together with the location of the wells and the interpreted horizons available. Ancillary data include a tomographic interval velocity field and a model-based AI inversion within the interval 1-5 s. All the data have been obtained from the UK Oil and Gas Authority under the Open Government license v.3.0. High-amplitude events that are probably related to igneous lenses stand out in the section below the Top Paleocene horizon. No specific reservoir targets are present on this 2D line, as the line was selected only to demonstrate the advantages and the drawbacks of the CARV method with respect to a standard AI inversion approach in the early stages of prospect identification. Figure 3.9B displays, for reference, the AI field that was obtained by applying Gardner's relationship ($b = 0.25, C = 310 \text{ kg/m}^3$) to the tomographic velocity field.

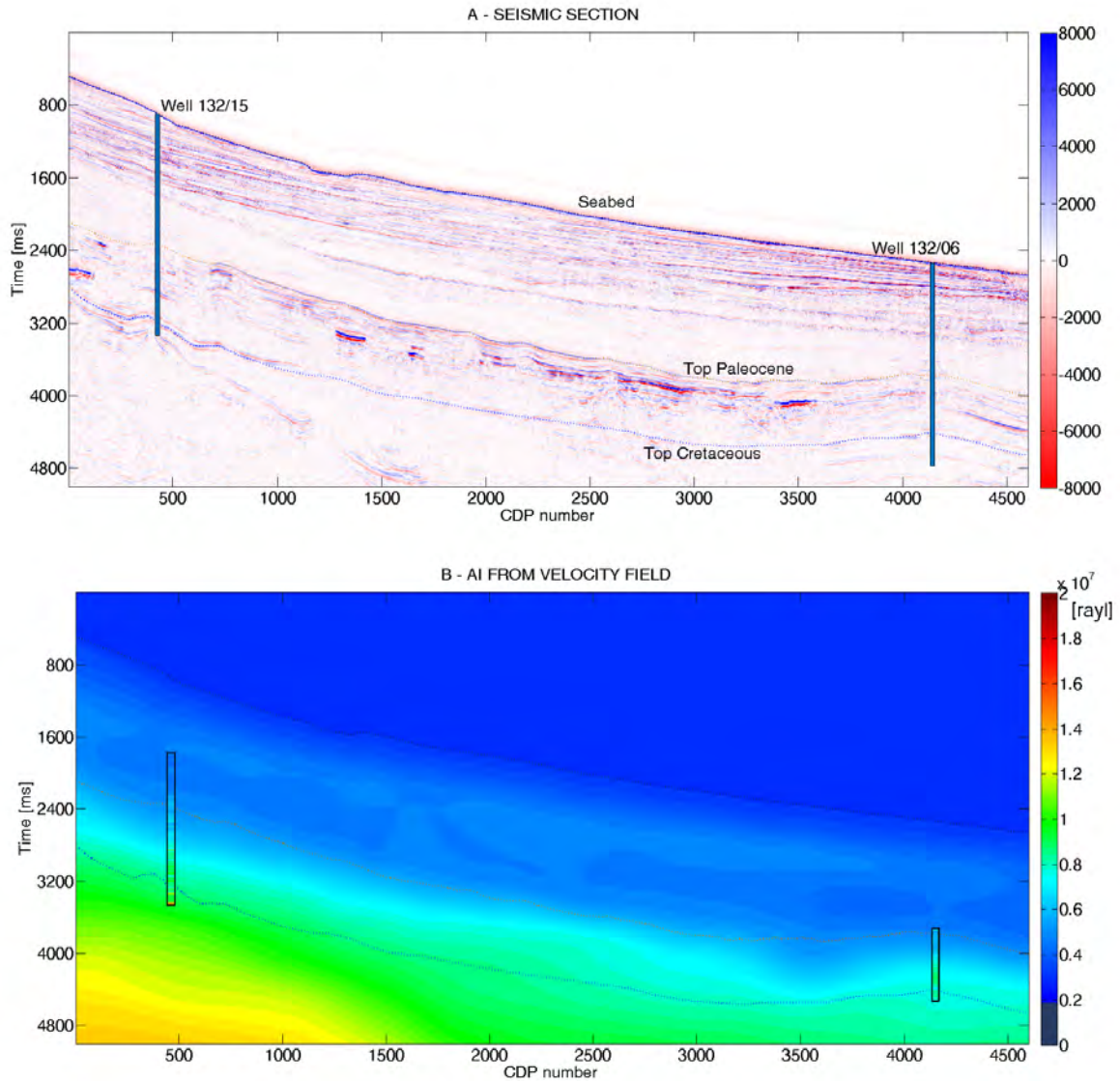


FIGURE 3.9: Post-stack seismic line 78 from the Rockall Trough survey (traces 1400-6000). © Crown Copyright. Well positions and horizons overlay the seismic section in Figure 3.9A. The AI [rayl] derived from tomographic velocity field and the Gardner's relationship is displayed in Figure 3.9B, together with AI derived from sonic and density logs within black boxes at well locations.

Different parametrizations of the CARV low-frequency reconstruction have been applied to a scaled version of the data. I decided to estimate a global scalar for the whole section directly from the data to show the potential of the inversion even in absence of well-log control. I estimated that the AI is $1.5 \cdot 10^6$ rayl above the water-bottom and $8.5 \cdot 10^6$ rayl 100 ms below the Top Cretaceous event. The latter figure has been chosen in accordance to the log values recorded in the Well 132/06 below the Top Cretaceous event, but a reasonable assumption is that the same degree of information may be available from background knowledge of the area of interest. I ran a first pass of the classical AR inversion algorithm directly on the seismic data with no constraints imposed at depth. After integration of the reconstructed (full-bandwidth) trace, I obtain an AI value 100 ms below the Top Cretaceous event which is, in general, different from

the assumption of $8.5 \cdot 10^6$ rayl. The ratio between the section average of the AI values thus obtained, and the expected $8.5 \cdot 10^6$ rayl value, provides a mean to estimate the scalar s of equation 3.1. Once the data amplitudes are calibrated to amplitudes pertaining to the reflectivity, the AR reconstruction is re-computed with impedance constraints at depth, with the AI derived from the tomographic interval velocity field, and with the lateral continuity constraint. The CARV reconstructed reflectivity is then integrated into AI from a starting value of $1.5 \cdot 10^6$ rayl in the water layer. I obtained my preferred inversion result on the Rockall Through line when the signal bandwidth is in the range 5 to 40 Hz (see Figure 3.11A). The inspection of the amplitude spectrum of the input data (Figure 3.10) was used for defining the signal bandwidth. The high-cut choice is not obvious from Figure 3.10, but I decided to be conservative and to avoid the attenuation and dispersion effects that are more pronounced at higher frequencies and in the deepest part of the section. The amplitude spectrum is flat in the above mentioned frequency range, at least until 2000 ms below the water bottom.

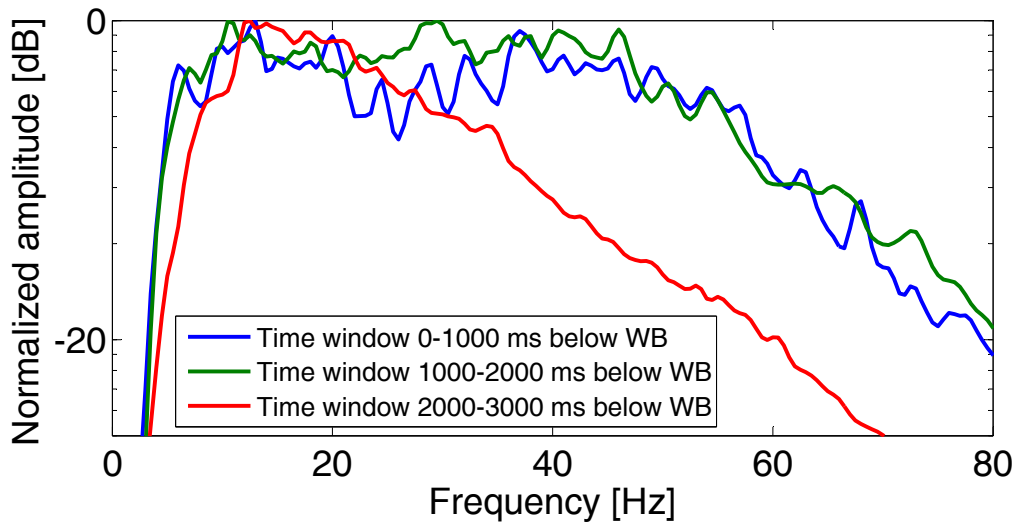


FIGURE 3.10: Average amplitude spectrum of the Rockall Trough seismic section within three time-windows. Values are normalized to their peak amplitude.

Figure 3.11 shows a comparison between the CARV inversion (Figure 3.11A) and a model-based inversion available from the UK Oil and Gas Authority (Figure 3.11B). I name the latter solution “legacy inversion”. Figure 3.11A is obtained by fixing the AR model order to 250 and by setting the parameter μ that governs the degree of spatial continuity in equation 3.20 to 0.2. The AI derived from the tomographic velocity field (Figure 3.9B) has been weighted in the inversion 3.11A by tuning the parameter (λ) from equation 3.20 to 0.3 times the ratio of maximum eigenvalues of \mathbf{G} and $\mathbf{L}^H\mathbf{L}$. The presence of two soft constraints on AI reduces the uncertainty and enhances the lateral continuity of the estimation at about the Top Paleocene ($6 \cdot 10^6 \pm 1 \cdot 10^6$ rayl) and the Top Cretaceous horizons ($8 \cdot 10^6 \pm 1.5 \cdot 10^6$ rayl). The lateral continuity is enhanced at about the timing of such horizons because, at those timings, similar values of AI are imposed to all the traces of the section. The impedance constraints are applied 100 ms after the picked

horizons to avoid trace-to-trace artefacts that may arise after the CARV reconstruction sharpens the seismic events. If soft constraints were applied at the timings of the picked horizons, each constraint might be enforced right before the reconstructed reflector in one trace and right after the reconstructed reflector in the adjacent trace, thus leading to unreasonably different AI interval property between the two traces at about the timing of the constraint. The legacy inversion of Figure 3.11B was obtained by merging the low-frequency AI model, derived from well logs and interpolated in a stratigraphically conformable manner across the seismic line, to the relative AI recursively derived from the seismograms. The well logs were smoothed using the wavelet provided in the legacy inversion project and overlain to the inversion results within rectangular boxes. Figure 3.11C shows the difference between the inversion of Figure 3.11A and the inversion of Figure 3.11B. Within the water column and in the few hundred ms below the seabed the differences are due to the incorrect extrapolation of the well information in the shallowest portion of the legacy model-based solution. Shallow areas around trace 500 show significant anomalies in the CARV reconstruction (black arrows). A pinch-out, which is a feature of potential interest, is apparent in the difference section (Figure 3.11C) at about trace 700 and at about 3,500 ms TWT (black arrows). This feature is present in the CARV result, but not in the legacy AI inversion, probably because of the limits of the model-based approach when the well population and the number of horizons used for extrapolating the log information are limited. On the contrary, the CARV inversion is not affected by these issues and it highlights an increase of AI underneath the pinch-out (Figure 3.11A) that is not evident in the tomographic velocity field (Figure 3.9B). Even though the pinch-out is also evident in the seismic data (Figure 3.9A), the additional piece of information contained in the CARV inversion is the estimate of the AI within the different layers. Figure 3.11B shows a hard layer (in yellow) at the depth corresponding to the pinch out. This layer extends across the section and I interpret it as being probably due to inaccurate extrapolation of the log information in the legacy model-based solution.

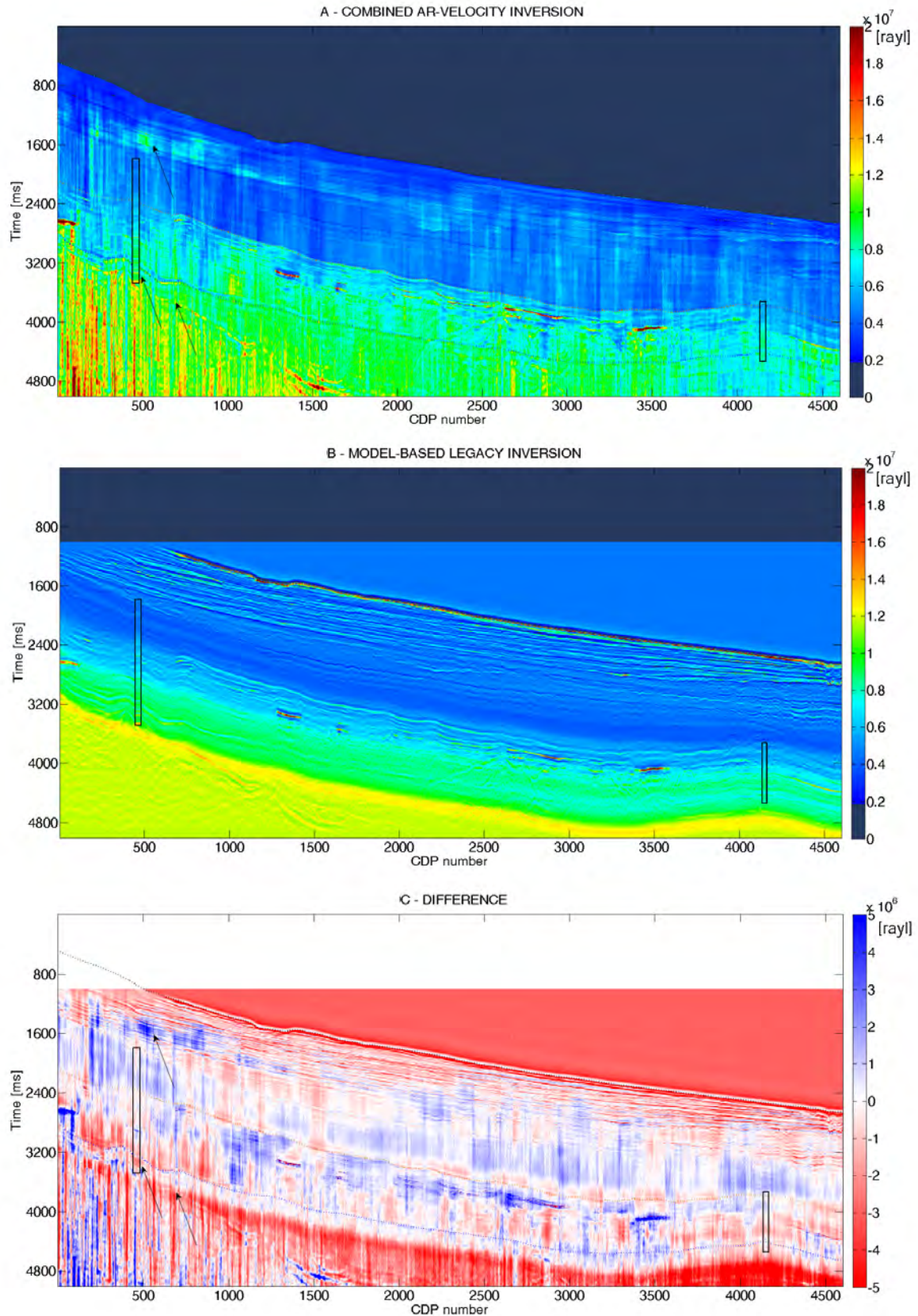


FIGURE 3.11: Panel 3.11A: AI inversion [rayl] combining the AR reconstruction and the velocity field regularization term with lateral continuity. Panel 3.11B: model-based legacy AI estimate [rayl]. Panel 3.11C: difference between the CARV inversion (3.11A) and the model-based legacy inversion (3.11B) [rayl].

Figure 3.12 shows the effects of not accounting for the continuity term in the CARV reconstruction (Panel 3.12A), the effects of not incorporating the velocity-derived AI in the AR reconstruction (Panel 3.12B), and the effects of changing the AI derived from the velocity field in the CARV reconstruction (Panel 3.11C). Solving the inverse problem of equation 3.20, which is the case where lateral continuity is imposed, provides a more realistic estimate than solving the problem of equation 3.12, which is the case where lateral continuity is not imposed ($\mu = 0$). The unsmoothed solution in Figure 3.12A shows more high-frequency spatial noise (vertical stripes) with respect to the smoothed solution of Figure 3.11A. The solution that did not use the smoothing term in the cost function, shows few traces with unreliable AI, for instance those with AI larger than $2 \cdot 10^6$ rayl in the water column. These features are indicated by red arrows in Figure 3.12A. Figure 3.12B represents the classical AR inversion with two soft constraints at depth, and with an additional lateral continuity weight. The weight ($\mu = 0.2$) has the same smoothing effect as the one adopted in Figure 3.11A. The incorporation of the interval velocity field is important to guide the solution toward accurate results: in absence of the velocity field information, as in Figure 3.12B, some deep parts of the section (at more than 4,000 ms for CDPs 1-1500) show lower AI values in comparison to those of Figure 3.11A. These lower AI values are comparable to much shallower formations and thus hard to justify on a geologic basis. To demonstrate the sensitivity of the CARV method to the variation of the interval velocity field, I show in Figure 3.12C the inversion result obtained if the tomographic-derived AI field is 5% higher than the AI field used for the inversion shown in Figure 3.11A. The colour scale in Figure 3.12C does not directly represent the AI values, but it is normalized by the AI values of the inversion 3.11A. This color scale choice enhances the effects of weighting in the solution the AI derived from an overall faster velocity field. Only a subtle generalized increase of the low-frequency content of the AI is noticeable with respect to the solution of Figure 3.11A. The two soft constraints on impedance further attenuate the background AI variation at about the time of their respective horizons.

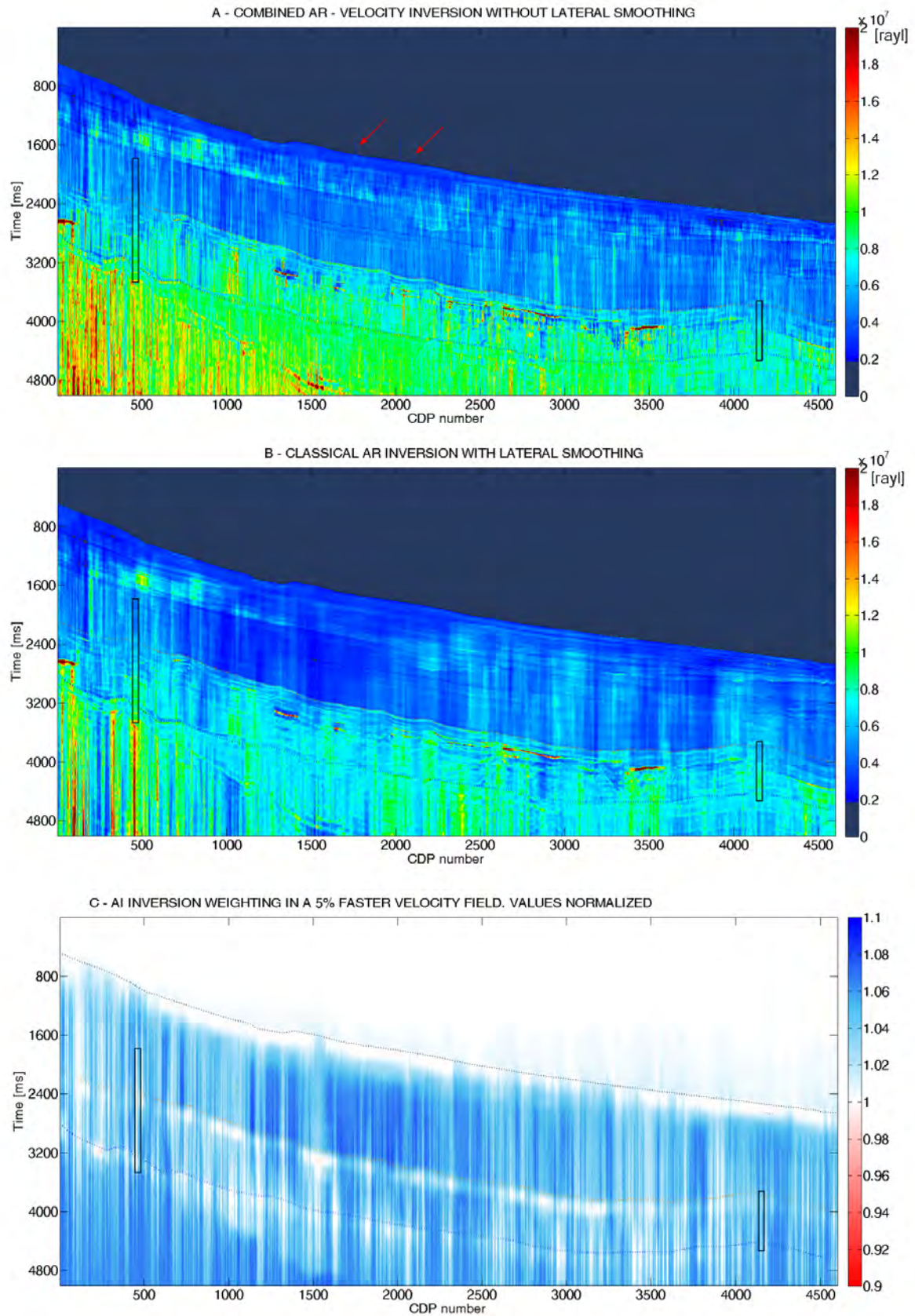


FIGURE 3.12: Effects of lateral continuity and ancillary information on the CARV inversion. Panel 3.12A [rayl] shows the result in absence of lateral smoothing, Panel 3.12B [rayl] shows the results of a classical AR inversion in absence of the AI derived from the velocity field. Panel 3.12C shows the ratio between the AI inversion when the AI derived from the tomographic velocity field is arbitrarily increased by 5%, and the AI inversion of Figure 3.11A.

Figure 3.13 highlights the role played by the low-frequencies on the AI inversion. Figure 3.13A shows the 0-5 Hz components of the CARV inversion in Figure 3.11A, while Figure 3.13B shows the low-frequency model used as input for the model-based inversion 3.11B. Both the CARV and the model-based inversion incorporate seismic data components higher than 5 Hz as recorded, to characterize the higher-frequencies of the AI. The CARV result of Figure 3.13A represents the AI information that I deem to be reliably reconstructed from the seismic data and the tomographic velocity field. Figure 3.13A shows a relatively high AI layer (indicated by the red arrows) at about 500 ms below the water bottom, and a change in impedance in the bottom left corner of the section (black arrows) that is neither related to the velocity field (Figure 3.9B) nor to the AI constraints at the two selected horizons. Figure 3.13A shows vertical stripes due to the incorporation of the information from the seismic events, particularly evident in the deepest part of the section. Those stripes are not present in Figure 3.13B, which is directly derived by a spatial extrapolation of well log data. The yellow region in the bottom of the low-frequency model of Figure 3.13B is probably due to the incorporation, in the legacy model, of a third well that lays outside of the 2D section that I discuss. The comparison between Figure 3.13A and 3.13B highlights the different low-frequency character that is responsible for the different mismatch of the two inversions at well locations.

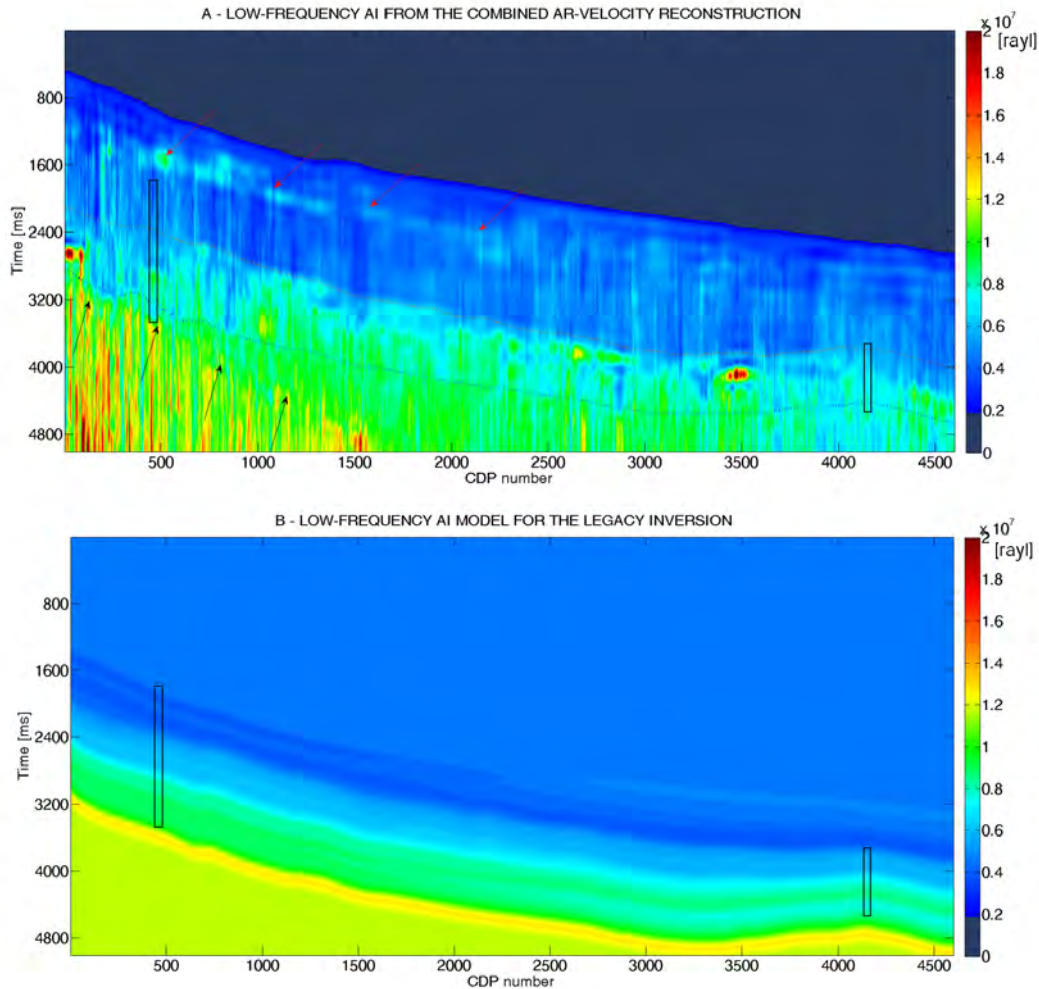


FIGURE 3.13: Comparison between the low frequency content of AI reconstructed via the CARV method (3.13A) [rayl] and via the low-frequency model for the legacy inversion (3.13B) [rayl].

Although the CARV reconstruction method appears to be a sensible solution for the low frequencies of AI at the scale of the entire section, the comparison of the results of Figure 3.11A and 3.11B at the two available wells, shows that the log matching is not as good as in the case of the legacy inversion. This result could be better appreciated in Figure 3.14, where the AI derived from well log measurements (red line) is compared to the model-based legacy inversion (blue line) and to the CARV inversion around the well location (gray lines). The poorer match of the CARV inversion to the log-derived AI is presumably due to the well log constraints used in the legacy AI inversion that the CARV method tries to incorporate with ancillary indirect information and inferences. Table 3.3 shows the RMS error of the two types of inversion (Figure 3.11A and 3.11B) with respect to the well log data. The error for the CARV inversion is computed on the average of the 25 traces around the well location. At well 132/15 the modified AR solution is comparable with the legacy AI along much of the well, although a relatively large mismatch exists between about 3250-3400 ms. At well 132/06 a significant mismatch exists around 4100-4350 ms, with a dominant frequency between 2 and 5 Hz (see Figure 3.14). The mismatch in this frequency range is possibly due to an incorrect AR low-frequency extension along part of the well log. A further measure to assess the quality of the AI inversion could be

the fraction of log data that is matched by the AI estimate within a given confidence level. If I set a threshold of the 15% on the relative error of the estimation (with respect to the log-derived AI), I observe that the legacy model-based inversion exceeds this value for 6% of the length of Well 132/06 log and for 16% of the length of Well 132/15. The CARV inversion exceeds the same threshold for 28% of the length of Well 132/06 and for 22% of the length of Well 132/15. All the misfit measures I approached agree on the fact that the CARV inversion has a poorer match than the legacy model-based inversion to log data.

WELL	METHOD	RMS ERROR [rayl]	% ERROR	METHOD	RMS ERROR [rayl]	% ERROR
132/15	Legacy model based	$57.5 \cdot 10^4$	8.5%	CARV	$73.4 \cdot 10^4$	9.6%
132/06	Legacy model based	$41.1 \cdot 10^4$	5.9%	CARV	$83.0 \cdot 10^4$	11.1%

TABLE 3.3: *Absolute and relative RMS error of the legacy model-based inversion and of the CARV inversion with respect to the AI derived from well logs.*

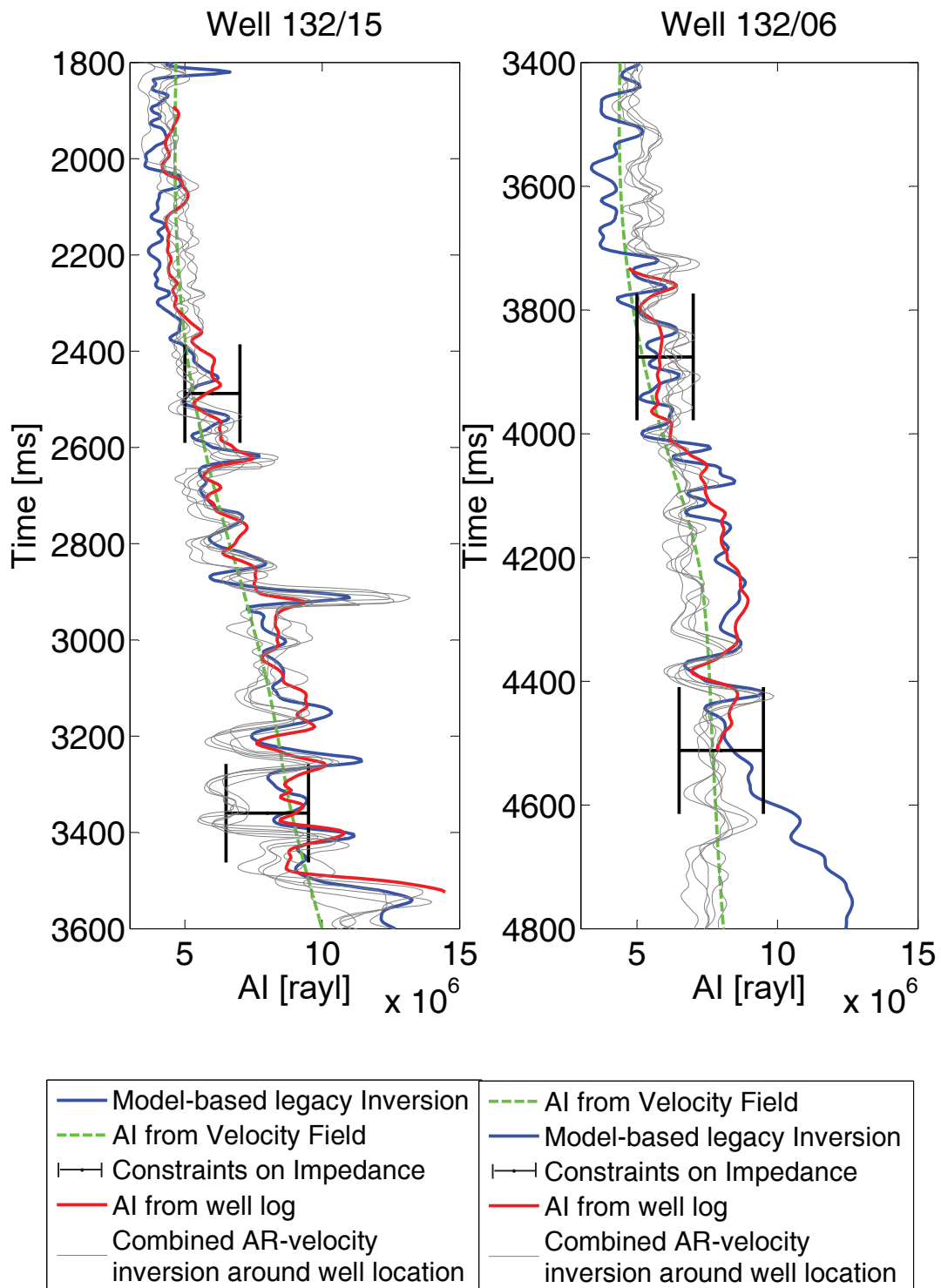


FIGURE 3.14: Detail of the AI inversion around the two well locations. The results refer to the inversions presented in Figure 3.11A and 3.11B. The CARV inversion is proposed every 5 traces for 25 traces around the two well locations.

3.4.3 Lateral Continuity Enhancement on Real Data

The approaches to lateral continuity that are theoretically described in section 3.3.6 and 3.3.7, are here presented with respect to the reference result of Figure 3.12A. The CARV algorithm does not consider the behaviour of the adjacent traces when reconstructing the low frequency components of the reflectivity in Figure 3.12A. The result presented in Figure 3.15 is still 1-D, but the input data have been filtered via principal component analysis on a sliding window of 200 traces. To reduce the effects of the incoherent noise, the 15% less energetic components of the data have been removed from the window. Although the vertical artefacts are different from Figure 3.12 to Figure 3.15, no significant improvement is appreciable with the principal component analysis approach. No harsher filters on the input data have been applied, in order to avoid damaging the genuine seismic events. The impact of the moving-average filter of Figure 3.16 and of the low-pass spatial filter of Figure 3.17 is more significant. Those filters have been designed on the results of the CARV inversion, therefore they could be as harsh as the trace-to-trace artefacts are adequately removed from the significant geologic information. The moving average filter works in 5 traces long window that slides trace by trace, while the spatial low-pass filter has a harsh cut-off at 0.05 of the Nyquist spatial frequency.

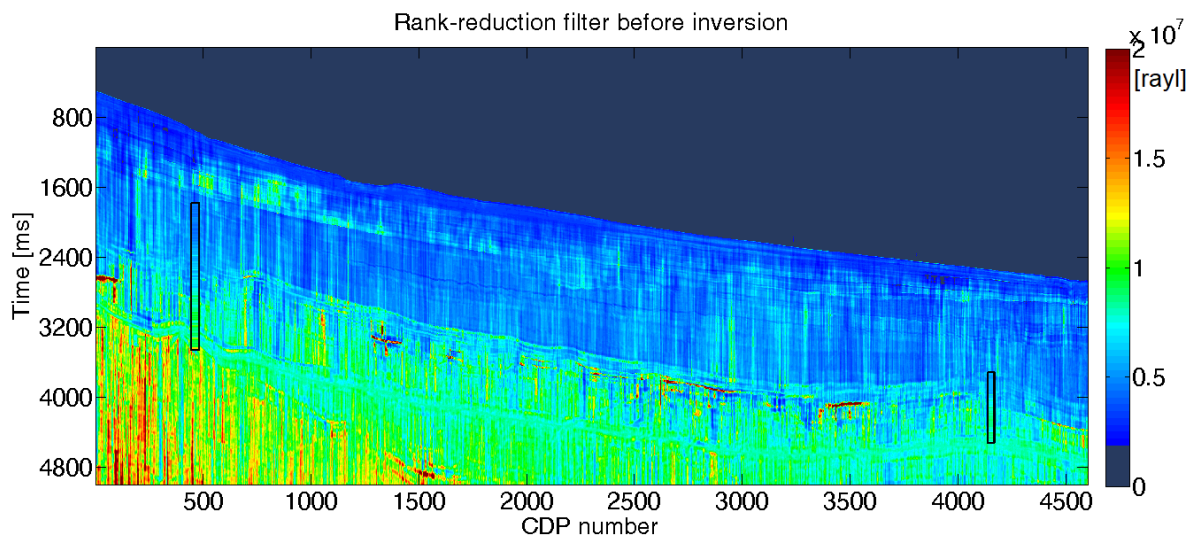


FIGURE 3.15: Principal component filter on the input data and subsequent CARV inversion for AI [rayl]. Filtering was performed in windows of 200 traces, by removing the 30 less energetic data components.

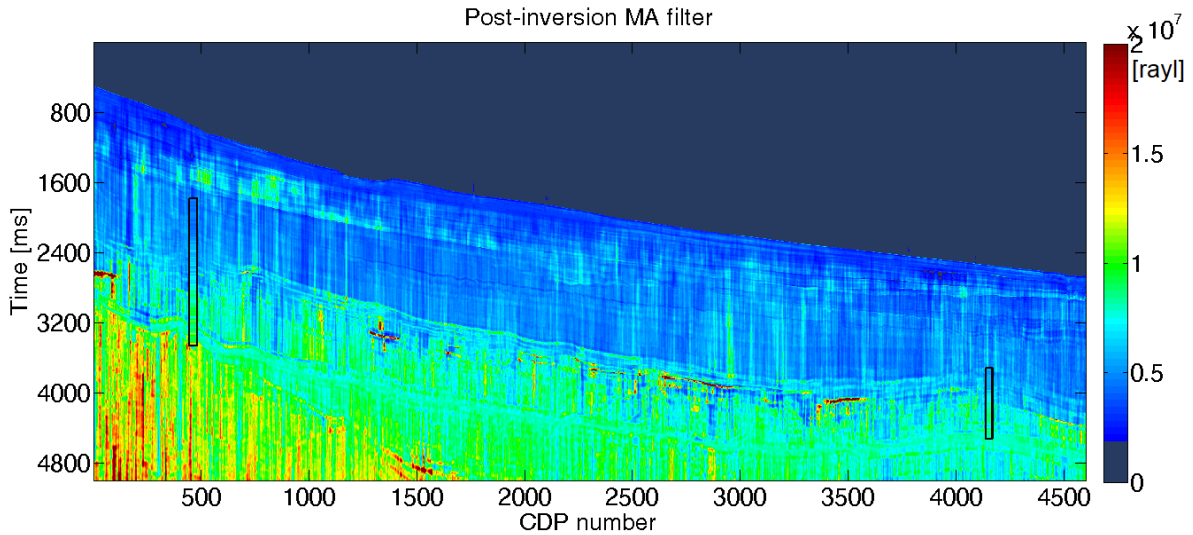


FIGURE 3.16: Moving Average (MA) filter on the CARV AI inversion result [rayl]. Filter length: 5 traces.

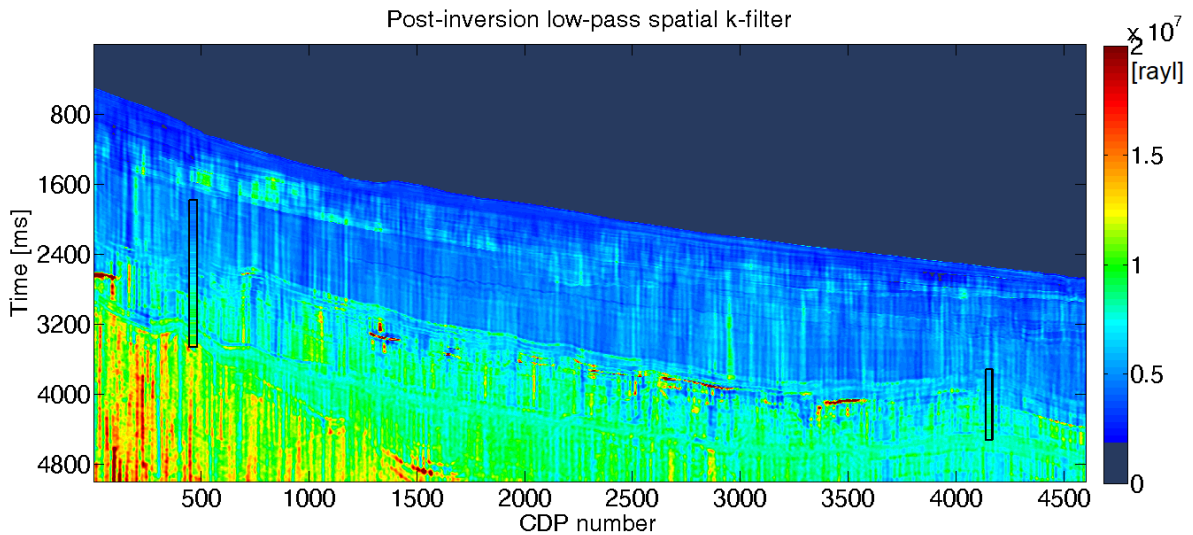


FIGURE 3.17: Low-pass spatial k-filter on the CARV AI inversion result [rayl]. The cut-off value is 0.05 times the spatial Nyquist frequency.

Adding a penalty term in the cost function appears to be a more desirable solution, as it avoids the introduction of corrective actions as the ones produced by the post-inversion filters. Figure 3.18 proposes the outcome of the CARV inversion when the cost function is expressed by equation 3.18. In this case, μ is set to 2 times the ratio between maximum eigenvalue of the matrix $\mathbf{G} = \mathbf{C}^H \mathbf{C}$ and the maximum eigenvalue of the matrix $\mathbf{D}^H \mathbf{D}$. High-frequency spatial variations of the inverted AI is significantly reduced especially in the shallow areas where the lateral variations of AI is less pronounced. By comparing this result with the result in which the penalty term deals with the reflectivity variation (Figure 3.11A), it is possible to notice that smoothing the reflectivity does not completely attenuate all the vertical bands in the AI estimation. On the contrary, the AI estimate of Figure 3.18 appears more continuous, with particular reference to the shallow areas, at the expenses of an higher computational cost. The inversion algorithm is implemented in patches of 10 traces when the weight on the AI continuity is enforced, while

it is implemented trace by trace (see section 3.3.8) when the weight on reflectivity is enforced. The hyperparameter μ does not assume the same significance in the two cases, becoming more difficult to compare the quality of the results, even though the geological interpretation that could be inferred from both smoothed estimates is very similar.

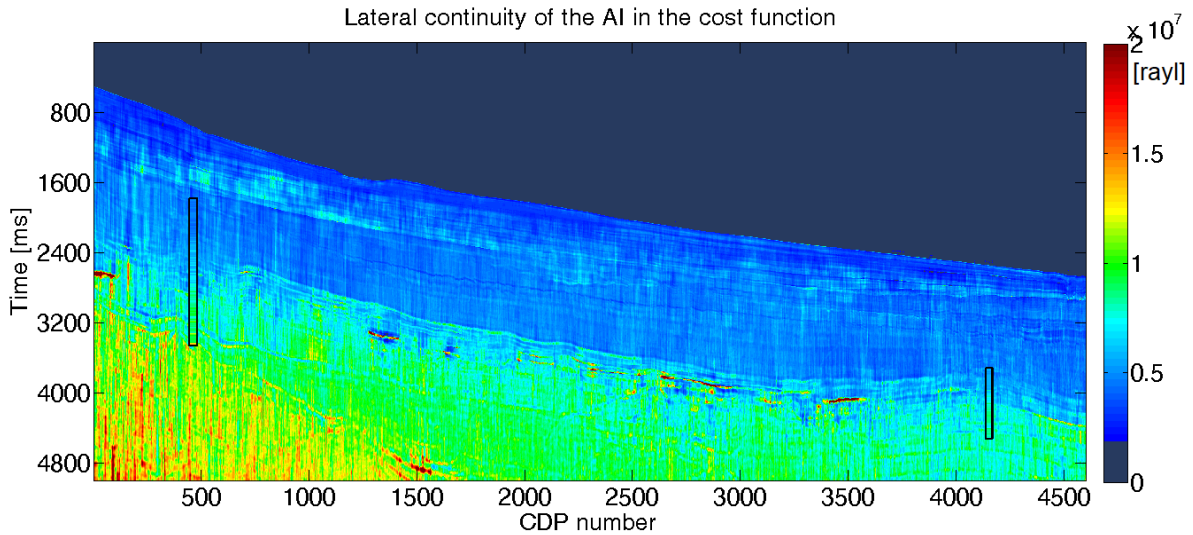


FIGURE 3.18: CARV AI inversion smoothed via the multi-trace inversion in overlapping windows. Length of the overlapping window: 10 traces. Sliding of 5 traces between the centre of one window and the centre of the following window.

3.5 Discussion and Conclusions

The combined AR-velocity (CARV) algorithm reconstructs the main features of AI of the synthetic examples proposed. The introduction of an accurate interval velocity field is useful to direct the low frequencies of the inverted AI to more accurate values. For example, the CARV results (black lines of Figure 3.7D, 3.7F, 3.7H) reconstruct the AI of the most complex Model 2 (red) better than the classical AR results (gray lines). This statement is supported by the RMS errors of the reconstruction proposed in Table 3.2. Synthetic cases show the effects of not considering the wavelet shape in the inversion. In particular, Figures 3.7G and 3.7H show spurious peaks and incorrect values in the AI estimate that are more pronounced than in Figure 3.7C and 3.7D where the wavelet is properly removed before inversion. This behaviour is also analytically discussed in the subsection 2.5.7 with reference to an AR model of order 1. The presence of wavelet effects in the data may invalidate the AR reconstruction: care must be taken during pre-processing steps to minimize this issue within the signal band-width. Spectral analysis on long time windows (see Figure 3.10) may help to identify a frequency band where the energy of the single components is balanced. The CARV approach also results in features of interest in the inverted test field-dataset that are not observed in the legacy inversion, which incorporates log data. The comparison between Figure 3.13A and Figure 3.9B shows that the low frequency of the CARV AI appears to contain more temporally and laterally varying character of possible geologic origin than the AI derived from the velocity field alone. The shallow areas that are characterized by a flat spectrum in the signal bandwidth show an interesting contribution of the AR reconstruction in revealing the higher impedance anomalies at about 500 ms

below the water bottom, at about CDPs 500-2000 (Figure 3.13A). The lateral variation of the low-frequency components of the CARV inversion of Figure 3.13A is more realistic (despite the vertical stripes) than the lateral variation of the low-frequency components of the legacy model-based inversion in Figure 3.13B, because it includes spatially-varying information in compliance with the seismic data. The very low-frequency differences between the two panels of Figure 3.13 are mainly due to the differences between the AI derived from the velocity field of Figure 3.9B and the very-low-frequencies of the legacy model-based inversion (Figure 3.13B), with a role played also by the AI constraints at about the two horizons where they are enforced. The spatially smooth very-low-frequency difference may account to a large extent for the differences that can be seen in Figure 3.11C. There is a tendency of the legacy model-based inversion to be more accurate at well locations because it was constructed to match the log data at low frequencies, while the CARV method does not incorporate the log data. Table 3 illustrates this bias, but the tie at much of the well depths is not dramatically different between the two inversion methods, as reported in the 3.4.2 section. Sources of error in the CARV inversion are also related to the uncertainty of the choice of the AI for the reference layer. This issue may not be solved once an interval velocity field is available for the poor accuracy of the velocity field in the shallow layers, and for the uncertainty on the reference density. For instance, Figure 3.9B shows some unrealistic velocities within the water-column. The estimation of the AI in the reference layer should be even more problematic for land data where there is no water column characterized by a very narrow range of AI. Furthermore, amplitudes of seismic data “are more reliable for marine than for land data” (Simm and Bacon, 2014). Even if I consider a lateral continuity term in the CARV reconstruction, the inversion shows a trace-to-trace variability that is still not completely mitigated. The trace-to-trace variability does not prevent the interpretation from being made at the global scale of the inverted 2D section: the signature of the vertical stripes is different from the signature of the geologic features in the CARV reconstruction. Weighting a smooth interval velocity field in the AR reconstruction also favours a laterally smooth solution. The interval velocity field weighting factor λ should be tuned by performing a sensitivity analysis of its effects on the result.

Figure 3.19 provides a measure of the sensitivity of the AI inversion depending on the CARV parametrization. Each of the four panels of Figure 3.19 shows the sample standard deviation among the AI models that can be obtained by sampling the most impacting parameters of the CARV reconstruction one at a time. The standard deviation is computed sample by sample for each trace of four Rockall Trough AI inversions. Figure 3.19A shows the sample standard deviation section that is obtained by varying the AR model order from 200 to 275, in increments of 25. The choice of the AR model order requires the knowledge that there are fewer reflectors in the section than the number of frequency components that can be resolved by the spectral estimation within the optimal bandwidth. In the real subsurface this condition is not always met. However, given that the AR models are less sensitive to model order than the ARMA models, and once ancillary information is available, the variability of the AI reconstruction that depends on this parameter is less than $2 \cdot 10^6$ rayl. Figure 3.19B shows that the sensitivity of the inversion to the scalar that transforms the relative amplitude of the seismogram into the reflectivity amplitude is also relatively small. In Figure 3.19B, I let the scalar vary from 50,000 to

65,000 in increments of 5,000. The limited impact of the scalar can be attributed to the use of ancillary information such as soft constraints at depth and the interval velocity field that make the reconstruction less sensitive to the amplitude variation of the input data. Figure 3.19C shows a measure of the variability that can be related to a change in the low frequency cut-off for fitting the AR model. The cut-off varies from 5 to 8 Hz in 1 Hz increments. The bandwidth choice appears to have a larger effect with respect to the other parameters, but a spectral analysis of the dataset to be inverted could greatly reduce this kind of uncertainty. Figure 3.19D shows the sample standard deviation among four AI inversions that have been obtained by letting the trade-off parameter λ vary in the range 0.1 to 0.4 times the ratio between the maximum eigenvalues of matrix \mathbf{G} and $\mathbf{L}^H\mathbf{L}$. The parameter λ weights in the CARV solution the interval velocity field, and its influence is more pronounced in the deepest part of the section where the recursion of equation 3.2 tends to provide less stable results if a classical AR approach is attempted. The variability in all the panels of Figure 3.19 is about one order of magnitude less than the estimated values of AI themselves. From a visual inspection of Figure 3.9A, the seismic events seem sparse enough for a correct AR modelling, but interference (see Figure 3.1) and attenuation (see Figure 3.10) tend to degrade the AR reconstruction.

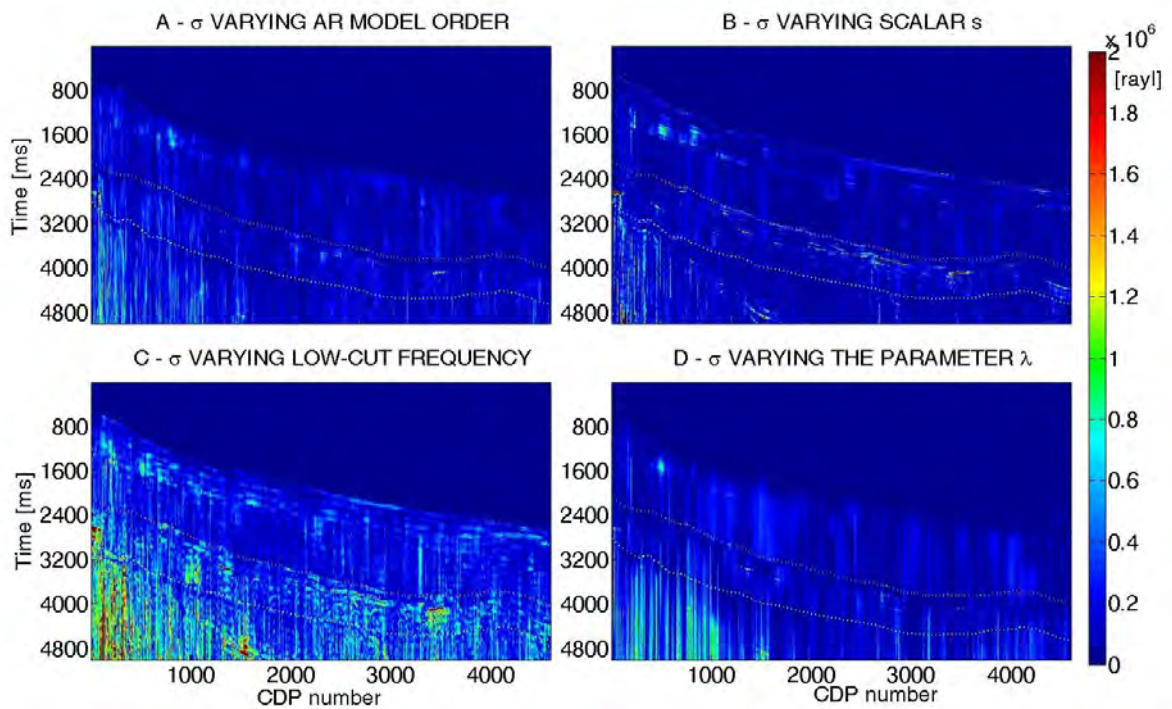


FIGURE 3.19: Sample standard deviation of the AI results among four different outputs when: the AR model order changes from 200 to 275 (3.19A), the scalar that maps the seismic data into reflectivity changes from 55,000 to 65,000 (3.19B), the low-cut frequency changes from 5 to 8 Hz (3.19C), the scalar that weights the velocity field changes from 0.1 to 0.4 (3.19D).

The CARV method proposed for the reconstruction of the full band of AI provides a more accurate solution than the classical AR algorithm on which it was based, at the expense of the larger amount of information required, some additional pre-conditioning work and parameter tuning. A reduced sensitivity to the parametrization choice is demonstrated on synthetic examples characterized by sparsity in the time domain representation of the reflectivity and on a seismic

section from the Rockall Trough area. Due to the hypothesis that the number of events is limited, that the acoustic impedance variation is only related to jumps at specific interfaces, and due to the necessity of a spectral estimation, the original AR reconstruction method is prone to inaccuracies. For this reason, the CARV reconstruction method benefits from the introduction of the seismic-based interval velocity field combined with a targeted rock physics relationship for the density, resulting in a more accurate evaluation of the low frequency components of the AI with respect to the classical AR approach. The match between the proposed inversion results and log information is comparable to the legacy model-based inversion for one of the two wells of the Rockall Trough test line. The misfit of the CARV inversion at the other well is significantly higher in a limited time-window. Trace-to-trace vertical artefacts were unavoidable in the implementation of the method. Regardless, the performance of the inversion procedure should be considered on the global scale of the test dataset where the signature of the geologic features of possible interest is different from the signature of the artefacts. It is worth stressing on the point that the separation between vertical artefacts and potential geological features is a strength of the CARV inversion.

Chapter 4

Sparsity-based Approach to Pre-stack Inversion

4.1 Introduction

Considering pre-stack data for elastic parameter estimation via autoregressive reconstruction is the natural extension of the post-stack CARV approach. This Chapter deals with the full information content of seismic gathers and it extends the discussion which has been proposed in Bianchin and Sacchi (2018) about few possible strategies for the low frequency reconstruction of seismic data. The ill-posed nature of seismic pre-stack data is twofold. In particular, further to the problem of estimating the low-frequency components of the reflectivity hidden in the seismic data (as per the discussion of Chapter 2), at least one elastic parameter in the three-terms AVA inversion (De Nicolao, Drufuca, and Rocca, 1993) is poorly resolved by the seismic experiment. Perez, Velis, and Sacchi, 2017 have proposed a LASSO solution (see section 2.4.2) that can theoretically estimate elastic parameters from reflection seismograms even if well log information is not available. A similar solution in terms of full bandwidth reconstruction is approached in this Chapter via AR modelling. This approach implies that the solution in terms of reflectivity is not necessarily the sparsest, but rather it is the one that is more compatible with a definite but limited number of events in the time domain. The novelty of the approach proposed here lays in the extension of the AR reconstruction to non zero incidence angles.

Once the low frequencies of reflectivity are reconstructed, it is possible to map the resulting reflectivity into Elastic Impedance (EI) at the angle (θ) the reconstructed trace ($r(\theta)$) refers to (Connolly, 1999):

$$EI(t, \theta) = EI(t_0, \theta) e^{2 \sum_{i=1}^t r_i(\theta)}. \quad (4.1)$$

If all traces within a Common Image Gather (CIG) undergo the AR completion process, the inversion for the absolute value of a set of elastic parameters (i.e. p-wave velocity (α) density (ρ) s-wave velocity (β)) can also be obtained from the reflected wave-field, provided that a Rock Physics regularisation term is introduced. Next section discusses the issue of offset to angle mapping, by proposing and testing three fast approaches that are not based on ray-tracing. Two workflows for the pre-stack reconstruction of seismic gathers are then theoretically discussed in section 4.3 and tested on synthetics in section 4.5.

4.2 Offset to Angle Mapping

Multichannel seismic data are recorded with the surface spatial information that is related to offset or source and receiver position. In order to invert the amplitudes of multichannel seismic data for the elastic parameters, data must be mapped into CIG sorted by incidence angle first. This is because a quantitative AVA reconstruction of elastic parameters can only be approached when the reflectivity related to the recorded data is organised by angle (see equation 4.6). Up to 30°-35° (Connolly, 1999) the approximation

$$\sin \theta = \frac{x(t)V_{int}(t)}{tV_{rms}(t)^2} \quad (4.2)$$

can be considered valid and the only parameters required for offset (x) to angle (θ) mapping are the interval (V_{int}) and RMS (V_{RMS}) velocity field at each sample t of each trace. Mode conversion can be neglected for this range of angles. A more accurate mapping for dipping events or wider angles can be obtained by migration algorithms (i.e. de Bruin, Wapenaar, and Berkhout (1990)) and ray-tracing (Simm and Bacon, 2014).

From move-out analysis only an approximation of the RMS velocity field can be obtained. Unless a tomographic analysis is available, the approximate RMS velocity should be further inverted into interval velocity to solve equation 4.2. This can be obtained by smoothing the Dix relationship (Dix, 1955) with a penalty term that accounts for the norm of the time domain derivative of the inverted interval velocity. Within the Dix formulation, $\mathbf{d} = \mathbf{V}_{RMS}^2$ is linearly related to the square of the input data $\mathbf{m} = \mathbf{V}_{INT}^2$. Instead of solving the linear problem

$$\mathbf{A}\mathbf{m} = \mathbf{d} \quad (4.3)$$

in which \mathbf{A} represents the integral operator proposed by Dix, a smooth solution along the time direction can be found by minimising the cost function

$$J = \|\mathbf{A}\mathbf{m} - \mathbf{d}\|_2^2 + \lambda^2 \|\mathbf{D}\mathbf{m}\|_2^2. \quad (4.4)$$

In the cost function 4.4

$$\mathbf{D} = \begin{bmatrix} 1 & -1 & 0 & \dots & 0 \\ 0 & 1 & -1 & \dots & 0 \\ \dots & & & & \\ 0 & \dots & 1 & -1 & \end{bmatrix}. \quad (4.5)$$

Errors in the RMS velocity field and an incorrect choice of the hyperparameter λ in equation 4.4 result in errors in the generation of the gathers and consequently in the reconstruction of the elastic properties. Few details need to be addressed before performing the offset to angle mapping:

- The choice on the number of angles to be adopted given a certain number of channels, their spacing and the target depth
- The binning of the seismic traces for each angle (possible issues are unpopulated bins in the shallow part and multiple populated bins in the deep part)

An entire line of research studies the problem of seismic data regularization (i.e. Fomel (2003)), and various techniques exist to map data with variable sampling rate and possible gaps from one domain into another. I briefly discuss here below three basic approaches to offset to angle mapping:

- Interpolation between the two traces that are closer to the centre of each angle bin
- Angle stack
- Weighted angle stack

The angle sampling is usually much sparser (one sampled angle every several degrees is a common figure for seismic inversion work-flows) than the offset sampling. This choice has the purpose of populating the shallow part of the angle gathers with traces coming from different channels. It is reasonable to choose the angle discretization based on the target depth, such that at least one channel is approximately mapped into one angle bin at the desired depth. The choice among the three regularisation strategies enlisted above, is discussed in the next subsections.

4.2.1 Interpolation Solution

Equation 4.2 provides a direct way to map offsets into angles but also angles into offsets. A possible choice for the common angle gather population is the value corresponding to the couple (x, t) that maps closest to the couple (θ_b, t) in equation 4.2 (where θ_b is the centre of the angle bin). This choice leads to evident discretization artefacts both in time and angle direction within an angle gather and it has not been considered. A smoother reconstruction of angle gathers can be obtained by interpolating the value of the two (x, t) samples that fall close to the (θ_b, t) value. The solution obtained by linear interpolation of the two closest traces in the (x, t) domain is mathematically expressed by

$$trace(\theta_b, t) = (\alpha)trace(x_i, t) + (1 - \alpha)trace(x_{i+1}, t). \quad (4.6)$$

The weight α is chosen according to the relative distance of each (x_i, t) trace to the actual mapping obtained for the central angle θ_b from equation 4.2. Drawbacks of this solution are related to the fact that for deep events the redundancy of traces that fall in the same angle bin at different offsets is ignored.

The solution on synthetic data is smooth (i.e. Figure 4.2) but as soon as there is some noise the result is strongly affected by it (Figure 4.3). This is something which is unavoidable in the shallow, but not in the deepest part of the trace where the redundancy of measurements at different offset could be accounted for with other methods.

4.2.2 Stack Solution

In order to make the reconstructed angle trace more robust to the presence of noise, angle gathers can be obtained by averaging the samples of the traces, sorted by offset, which fall in the same angle bin for a given TWT. In this way the amplitude information is partially distorted by the stacking operator. By comparing the angle gathers of Figure 4.2 and 4.3 the stacking

method provides very similar results to the interpolation method in the ideal case where no noise is present. However, in presence of noise (Figures 4.3 and 4.4) the results of the stack appear more even across angles, with particular reference to deep and target reflectors of Figure 4.3 that remain closer to the undisturbed amplitudes of Figure 4.2. The noise present in the angle gathers thus obtained is more likely not to be stationary along the time direction because of the attenuating effect of the many traces stacked for each angle in the deep part of the seismogram.

4.2.3 Weighted Stack Solution

A further method for the reconstruction of angle gathers from data sorted by increasing offsets has been studied. This method represents a trade-off between the interpolation and the stack procedure. The method first calculates for each central angle of the bin and any given TWT, the samples sorted by offset that fall in the angle bin. Then, those values are stacked together, with a weight that depends on the distance from the central angle of the angle bin.

The weight chosen is

$$w_i = 1 - \frac{|\theta - \theta_b|}{n} \quad (4.7)$$

where n is the number of traces summed for each angle and each TWT. With this choice, the values that fall closer to the centre of the angle bin have an higher impact to the amplitude value of the data than the values that are closer to the border of the bin.

4.2.4 Mapping of Synthetic and Real Data

Results are presented with particular reference to the synthetic case where the three events highlighted in Figure 4.1 are analysed in Figures 4.2, and 4.3. Please note that the angles chosen for the mapping increment by 3 degrees from 3 to 36 degrees in Figure 4.2. The abrupt muting in the bottom panels of Figures 4.2 and 4.3 is due to the choice of the angle mute at 36 degrees. The mapping is also presented in wiggle display on the real sample CIG gather of Figure 4.4. The gather refer to the Penobscot dataset which is fully described in Chapter 7.

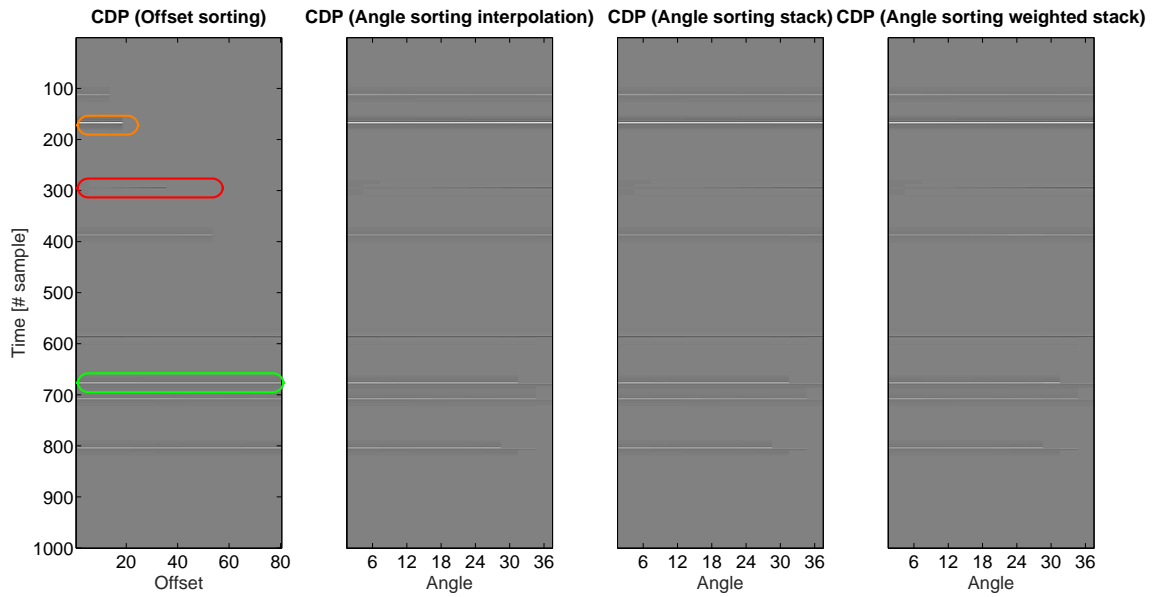


FIGURE 4.1: Synthetic CIG obtained by the convolution of a sparse reflectivity with a 25 Hz Ricker wavelet. Data are corrected for the normal move-out. A mute at 36° has been applied to the data. The panel on the left displays the CIG sorted by offset, and the other panels present the three different mapping methods described in the text. The events highlighted by the orange, red and green boxes correspond to the shallow, the deep, and the target events of Figures 4.2 and 4.3, respectively.

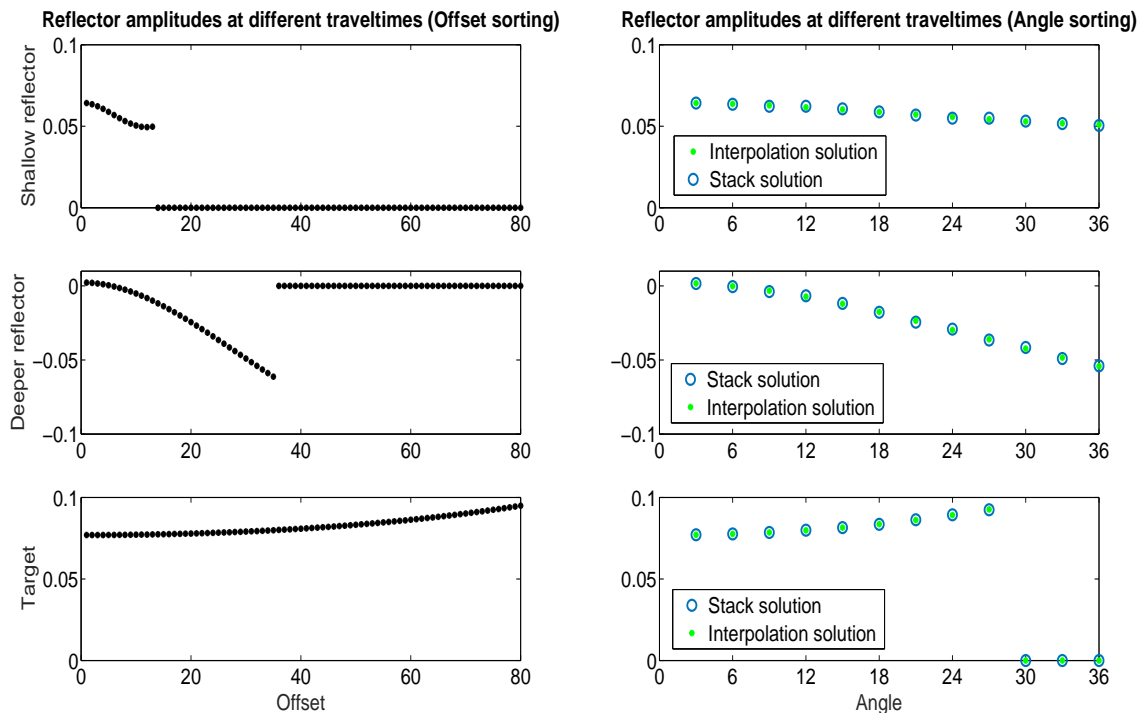


FIGURE 4.2: Amplitudes for the three events highlighted in Figure 4.1. The panel on the left shows the peak amplitude of the selected reflectors sorted by offset, the panels on the right show the peak amplitudes after angle mapping. Case without noise.

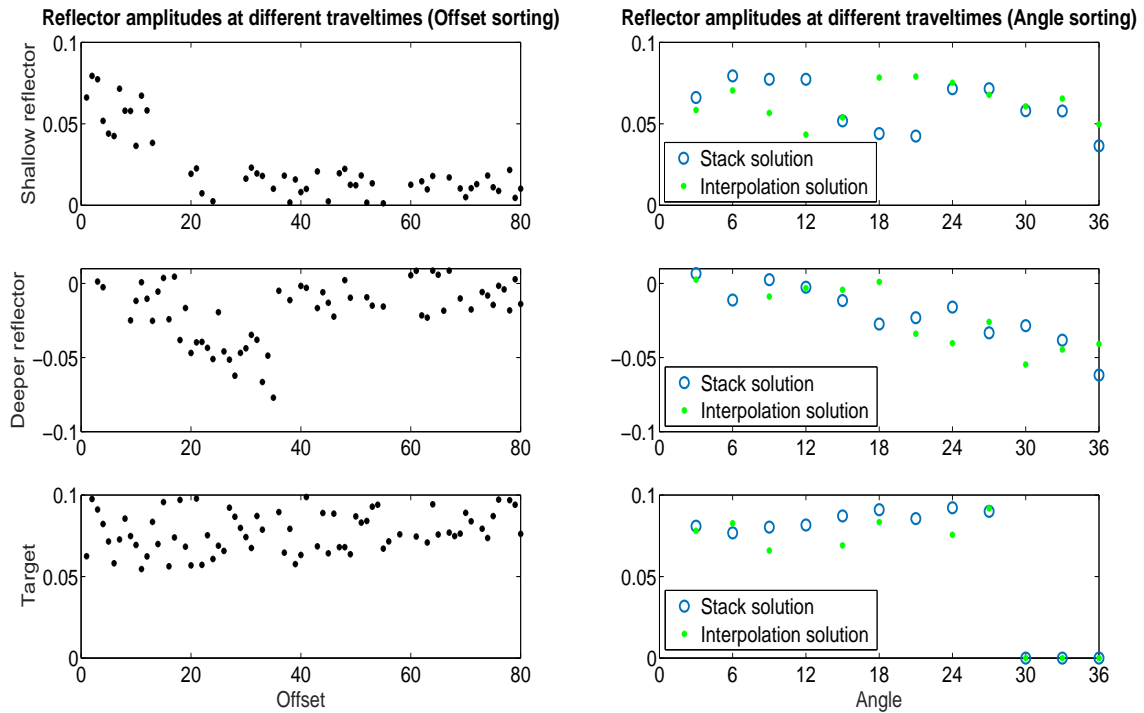


FIGURE 4.3: Amplitudes for the three events highlighted in Figure 4.1. The panel on the left shows the peak amplitude of the selected reflectors sorted by offset, the panels on the right show the peak amplitudes after angle mapping. Case with $S/N = 20$ dB.

The results of the three methods proposed for mapping offsets into angles are displayed for a CIG of the Penobscot marine dataset. On the real dataset no significant difference is evidenced among angle gathers corresponding to the stack, the interpolated, and the weighted stack solution.

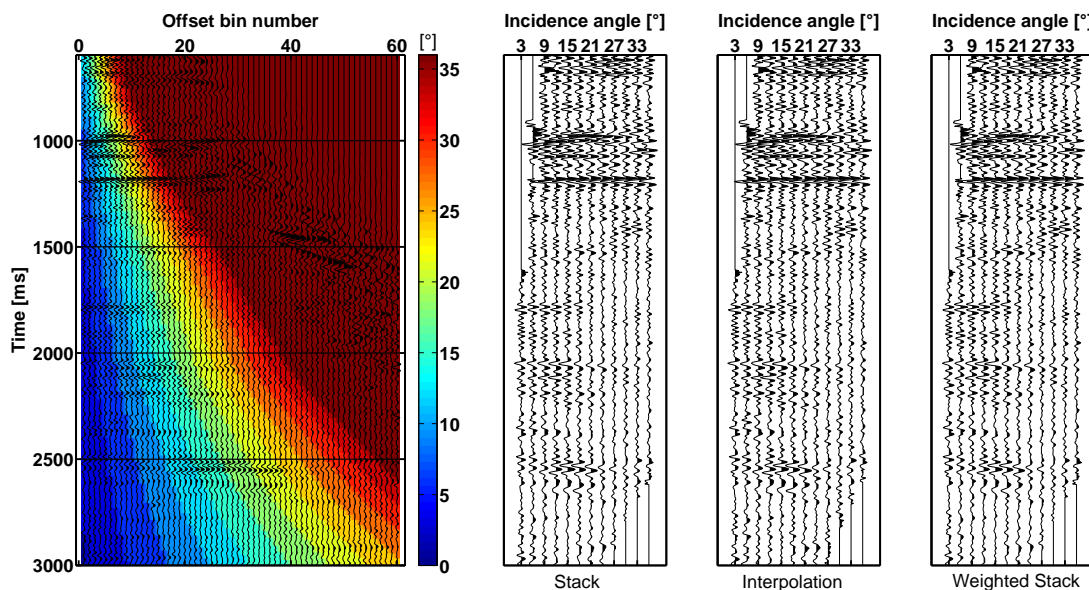


FIGURE 4.4: Comparison among the three methods for offset to angle binning described in the current section on Inline 1300 and Crossline 400 of the Penobscot dataset (see Chapter 7).

Angle 3° is noisy for all the CIGs of the survey and for all the three methods adopted for mapping offsets into angles. The trace-envelope representation of Figure 4.5 shows a decay of amplitude of the event highlighted by the black box, at about 1200 ms TWT, when the incidence angle is higher than 30° . This is likely to be due to energy conversion with such geometry: offset bins higher than 30 should not be taken into account for the comparison of Figure 4.5. The comparison of Figure 4.5 confirms that the AVA behaviour of the event shows a limited dependency on the angle mapping method in the case of the selected CIG.

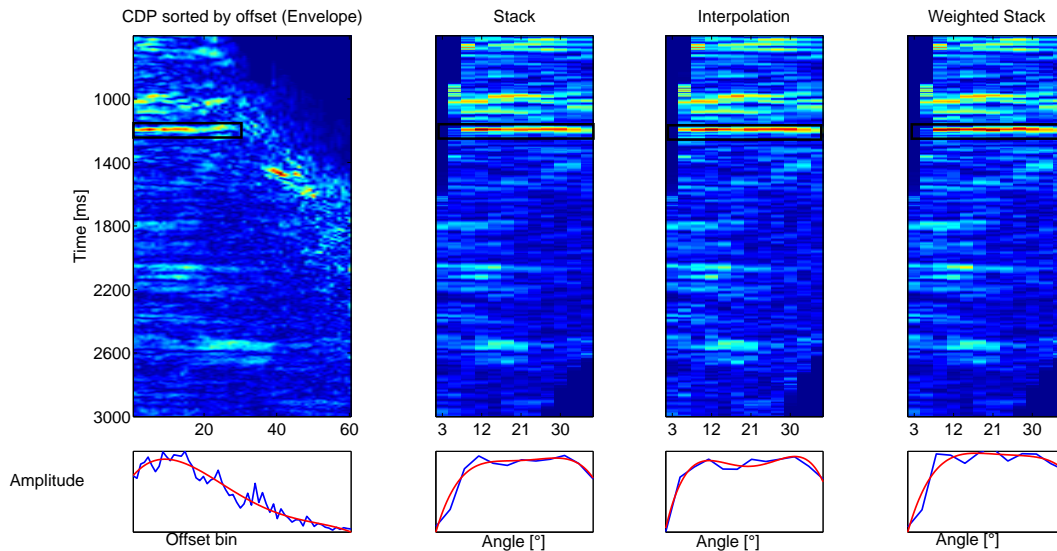


FIGURE 4.5: Comparison between the envelopes of the CIG sorted by offset (left) and the CIG sorted by angle when the angle mapping is performed by stacking, by interpolating the two closest traces to the central angle, and by weighted stacking of the offsets that fall in each angle bin depending on the distance from the central angle. Below the gathers the mean amplitude of a 40 ms window across the event highlighted by the black box is shown (blue) together with its smoothed version (red).

None of the three offset to angle mapping methods shows a better performance with respect to the other two. However, the weighted stack is selected as the approach of choice for the results on real data. This choice mitigates the features of the other two methods. The number of angles adopted for the inversion only marginally affects the results of the inversion, being a larger number of angles more prone to display residual noise (stack becomes less effective) than a smaller number, but at the same time being the inversion fed with more data. However, there is a limit on the number of angles bins that is related to the number of rays that illuminate the shallowest reflector of interest. In order to avoid discretization artefacts (duplication of samples into different angle bins), the number of angles must be less than the number of offsets that are available for the first reflector of interest. A final remark from this analysis is that when mapping offsets into angles via the stack and the weighted stack procedure, white noise in CIG/offset domain is transformed into non stationary noise in CIG/angle domain. This is because the stacking fold increases at depth, leading to a statistical reduction of the random noise at longer travel-times that is not happening at shorter travel-times.

4.3 Autoregressive Recovery of Elastic Parameters

Two work-flows for pre-stack inversion are here described. They both assume that seismograms represent a bandlimited version of reflectivity at a definite incidence angle, thus data must be properly processed and organised by incidence angle before inversion. Both work-flows follow the work of Walker and Ulrych (1983) as far as it concerns the low frequency completion. This is performed by constructing the Toeplitz autocorrelation matrix \mathbf{G} of the estimated AR coefficients. Walker and Ulrych obtained the low frequency components of the reflectivity as the solution for \mathbf{R} of the system in equation 2.40. I propose a modified approach for obtaining \mathbf{R} which shares similarities to Ulrych and Walker (1984) short note. The approach assumes to minimise a distance from the prediction error given soft real-value constraints on the elastic property of interest at depth ($\mathbf{EI}, \alpha, \beta, \rho$). In other words

$$\min_{\mathbf{R}} \|\mathbf{GR} - \mathbf{B}\|_2^2 \quad s.t. \quad \mathbf{EI} - \Delta\mathbf{EI} \leq \mathbf{HR} \leq \mathbf{EI} + \Delta\mathbf{EI}. \quad (4.8)$$

For the pre-stack case m angles may be available and the reconstruction process can be performed independently on an angle by angle basis. Equation (4.9) gathers in a single system all the uncoupled low frequency reconstructions at different angles. In this case \mathbf{G}' and \mathbf{B}' indicate $\mathbf{G}^H\mathbf{G}$ and $\mathbf{G}^H\mathbf{B}$, respectively.

$$\begin{bmatrix} \mathbf{G}'_1 & \mathbf{0} & \mathbf{0} \\ \mathbf{0} & \dots & \mathbf{0} \\ \mathbf{0} & \mathbf{0} & \mathbf{G}'_m \end{bmatrix} \begin{bmatrix} \mathbf{R}_1 \\ \dots \\ \mathbf{R}_m \end{bmatrix} \approx \begin{bmatrix} \mathbf{B}'_1 \\ \dots \\ \mathbf{B}'_m \end{bmatrix} \quad s.t. \quad \begin{bmatrix} \mathbf{EI}_1 - \Delta\mathbf{EI}_1 \\ \dots \\ \mathbf{EI}_m - \Delta\mathbf{EI}_m \end{bmatrix} \leq \begin{bmatrix} \mathbf{H}_1 & \mathbf{0} & \mathbf{0} \\ \mathbf{0} & \dots & \mathbf{0} \\ \mathbf{0} & \mathbf{0} & \mathbf{H}_m \end{bmatrix} \begin{bmatrix} \mathbf{R}_1 \\ \dots \\ \mathbf{R}_m \end{bmatrix} \leq \begin{bmatrix} \mathbf{EI}_1 + \Delta\mathbf{EI}_1 \\ \dots \\ \mathbf{EI}_m + \Delta\mathbf{EI}_m \end{bmatrix}. \quad (4.9)$$

The reconstructed low frequency components of reflectivity $[\mathbf{R}_1, \dots, \mathbf{R}_m]$ are added to the the Fourier components of the reflectivity pertaining to a user defined seismic bandwidth. At this point, by the knowledge of a reference value of EI at travel-time t_0 and summation in time domain (assuming the weak contrast approximation of equation 4.1), the estimation of the absolute value of EI can be obtained for any time and any angle.

The subsequent elastic parameter (AVA) inversion can be performed in a second stage or simultaneously with the harmonic extrapolation. In both cases, the physical relationship between the time variation of elastic parameters and the time variation of the reflectivity (r) depending on the angle of incidence (θ) has been approximate by the Aki and Richards (1980) equation (4.10) with a constant $K = \beta^2/\alpha^2$ value

$$r(\theta, t) = 0.5[1 + \tan^2\theta]\Delta \log(\alpha(t)) - [4K\sin^2\theta]\Delta \log(\beta(t)) + 0.5[1 - 4K\sin^2\theta]\Delta \log(\rho(t)). \quad (4.10)$$

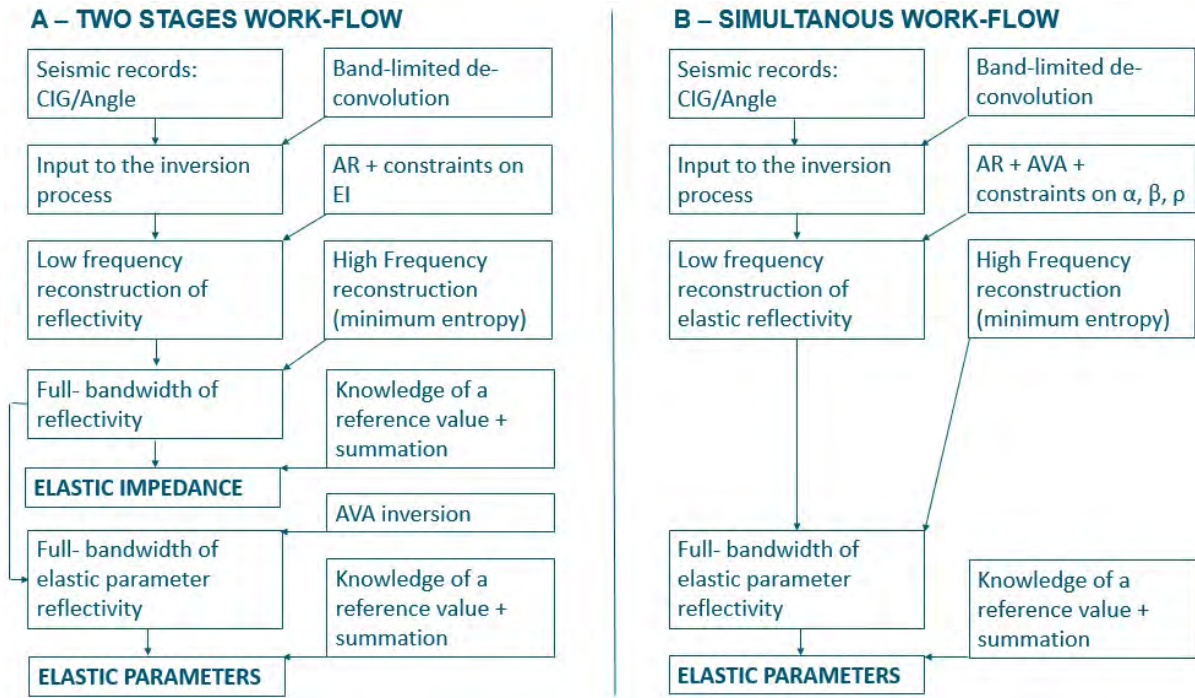


FIGURE 4.6: Schematic description of the two work-flows for the full-bandwidth estimation of elastic parameters from seismic pre-stack data. The two stages workflow (A) allows an estimate of the elastic impedance as by-product. The constraints that can be set at depth are different in the two cases.

The two-stage inversion has a lower computational cost than the simultaneous inversion and yet it allows to obtain a full bandwidth estimate of a quantity $[\Delta \log(\alpha(t)), \Delta \log(\beta(t)), \Delta \log(\rho(t))]$ related to elastic parameters. However, geological or well log constraints can only be set in terms of EI values at a given depth in the first case (within the system of equations 4.9). The inversion for the reflectivity of elastic parameters can be achieved provided that there are at least 3 angles available and a relationship between elastic parameters is accounted for as a regularization term (Downton, 2005). Gardner relationship $[\rho = C\alpha^b]$ (Gardner, Gardner, and Gregory, 1974) with C and b being constants, and a stationary version of the Mudrock Line $[\beta = h\alpha + k]$ (Castagna, Batzle, and Eastwood, 1985) with h and k being constants, may be used for this purpose by computing the following forms of parameters \mathbf{P} and \mathbf{Q}

$$\mathbf{P} = [g\Delta \log(\alpha(t)) - \Delta \log(\rho(t))] \approx 0 \quad \mathbf{Q} = [\Delta \log(\alpha(t)) - \Delta \log(\beta(t))] \approx 0 \quad (4.11)$$

If the aim of the inversion process is purely an estimate of elastic parameters (α, β, ρ) , the AVA inversion can be performed simultaneously to the low frequency completion. The problem in equation (4.9) can be modified by transforming the model parameter vector \mathbf{R} into the model parameter $\mathbf{e}_L = [\Delta \log(\alpha_L), \Delta \log(\beta_L), \Delta \log(\rho_L)]$ containing the low frequency components of elastic parameters in a long vector notation. This leads to equation (4.12) in which $\mathcal{F}, \mathcal{F}^{-1}$

symbols indicate the forward and inverse discrete Fourier transform operations:

$$\begin{bmatrix} \mathbf{G}_1 & 0 & 0 \\ 0 & \dots & 0 \\ 0 & 0 & \mathbf{G}_m \end{bmatrix} \begin{bmatrix} \mathcal{F} & 0 & 0 \\ 0 & \dots & 0 \\ 0 & 0 & \mathcal{F} \end{bmatrix} [\mathbf{A}] \begin{bmatrix} \mathcal{F}^{-1} & 0 & 0 \\ 0 & \mathcal{F}^{-1} & 0 \\ 0 & 0 & \mathcal{F}^{-1} \end{bmatrix} \begin{bmatrix} \Delta \log(\boldsymbol{\alpha}_L) \\ \Delta \log(\boldsymbol{\beta}_L) \\ \Delta \log(\boldsymbol{\rho}_L) \end{bmatrix} = \begin{bmatrix} \mathbf{B}_1 \\ \dots \\ \mathbf{B}_m \end{bmatrix}. \quad (4.12)$$

The system can be rewritten in a compact form as follows

$$[\mathbf{G}][\mathcal{F}_{full}][\mathbf{A}][\mathcal{F}_{full}^{-1}][\mathbf{e}_L] = [\mathbf{B}], \quad (4.13)$$

where \mathbf{A} is the AVA operator defined by equation (4.10). Given that \mathbf{A} is expressed in time domain, the forward and backward Fourier transforms are the computational price to pay in order to apply the AR completion in frequency domain. More importantly, the operator \mathbf{A} is known to be ill-conditioned even when a broad range of angles is available (De Nicola, Drufulca, and Rocca, 1993) thus the system (4.12) does not lead to a stable solution when inverted for \mathbf{e}_L . I rely on matrices \mathbf{P} and \mathbf{Q} from equation (4.11) to stabilise the solution. Those equations are expressed in time domain, and for this reason they couple the solution at low frequency ($\mathbf{e}_L = [\Delta \log(\boldsymbol{\alpha}_L), \Delta \log(\boldsymbol{\beta}_L), \Delta \log(\boldsymbol{\rho}_L)]$) to the one within the signal bandwidth ($\mathbf{e}_M = [\Delta \log(\boldsymbol{\alpha}_M), \Delta \log(\boldsymbol{\beta}_M), \Delta \log(\boldsymbol{\rho}_M)]$). It is worth noting that higher frequency components add no significant contribution to the reconstruction of elastic parameters after the integration of the reflectivity (Oldenburg, Scheuer, and Levy, 1983) and can either be neglected or reconstructed as proposed by Walker and Ulrych (1983). The system in equation 4.12 is first augmented as it follows to include the signal bandwidth components

$$\begin{bmatrix} \mathbf{G} & \mathbf{0} \\ \mathbf{0} & \mathbf{1} \end{bmatrix} \begin{bmatrix} \mathcal{F}_{full} & \mathbf{0} \\ \mathbf{0} & \mathbf{1} \end{bmatrix} \begin{bmatrix} \mathbf{A} & \mathbf{0} \\ \mathbf{0} & \mathbf{A} \end{bmatrix} \begin{bmatrix} \mathcal{F}_{Lfull}^{-1} & \mathbf{0} \\ \mathbf{0} & \mathcal{F}_{Mfull}^{-1} \end{bmatrix} \begin{bmatrix} \mathbf{e}_L \\ \mathbf{e}_M \end{bmatrix} = \begin{bmatrix} \mathbf{B} \\ \mathbf{s} \end{bmatrix} \quad (4.14)$$

with \mathbf{s} being the long vector notation of the seismic traces within the seismic bandwidth of the CIG to be inverted. After augmentation, the regularisation term coming from the above mentioned Rock Physics relationships can be introduced in a resulting cost function

$$\min_{\mathbf{E}} \|\mathbf{CE} - \mathbf{D}\|_2^2 + \lambda^2 \|\mathbf{P}\mathcal{F}_{LM}^{-1}\mathbf{e}\|_2^2 + \mu^2 \|\mathbf{Q}\mathcal{F}_{LM}^{-1}\mathbf{e}\|_2^2 \quad s.t. \quad \mathbf{F} - \Delta\mathbf{F} \leq \mathbf{HE} \leq \mathbf{F} + \Delta\mathbf{F} \quad (4.15)$$

where $\mathbf{CE} - \mathbf{D}$ is the compact representation of the problem expressed in equation (4.14). \mathbf{e} corresponds to $[\mathbf{e}_L, \mathbf{e}_M]$ and \mathcal{F}_{LM}^{-1} is the discrete inverse Fourier transform operator that maps \mathbf{E} into its time domain representation. In addition, λ^2 and μ^2 are hyperparameters that can be tuned to obtain either a solution closer to the Rock Physics relationships or more influenced by the data (but also more prone to instability). It is advisable to keep those parameters as low as the solution in terms of s-wave velocity and density shows both a stable behaviour and features compatible with the solution in terms of p-wave velocity. Constraints $(\mathbf{F} - \Delta\mathbf{F} \leq \mathbf{HE} \leq \mathbf{F} + \Delta\mathbf{F})$ can be imposed on the solution in terms of elastic parameter values at a given depth $(\boldsymbol{\alpha}, \boldsymbol{\beta}, \boldsymbol{\rho})$.

In an extended form the constraints of equation (4.15) become

$$\begin{bmatrix} \mathbf{H}_{\alpha L} & 0 & 0 & \mathbf{H}_{\alpha M} & 0 & 0 \\ 0 & \mathbf{H}_{\beta L} & 0 & 0 & \mathbf{H}_{\beta M} & 0 \\ 0 & 0 & \mathbf{H}_{\rho L} & 0 & 0 & \mathbf{H}_{\rho M} \\ -\mathbf{H}_{\alpha L} & 0 & 0 & -\mathbf{H}_{\alpha M} & 0 & 0 \\ 0 & -\mathbf{H}_{\beta L} & 0 & 0 & -\mathbf{H}_{\beta M} & 0 \\ 0 & 0 & -\mathbf{H}_{\rho L} & 0 & 0 & -\mathbf{H}_{\rho M} \end{bmatrix} \begin{bmatrix} \Delta \log(\alpha_L) \\ \Delta \log(\beta_L) \\ \Delta \log(\rho_L) \\ \Delta \log(\alpha_M) \\ \Delta \log(\beta_M) \\ \Delta \log(\rho_M) \end{bmatrix} \leq \begin{bmatrix} \alpha + \Delta\alpha \\ \beta + \Delta\beta \\ \rho + \Delta\rho \\ -\alpha + \Delta\alpha \\ -\beta + \Delta\beta \\ -\rho + \Delta\rho \end{bmatrix}. \quad (4.16)$$

4.4 Mapping between Constraints on Vp Vs and Density into Constraints on EI

It is straightforward to impose constraints at depth, expressed in terms of p-wave, s-wave velocity and bulk density from well log data, and from other a priori knowledge, in the one-stage approach. In the two-stages approach described by equation 4.8, the constraints on EI may require an additional comment. In case well logs measure the interval properties of three elastic parameters it is possible to associate to the seismic traces around the well location an EI constraint from equation 4.17:

$$EI(\theta, t) = \alpha(t)^{1+\tan^2(\theta)} \beta(t)^{-8K\sin^2(\theta)} \rho(t)^{1-4K\sin^2(\theta)}. \quad (4.17)$$

This task becomes more problematic when only one or two of the elastic parameters are investigated from logs or brought in the problem by geologic a priori information. The problem is relevant because the absolute value of EI is strongly dependent on the incidence angle. A possible way to treat the problem is to normalize the angle dependency of the EI by dividing for the values of the elastic parameters at the reference travel-time (t_0) (Whitcombe, 2002):

$$EI_n(\theta, t) = AI(t) \frac{\alpha(t)^{\tan^2\theta}}{\alpha(t_0)} \frac{\beta(t)^{-8K\sin^2(\theta)}}{\beta(t_0)} \frac{\rho(t)^{-4K\sin^2(\theta)}}{\rho(t_0)}. \quad (4.18)$$

It is easier to set constraints on EI_n rather than on EI at different angles. Only the absolute value of AI at depth and an assumption on the relative variation of the elastic parameters is required to set constraints on EI_n . The normalisation is particularly good when the percentage change of the interval properties is reduced in the inversion window. As long as α, β, ρ remain close to their reference value ($\alpha(t_0), \beta(t_0), \rho(t_0)$), $EI_n(t, \theta) \approx AI(t)$. The knowledge of the AI at selected depths could become a rough estimate for the EI in those cases.

A different approach to EI constraint estimation is that of approximating $\tan^2\theta$ with $\sin^2\theta$ at small incidence angles. This choice allows to rewrite equation 4.17 as:

$$EI(\theta, t) = AI(t) \alpha(t)^{\sin^2(\theta)} \beta(t)^{-8K\sin^2(\theta)} \rho(t)^{-4K\sin^2(\theta)}. \quad (4.19)$$

Taking logarithms and re-arranging equation 4.19

$$\log(EI(\theta, t)) = \log(AI(t)) + \sin^2(\theta) [\log(\alpha(t)) - 8K \log(\beta(t)) - 4K \log(\rho(t))]. \quad (4.20)$$

After exponentiation equation 4.20 becomes

$$EI(\theta, t) = AI(t)e^{\sin^2(\theta)[\log(\alpha(t)) - 8K\log(\beta(t)) - 4K\log(\rho(t))]} = AI(t) + e^{\sin^2(\theta)c}. \quad (4.21)$$

If the term c from equation 4.21 can be somehow estimated from a priori information (AVA background trend estimates available for the target events in the region), it is then possible to extend the constraint on AI at depth to constraints on EI at incidence angles different from 0.

4.5 Synthetic Example

The application of the two stages and single stage algorithms described in the section 4.3, is presented on the same synthetic CIG. The inversion of a window of the Marmousi II model (Martin, Marfurt, and Larsen, 2005) is also presented to provide a further insight into the potentialities of the inversion.

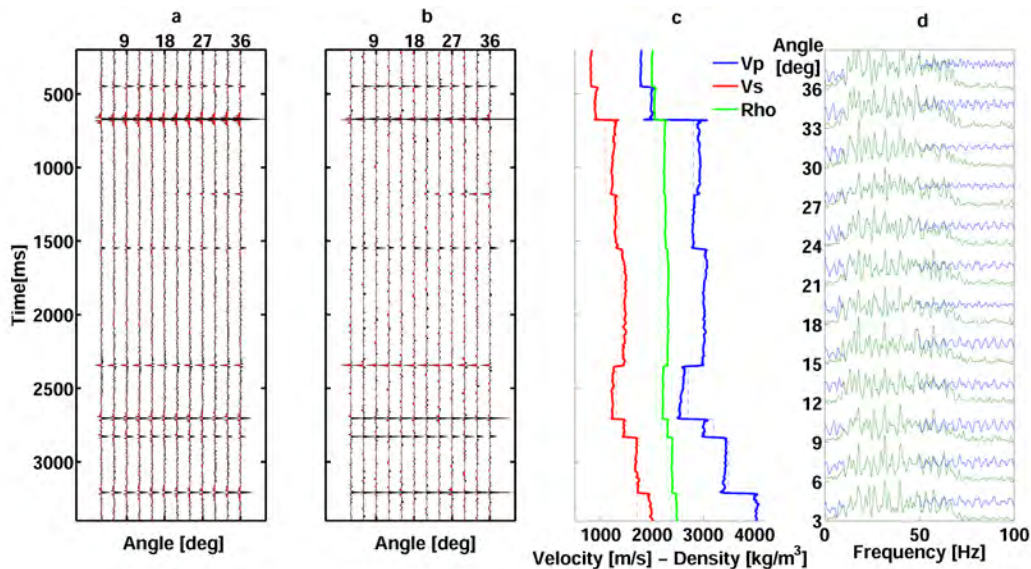


FIGURE 4.7: Two stages inversion. The input CIG in panel (a) is band-limited (Butterworth zero-phase 8-70 Hz cutoff) with additive white noise (S/N 26 dB in terms of ratio of maximum amplitudes). Low and high frequencies are reconstructed in panel (b). Panel (c) shows the model elastic parameters (dotted) and the reconstructed ones. Panel (d) displays the amplitude spectrum of the reconstructed reflectivity (blue) in comparison to the spectrum of the input trace (green) at different angles.

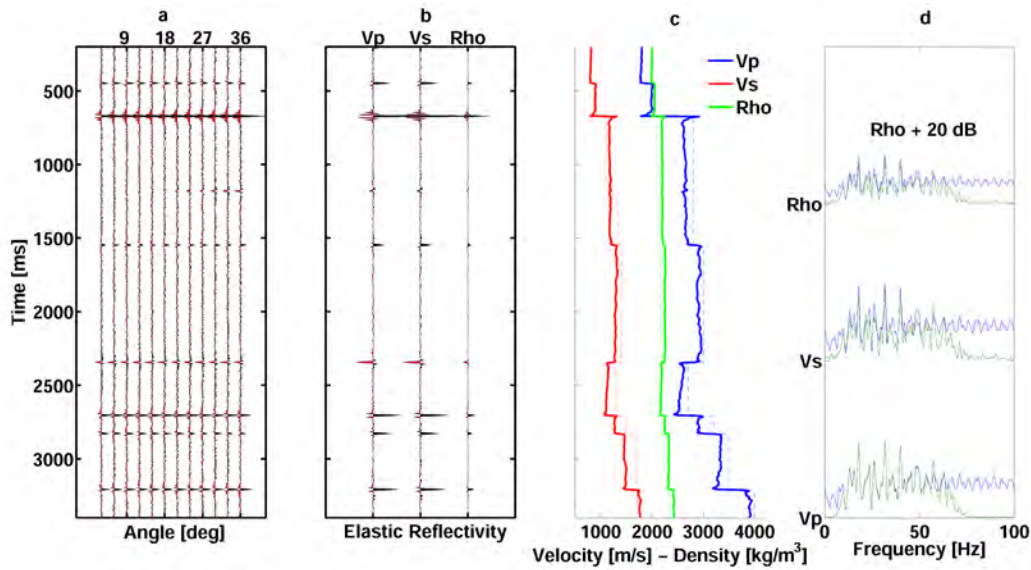


FIGURE 4.8: *Simultaneous inversion.* The input in panel (a) is the same as in Figure 4.7 but the direct inversion produces the reflectivity of elastic parameters (b). The time summation of this result produces panel (c). Differences with panel (c) are due to the different role the regularisation terms play in the two work-flows. Panel (d) describes the amplitude spectrum of reconstructed elastic parameters (blue) in comparison to the reconstructed spectrum in absence of low and high frequency completion (green).

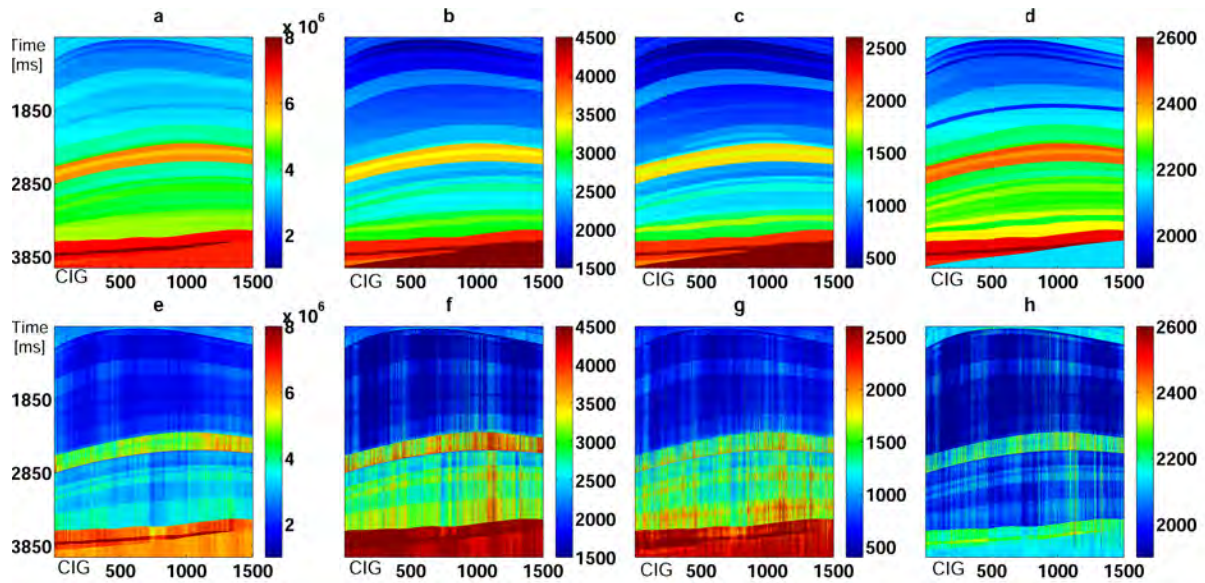


FIGURE 4.9: *Inversion of a window of the Marmousi II model.* Forward modelling by Aki-Richards equation and Butterworth bandpass filter (8-70 Hz) plus white noise (S/N 26 dB). Panels (a),(b),(c),(d) show the input model for $EI(15^\circ)[\text{rayl}]$, $\alpha[\text{m/s}]$, $\beta[\text{m/s}]$, $\rho[\text{kg/m}^3]$ respectively. Panel (e) shows the reconstructed $EI(15^\circ)$ via the two stages work-flow.(f),(g),(h) show the reconstruction of α , β , ρ obtained by the one stage work-flow. One constraint on EI , α , β , ρ at the end of the time window.

4.6 Discussion

The AVA analysis on CIGs sorted by incidence angle is based on an offset to angle regularisation choice. The regularization method becomes significant when S/N is particularly poor.

Nonetheless, the type of offset-to-angle mapping should always been considered when evaluating quantitative outcomes from the AVA analysis. The topic of elastic inversion has also been introduced with reference to synthetic examples in this Chapter. Application of the above discussed methods on real data is shown in Chapter 6 and 7. Synthetic examples suggest that both the one- and the two-stages pre-stack inversion algorithms have the potential to successfully identify the main variations of elastic parameters with depth on real data. Controlled-amplitude processing and removal of wavelet effects is required for a successful reconstruction on real data. Due to the range of angles available, anomalies only on the s-wave velocity and density are not always singled out properly. The inherent trace-to-trace instability might be attenuated by considering lateral continuity across CIGs.

Chapter 5

Stabilising Effects of Rock Physics Relationships for the Linear AVA Inversion

5.1 Introduction

This Chapter provides a picture of the feasibility of the linear AVA inversion problem provided that Rock Physics relationships are introduced in the forward modelling kernel. Although the AVA formulation is a well-established methodology for inferring elastic properties from multi-channel seismic data, no assessment on the robustness of the method depending on the degree of correlation among elastic parameters from Rock Physics relationships is provided in the relevant literature. This analysis is of paramount importance for a successful application of the pre-stack inversion methods described in Chapter 4. In fact, the resolving power of the seismic amplitudes for determining the elastic parameter and density reflectivities is based on the data quality and on the a priori knowledge of the correlations among the different parameters.

Different formulations exist for the AVA relationship depending on the quality of the data available. In this Chapter I analyse the linear three-term expression proposed by Aki and Richards (1980), which is considered to be a small angle approximation (Connolly (1999) recommends limiting its adoption up to 30° - 35°) of the Zoeppritz equations for the P-P reflected wave-field. De Nicolao, Drufuca, and Rocca (1993) present a fundamental analysis on the potentialities of the linear AVA inversion for elastic parameter estimates. They highlight the ill-conditioned nature of the problem, which makes the resulting three-term inversion completely unreliable unless further assumptions are considered. Several authors (e.g. Ursenbach and Stewart (2008)) analysed the stabilizing effects of reducing the number of elastic parameters to be inverted. A common choice is to invert pre-stack CIGs data for only two elastic parameters. The two-term inversion is obtained either by assuming that a certain Rock Physics relationship holds true (e.g. Smith and Gildow (1987), and more recently Russell and Hedlin (2019)) or by neglecting the contribution brought about by one of the elastic parameters to the reflectivity in case the data are available in a suitable angle range (i.e. Fatti et al. (1994)). A more general strategy aiming at stabilizing the three-term solution is proposed by Downton (2005). The strategy consists on infusing a priori rock physics information in the inversion by a convenient weighting factor. Tikhonov regularization (Tikhonov and Arsenin, 1977) and its Bayesian counterpart are the approaches studied here to this end. I adopt the weak contrast approximation to extend the

linear mapping from reflectivity at different incidence angles to the variation of the logarithms of elastic parameters as expressed in equation 4.10. The parameter K represents the background $\frac{\beta^2}{\alpha^2}$ and it is a constant for the linear AVA problem (i.e. Gholami, Aghamiry, and Abbasi (2018) discuss the implications of keeping K constant). A well conditioned mapping exists between different sets of elastic parameters (Downton, 2005), therefore retrieving p-wave and s-wave impedance instead of p-wave and s-wave velocity produces only a minor difference in the sensitivity analysis I present. Assuming the errors on the data to be independent and randomly distributed, I estimate the model parameters by solving

$$\min_{\mathbf{m}} \|\mathbf{A}\mathbf{m} - \mathbf{d}\|_2^2. \quad (5.1)$$

In equation 5.1 \mathbf{A} represents the AVA relationship expressed by equation 4.10 at different incidence angles, $\mathbf{m} = [\Delta \log(\alpha); \Delta \log(\beta); \Delta \log(\rho)]$, and \mathbf{d} represents a CIG sorted by incidence angle in a long vector notation. De Nicolao, Drufuca, and Rocca (1993) explicitly formulated the least squares matrix of the inverse problem ($\mathbf{A}^t \mathbf{A}$) as a function of the maximum incidence angle (θ_m) and of the parameter $\gamma = \frac{\alpha}{\beta} = \frac{1}{\sqrt{K}}$. They showed that the problem posed in these terms is poorly conditioned such that it is impossible to independently resolve all the three components of the model given the typical S/N that characterizes seismic surveys. The explicit formulation of the matrix of the inverse problem is:

$$\mathbf{A}^t \mathbf{A} = \mathbf{T} = \begin{pmatrix} \frac{\sin\theta_m + 2\sin\theta_m \cos^2\theta_m}{12\theta_m \cos^3\theta_m} & \frac{2}{\gamma^2} - \frac{2\sin\theta_m}{\theta_m \gamma^2 \cos\theta_m} & \frac{1}{\gamma^2} + \frac{-4\sin\theta_m + \gamma^2 \sin\theta_m}{4\theta_m \gamma^2 \cos\theta_m} \\ \frac{2}{\gamma^2} - \frac{2\sin\theta_m}{\theta_m \gamma^2 \cos\theta_m} & \frac{6}{\gamma^4} - \frac{6\cos\theta_m \sin\theta_m - 4\cos\theta_m \sin^3\theta_m}{\theta_m \gamma^4} & \frac{3-\gamma^2}{\gamma^4} + \frac{(-3+\gamma^2-2\sin^2\theta_m)\cos\theta_m \sin\theta_m}{\theta_m \gamma^4} \\ \frac{1}{\gamma^2} + \frac{-4\sin\theta_m + \gamma^2 \sin\theta_m}{4\theta_m \gamma^2 \cos\theta_m} & \frac{3-\gamma^2}{\gamma^4} + \frac{(-3+\gamma^2-2\sin^2\theta_m)\cos\theta_m \sin\theta_m}{\theta_m \gamma^4} & \frac{6-4\gamma^2+\gamma^4}{4\gamma^4} + \frac{(-6+4\gamma^2-4\sin^2\theta_m)\sin\theta_m \cos\theta_m}{4\theta_m \gamma^4} \end{pmatrix}. \quad (5.2)$$

Aleardi (2015) analysed the condition number of matrix 5.2 with respect to the variation of the parameter γ and pointed out that the smaller $\frac{\alpha}{\beta}$, the more resolved are the different model components. An analysis that takes into account not only the effects of the maximum incidence angle and the background $\frac{\alpha}{\beta}$ but also the correlations derived from Rock Physics is described in the following sections both as regularization and as a Bayesian inference problem. The aim of this Chapter is to provide a tool to assess the amount of model-based information (a priori rock-physics correlations) that is needed to obtain a stable solution of the AVA problem.

5.2 Theory

The ill-conditioned nature of the problem expressed in equation 5.1 can be tackled by modifying the cost function with a regularisation term derived from a priori knowledge. The resulting problem can be expressed as

$$\min_{\mathbf{m}} \|\mathbf{A}\mathbf{m} - \mathbf{d}\|_2^2 + \psi^2 \|\mathbf{S}\mathbf{m}\|_2^2, \quad (5.3)$$

where \mathbf{S} describes the correlation between the elastic parameter reflectivities and ψ^2 controls the amount of a priori information infused in the solution. Buland and Omre (2003) introduced rock-physics empirical relationships, calibrated at well locations, to correlate the elastic parameters. Those relationships allowed them to obtain a three-term linear inversion in a probabilistic framework. I adopt two assumptions from the work of Buland and Omre (2003): I consider the

data errors to be random and the a priori distribution of elastic parameter reflectivity to be Gaussian. Although some authors adopted longer-tailed a priori models (Downton and Lines (2005), Alemie and Sacchi (2011)), Downton (2005) and Buland and Omre (2003) motivate the choice of a Gaussian distribution for the elastic parameter reflectivity by means of well log analysis on short time windows. The objective here is to test the importance of the amount of a priori information on the result rather than recommending a specific rock-physics model, therefore I do not deepen into the implications of this model choice. The prior Gaussian model is fully described by its expected value ($\bar{\mathbf{m}}$) and its covariance matrix (Σ). In the framework of Bayesian inference, the posterior distribution of elastic parameter reflectivity is described by

$$p(\mathbf{m}|\mathbf{d}) \propto \frac{1}{(2\pi)^{3/2}} \frac{1}{\sqrt{\det(\Sigma)}} e^{-0.5(\mathbf{m}-\bar{\mathbf{m}})^t \Sigma^{-1} (\mathbf{m}-\bar{\mathbf{m}})} \frac{1}{(2\pi)^{N/2} \sqrt{|C_d|}} e^{-0.5(\mathbf{A}\mathbf{m}-\mathbf{d})^t C_d^{-1} (\mathbf{A}\mathbf{m}-\mathbf{d})}. \quad (5.4)$$

The maximisation of equation 5.4, or equivalently of its logarithm, with respect to \mathbf{m} provides the expected model vector. In equation 5.4, C_d is the data covariance matrix which, under the hypothesis of random independent errors on the data, is assumed to be a scaled version of the identity matrix. The parameter N represents the number of incidence angles available for inversion and it is a known value once the processed seismic gathers are organised by incidence angle. The number of observations must be equal or greater than the number of elastic parameter components to be independently resolved ($N \geq 3$), but, given the a priori information, an estimate of the three parameters can be obtained even with fewer observations (Figure 5.1). The maximisation of equation 5.4 with respect to \mathbf{m} , leads to the solution of equation 2.67. The maximization of the posterior probability is equivalent to find a solution of a problem properly cast in the form of equation 5.3 (Ulrych, Sacchi, and Woodbury, 2001). In case the variance of the data errors is equal to 1, C_d becomes the identity matrix and the matrix of the inverse problem is represented by the expression (Downton, 2005):

$$\mathbf{A}^t \mathbf{A} + \Sigma^{-1}. \quad (5.5)$$

Expression 5.5 is independent from the actual data values. The covariance matrix (Σ) is symmetric, therefore it is fully defined by only six of its components. The larger the variances of the elastic parameters, the less informative is the a priori information. On the contrary, small ratios between diagonal and non diagonal elements of the covariance matrix indicate stronger mutual relationships between different elastic parameter reflectivities.

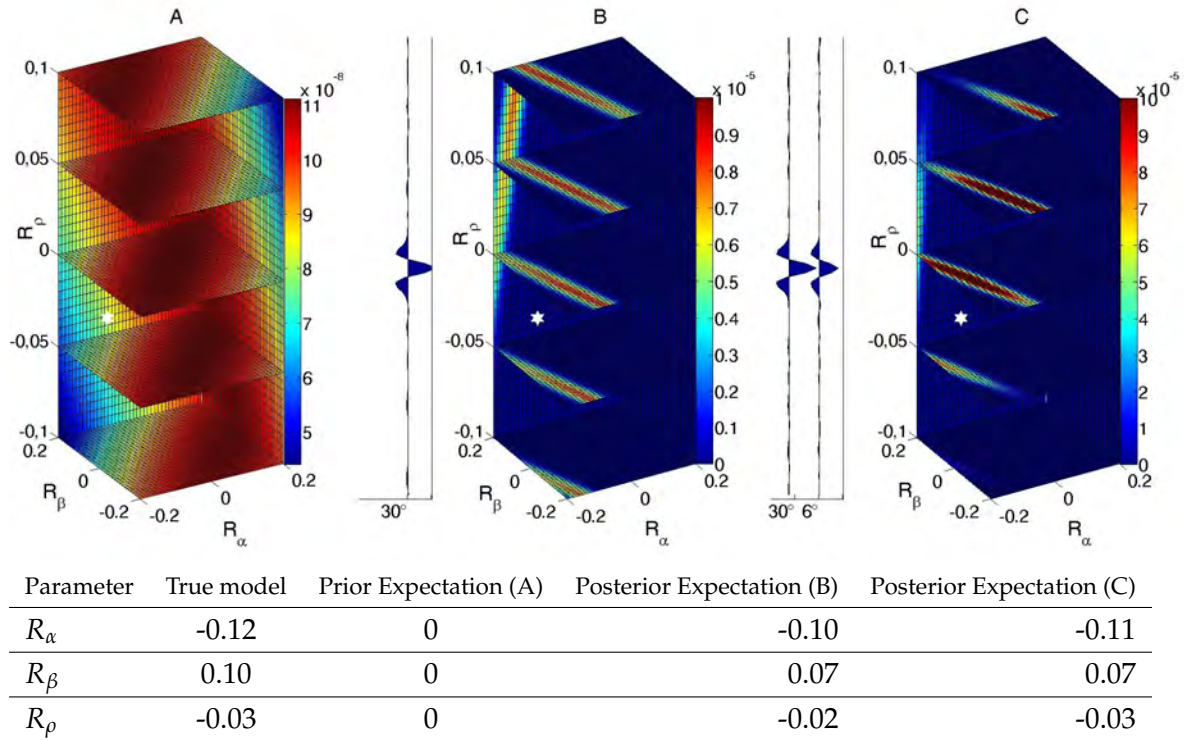


FIGURE 5.1: Sampling of the probability density function of the three-term reflectivity model ($R_\alpha, R_\beta, R_\rho$) when only one (Panel B) and two channels (Panel C) are available for the AVA inversion ($S/N = 26$ dB). Given the zero-mean a priori Gaussian model (Panel A), the posterior distribution is calculated and compared with the model reflectivity that generated the two synthetic examples (indicated by a white star). When only one angle is available, the posterior distribution shows an elongated distribution, indicating a poorer resolution with respect to the case when two angles are available (Panel C). The background $\gamma = 2$.

5.3 Method

I here analyse the degree of resolution of each component of the elastic parameter reflectivity depending on the confidence on the a priori information, on the range of angles available and on the background Poisson ratio. I do so by evaluating the eigenvalues and the corresponding eigenvectors of the matrix 5.5. I consider the differential Gardner relationship (Gardner, Gardner, and Gregory, 1974) and an approximation of the Mudrock line (Castagna, Batzle, and Eastwood, 1985) to correlate the model of elastic parameters as per equations 5.6 and 5.7:

$$\Delta \log(\alpha) - k_1 \Delta \log(\rho) = 0, \quad (5.6)$$

$$\Delta \log(\alpha) - k_2 \Delta \log(\beta) = 0. \quad (5.7)$$

The coefficients k_1 and k_2 must be tuned depending on the subsurface materials. k_1 is often a value close to 4 (Gardner, Gardner, and Gregory, 1974), while the Mudrock line equation does not provide a linear relationship between the variation of logarithms of p- and s-wave velocity (Downton, 2005). The stationary approximation of equation 5.7 with $k_2 = 1$ describes the Mudrock line best when when the s-wave contrast on an interface is reduced or when the s-wave velocity is high. If those conditions are not met, equation 5.7 is still valid on a target

TABLE 5.1: Sampling of the parameters that intervene in matrix 5.10. The sensitivity analysis has been carried out for all the combinations of the parameters in Table 1 for a total of 1296 eigenproblems.

Parameter	Minimum value	Maximum value	Increment [or sampling array]
λ^2	0	0.1	[0, 0.001, 0.004, 0.01, 0.04, 0.1]
μ^2	0	0.1	[0, 0.001, 0.004, 0.01, 0.04, 0.1]
γ^2	3	9	6
θ_m	2°	36°	2°
k_1	4	4	
k_2	1	1	

event, provided that the parameter k_2 is allowed to vary. Although both equation 5.7 and the background γ describe the ratio between the p-wave and s-wave velocity, those two terms deal with a different frequency content: γ describes the low frequency interval property, while k_2 describes the high frequency interface response. Given the two rock-physics relationships with their degree of uncertainty (λ^2 for the Gardner relationship and μ^2 for the approximate Mudrock line) I can construct the model covariance matrix Σ such as

$$\Sigma^{-1} = \begin{pmatrix} \lambda^2 \frac{1}{1+k_1^2} + \mu^2 \frac{1}{1+k_2^2} & -\mu^2 \frac{k_2}{1+k_2^2} & -\lambda^2 \frac{k_1}{1+k_1^2} \\ -\mu^2 \frac{k_2}{1+k_2^2} & \mu^2 \frac{k_2^2}{1+k_2^2} & 0 \\ -\lambda^2 \frac{k_1}{1+k_1^2} & 0 & \lambda^2 \frac{k_1^2}{1+k_1^2} \end{pmatrix}, \quad (5.8)$$

and I can also re-formulate the problem expressed in equation 5.3 as

$$\min_{\mathbf{m}} \|\mathbf{A}\mathbf{m} - \mathbf{d}\|_2^2 + \lambda^2 \|\mathbf{P}\mathbf{m}\|_2^2 + \mu^2 \|\mathbf{Q}\mathbf{m}\|_2^2. \quad (5.9)$$

In equation 5.9, \mathbf{P} is the matrix form of the differential Gardner relationship, and \mathbf{Q} is the matrix form of the relationship I assumed between the logarithms of p- and s-wave reflectivity. The regularised version of matrix 5.2 becomes a function not only of the maximum incidence angle and of the parameter γ but also of the hyperparameters (λ^2, μ^2) and of the rock-physics exponents $k_1 = 4$ and $k_2 = 1$:

$$\mathbf{A}^t \mathbf{A} + \lambda^2 \mathbf{P}^t \mathbf{P} + \mu^2 \mathbf{Q}^t \mathbf{Q} = \mathbf{A}^t \mathbf{A} + \Sigma^{-1} = \begin{pmatrix} T_{1,1}(\theta_m, \gamma) + \lambda^2 \frac{1}{1+|k_1|^2} + \mu^2 \frac{1}{1+|k_2|^2} & T_{1,2}(\theta_m, \gamma) - \mu^2 \frac{k_2}{1+|k_2|^2} & T_{1,3}(\theta_m, \gamma) - \lambda^2 \frac{k_1}{1+|k_1|^2} \\ T_{2,1}(\theta_m, \gamma) - \mu^2 \frac{k_2}{1+|k_2|^2} & T_{2,2}(\theta_m, \gamma) + \mu^2 \frac{k_2^2}{1+|k_2|^2} & T_{2,3}(\theta_m, \gamma) \\ T_{3,1}(\theta_m, \gamma) - \lambda^2 \frac{k_1}{1+|k_1|^2} & T_{3,2}(\theta_m, \gamma) & T_{3,3}(\theta_m, \gamma) + \lambda^2 \frac{k_1^2}{1+|k_1|^2} \end{pmatrix}. \quad (5.10)$$

In equation 5.10, $T_{a,b}$ with $a, b=1,2,3$, represent the elements of the aforementioned matrix \mathbf{T} (5.2). I investigate the effects of the parameters $\lambda^2, \mu^2, \gamma, \theta_m$ by numerically sampling the matrix 5.10 within the range presented in Table 5.1. This range is valid both for hydrocarbon exploration and for near surface targets. γ^2 is related to the Poisson ratio, and for non auxetic materials (such as rocks) is limited to values equal or larger than 2 (Poisson ratio ≥ 0).

5.4 Results

At least one, and in favourable cases two components of \mathbf{m} can be independently resolved from the seismic data without regularisation. For instance, Aleardi (2015) set a -40 to -50 dB threshold for the ratio between the minimum and the maximum eigenvalue of matrices 5.10 or 5.5 to resolve independent features of the single components of the model \mathbf{m} . This figure, however, depends on the S/N of the data to be inverted. I overcome this issue by fixing the data covariance matrix \mathbf{C}_d to the identity matrix such that I can directly relate the uncertainty on the posterior model, with the uncertainty described in the matrix of the inverse problem. Figures 5.2 and 5.3 show the three eigenvalues of matrix 5.10 as a function of the maximum incidence angle (θ_m), varying the hyperparameters λ^2 and μ^2 . Non-regularised results are presented for consistency with the work of De Nicolao, Drufuca, and Rocca (1993) in panels A of both Figure 5.2, and 5.3. After regularisation, the -50 dB threshold can be achieved with incidence angles up to 30 degrees (panels I for Figure 5.2 and 5.3). I also present the absolute value of the directional cosines of the eigenvectors corresponding to the three eigenvalues in Figure 5.4, 5.5 and 5.6. For clarity, the results are presented by fixing $\gamma = \sqrt{3}$. As described by De Nicolao, Drufuca, and Rocca (1993), the eigenvector corresponding to the first eigenvalue is directed toward the product of density and p-wave velocity reflectivity at small incidence angles. This fact is maintained after regularisation, meaning that the adopted a priori correlations preserve the reconstruction of the acoustic impedance reflectivity. The eigenvector corresponding to the intermediate eigenvalue points to a combination of all the three elastic parameter reflectivity in the non-regularised case (see panel A in Figure 5.5). After the regularisation with rock-physics relationships, the second eigenvector mainly influences the s-wave reflectivity when the Gardner relationship term dominates (see panels D,G,H in Figure 5.5). The directional cosine of the eigenvector corresponding to the smallest eigenvalue was neglected in the paper from De Nicolao, Drufuca, and Rocca (1993) for the little relevance it had. After regularisation, this eigenvector becomes significant as the amplitude of its associated eigenvalue is approaching the amplitude of the other eigenvalues. Opposite to what happens for the eigenvector corresponding to the intermediate eigenvalue, when the Gardner term is prevailing the third eigenvector points to acoustic impedance at near angles (this is particularly evident in panels D and G of Figure 5.6) while the third eigenvalue points to a mix of elastic properties when the effect of the Mudrock line is more relevant.

The maximum incidence angle and the two hyperparameters λ and μ have a strong influence on the stability. This influence is justified in light of the weighting effect the hyperparameters play in transforming the three-terms AVA model into something similar to a two- or even one-term inversion. The AVA problem is less stable with an increase of the background $\frac{\alpha}{\beta}$ values (Aleardi, 2015). However, by comparing Figure 5.2 to Figure 5.3, the ratio between the minimum and the maximum eigenvalue evidences the same behaviour when the Gardner regularisation term is prevailing, while the behaviour is different when the correlation between α and β in the regularisation term is stronger.

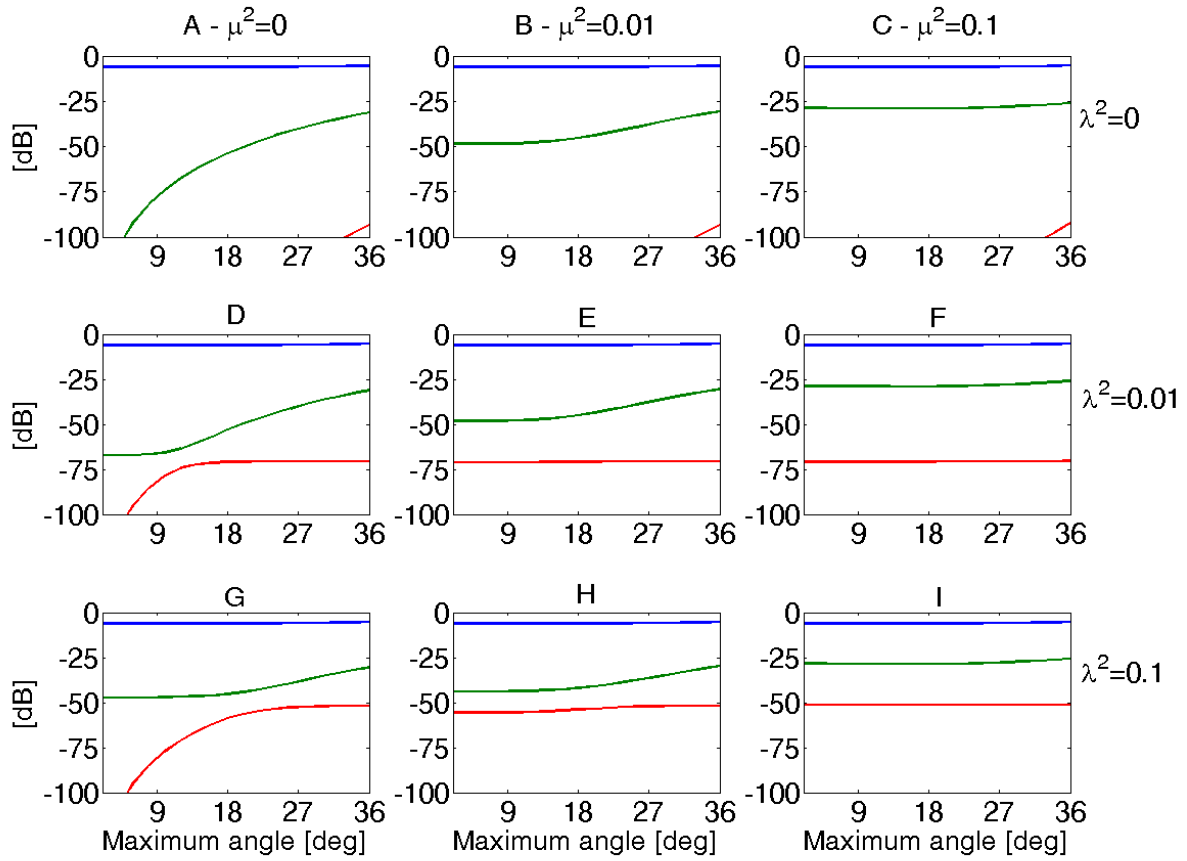


FIGURE 5.2: Variation of the eigenvalues of matrix 5.10 depending on the range of angles available. The blue line indicates the largest eigenvalue as a function of the maximum incidence angle. Red and green line indicate the intermediate and the smallest eigenvalue, respectively. Panels from left to right show the effects of increasing the hyperparameter μ^2 , which introduces the correlation related to the Mudrock line, while panels from top to bottom show the effects of increasing the hyperparameter λ^2 which introduces the correlation related to the Gardner relationship. The maximum incidence angle increases every 2° along the horizontal axis. The background $\gamma = \sqrt{3}$.

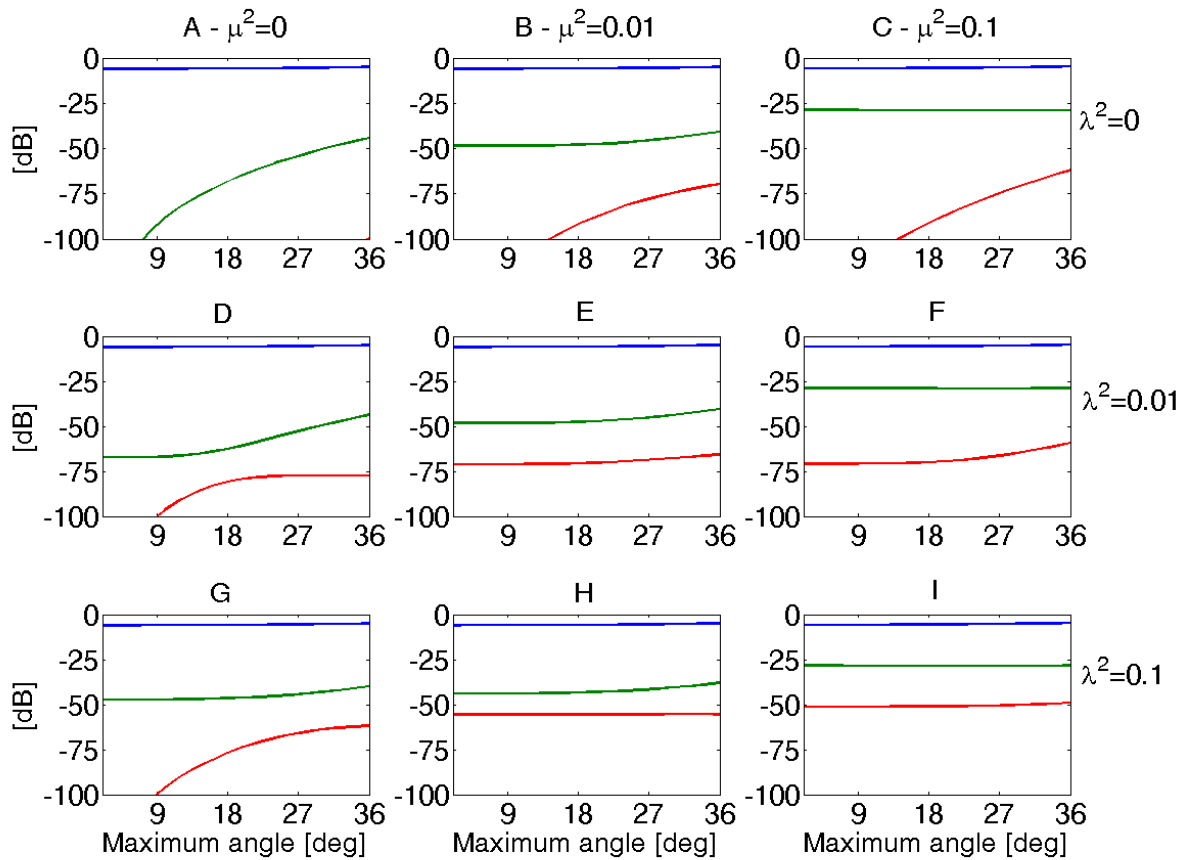


FIGURE 5.3: Variation of the eigenvalues of matrix 5.10 depending on the ranges of angles available. The analysis is presented in the same way as in Figure 5.2 with the results in blue referring to the largest eigenvalue, the red and the green results to the intermediate and the smallest eigenvalue respectively. In this case the background $\gamma = 3$.

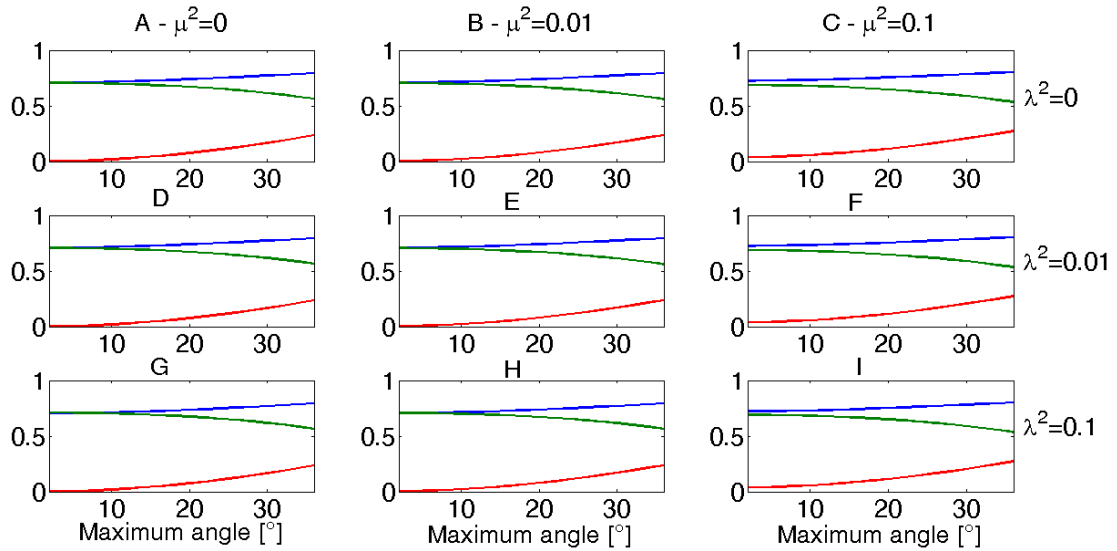


FIGURE 5.4: Absolute value of the directional cosines of the of eigenvector corresponding to the largest eigenvalue of the matrix 5.10 in the model space. The blue curve indicates the eigenvector component in the $\Delta \log(\alpha)$ direction, the red and the green curves the components in the $\Delta \log(\beta)$ and $\Delta \log(\rho)$ directions respectively. Panel A shows the non-regularised solution, which is the same solution proposed by De Nicolao, Drufuca, and Rocca (1993) for $\gamma = \sqrt{3}$. The hyperparameter choice (λ^2, μ^2) is consistent with the one presented for the eigenvalues displayed in Figure 5.2.

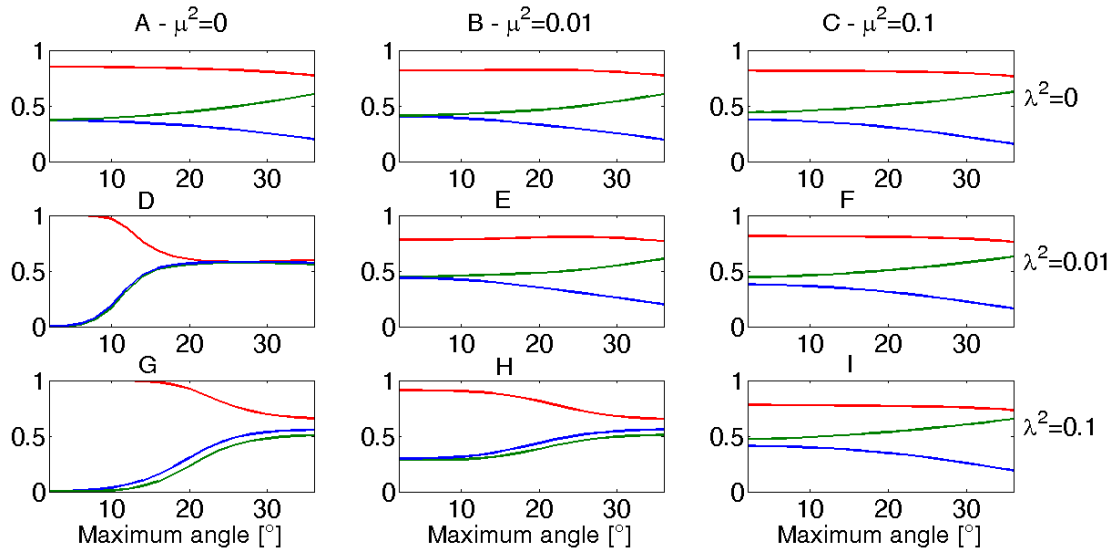


FIGURE 5.5: Absolute value of the directional cosines of the of eigenvector corresponding to the intermediate eigenvalue of the matrix 5.10. $\gamma = \sqrt{3}$. The colour palette is the same as in Figure 5.4: blue indicates the component along $\Delta \log(\alpha)$, red along $\Delta \log(\beta)$, and green along $\Delta \log(\rho)$.

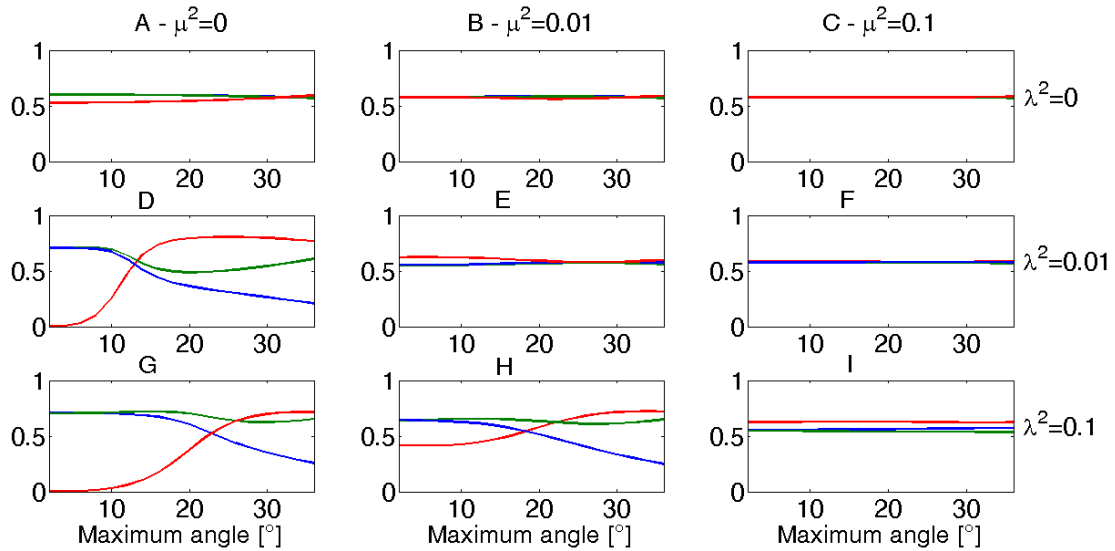


FIGURE 5.6: Absolute value of the directional cosines of the of eigenvector corresponding to the smallest eigenvalue of the matrix 5.10 in the model space. $\gamma = \sqrt{3}$. The colour palette is the same as in Figure 5.4: blue indicates the component along $\Delta \log(\alpha)$, red along $\Delta \log(\beta)$, and green along $\Delta \log(\rho)$.

5.5 Discussion and Conclusions

A picture of the feasibility of the linearised AVA inversion, depending on the confidence on the a priori information available, has been provided in this Chapter. The range of parameters that have been selected for the feasibility analysis is in according to the relevant literature for oil and gas exploration targets. The maximum incidence angle is limited to 36 degrees because the Aki-Richards approximation of equation 4.10 is considered no longer valid for larger incidence angles. I used a regular grid for sampling the model parameter space, but it is worth acknowledging that a low discrepancy sequence would have sampled more evenly the parameter space in the hypothesis of a uniform probability distribution of those parameters. The choice of a low-discrepancy sequence could become more important in case the analysis is extended to the role played by the variation of the parameters k_1 and k_2 in the stability of the problem. The drawback of the proposed regularisation consists on finding solutions that show linear dependences between the elastic parameter reflectivities. This fact does not constitute a critical issue since most of the seismic events actually follow this trend. However, it is worth acknowledging that exploration targets that show relevant anomalies on the background elastic properties represent a challenge for the proposed method. This analysis provides a useful tool for a wider adoption of the Rock Physics regularization terms in the linear AVA inversion. The concept of two- and three-terms AVA inversion can be extended to intermediate cases in which the relationships among elastic parameters are known on statistical grounds. Following the analysis I propose, those intermediate cases can be solved by including as little a priori Rock Physics information as necessary to stabilize the solution depending on the uncertainty on the data available, the acquisition geometry, and the background geological knowledge of the area of interest. A further extension of the research could address the problem of analysing

the stability of the regularized inversion when the parameters of the model \mathbf{m} are different (for example AI , Poisson ratio, ρ).

Chapter 6

Acoustic and Elastic Inversion on a Test Land Dataset

6.1 Introduction

I make use of a 2-D line and an inline of a 3-D dataset from a land seismic survey to test the post-stack CARV reconstruction method discussed in Chapter 3, and the pre-stack reconstruction methods discussed Chapter 4 on properly conditioned input data. The 2-D line has been used to estimate the AI while the pre-stack inline has been used to invert for the p-wave and s-wave velocity and for the bulk density, providing as a by-product an estimate of the AI. Before applying the reconstruction and inversion approaches, a pre-conditioning work on the seismic data has been performed. One of the issues that characterizes the recursive inversion of land data is the selection of the AI for the reference layer. A further unknown is the scalar to adopt for mapping the bandlimited processed data into a bandlimited version of the reflectivity. I overcome both issues by calibrating the two values to the values derived from well logs. In fact, a sonic and density log is available nearby the two lines, at the location indicated in Figure 6.1. The dataset is obtained by courtesy of Eni.

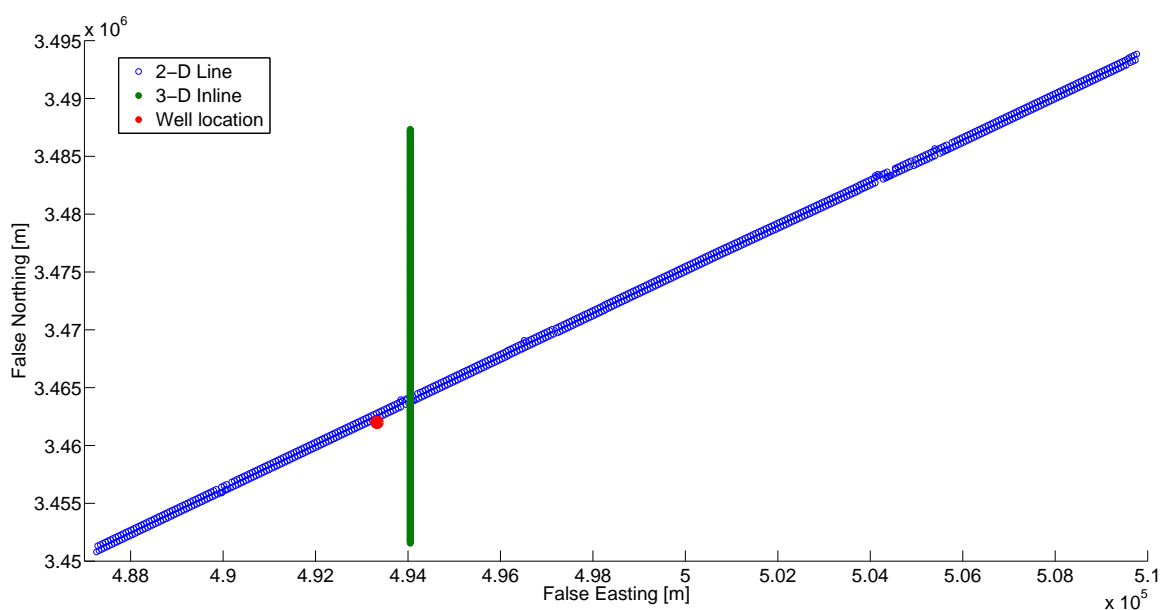


FIGURE 6.1: Relative planimetric position of the Eni land data available.

Data coordinates have been kept confidential and are not available for the present work, however this fact does not affect the results presented. The well logs available consist of a sonic, and a neutron density within the interval 1148 to 2236 ms. The two well logs are acquired at a nominal depth interval of 6 inches. Log data have been resampled to 4 ms (relying on the sonic log for the depth to travel-time mapping), after an anti-alias low-pass filter. After resampling, a median filter over a sliding window of 3 samples has been applied to enhance the blocky structure of the two interval properties. The results thus obtained are presented in Figure 6.2. In order to compare the seismic to well log data (see Figure 6.26), the reflectivity calculated from the blocked AI has been convolved with a 25 Hz Ricker wavelet, roughly corresponding to the peak frequency of the seismic signal.

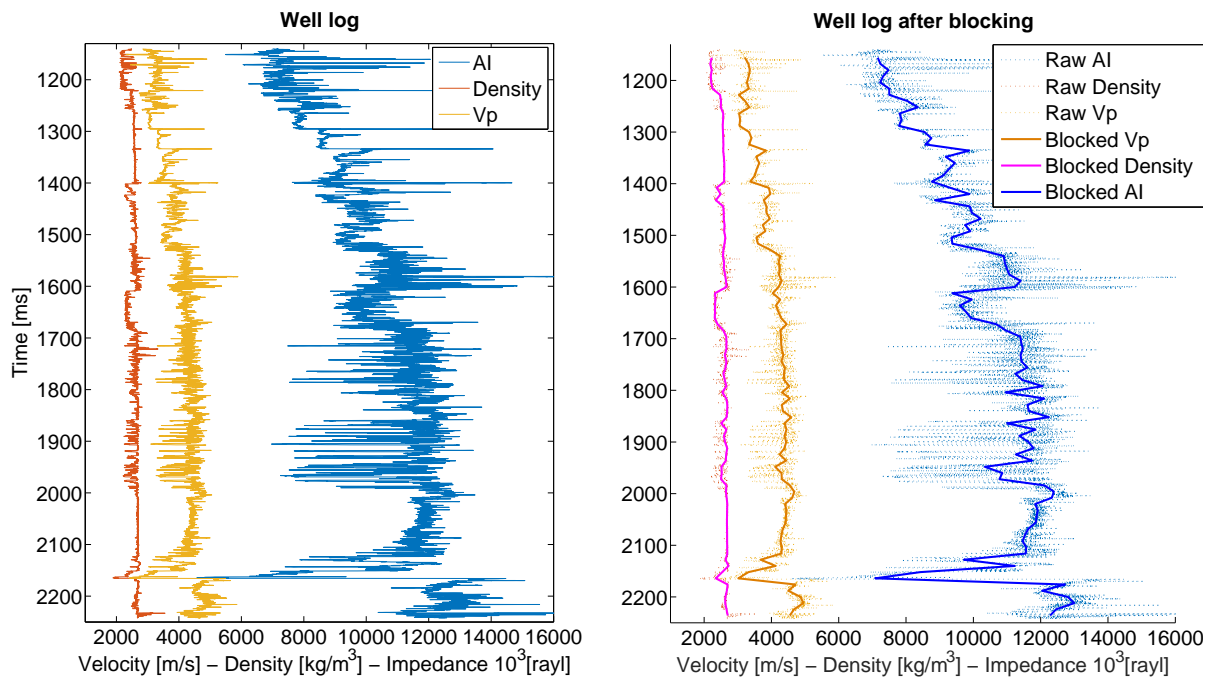


FIGURE 6.2: Well log data and well log blocking for seismic-to-well tie. The depth-to-time calibration was provided for the interval 1728-2236 ms, while the shallow interval has been calibrated by using the sonic log information.

The 2-D line consists of 803 post-stack traces. Traces are made up of 1375 samples for a total duration of 5.5 seconds. The sampling interval is 4 ms and the spectrum of the signal ranges from roughly 8 to 40 Hz (Figure 6.17 presents the average amplitude spectrum). No further information is available on the 2-D line: I consider the data as properly processed and migrated. The only issue that is evident when comparing the 2-D line to the Inline from the 3-D volume and to the well log is the polarity of the data. I chose to reverse the polarity for the 2-D line: the comparison between Figure 6.3, Figure 6.5 and the well logs on the event at about 2100 ms justifies this choice.

The Inline from the 3-D volume consists of 1571 CDP gathers sampled every 4 ms for a total length of the trace of 6 s. The nominal fold of each gather is 110 with the offset bins 50 m wide, ranging from 75 to 5475 m. The nominal CDP spacing is 22.5 m and data have been processed and migrated (with a Kirchhoff pre-stack-time algorithm). A de-absorption filter has been applied to balance the amplitude spectrum of the data: its effects are evident in Figure

6.17 where the mean amplitude spectrum of the Inline is compared to the mean amplitude spectrum of the 2-D line. The spectral balancing on the Inline is expected to provide more confidence in the CARV inversion obtained on this dataset rather than on the one obtained from the 2-D line. Data are NMO corrected and a surface consistent deconvolution filter has been applied to enhance the lateral continuity of the events. The pre-stack data show poor continuity across CDP and offset direction (see Figure 1.6 for reference). A migration velocity field is also provided every 500 m for the Inline. I assumed the migration velocity to be an RMS velocity field and I estimated a smooth interval velocity field from a regularised version of the Dix formula (see equation 4.4). The RMS and interval velocity field are presented in Figure 6.6.

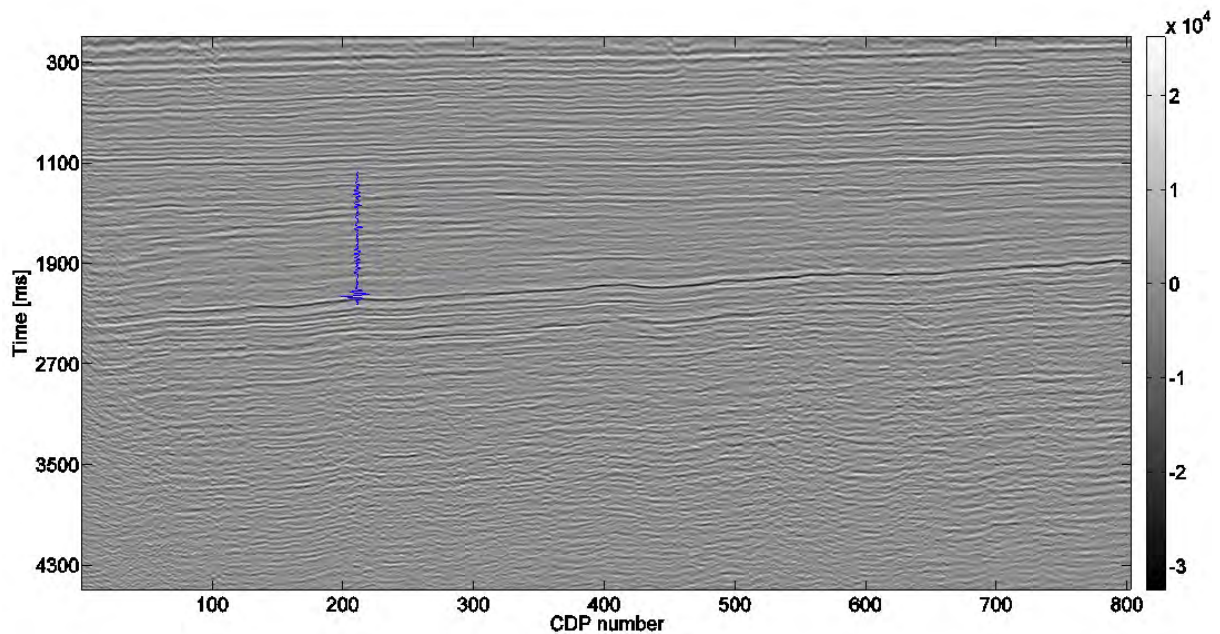


FIGURE 6.3: 2-D seismic line stack with the synthetic trace derived from well logs overlaid in blue.

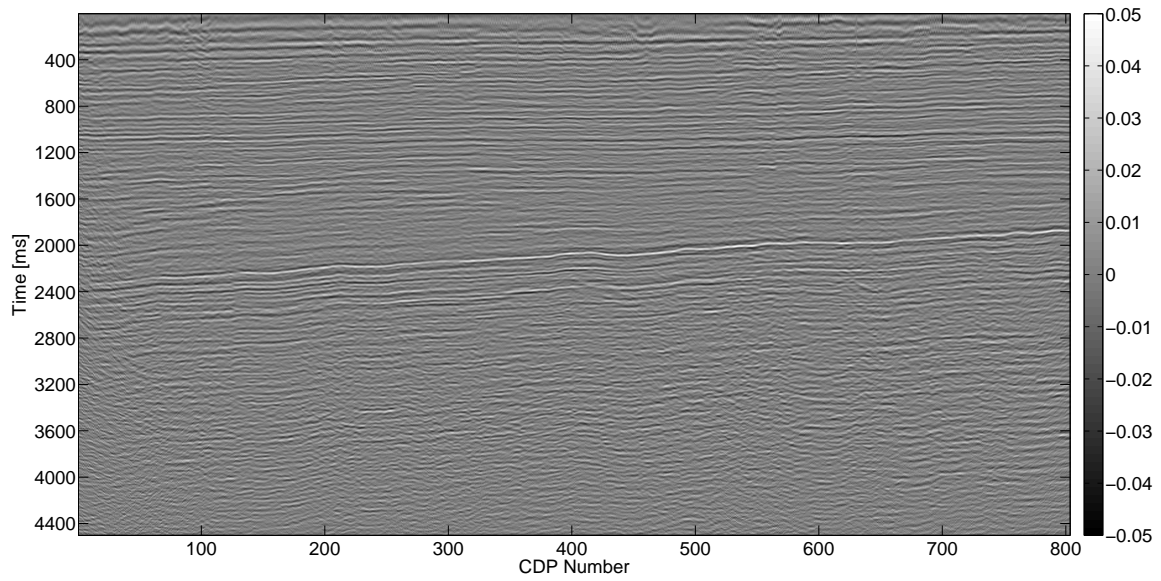


FIGURE 6.4: 2-D seismic line stack after polarity reversal and scaling to amplitudes pertaining to the reflectivity.

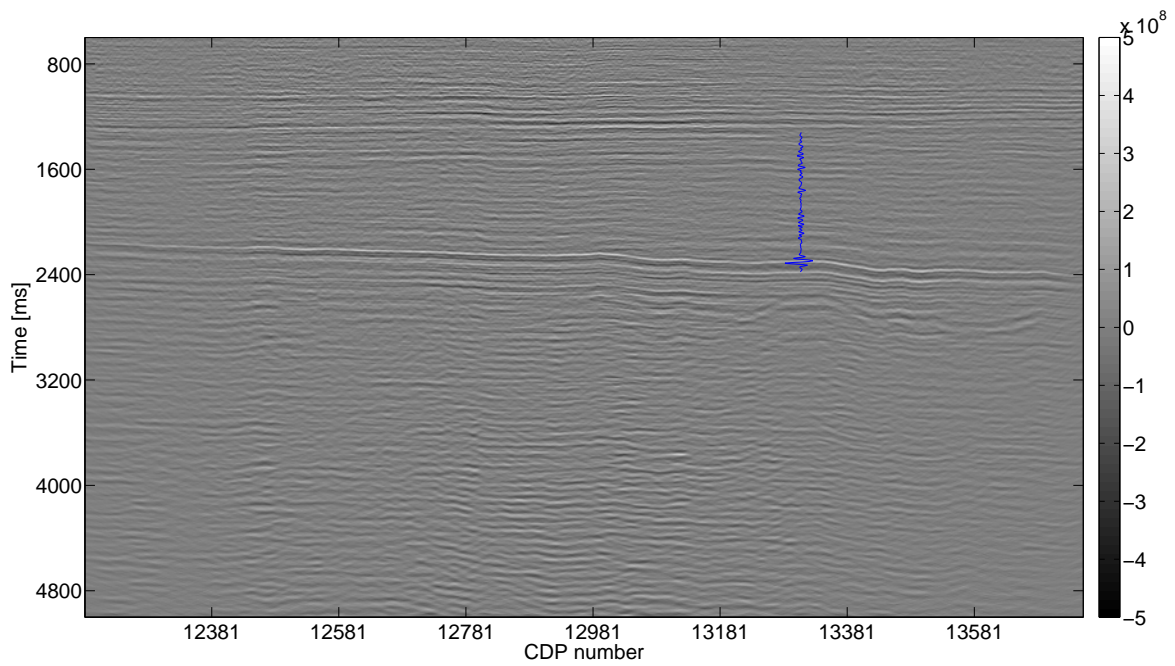


FIGURE 6.5: Stack of the Inline available in the angle range $6^\circ - 33^\circ$ with the synthetic trace derived from well log overlaid in blue.

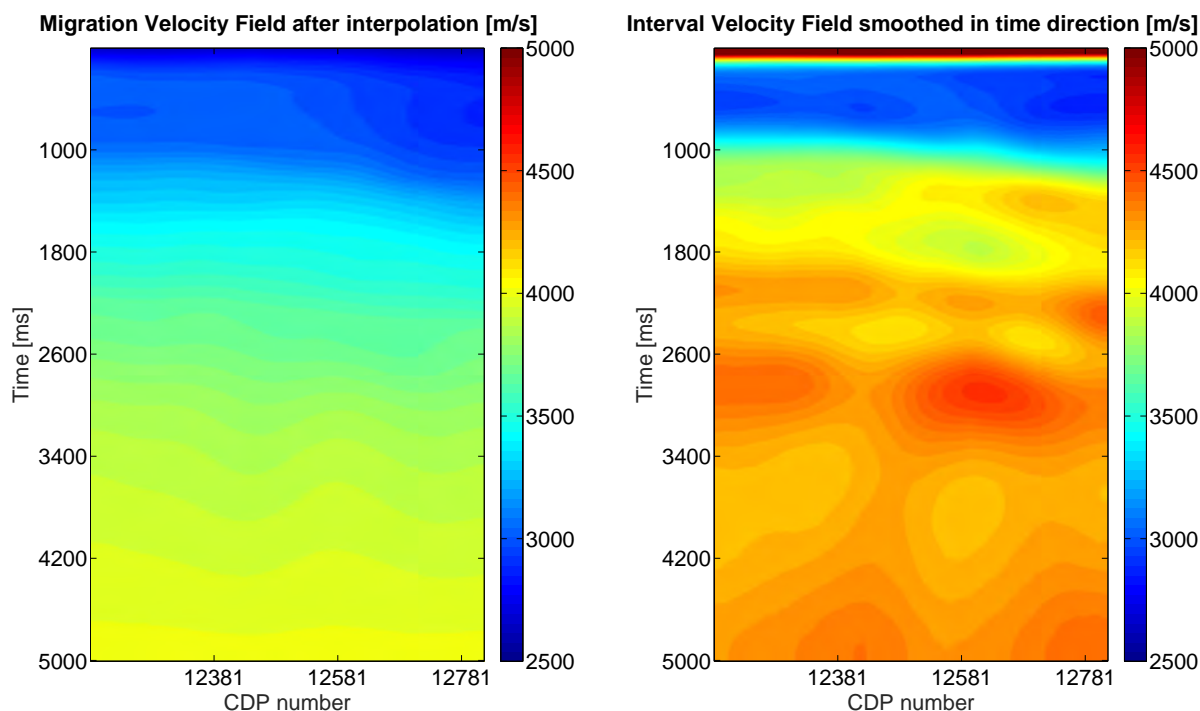


FIGURE 6.6: Velocity field available for the Inline. In the panel on the left the migration velocity field is shown after spatial interpolation every trace, and in the panel on the right the derived interval velocity field is presented. The shallow zone of the interval velocity field (roughly 0-400 ms) is not reliable because of inversion artefacts.

6.2 Seismic Data Pre-conditioning

There are critical issues in the Inline data that must be addressed before performing any kind of amplitude inversion. The strong residual Moveout energy and the channel-to-channel artefacts that are visible both on Panel A of Figure 6.7 and on Figure 6.8 are particularly concerning. A pre-conditioning workflow that aims at mitigating those issues, consists of:

- Dead channels removal (offset 5125 m to 5475 m)
- Linear noise attenuation (energy with apparent velocity less or equal to 2000 m/s is removed)
- Incoherent noise attenuation via rank-reduction (Multichannel Singular Spectrum Analysis)
- Residual multiple attenuation in the parabolic Radon domain

I chose this processing flow to first target unwanted energy that is well isolated from the primary signal: dead channels are easily removed in CDP/offset domain, and low-velocity linear noise is well isolated from the primary events in the $f - k$ domain. I then adopted the rank reduction approach to remove incoherent noise which is problematic for the recursive inversion and which could be smeared over the CDP when performing the parabolic forward and backward Radon transform. I eventually attenuate the energy that shows residual Moveout,

paying particular attention to protect near channels. The Radon transform algorithm has been taken from the Sacchi and SAIG (*SeismicLab*)[©] package under the GNU general public license and it has been further developed as part of the thesis.

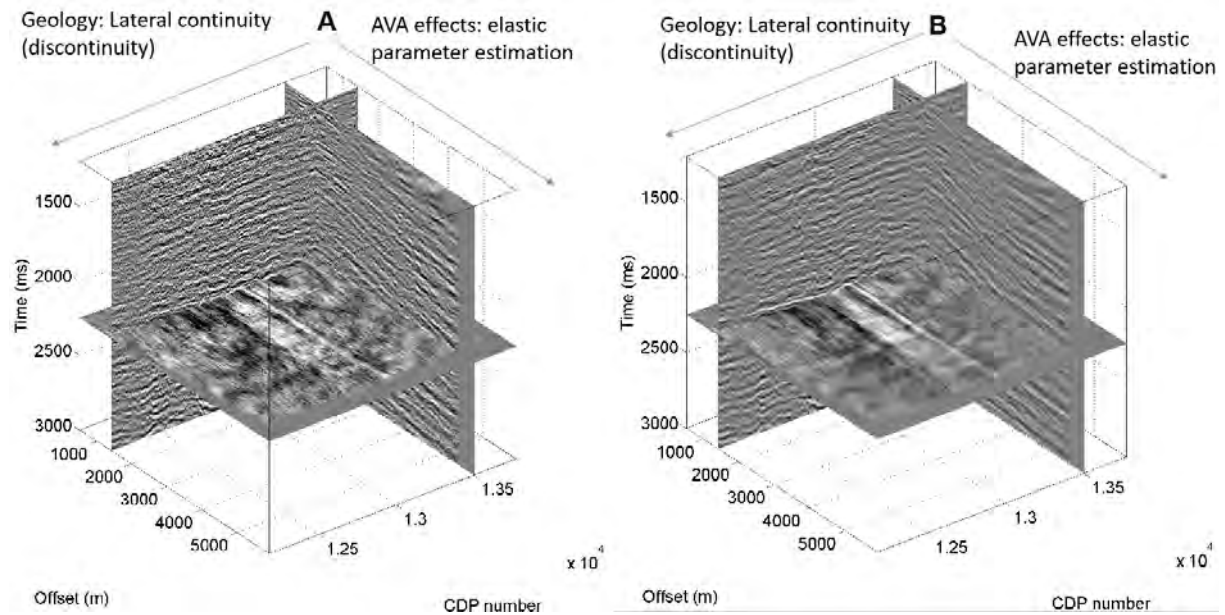


FIGURE 6.7: *Slice of the pre-stack inline cube: one common offset plane, one CDP plane, and one timeslice is displayed. Panel A shows the data as received, and Panel B shows the data after a pre-conditioning work for inversion. The pre-stack data are noisy and only a single event is clearly evident in the timeslice.*

The input CDP gathers are strongly affected by linear noise which has been tackled by a filter in the $f - k$ domain. The filter removes all the energy that shows an apparent velocity less or equal than 2000 m/s. The target area I selected for inversion is included in the range 1200-3500 ms, where the migration velocity of Figure 6.6 suggests that no primary event is slower than 2000 m/s. To avoid primary leakage the input data are restored outside the fan limited by the apparent velocity 200 m/s and 1700 m/s in the traveltime-offset domain. The results of this operation are presented for 5 sample CDP gathers in Figure 6.9.

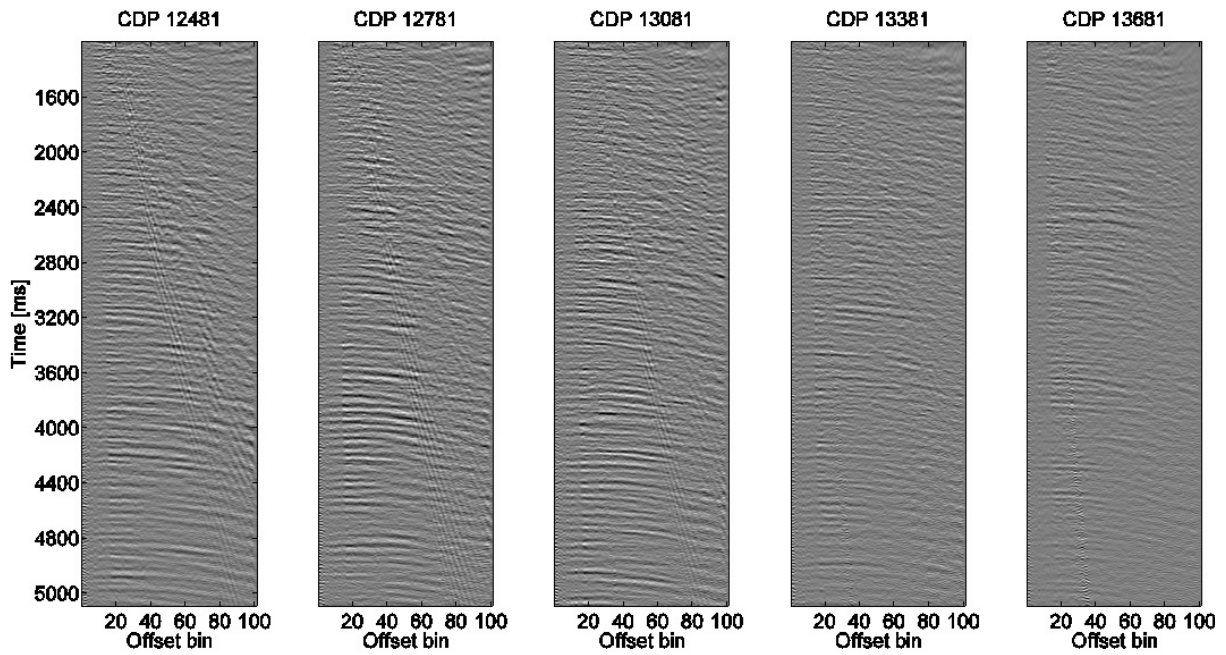


FIGURE 6.8: Selection of sample CDP gathers after migration. Linear noise and residual moveout energy is particularly concerning for a recursive amplitude inversion at depth.

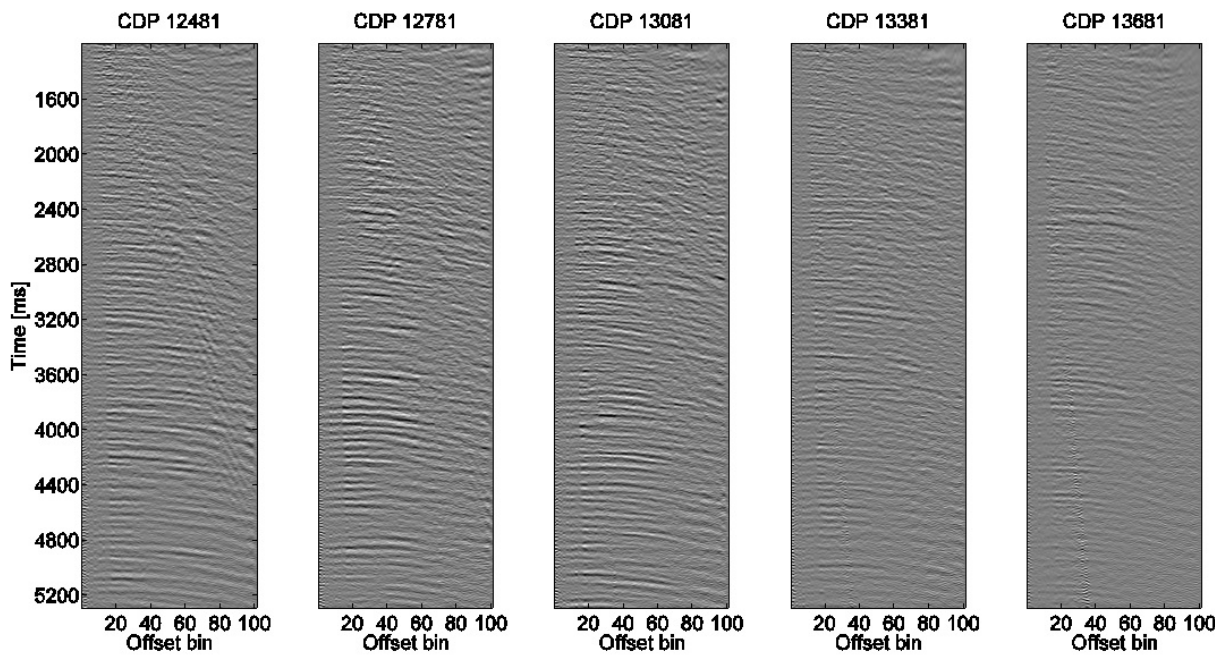


FIGURE 6.9: Selection of sample CDP gathers after linear noise attenuation in the $f-k$ domain.

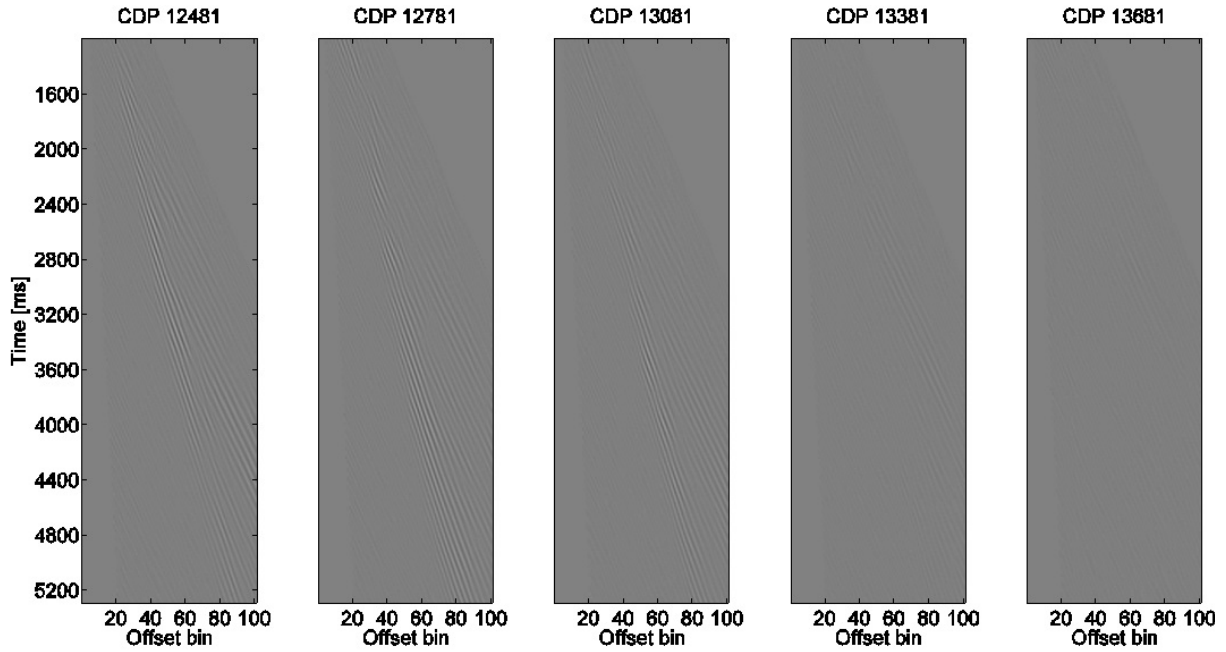


FIGURE 6.10: Difference between Figure 6.8 and Figure 6.9. The filter in the $f - k$ domain partially attenuate the direct arrivals with no damage on the primary events.

A multichannel Singular Spectrum Analysis (Oropeza and Sacchi, 2011) in windows of 101 offsets and 101 CDP gathers has been applied to each frequency component from 5 to 50 Hz. The other frequency components are not taken into account by the parametrisation of the CARV inversion, therefore they are not considered for data pre-conditioning. The 100 linear events that show the largest energy are kept in each spatial window, this attenuates the incoherent noise while preserving the characteristics of the flat events in the NMO-corrected data (see the difference Figure 6.12). The window overlapping is 30% in the CDP direction.

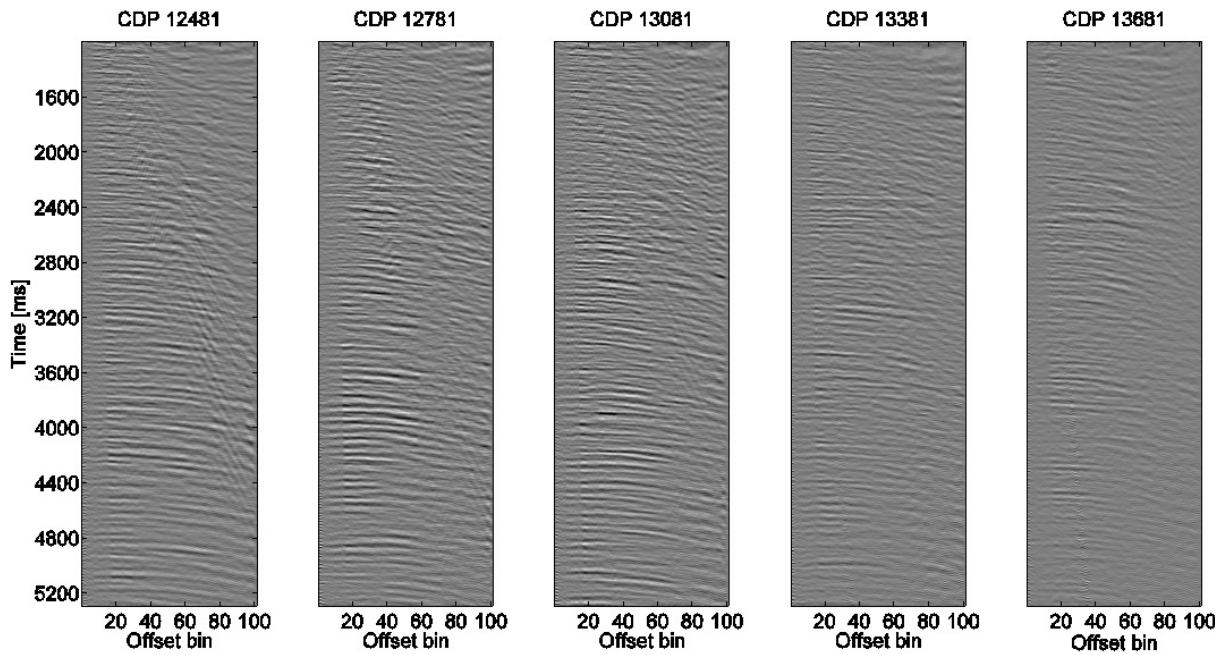


FIGURE 6.11: Selection of the same sample CDP gathers as displayed in Figure 6.8 after the $f - k$ filter and the rank reduction via multichannel Singular Spectrum Analysis.

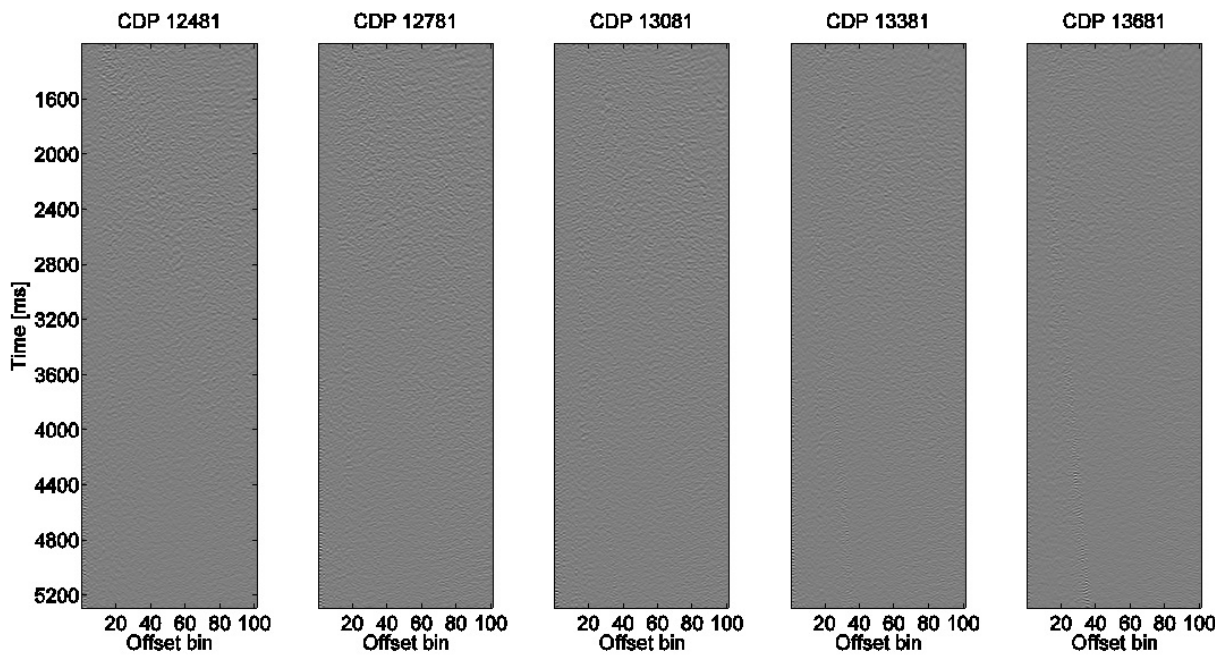


FIGURE 6.12: Difference between Figure 6.9 and Figure 6.11. Only a faint residual signal can be seen at far offsets in the shallow part of CDP 12481. Those offset are not considered within the selection of angles adopted for the pre- and post-stack inversion.

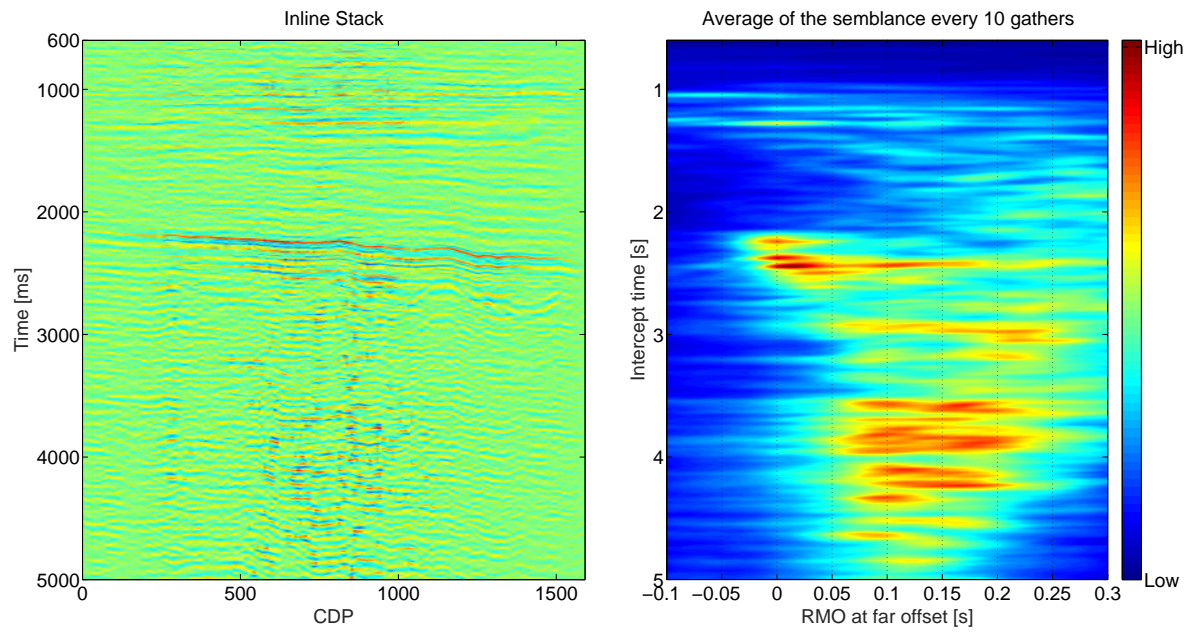


FIGURE 6.13: *Residual moveout analysis. Average across CDP locations of the energy that sums across parabolic events in CDP/offset domain. Across and below the main event most of the energy comes from events that show a significant residual Moveout.*

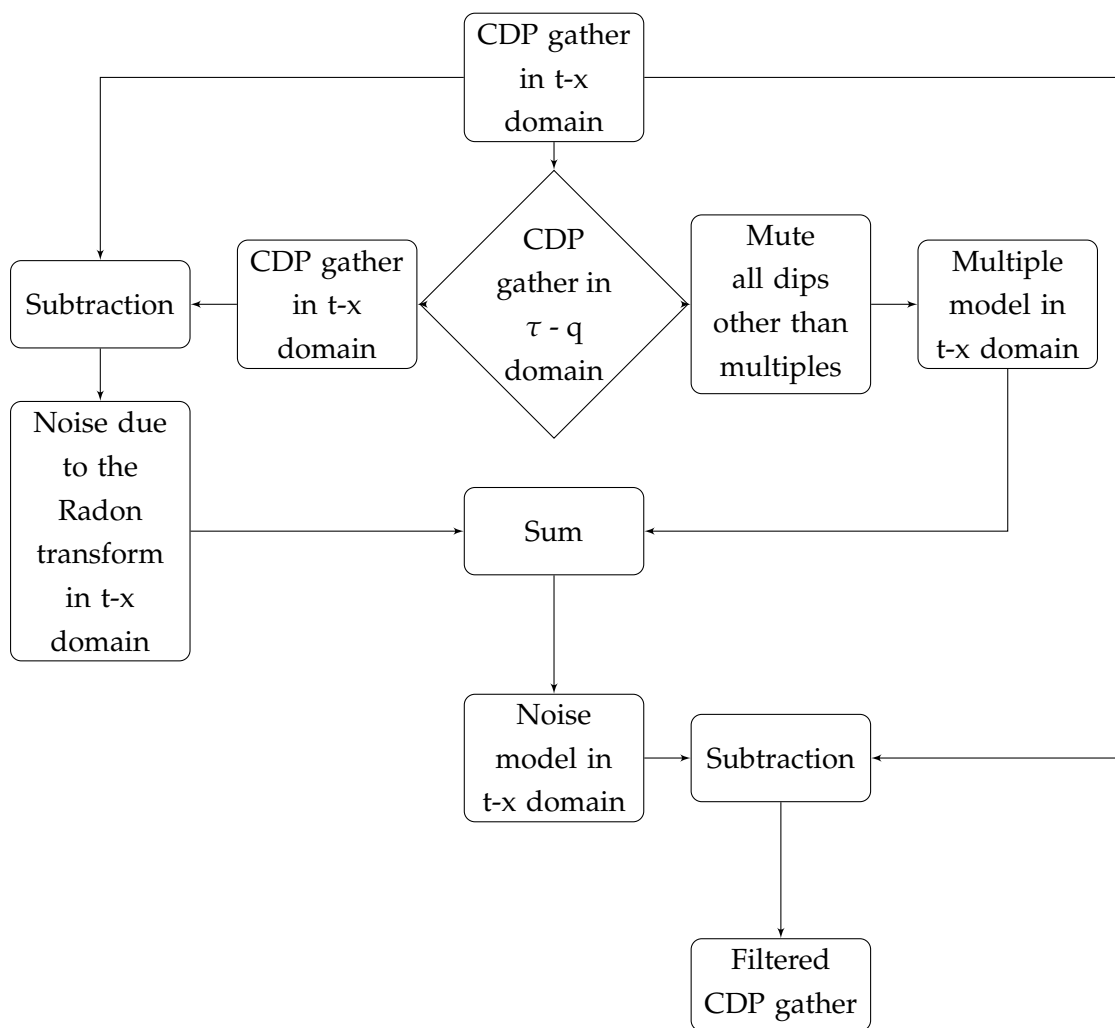


FIGURE 6.14: Schematic representation of the residual Moveout energy attenuation workflow. I named the CDP / offset data domain with the $t - x$ label and the intercept / curvature data domain with the $\tau - q$ label.

The presence of residual Moveout energy is evident from a visual inspection of the CDP gathers of Figure 6.11 and it is also highlighted by the semblance analysis proposed in Figure 6.13. The issue is tackled by a mute in the parabolic Radon domain. The algorithm used is schematically represented in Figure 6.14. The aperture of the Radon transform is 4000 ms at far offset (5075 m), the maximum frequency that is transformed into Radon domain is 50 Hz, which is compatible with the choice of sampling the curvature of the events at 10 ms at offset 5075 m. The mute is applied to the energy that shows a residual Moveout at far offset between 120 and 400 ms. The nearest 5 offsets have been protected from the processing with a further 5 offsets in which the input and the processed data are linearly tapered: this is to avoid near-angle primary damage from the forward and backward Radon transform. The processed seismic gathers are presented in Figure 6.15 and the residual Moveout energy removed is presented in the difference of Figure 6.16. Minor leakage is present at far offsets in the shallow portion of the CDP gather 12481, which is not concerning because of the angle mute I intend to use for the inversion.

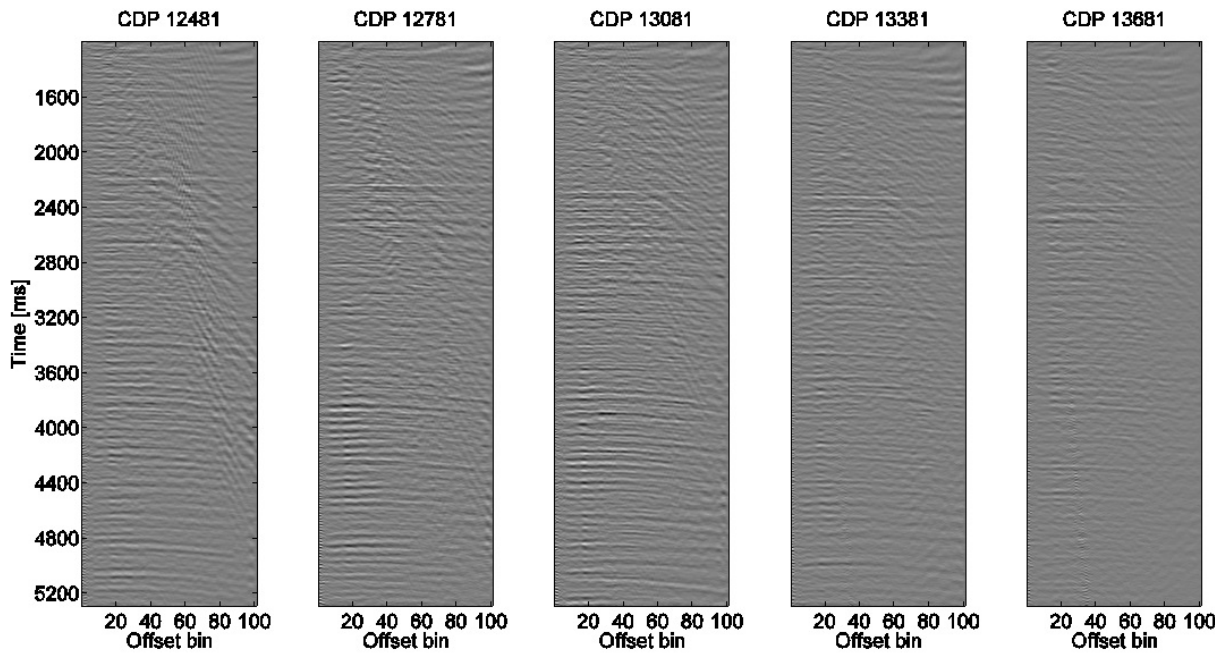


FIGURE 6.15: Selection of the same sample CDP gathers as displayed in Figure 6.11 after the residual Moveout energy attenuation performed in Radon domain. Not all the residual Moveout energy has been removed but the S/N of the flat events is enhanced with respect to the data of Figure 6.11.

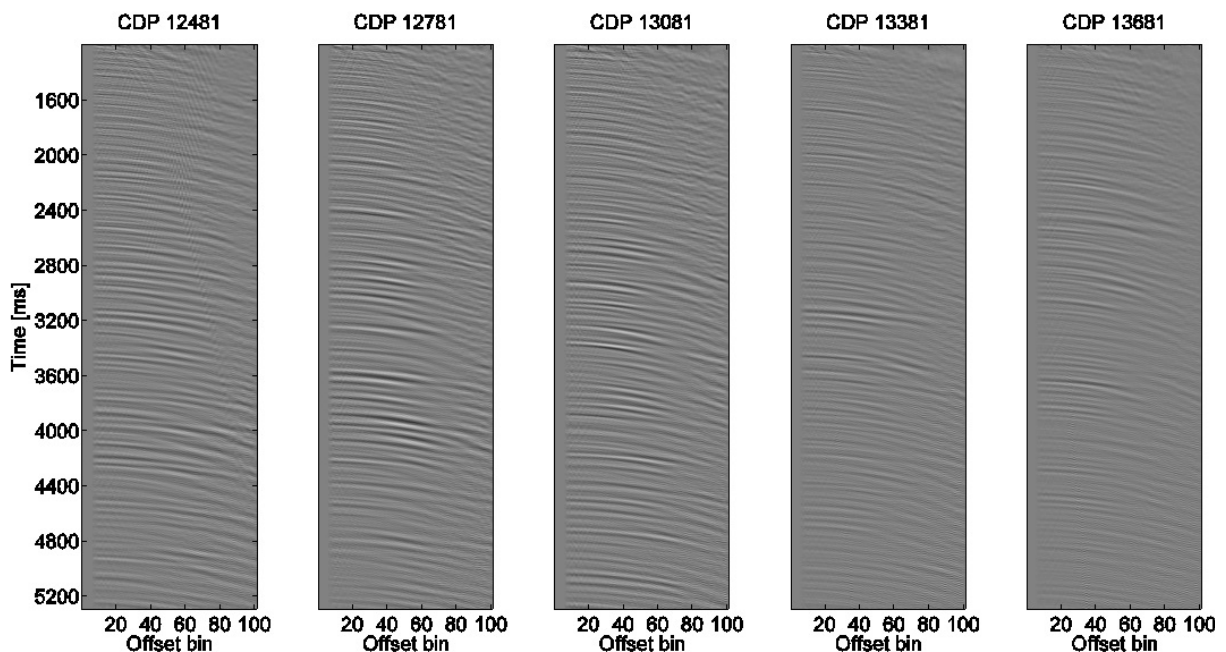


FIGURE 6.16: Difference between Figure 6.11 and Figure 6.15. Much of the residual Moveout energy is removed from the CDP gathers and only a minor leakage is present in CDP 12481.

6.3 Post-stack Inversion

I apply the CARV algorithm for the post-stack inversion described in Chapter 3 on both the 2-D line and on the Inline. The mean amplitude spectrum across the section presented in Figure 6.17, provides some hints for selecting the cut-off frequency for AR modelling.

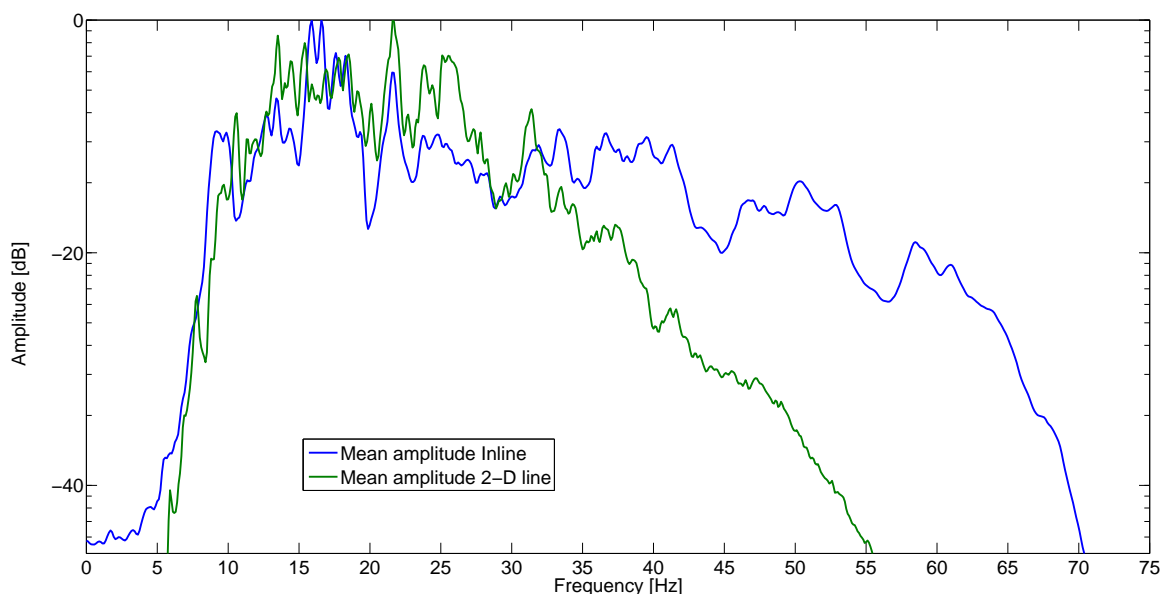


FIGURE 6.17: Comparison between the mean amplitude spectrum of the 2-D line and the Inline extracted from the 3-D volume. Both spectra are normalised to their peak amplitude. The Inline shows a larger bandwidth.

6.3.1 2D Section

I applied the CARV inversion method detailed in Chapter 3 to the land seismic data of Figure 6.4. I tested the range 7-11 Hz, in increments of 1 Hz, for the low-cut, and the range 36-44 Hz, in increments of 2 Hz, for the high-cut frequency, and the AR model order length from 75 to 90 in increments of 5. The results of this sensitivity analysis are presented in Figure 6.21 as the sample standard deviations among the outcomes at each temporal sample and trace location. I then chose the range 8-40 Hz for fitting an AR process of length 80. As far as it concerns the 2-D line I first identified three horizons (see Figure 6.18). The first horizon served to extend the reference AI (3000000 rayl) from the well log to all the traces in the section. The other two horizons have been used to set the constraints on impedance at depth. The AI on the green horizon is set to 8500000 ± 500000 rayl, while the AI on the red horizon is set to 12500000 ± 500000 rayl. A scalar that transforms the data into amplitudes related to reflectivity, has been calibrated on the event highlighted by the red horizon (Figure 6.18) for 25 traces around the well location.

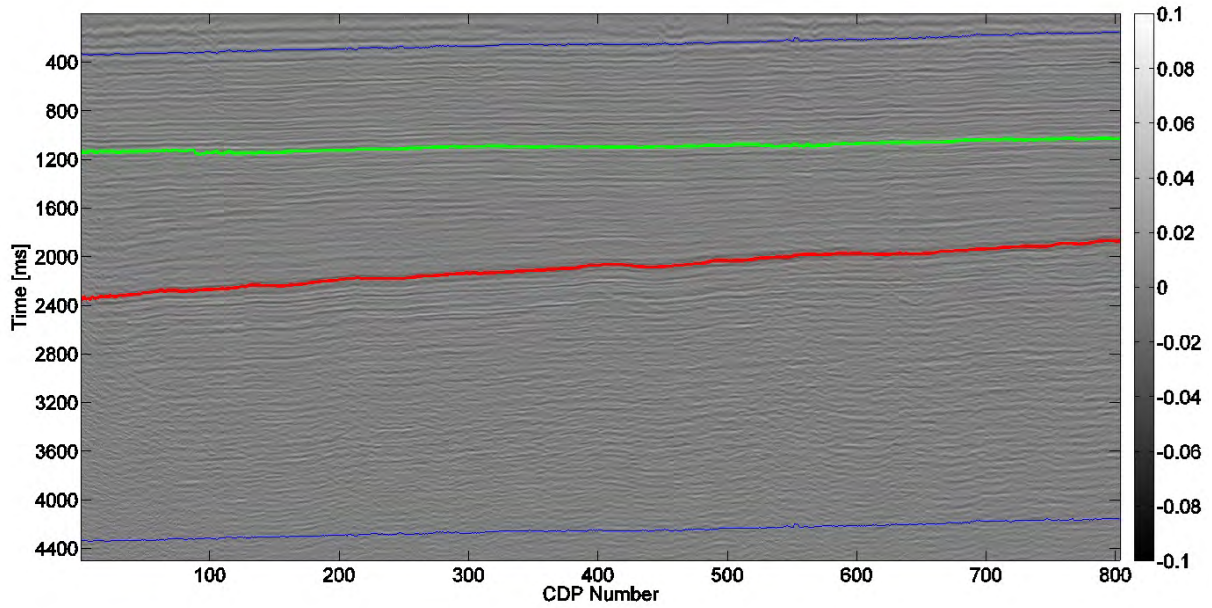


FIGURE 6.18: Window of the 2-D line selected for inversion with 2 picked horizons (green and red curve). The blue lines indicate the limits adopted for the inversion.

AR model orders in the range 75 to 90 have been tested with 80 being the order chosen for the results presented. The results, in presence of the soft constraints only, and with regularisation derived from the velocity field ($\lambda=0.3$ the ratio of the maximum eigenvalues of the matrix \mathbf{G} and $\mathbf{L}^t\mathbf{L}$ in equation 3.12) are reported in Figure 6.19 and 6.20 respectively. A lateral continuity weight is also imposed in those inversion results.

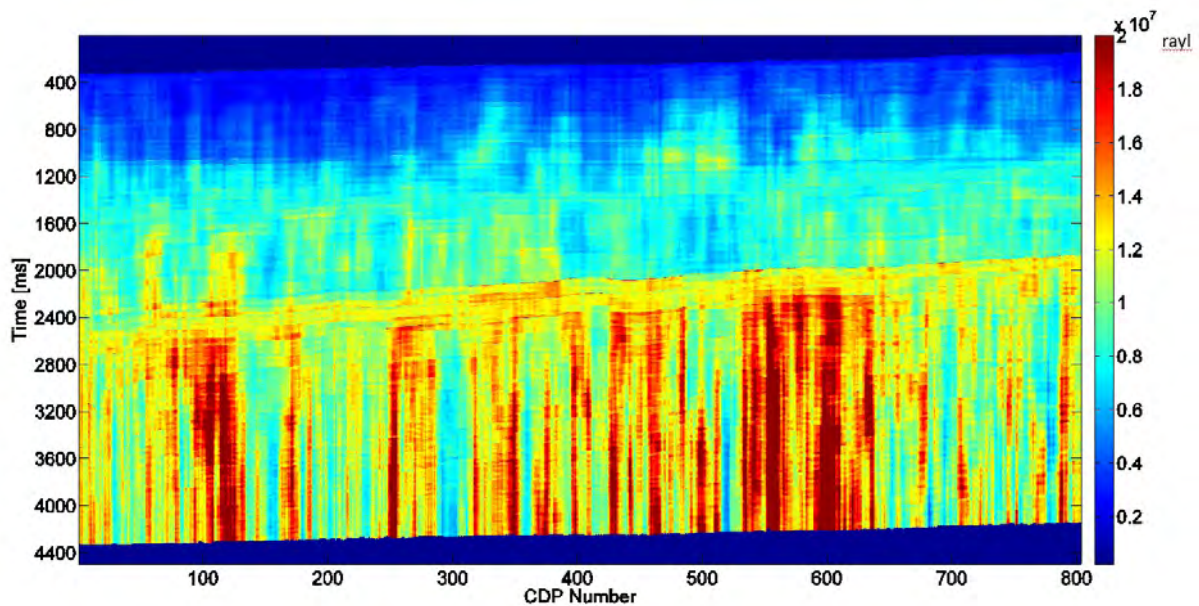


FIGURE 6.19: AR inversion of AI on the 2D line with two soft constraints on impedance. Despite lateral continuity enhancement, trace-to-trace instability is still present in the results.

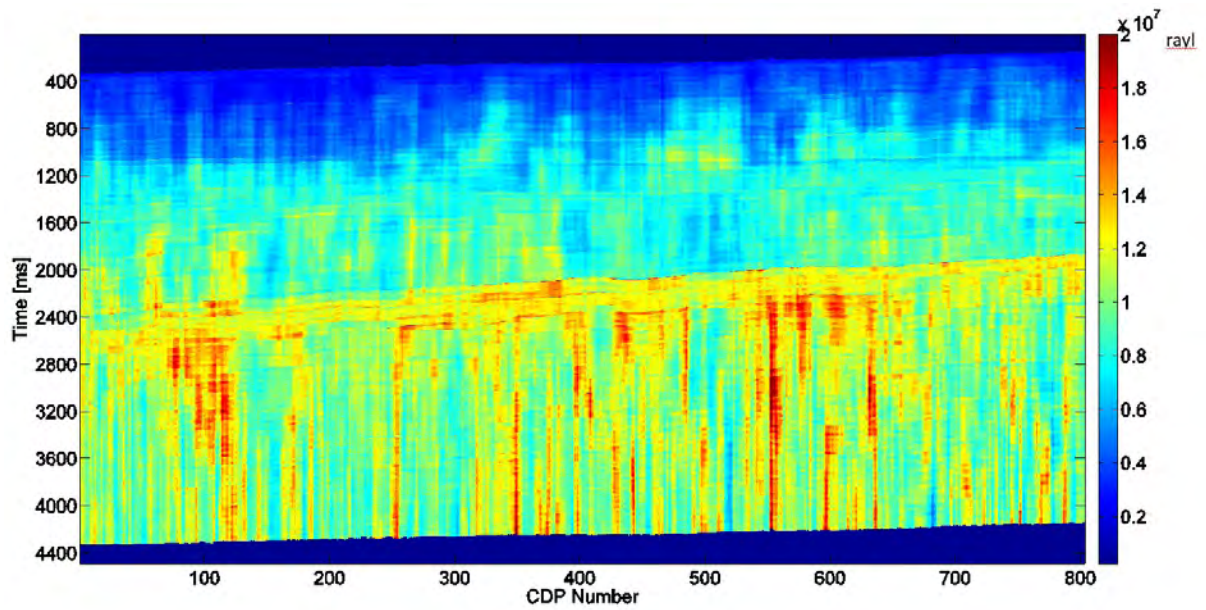


FIGURE 6.20: AR inversion of AI on the 2-D line with two soft constraints on impedance and the information coming from the interval velocity field at the Inline location that crosses the 2D line. This velocity field has been extended to the whole 2-D line. The result is more stable than in Figure 6.19, but results do not appear reliable when checked against well log control.

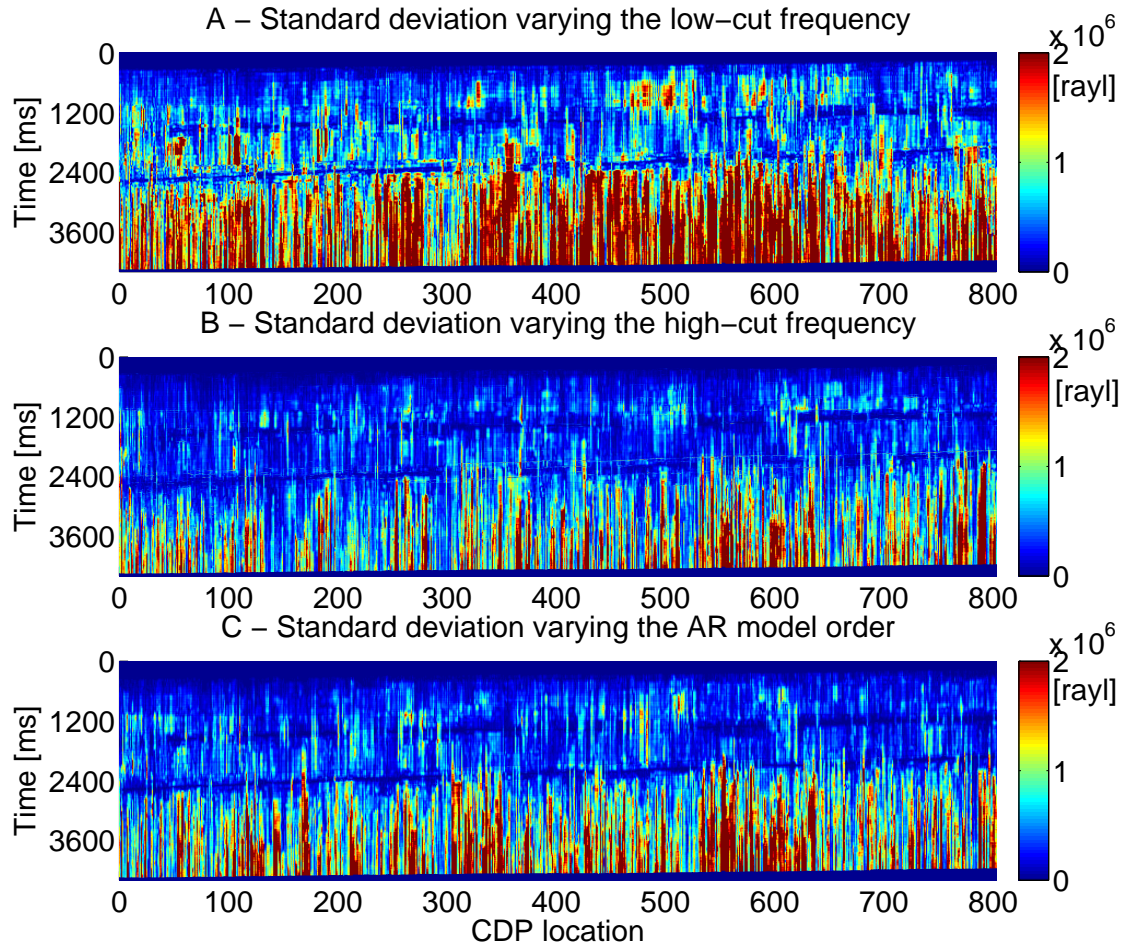


FIGURE 6.21: Standard deviation varying model low-cut frequency (Panel A), high-cut frequency (Panel B), and the AR model order (Panel C). The standard deviation refers to the deviation on the mean value when varying one parameter at the time. The effects of the constraints on AI are clearly evident as zones of low standard deviation in all the panels.

6.3.2 3D Inline

The pre-conditioned seismic gathers from the Inline have been stacked with a 24° angle mute for the purpose of post-stack AI inversion. A window of 1800 ms has been selected for inversion, starting below the blue horizon at about the top of the seismic section of Figure 6.22. The results presented in Figure 6.23, 6.24, and 6.25 are based on a signal bandwidth range 8-45 Hz and on an AR model order equal to 50. A constraint on AI (12500000 ± 500000 rayl) at the horizon indicated by the red arrows in Figure 6.22 and a lateral continuity weight are also included in the inversion to mitigate the trace-to-trace instability. The reflectivity bandwidth extension displayed in Figure 6.23 shows that the main events are effectively sharpened, but the recursive nature of the AI estimation make the reconstruction at depth scarcely reliable at the well location (Figure 6.26) both in the case of the AR inversion (Figure 6.24) and in the case of the CARV inversion (Figure 6.25).

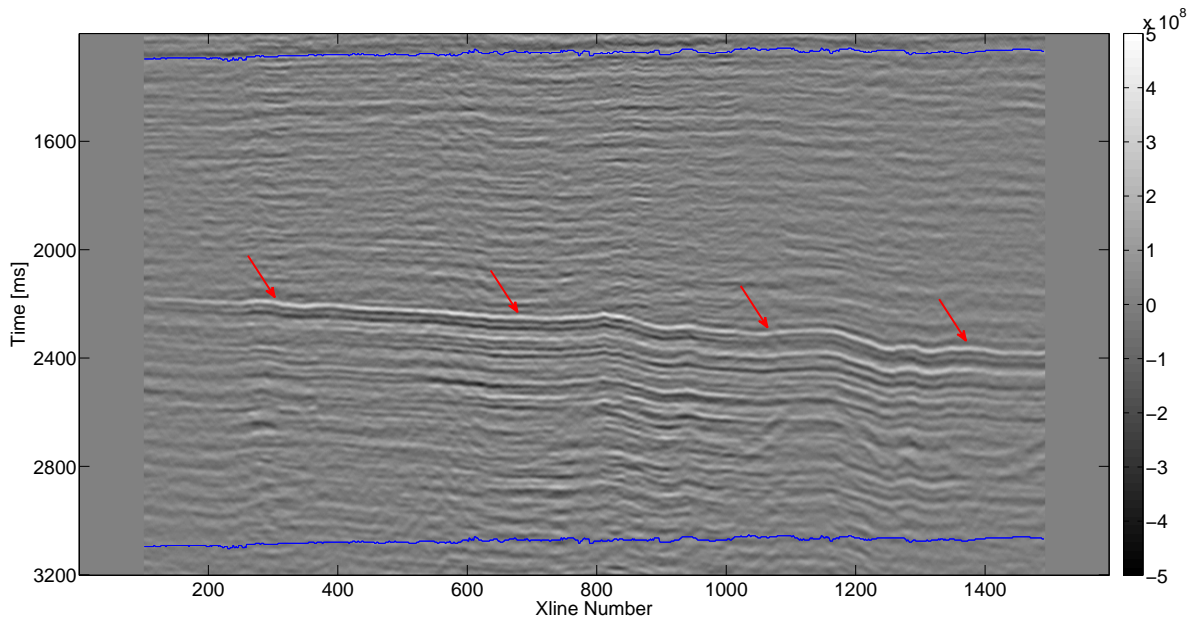


FIGURE 6.22: *Inline stack section after data pre-conditioning. The data have been inverted within the time window limited by the blue lines. Red arrows indicate the horizon where I set the constraint on AI.*

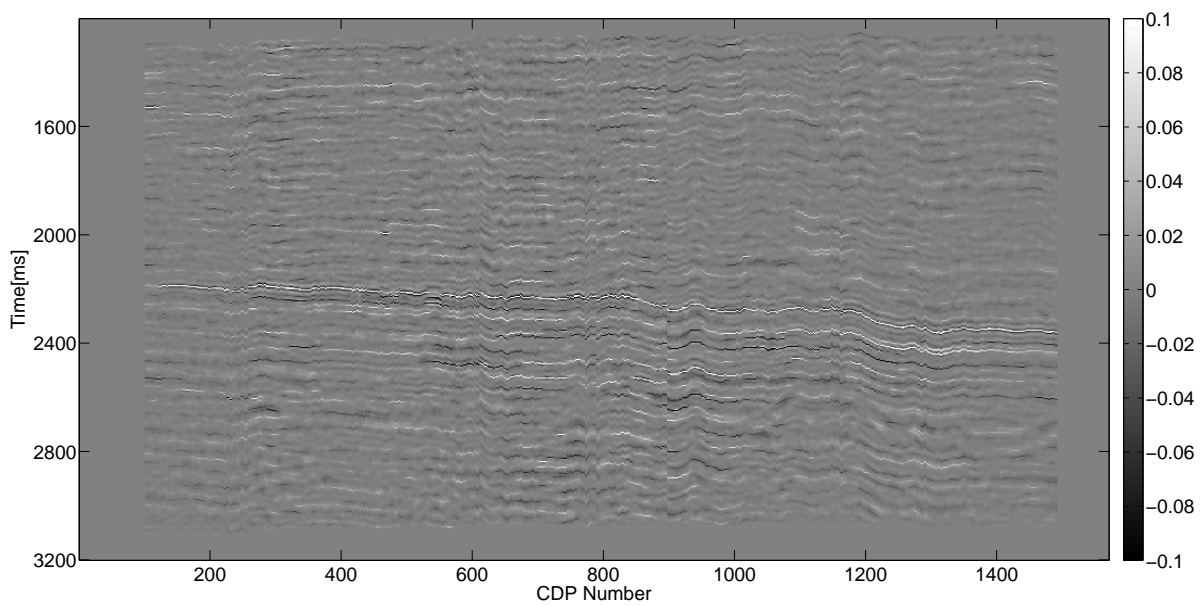


FIGURE 6.23: *Reconstructed reflectivity via the CARV method. The low frequency reconstruction is performed via the AR harmonic interpolation method, while the high frequency extension is performed via minimum entropy deconvolution as described in section 3.3.9.*

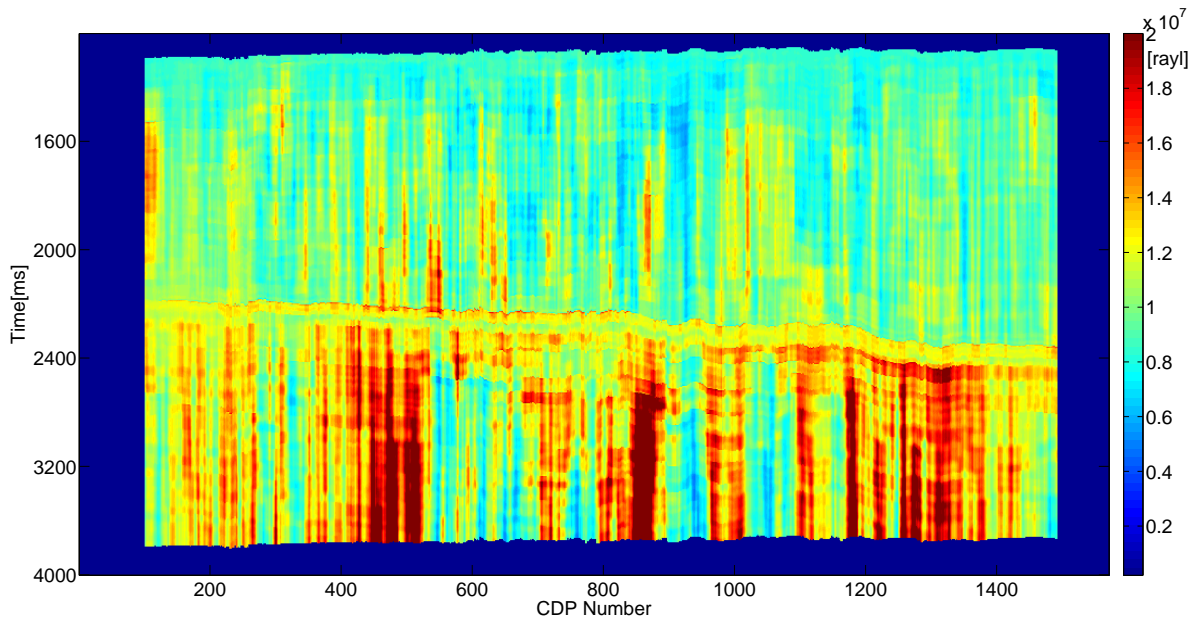


FIGURE 6.24: AR inversion of AI [rayl] on the Inline with a soft constraint on impedance at depth.

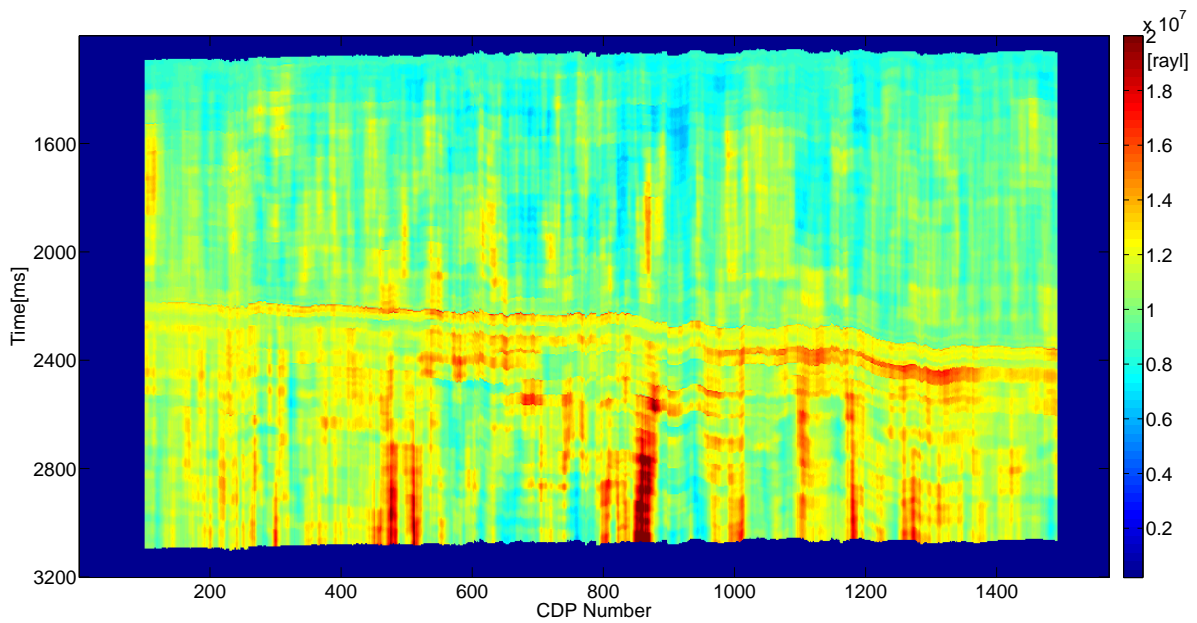


FIGURE 6.25: CARV inversion of AI [rayl] on the Inline with a soft constraint on impedance at depth and the information coming from the interval velocity field of Figure 6.6.

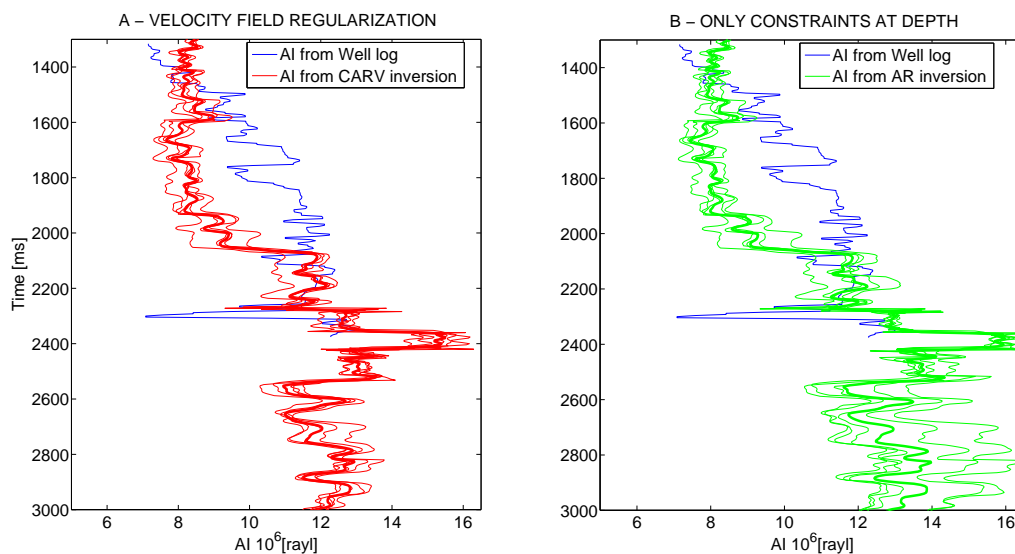


FIGURE 6.26: Comparison between the AI derived from well log and the AI derived from the CARV inversion of Figure 6.25 (A) and the AR inversion of Figure 6.24 (B). Both the results reconstruct a biased version of AI for the 5 traces around the well location. The comparison between Panel A and Panel B highlights the role played by the velocity field term in narrowing the uncertainty on the AI reconstruction at depth where no geologic constraint has been set.

6.4 Pre-stack Inversion

I applied the methods presented in section 4.3 in the attempt to recover the elastic parameters from the Inline of the land dataset. CIGs have been sorted from offset to incidence angle via the weighted stack approach of section 4.2.3. Together with the two AR approaches of section 4.3, I investigated the sparse-spike method of Perez, Velis, and Sacchi (2017) to invert the pre-stack data for three elastic parameters. This method is very similar to the one-stage workflow presented in Figure 4.6, other than the low-frequency reconstruction is not performed by AR models, but rather by minimising the L1 norm of the elastic parameters reflectivity. I show a single output for each method and for each of the three elastic parameters (α, β, ρ) in order to provide an overview of the results that have been achieved on the specific dataset. The estimates are far from being a reliable reconstruction of the elastic properties because of unrealistic trace-to-trace variability and questionable absolute values at depth. The reasons for the failure of the method are to be sought in the noisy nature of the input data, in the unstable behaviour of the mapping between reflectivity and elastic parameters, and in the subjective choice of the a priori information that is required to stabilise the AVA inversion (2 out of 3 interval properties are roughly a scaled version of each other in the presented results). The inversion for the AVA gradient and intercept only appears more stable (Figures 6.27 and 6.28). In those Figures, the intercept is integrated into AI and the gradient value is kept as an indication of the AVA behaviour at single interfaces. Figures 6.29, 6.30, and 6.31 have been obtained with a two-stages inversion (see section 4.3) and one constraint on EI at the depth corresponding to the horizon indicated by the red arrows in Figure 6.22. The value of EI has been constrained in the range 11000000-14000000 rayl at normal incidence angle and the ranges for the EI at different incidence angles have been

obtained by assuming a p-wave velocity of 4700 m/s, an s-wave velocity of 2879 m/s and a density of 2650 kg/m^3 in equation 4.17. For the case of the one-stage and the sparse-spike inversion of Perez, Velis, and Sacchi (2017) the constraints at the main event are set with respect to the three interval parameters (see section 4.3). They are $\alpha = 4700 \pm 400 \text{ m/s}$, $\beta = 2879 \pm 1000 \text{ m/s}$, $\rho = 2650 \pm 200 \text{ kg/m}^3$. The s-wave to p-wave velocity has been considered constant for the whole temporal window of the inversion and equal to 0.47. For the one- and two-stages AR reconstruction the signal bandwidth has been identified in the range 8-42 Hz and the AR model order equal to 50. The angles available span the range $6 - 30^\circ$. Table 6.1 describes the remaining parameters adopted for the inversion results displayed below. In order to limit the impact of the regularization on the result no lateral continuity weight is considered for all the three-term pre-stack estimates proposed. In table 6.1, α_0 , β_0 , ρ_0 are the mechanical parameters at the reference depth, while λ^2 and μ^2 are the two hyperparameters related to Gardner and the Mudrock line that are used to stabilise the inversion.

TABLE 6.1: *Parametrization adopted for the pre-stack inversion.*

Inversion approach	Parameters
Two-stages	$\lambda^2 = 0.01$
	$\mu^2 = 0.03$
	$\alpha_0 = 3000 \text{ m/s}$
	$\beta_0 = 1413 \text{ m/s}$
	$\rho_0 = 2200 \text{ m/s}$
One stage	$\lambda^2 = 0.03$
	$\mu^2 = 0.01$
	$\alpha_0 = 3000 \text{ m/s}$
	$\beta_0 = 1413 \text{ m/s}$
	$\rho_0 = 2200 \text{ m/s}$
Sparse-spike	$\lambda^2 = 0.01$
	$\mu^2 = 0.01$
	$\alpha_0 = 3000 \text{ m/s}$
	$\beta_0 = 1413 \text{ m/s}$
	$\rho_0 = 2200 \text{ m/s}$

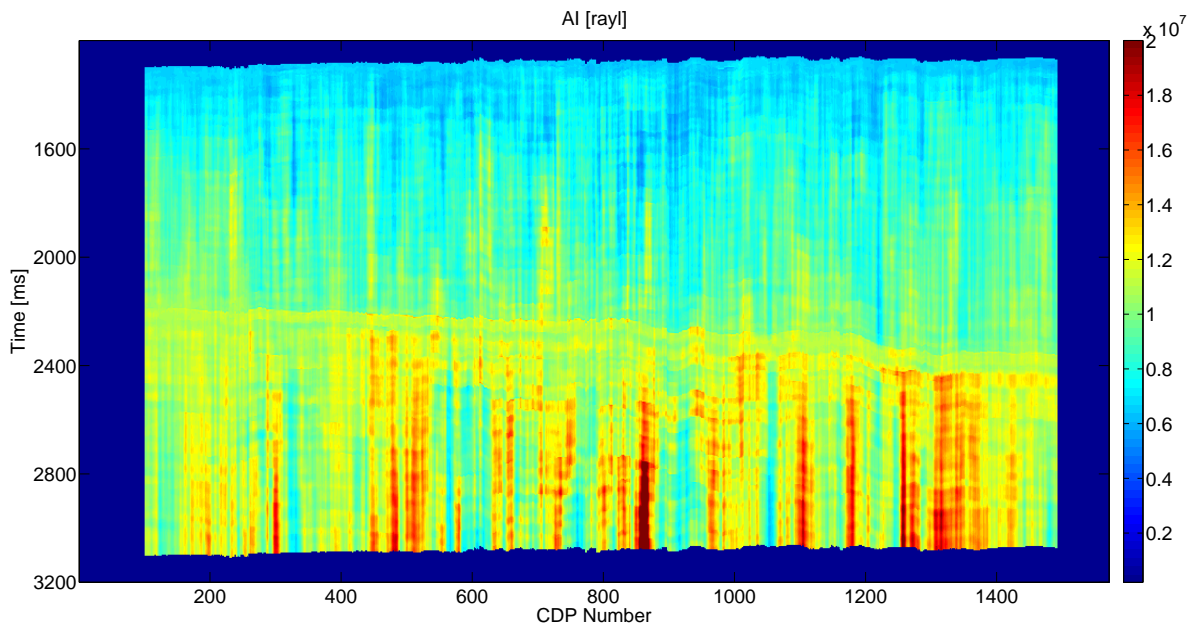


FIGURE 6.27: *Pre-stack estimation of the AI impedance via a two-stages workflow from incidence angles in the range $6 - 30^\circ$. Two-terms inversion. The intercept has been integrated to obtain an estimate of the AI at normal incidence angle [rayl]. This result is different from the one obtained in Figure 6.24 both because of the different range of angles available and because of the different method adopted in the reconstruction.*

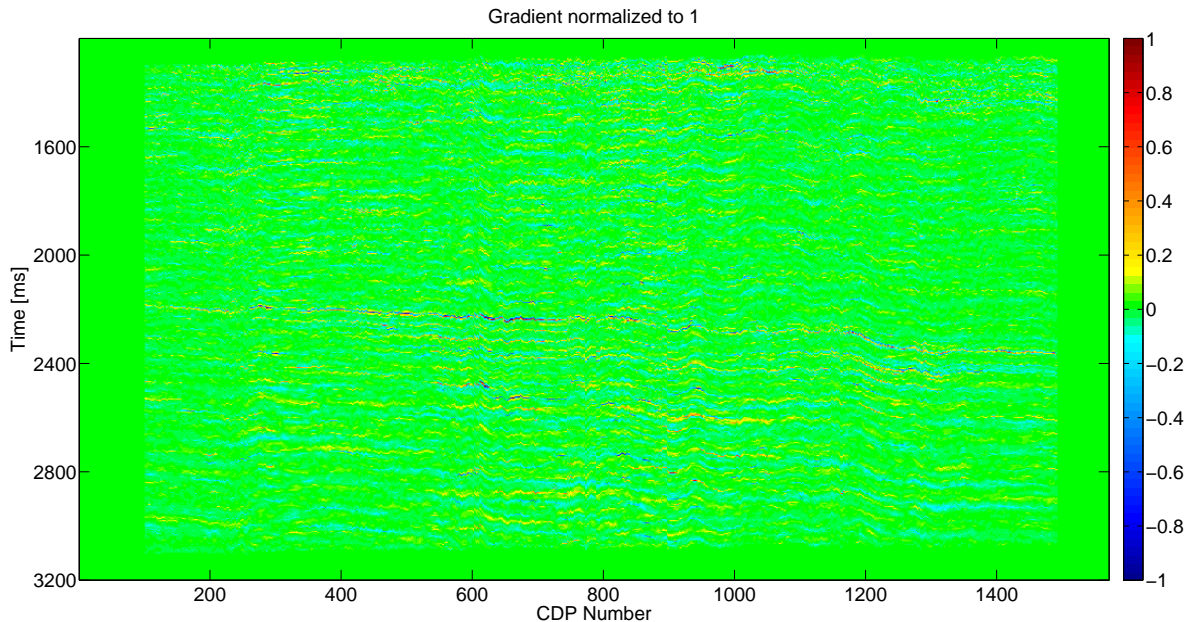


FIGURE 6.28: *Two-stages reconstruction of the full bandwidth of the AVA gradient (two-terms inversion). On the main event different behaviours may be identified, with a prevailing increase in amplitude with incidence angle.*

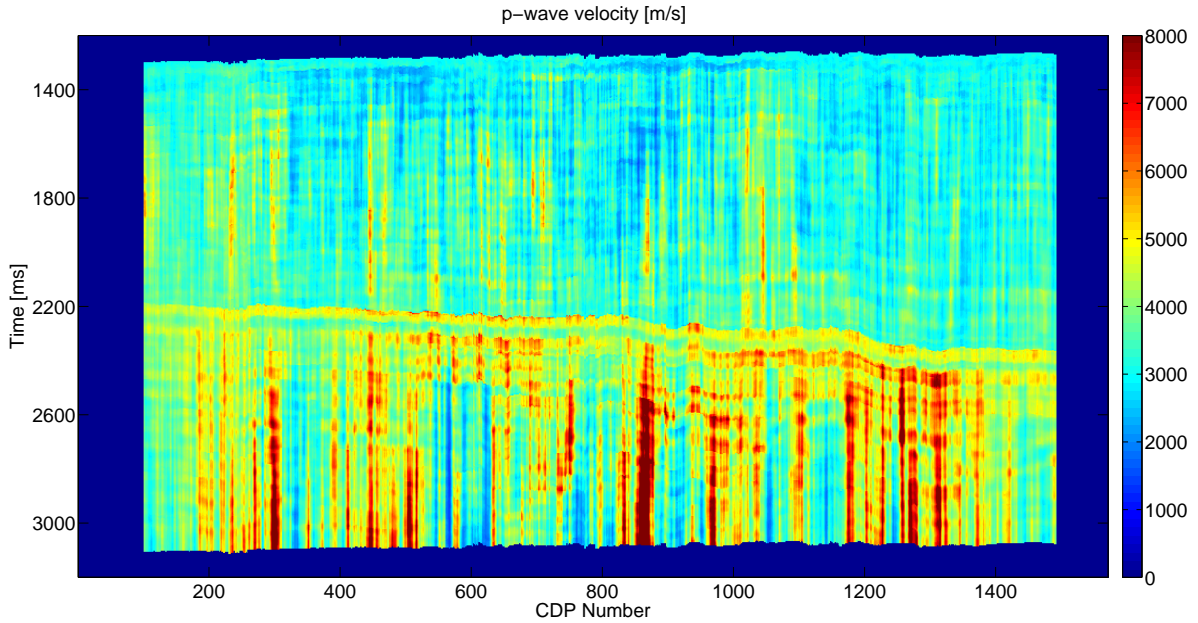


FIGURE 6.29: Reconstruction of the p -wave velocity from the two-stages algorithm [m/s]. The most evident set of events is clearly evidenced in the inversion result while the remaining part of the inversion is very noisy.

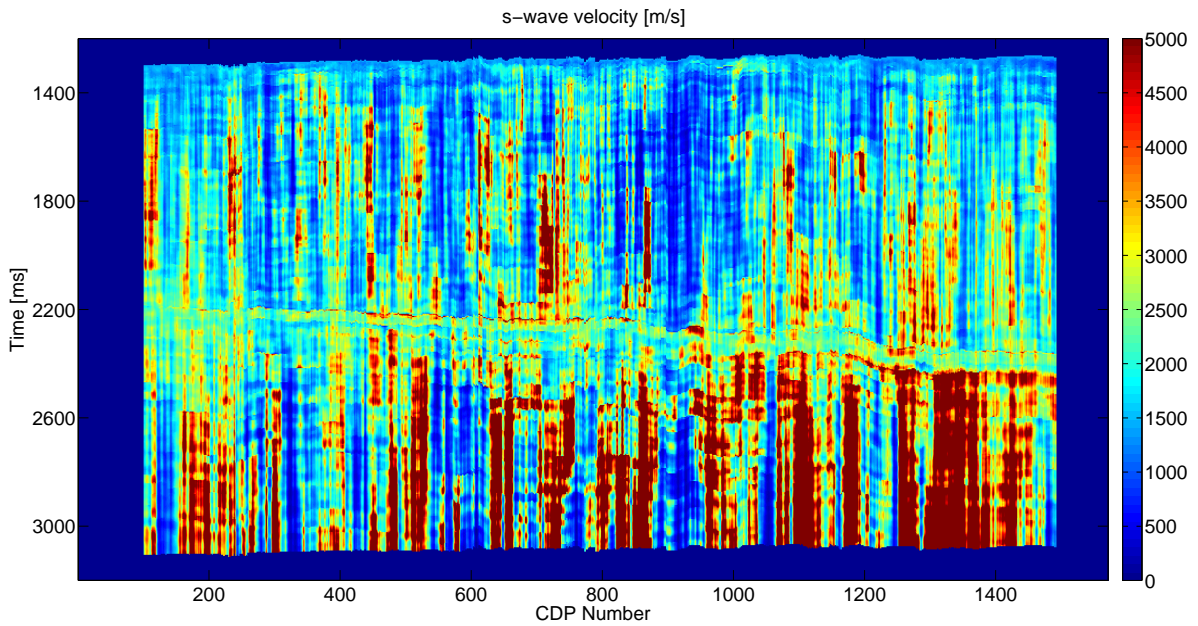


FIGURE 6.30: Reconstruction of the s -wave velocity from the two-stages algorithm [m/s]. The result is noisier than in the case of the p -wave velocity output.

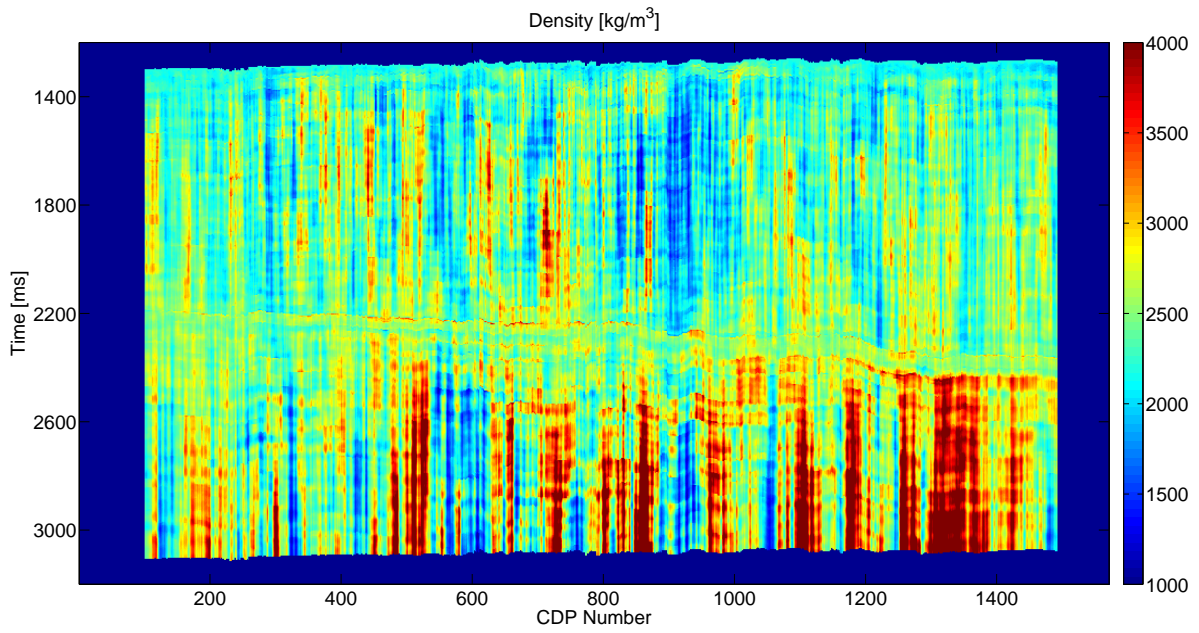


FIGURE 6.31: *Reconstruction of the bulk density from the two-stages algorithm [kg/m^3].*

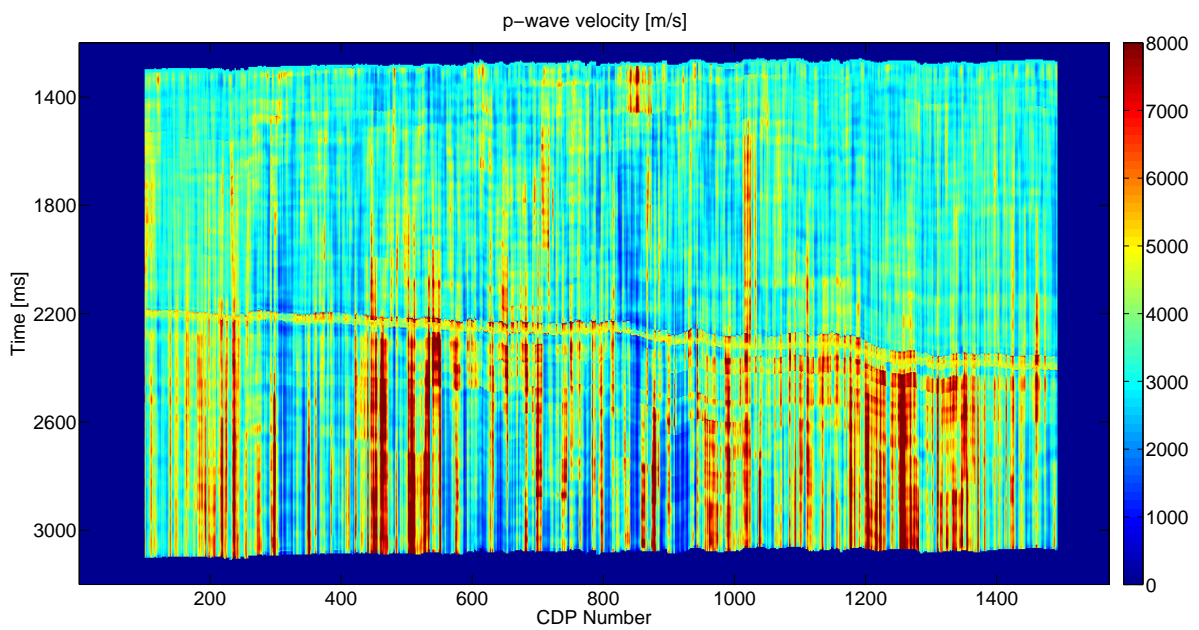


FIGURE 6.32: *Reconstruction of the p-wave velocity from the one-stage algorithm [m/s]. Artefacts due to the presence of the constraint around the main horizon are evident in the estimation.*

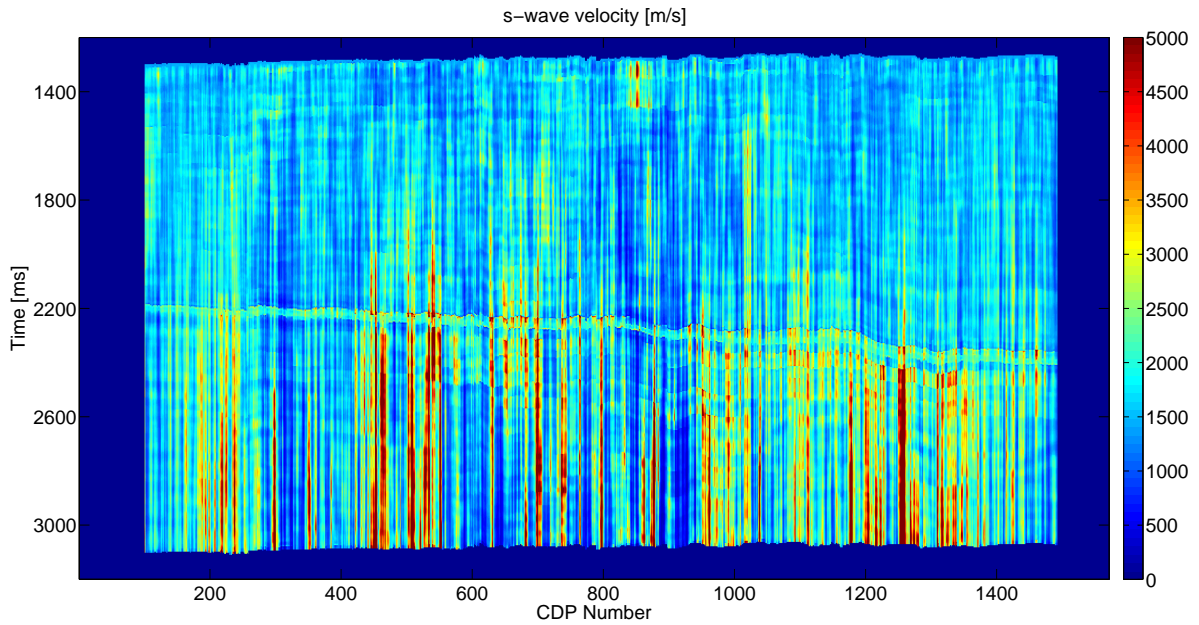


FIGURE 6.33: Reconstruction of the *s*-wave velocity from the one-stage algorithm [m/s]. Artefacts due to the presence of the constraint around the main horizon are evident in the estimation.

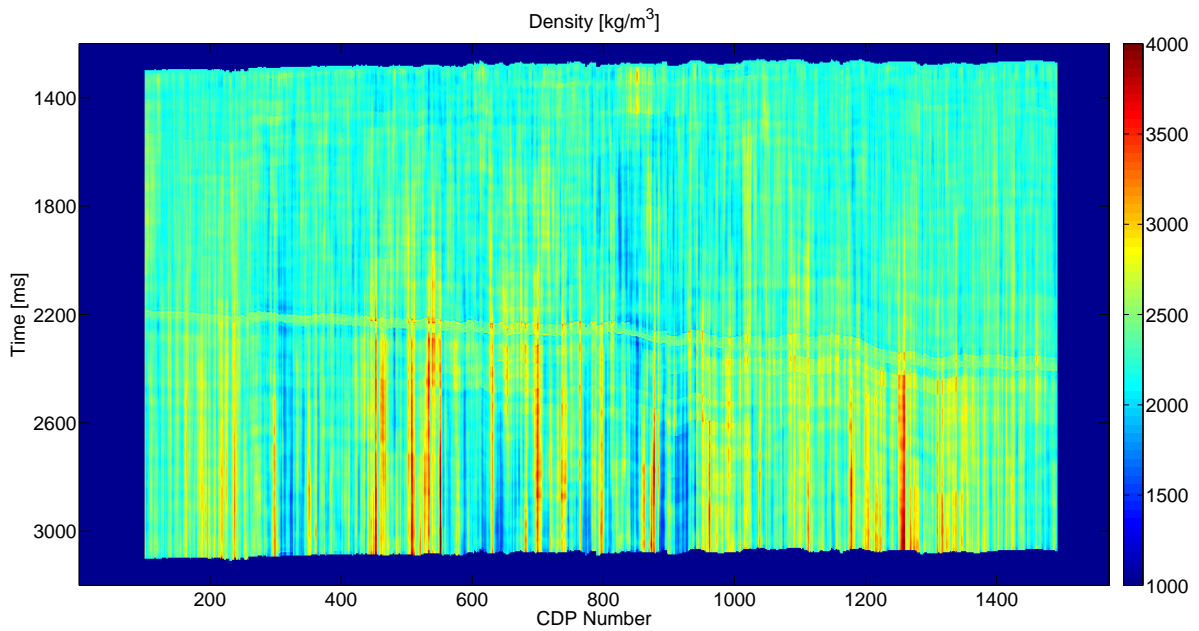


FIGURE 6.34: Reconstruction of the bulk density from the one-stage algorithm [kg/m³]. Artefacts due to the presence of the constraint around the main horizon are evident in the estimation.

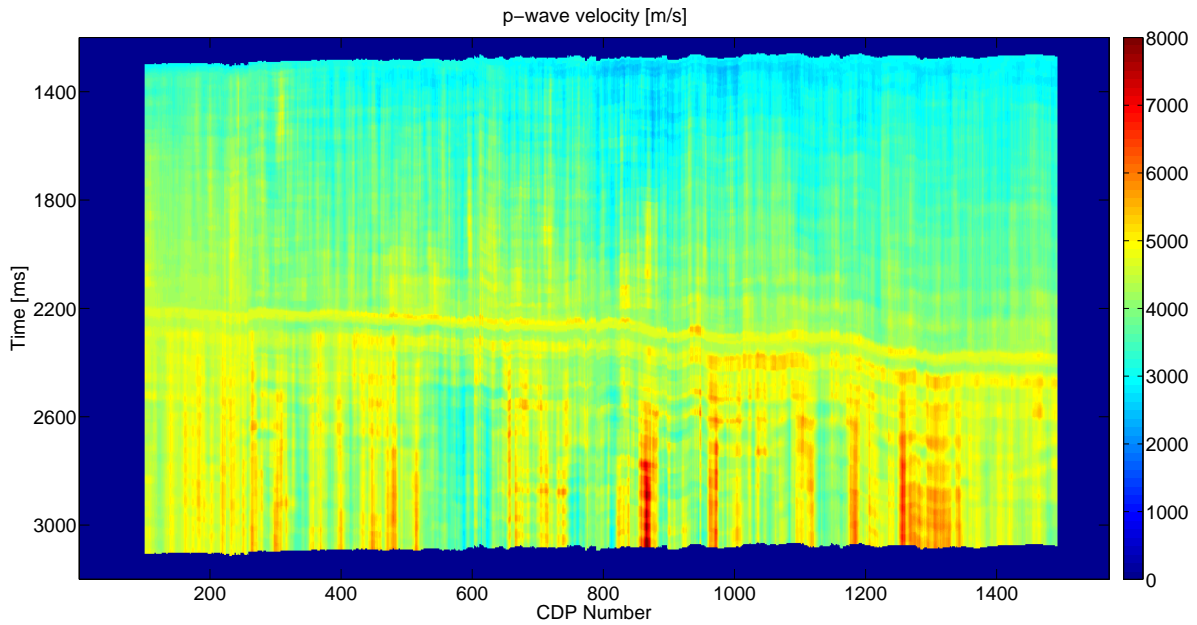


FIGURE 6.35: Reconstruction of the *p*-wave velocity from the sparse-spike method in time domain [m/s]. The background trend of the interval property is added by an additional term in the original Perez, Velis, and Sacchi (2017) formulation.

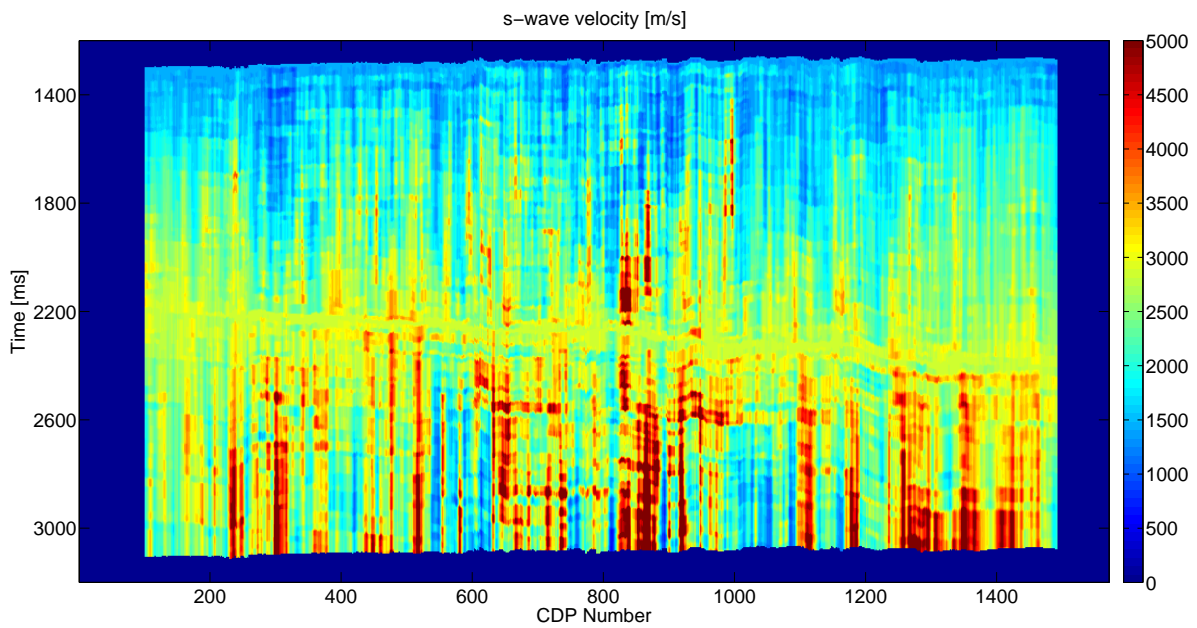


FIGURE 6.36: Reconstruction of the *s*-wave velocity from the sparse-spike method in time domain [m/s]. The background trend of the interval property is added by an additional term in the original Perez, Velis, and Sacchi (2017) formulation.

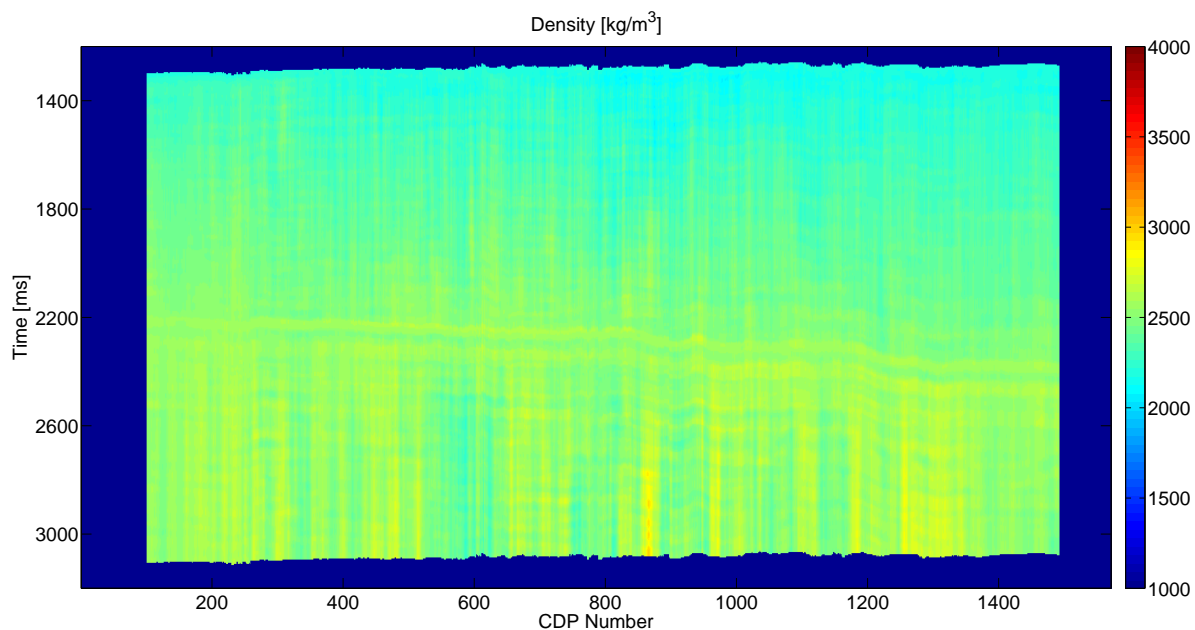


FIGURE 6.37: Reconstruction of the bulk density from the sparse-spike method in time domain [kg/m^3]. The background trend of the interval property is added by an additional term in the original Perez, Velis, and Sacchi (2017) formulation.

6.5 Discussion

The post-stack CARV inversion has not proven effective in singling out the absolute values of the AI at depth on the land dataset. This is well documented by the mistie at well location (Figure 6.26) and it might be caused by the large uncertainty related to the values of the interval velocity field derived from the stacking velocities, by the poor S/N of both the 2-D section and the Inline, and by the uncertainty associated with the AI value at a reference level. Nonetheless, the layers underneath the most evident event in the stacks at about 2400 ms TWT, have been characterized with a realistic lateral variation of the AI property both on the 2-D section (Figure 6.20) and on the Inline (Figure 6.25). Well log control is not effective to validate the inversion in this interval of depths, also because the same well was used to set an AI constraint at a nearby depth.

The pre-stack approach is even more speculative: Rock Physics relationships that are not necessarily met in the true subsurface, are included in the inversion process. The p-wave estimate of Figure 6.29 is similar, at least in the few hundred ms below the main event in the section, to the AI of Figure 6.25 which was obtained with the CARV approach. This result, together with the AI estimated in Figure 6.27 from the pre-stack data, support the ability of the two stages method to provide well-behaved solutions, while the one-stage workflow provides more unrealistic results, especially because it clearly shows only one layer of relatively uniform elastic properties underneath the main event. The pre-stack sparse-spike approach has proven to be very sensitive to the choice of the hyperparameters that govern the amount of sparsity and the amount of Rock Physics correlations into the elastic parameter estimation, and for this reason the significance of the estimates thus obtained appear more questionable. Overall, the inversion attempts made on the land dataset have been unsatisfactory, nonetheless subtle features of

potential interest have been highlighted by the proposed inversions, but they must be assessed with care if further knowledge on the area under investigation is available.

Chapter 7

Acoustic and Elastic Inversion on a Test Marine Dataset

7.1 Introduction

An Inline from a marine dataset offshore Nova Scotia has been studied for the purpose of testing the pre- and post-stack harmonic reconstruction methods that are described in Chapters 3 and 4. Data are pre-stack time migrated, and they refer to the Inline 1300, for a total of 481 cross-lines over the Penobscot prospect in the Scotian Continental Shelf. The sampling interval is 4 ms and seismic data are binned in a 12.5 m by 12.5 m grid, with nominal fold of 60, ranging from offset 175 m to 3175 m. Five interpreted horizons, including the seabed, are also available for constraining the inversion of the elastic parameters because of the presence of a nearby borehole with well log data. They are named Horizon A to Horizon E, with the last letter sorted by alphabetical order from shallow to deep events. Data are owned by the Nova Scotia Department of Energy. Data conditioned for AVA inversion have been obtained from <https://opendtect.org/osr/pmwiki.php/Main/PENOBSCOT3DSABLEISLAND> (last accessed on 03/05/2018) and they have been rotated to zero-phase and stacked in Figure 7.1. After data pre-conditioning which includes the estimation of an interval velocity field, post-stack results are presented both for the full section and for a target window that does not include the laterally heterogeneous seabed. The pre-stack inversion is then proposed on the target window, with a final discussion of the obtained results.

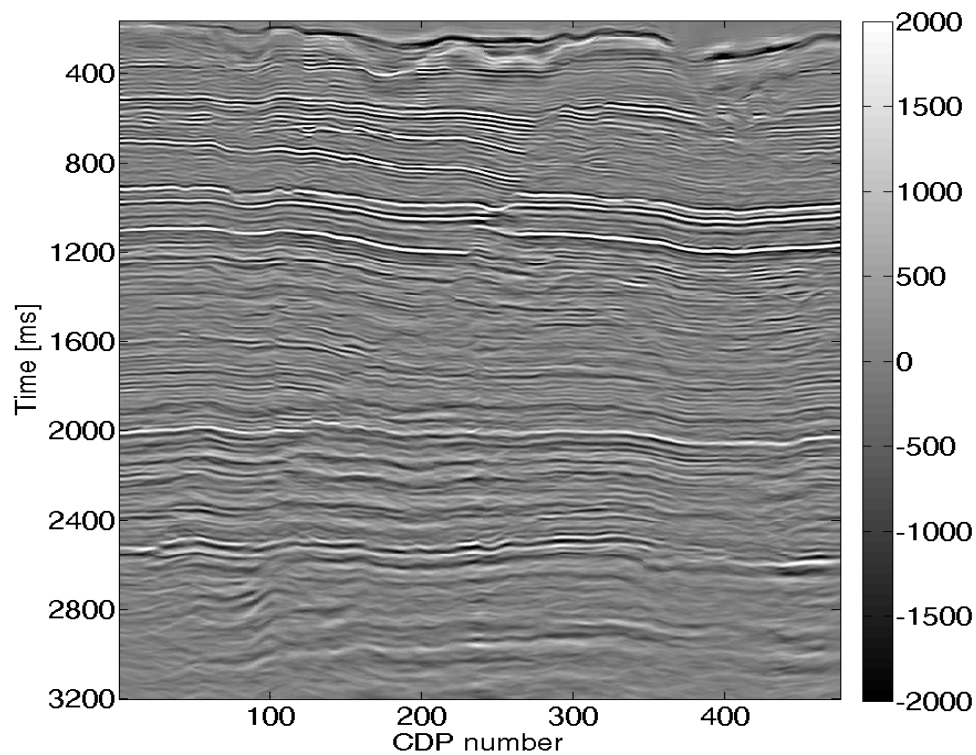


FIGURE 7.1: *Seismic section considered for elastic parameter inversion. Data available from the Nova Scotia department of Energy have been bulk-shifted by 90 degrees to obtain a zero-phase seismic dataset.*

The target window for the inversion, 1400 ms long below the Horizon C, is shown in Figure 7.2 between the solid blue curves. This window focuses on the effects of a fault zone in the sedimentary sequences of the basin.

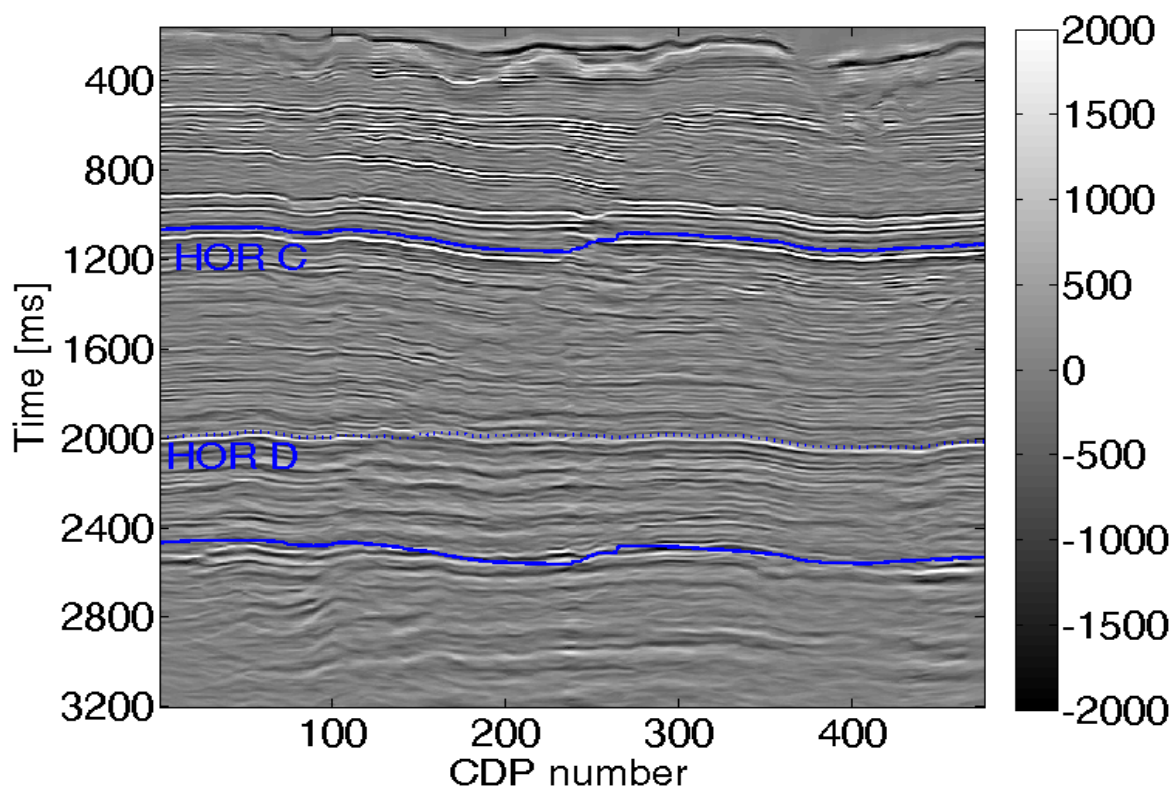


FIGURE 7.2: Seismic data presented in Figure 7.1 are overlaid with the Horizon C and Horizon D. The temporal window that spans 1400 ms below the interpreted Horizon C (down to the solid blue line deeper than 2400 ms) is used for testing both the post- and pre-stack seismic inversion methods discussed in the thesis.

A velocity field obtained from NMO analysis, has been adopted for mapping the pre-stack gathers from offset to incidence angle. The mapping has been achieved by assuming that the stacking velocity approximates the RMS velocity and by smoothing the Dix relationship (as per equation 4.4) to estimate the interval velocity (Figure 7.4). The stacking and the interval velocity fields are shown in Figures 7.3 and 7.4 within the temporal window displayed in Figure 7.2. Although the RMS and the interval velocity fields of Figure 7.3 and 7.4 are only shown within a temporal window, they are available from the seabed to the depth corresponding to 3200 ms TWT. Given the estimated interval velocity field of Figure 7.4, the aspect ratio of the seismic section of Figures 7.1 and 7.2 is close to be 1:1 in the deeper part, while the shallow part is more horizontally stretched.

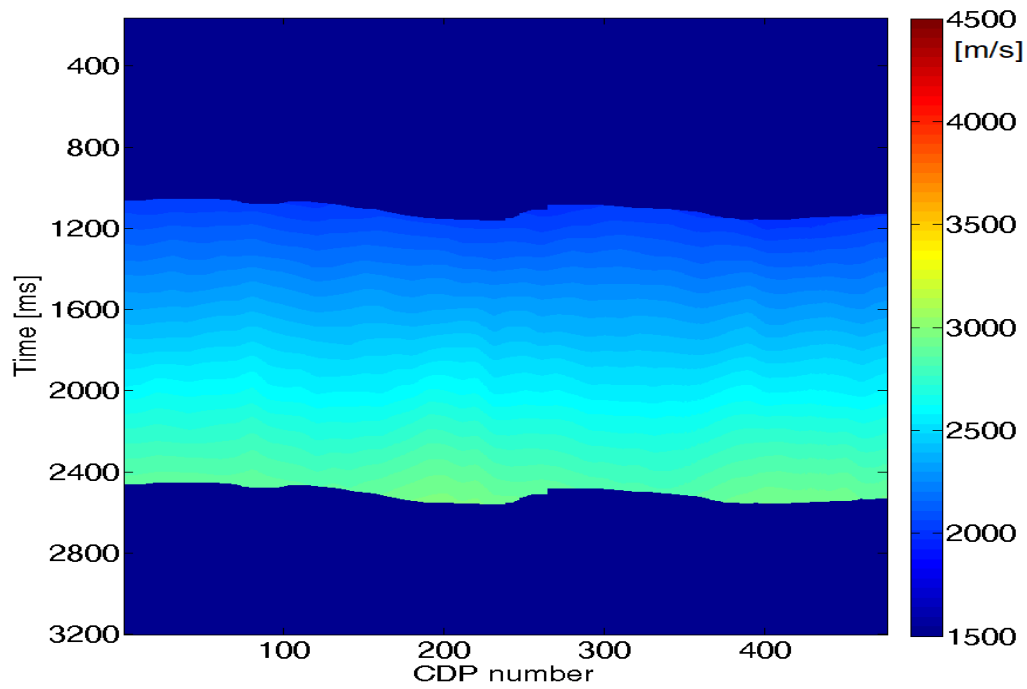


FIGURE 7.3: *Stacking Velocity field [m/s]. This velocity field is assumed to be an RMS velocity field for the subsequent analysis.*

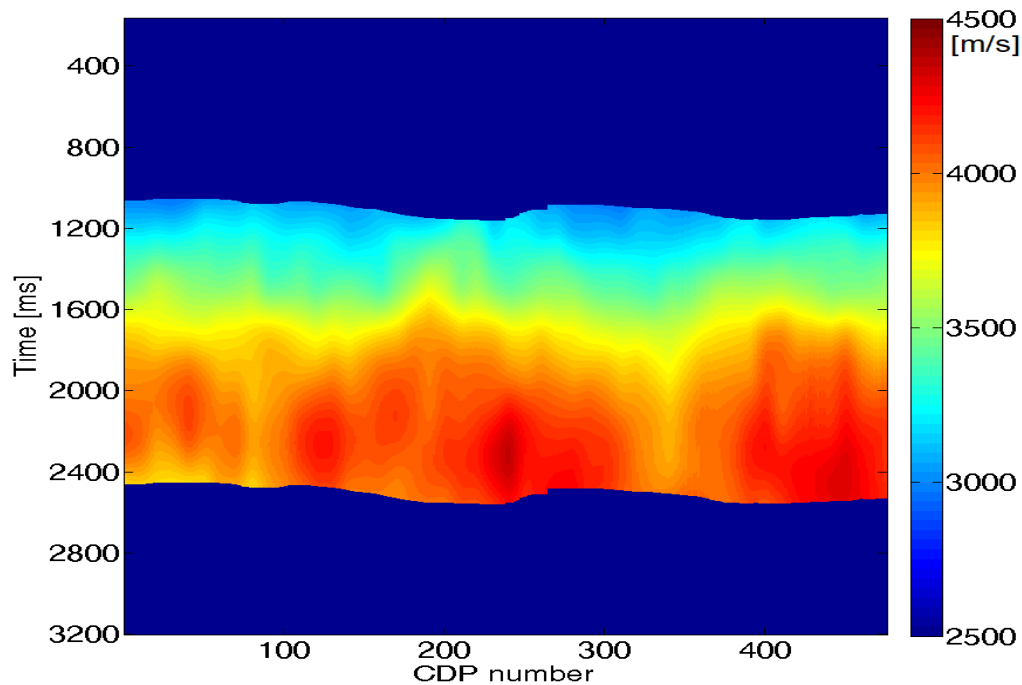


FIGURE 7.4: *Interval velocity field obtained from the stacking velocity [m/s] via equation 4.4.*

7.2 Post-stack inversion

The CARV inversion has been tested on the seismic data of Figure 7.1 which have been, in turn, obtained with a 6 to 33 degrees angle mute. To perform the inversion, a order 80 AR model has been fitted to the bandwidth 7-55 Hz, where the S/N is higher. The reference AI has been set to $1.5 \cdot 10^6$ rayl in the water layer. Two constraints on AI have been set at the depths corresponding to Horizon C ($5 \pm 1 \cdot 10^6$ rayl) and Horizon D ($8 \pm 1.5 \cdot 10^6$ rayl). The hyperparameter that weights the velocity field of Figure 7.4 in the AR solution is set to 0.3 the ratio between the maximum eigenvalue of the matrix \mathbf{G} and $\mathbf{L}^H \mathbf{L}$ in the cost function 3.13.

A laterally smoothed estimated of AI is presented in Figure 7.6. To obtain such estimate, the hyperparameter μ that governs the degree of lateral smoothing has been set to 0.2 in the cost function 3.20. The main difference between the smoothed and the non-smoothed estimate is evident in sedimentary sequences shallower than the Horizon C. In both cases, the AI estimates are strongly influenced by vertical stripes that prevent a geologic interpretation of the AI sections above the Horizon C event.

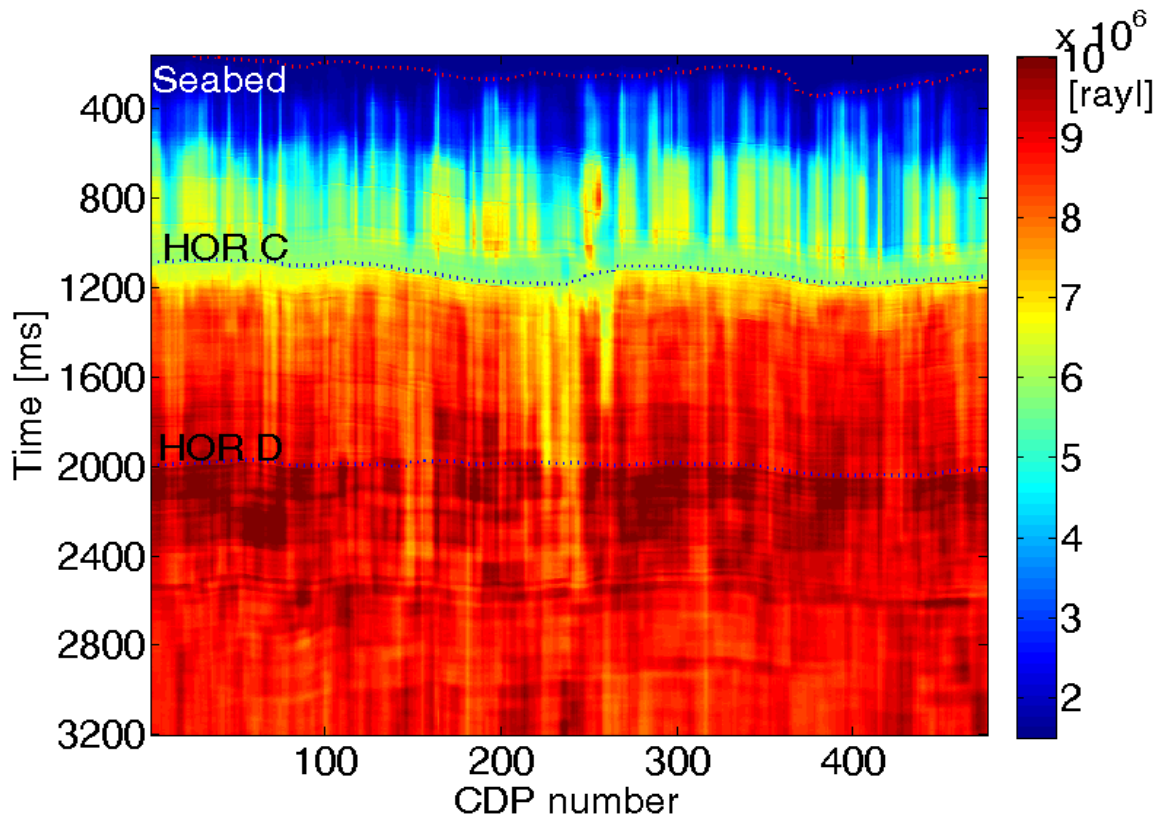


FIGURE 7.5: AI [rayl] estimated from post-stack seismic data via the CARV approach described in Chapter 3.

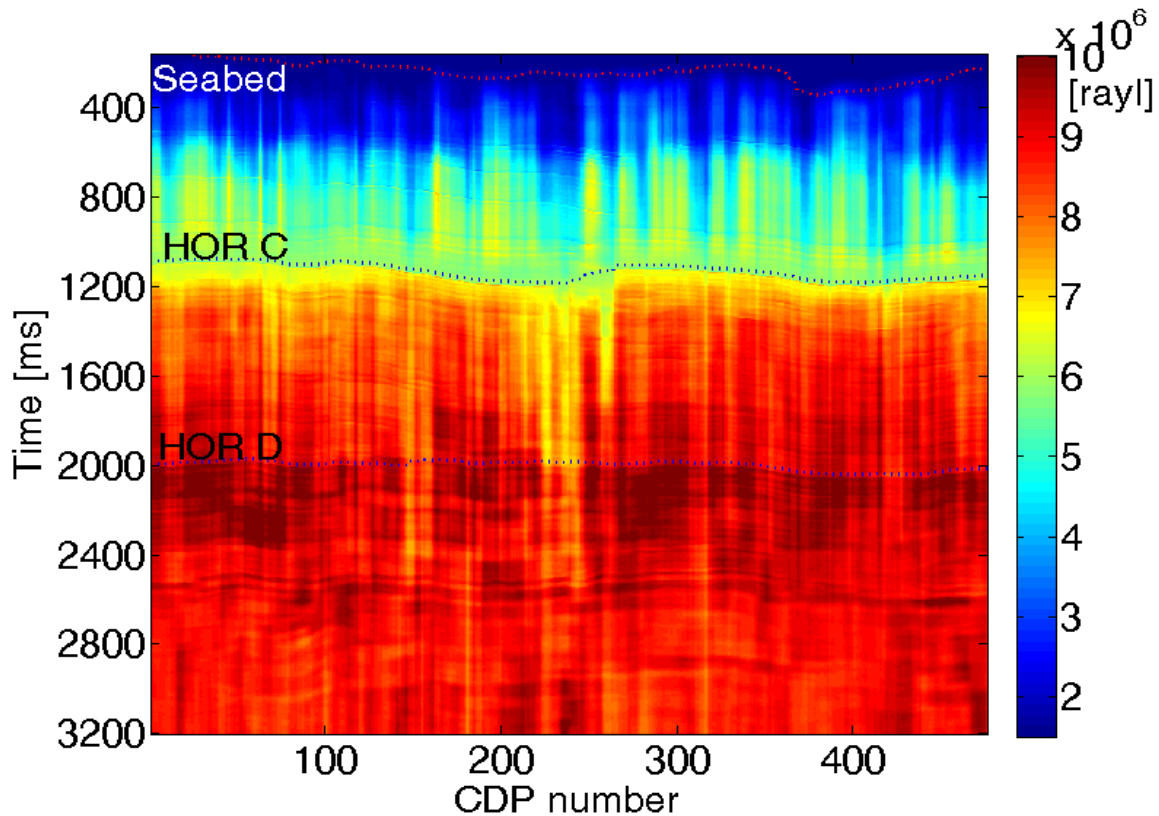


FIGURE 7.6: AI [rayl] estimated from post-stack seismic data via the CARV approach described in Chapter 3, in which the lateral continuity of the estimate has been enforced (see section 3.3.6).

The CARV AI inversion is further proposed on the temporal window highlighted by the solid blue curves in Figure 7.2. In this case, the reference AI is no longer the water layer, but a stronger assumption about the mechanical properties of the levels above the Horizon C has been made: the AI of the sample corresponding to the picked Horizon C is assumed to be $6 \cdot 10^6$ rayl across the section. This test was made to compare the results of the post-stack inversion to the results of the pre-stack inversion, which could only be performed in the range of depths where a sufficient number of ray-paths with different illumination geometry investigate the same subsurface location. In this case, the effects of the fault area between CDP 200 and 300 is more clear because of the overburden artefacts are removed from the inversion. The effects of the fault on the inversion of Figure 7.7 are evident: the poor illumination of the flanks of the fault generates an unreliable CARV AI estimate at depth. The presence of two clear events in the seismic section of Figure 7.2, one corresponding to the Horizon C and one corresponding to Horizon D, is clearly evidenced in the AI inversion of Figure 7.7. Both Horizons are identified as a “hard event”, generating an increase of AI with depth. This piece of information is partially influenced by the a priori constraints set for the inversion. More interestingly, Figure 7.7 points out the possible presence of a hard layer until about 150 ms below the Horizon D, with a generalized decrease of AI below it (black arrows point to this coherent feature of the AI inversion where no constraints at depth have been set).

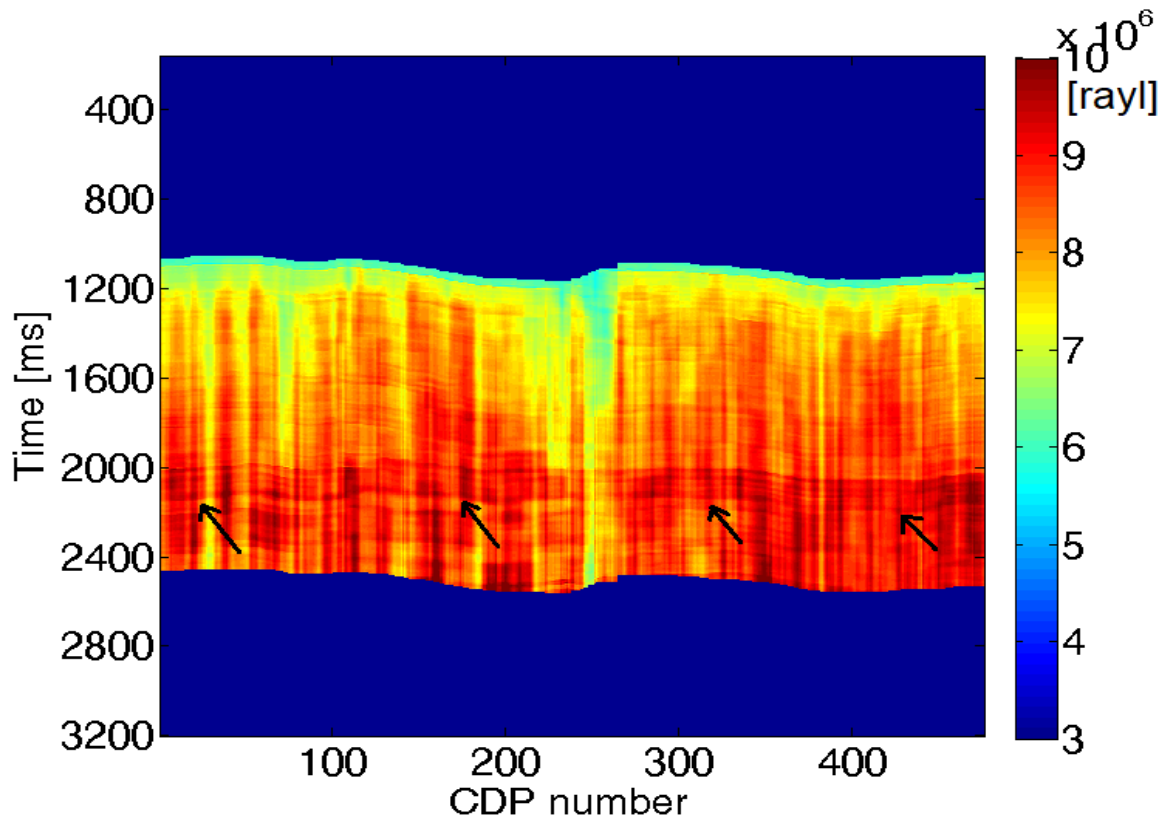


FIGURE 7.7: AI [rayl] estimated from post-stack seismic data via the CARV approach described in Chapter 3 in the time window of Figure 7.2.

7.3 Pre-stack inversion

The same inline used for post-stack estimation of AI has been considered for testing the pre-stack reconstruction of the low-frequency components of the reflectivity. I used the weighted stack approach (see section 4.2.3) to sort the pre-stack CIG from offset to incidence angle. The reconstruction has been performed via the AR modelling (two-stages work-flow) for the purpose of estimating the elastic parameters (α , β , ρ) and the elastic impedance in the range 6° - 33° . I perform the inversion for the temporal window highlighted by the blue solid lines in Figure 7.2. I assumed the EI of the first inverted sample to be constant throughout the line and equal to $6 \cdot 10^6$ rayl. One constraint on elastic parameters has been provided 20 ms below the Horizon D, following the indications coming from the log data of the nearby well B-41 ($\alpha = 4000$ m/s, $\beta = 1500$ m/s, $\rho = 2400$ kg/m³). No velocity-related regularisation term has been considered. The EI inversion, sampled at the incidence angles of 6° , 18° , and 30° is proposed in Figures 7.8, 7.9, and 7.10 respectively. It is worth noting the decay in seismic amplitude with incidence angle, that produces an EI estimate at 30° smoother than at 6° . A hard layer below the Horizon D event is still visible on EI, and no anomaly of potential relevance is evident at far angles.

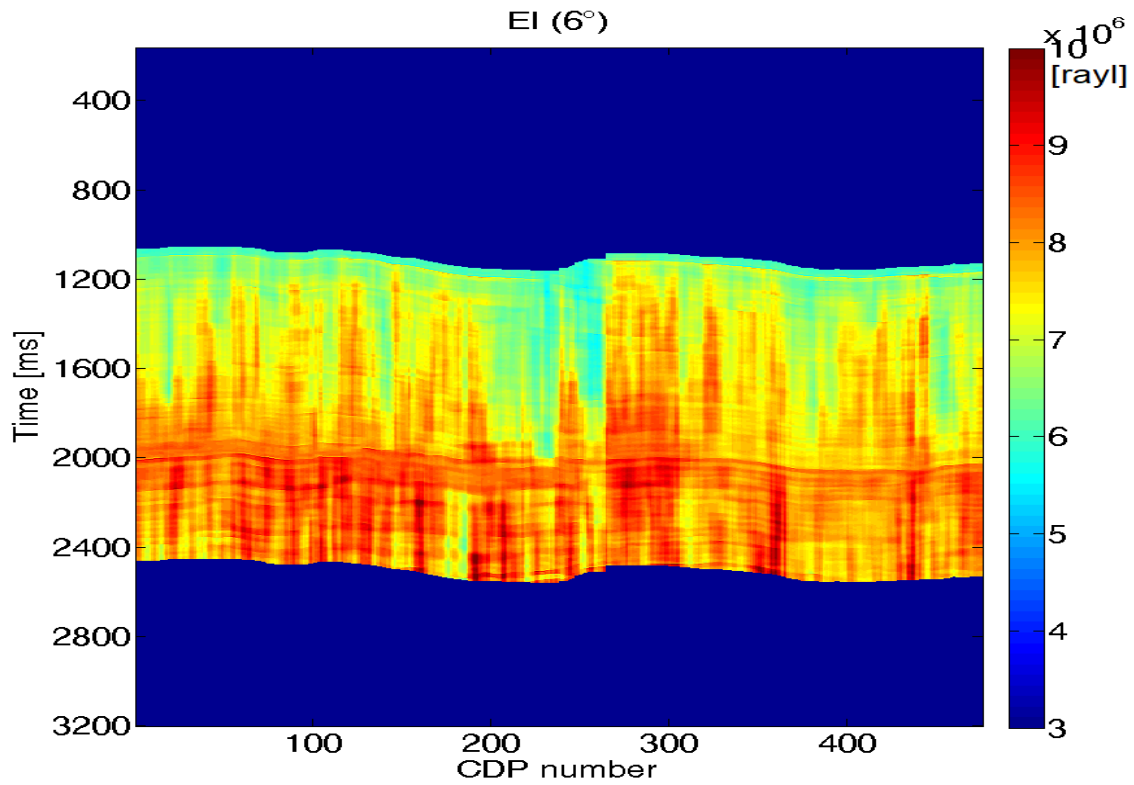


FIGURE 7.8: Estimated Elastic Impedance [rayl] at incidence angle of 6 degrees.

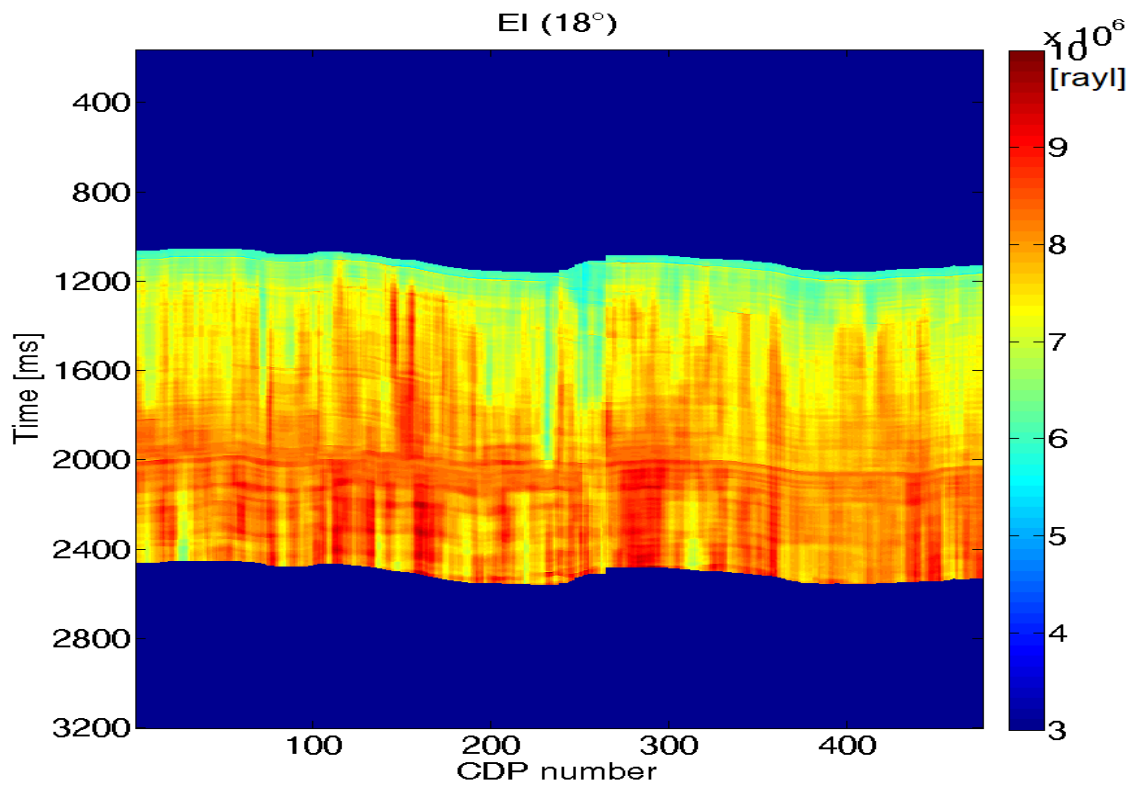


FIGURE 7.9: Estimated Elastic Impedance [rayl] at incidence angle of 18 degrees.

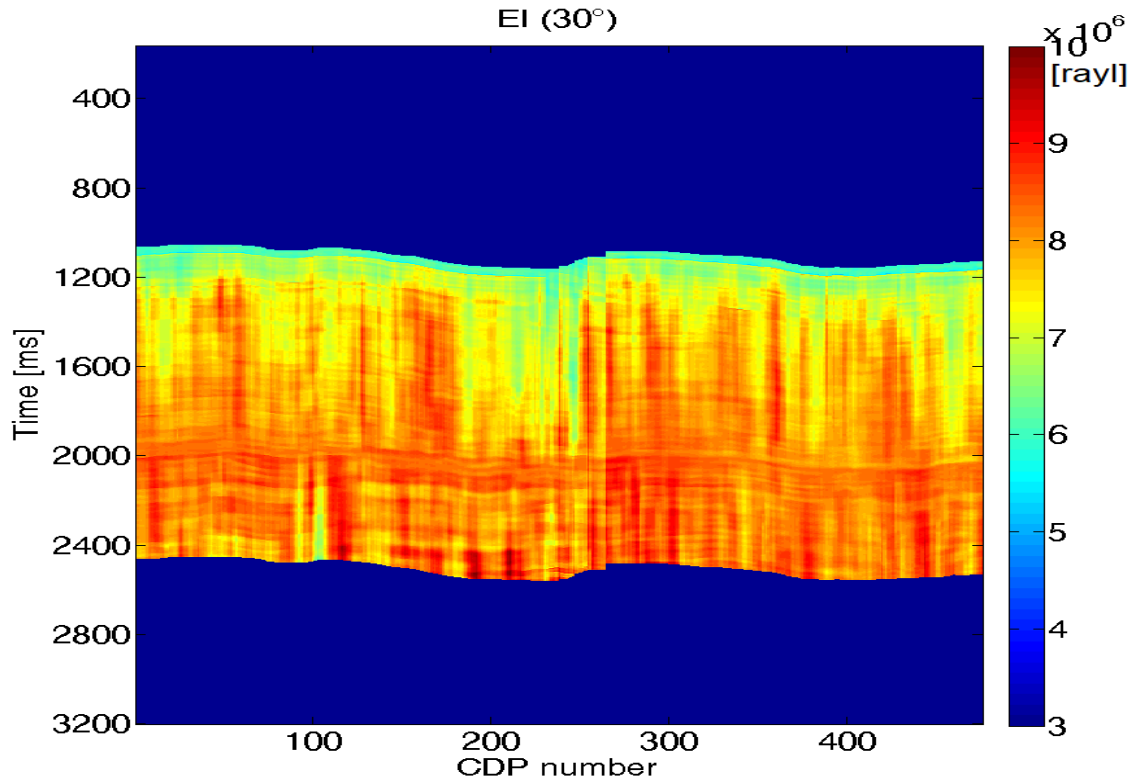


FIGURE 7.10: Estimated Elastic Impedance [rayl] at incidence angle of 30 degrees.

Once the reflectivity (and the derived EI) is reconstructed at each incidence angle, any set of elastic properties could be extracted as long as a stable mapping is obtained by properly regularizing the Aki Richards equation 4.10 (see Chapter 5 for more details on the regularization strategy). I made the choice of correlating the density and p-wave velocity field, and the p- and s-wave velocity field as described in equation 4.15, with λ^2 equal to 0.1 times the ratio of the maximum eigenvalues of the matrix $\mathbf{C}^t\mathbf{C}$ and the matrix $\mathcal{F}_{LM}^{-1}\mathbf{P}^t\mathbf{P}\mathcal{F}_{LM}^{-1t}$ and μ^2 equal to 0.05 times the ratio of the maximum eigenvalues of the matrix $\mathbf{C}^t\mathbf{C}$ and the matrix $\mathcal{F}_{LM}^{-1t}\mathbf{Q}^t\mathbf{Q}\mathcal{F}_{LM}^{-1}$. The results thus obtained are presented in terms of p-wave velocity, s-wave velocity and bulk density in Figures 7.12, 7.13, and 7.14 respectively. The combination of the p-wave velocity and bulk density is also presented in terms of AI in Figure 7.11. This result, that does not include the information coming from the interval velocity field, is comparable to the post-stack result of Figure 7.7, which, on the contrary, does not account for the effects of non-normal incidence ray-paths. The main difference between the two results is the absolute value of the estimated AI while the structural character of two inversions is similar.

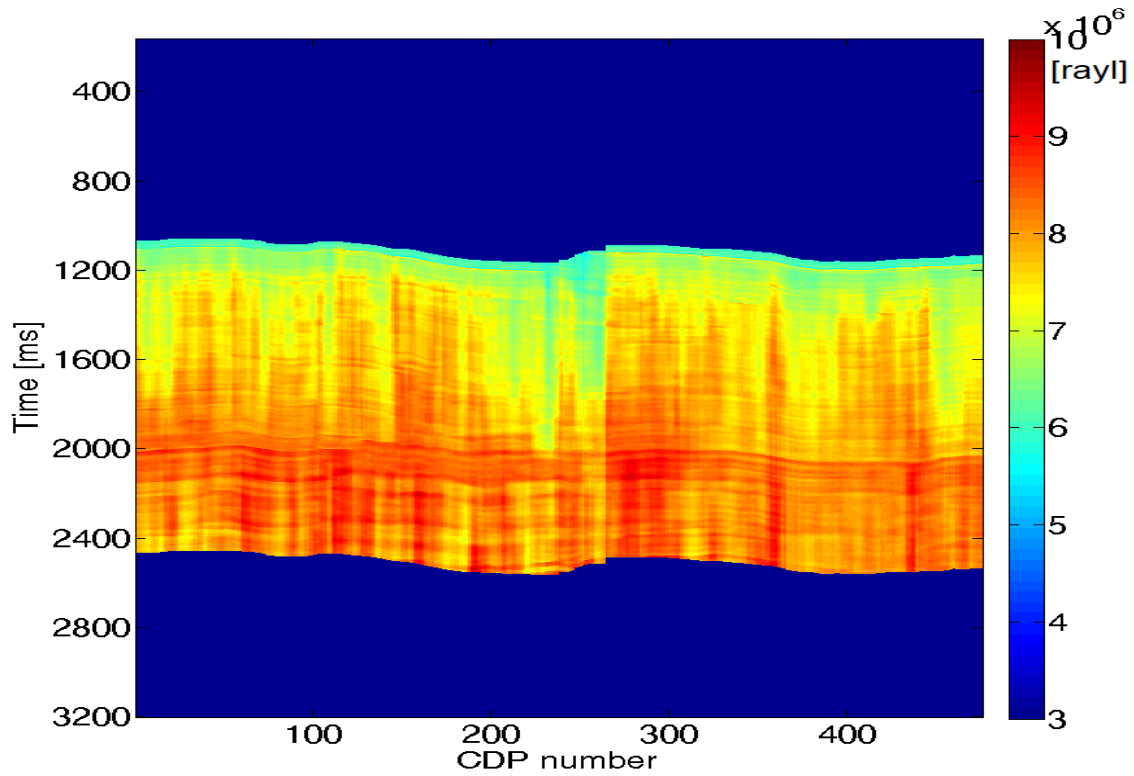


FIGURE 7.11: Estimated AI from AVA intercept [rayl]. The estimate proposed here could be compared with the post-stack estimate presented in Figure 7.7

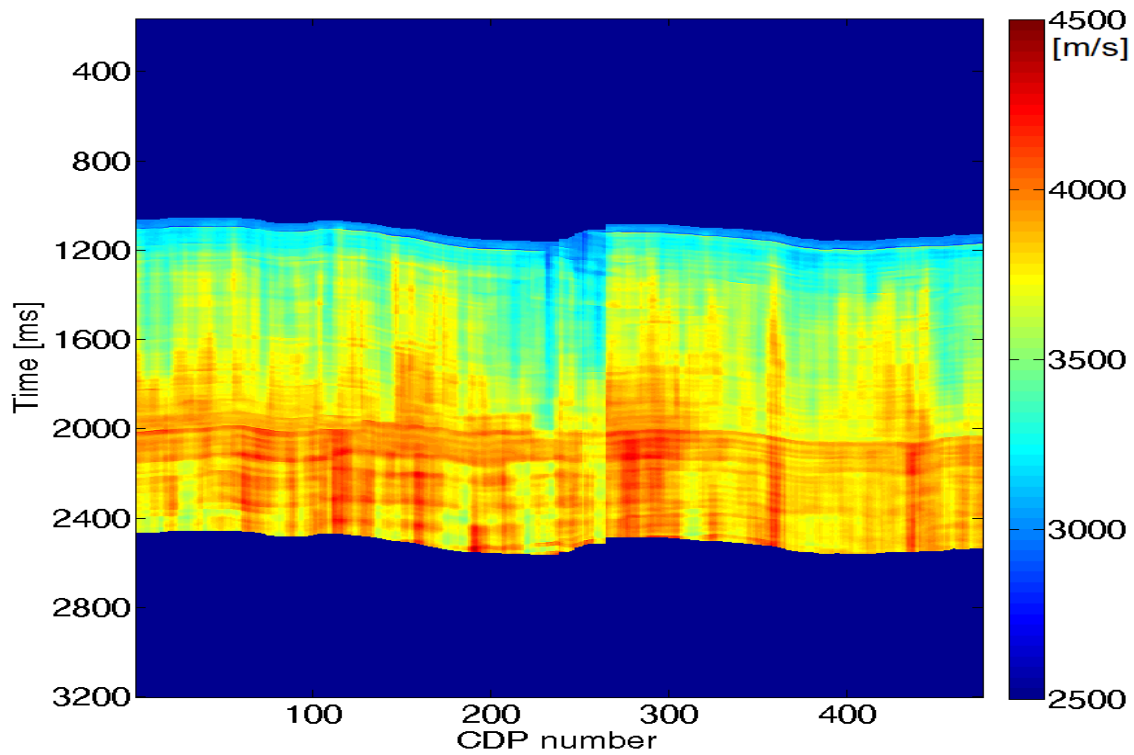
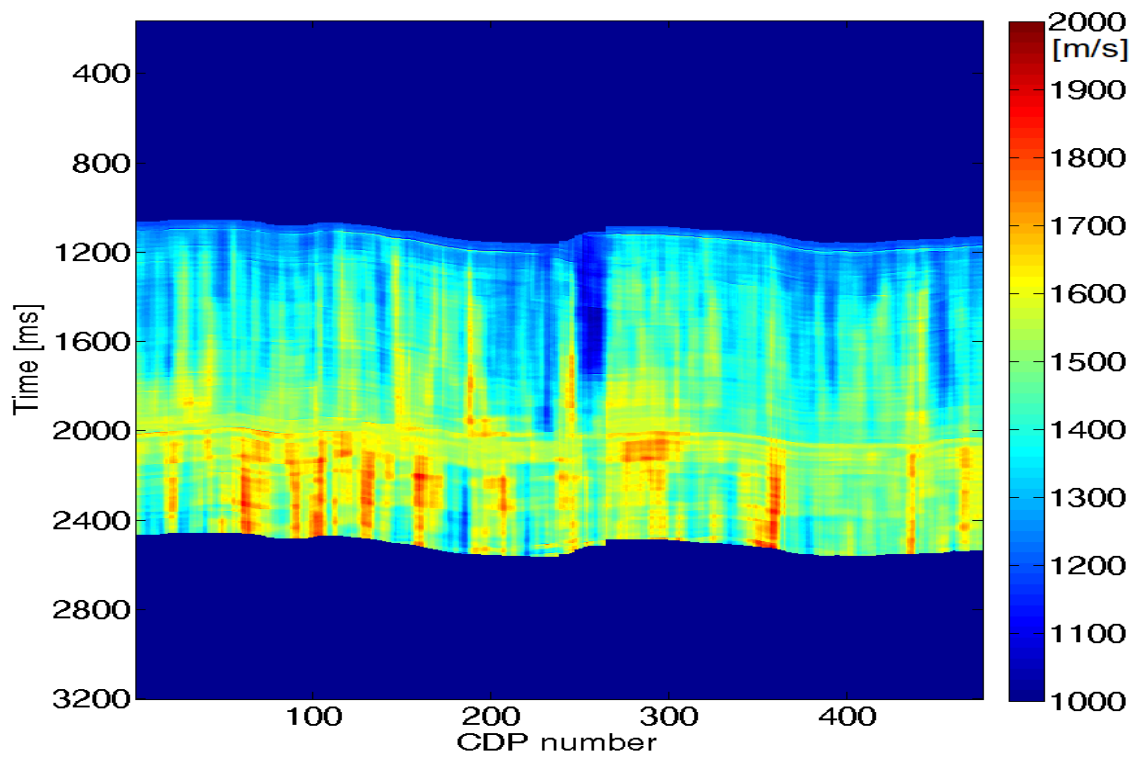
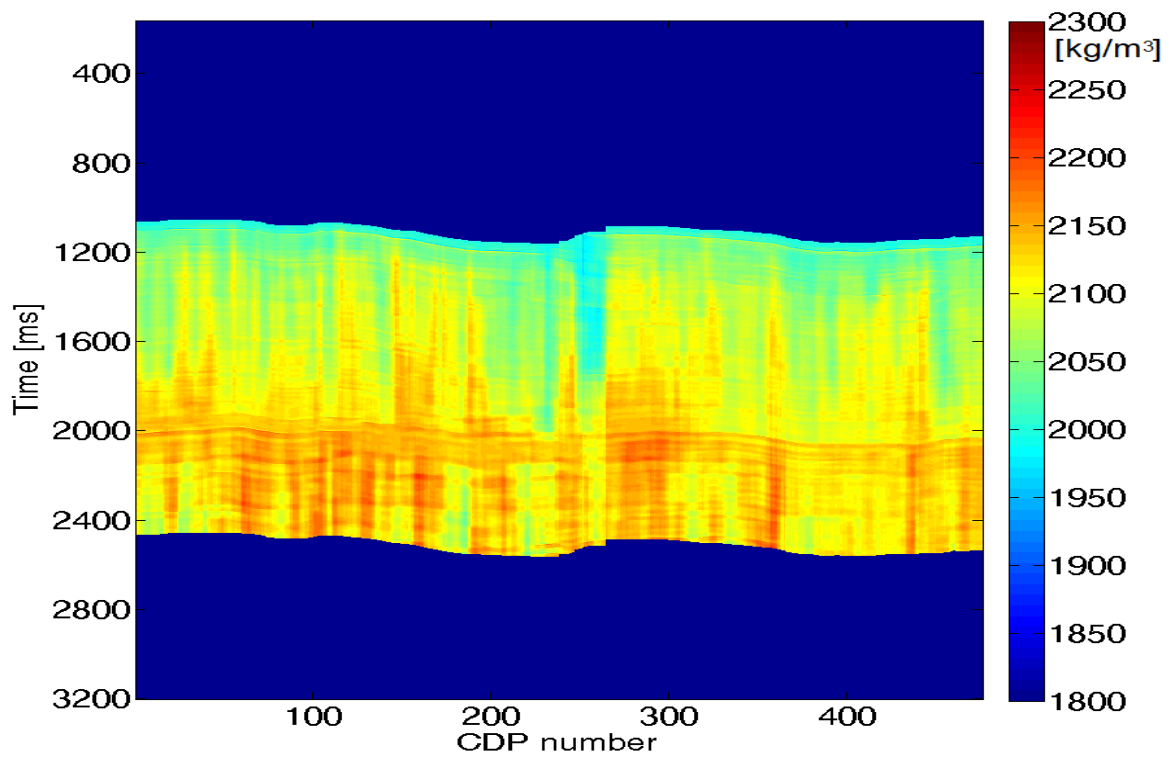


FIGURE 7.12: Estimated p-wave velocity [m/s] from the two-stages workflow.

FIGURE 7.13: Estimated *s*-wave velocity [m/s] from the two-stages workflow.FIGURE 7.14: Estimated bulk density [kg/m^3] from the two-stages workflow.

7.4 Discussion

The marine seismic data from the Penobscot area show a very consistent trace-to-trace amplitude on the target Horizon C and Horizon D events. Nonetheless, the shallow part of the survey shows an alternation of bright and dimmed patches. This is clearly documented by Figure 7.15, where a comparison between the envelope of the seismic amplitudes across the section for a time-window of 40 ms around the seabed and the Horizon C is shown. The seismic event identified as Horizon C is much more continuous than the seabed, and it only interrupts at about CDP 250 because of the presence of a fault.

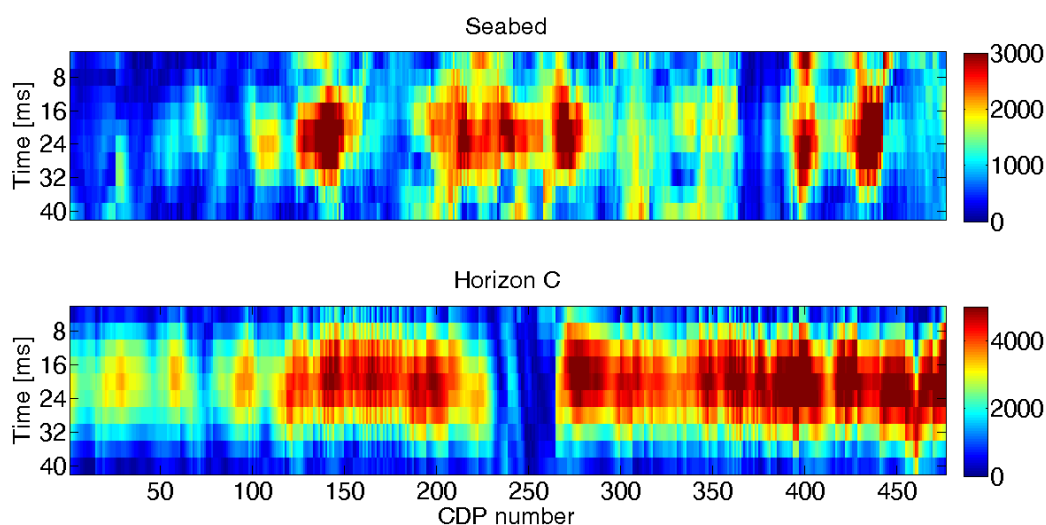


FIGURE 7.15: *Envelope of the 40 ms seismic window across the seabed (top panel) and the Horizon C (bottom panel). Amplitudes of Horizon C are much more continuous (except on the faulting zone) than amplitudes of the seabed.*

Due to the amplitude issues evidenced in the shallow part of the seismic section, the AI inversion of Figures 7.5 and 7.6 appear less realistic than the following inversion results, which do not take into account the effects of the shallow marine sediments. The price to pay in this case, is the bias introduced by the arbitrary choice of a constant value for the elastic properties at about the depths corresponding to Horizon C. In fact, the absolute values of the inversion results of Figure 7.7 and of all the pre-stack inversion results are accurate as much as the reference value for the recursive inversion is accurate. This scenario is similar to the scenario of a land dataset inversion. The presence of the fault at about CDP 200 to CDP 300 is particularly evident in the p-wave velocity, s-wave velocity, and bulk density estimates of Figures 7.12, 7.13, and 7.14 because of the missing “hard event” on the Horizon C at those locations. The post-stack AI estimate of Figure 7.7 is fairly consistent with the pre-stack AI estimation of Figure 7.11, even though the latter shows slightly lower AI values. The difference could be ascribed to the role of a possibly incorrect interval velocity field regularization term in the post-stack solution, but also to a possibly incorrect Rock Physics regularisation term in the three-terms pre-stack AVA solution. Overall, the results presented in this Chapter show the potentialities of both the pre- and post-stack methodologies to highlight features of possible geologic interest, but they also warn on the data quality that is required to obtain significant results via a recursive inversion. Not all the marine dataset appear suitable for a quantitative CARV inversion, especially in the

presence of faults and steeply dipping events. As far as it concerns the pre-stack recursive methods on the Penobscot test dataset, interesting features at about the stronger events appear in the estimates, but no definitive validation is reached.

Chapter 8

Sparsity-based Inversion of Ground Penetrating Radar Data

8.1 Introduction

Ground Penetrating Radar (GPR) is a non-invasive exploration method that aims at investigating the electromagnetic (EM) properties of the subsurface. In the context of this thesis, I only highlight the few details of the method required for setting the context for GPR amplitude inversion. More detailed description of the method can be found for instance in Jol (2009) or Daniels (1996). The aim of this Chapter is to extend the methods developed for seismic data reconstruction and inversion to GPR data. After a brief introduction to the GPR method, two sparsity-based workflows for bandwidth extension are theoretically described. The application of the workflows on a GPR section requires data pre-conditioning, which is presented before the discussion on the inversion results.

GPR data are typically acquired by means of two antennas, one being a source of an electromagnetic-controlled pulse and the other being used to record the reflected energy. For most of the applications and as far as it concern this thesis, single fold small offset GPR traces are considered. Despite the fact that electromagnetic and seismic data show some similarities (they are both digital records of a wave-field recorded near the surface in which pulses -events- may be singled out), there are relevant differences between the two methods. The amount of scattered energy is generally higher for GPR data (Jol, 2009), directionality is much pronounced (Davis and Annan, 1989) and the bandwidth is much narrower (in terms of octaves within -6dB from the peak amplitude) for radar than in the seismic case. The electromagnetic wave absorption is governed by electrical conductivity of the materials investigated. In most of the cases, GPR wave absorption is much stronger than seismic wave absorption for each oscillation cycle. For low conductivity materials and in absence of ferromagnetic minerals, intrinsic attenuation as well as dispersion become negligible, penetration increases, and interfaces between materials of different dielectric properties may be singled out from GPR data. Further details about the physical similarities and differences between GPR and reflection seismic data can be found for instance in the classical work of Ursin (1983).

If conductivity can be neglected and the magnetic permittivity can be approximated to the free-space magnetic permittivity, given that the GPR bandwidth is well below the relaxation frequency, electromagnetic impedance is only related to the variation of dielectric permittivity ($\epsilon(t)$). In this case, a reconstruction in reflectivity domain $r(t)$ can be biunivocally related to a

reconstruction in permittivity domain. For vertically incident EM wave:

$$r(t) = \frac{\sqrt{\epsilon(t+1)} - \sqrt{\epsilon(t)}}{\sqrt{\epsilon(t+1)} + \sqrt{\epsilon(t)}}. \quad (8.1)$$

Under the above mentioned assumptions the velocity of the electromagnetic wave can be further estimated by

$$v(t) = \frac{c\sqrt{\epsilon_0}}{\sqrt{\epsilon(t)}} \quad (8.2)$$

where ϵ_0 represents the vacuum permittivity and c represents the speed of an electromagnetic wave in vacuum. This results in a relationship between GPR reflectivity and the propagation velocity:

$$v(t) = \frac{c(t)\sqrt{\epsilon_0}}{\sqrt{\epsilon(t_0)e^{4\sum_{u=0}^t r(u)}}}. \quad (8.3)$$

Once the permittivity of the first layer is assumed to be known, the equation 8.3 allows to recursively obtain an estimate of the propagation velocity at increasing depths.

8.2 Work-flow for GPR Data Inversion

Two different work-flows for GPR data inversion have been analysed:

1. A minimum L1-norm reflectivity reconstruction with impedance constraints at depth
2. A layer-stripping minimum L1-norm reflectivity reconstruction on selected horizons

They both assume that the amplitudes of recorded data can be deterministically related to the subsurface interface properties in terms of variation of dielectric constant between two homogeneous isotropic layers. This assumption has strongly been questioned due to source and receiver coupling, scattered energy, illumination issues, poor S/N (i.e. Jazayeri, Ebrahimi, and Kruse (2017)). The results of the inversion algorithms are analysed in light of these issues in the Discussion section. The amplitude inversion algorithms reconstruct the trace in reflectivity domain and then summation across interfaces allows to obtain the interval properties in terms of electromagnetic impedance or velocity.

The minimum L1 norm reflectivity work-flow represents a modification of the Gholami and Sacchi (2012) algorithm, which was originally developed for the reconstruction of seismic reflection data. It enforces sparsity of reflectivity by assuming the presence of a limited number of homogeneous layers in the subsurface and the knowledge of a stationary wavelet, and it allows to include a weight in the inversion problem to account for the misfit on impedance constraints at depth. Lateral continuity of the reconstructed reflectivity can also be enhanced, nevertheless the recursive nature of the amplitude inversion approach leads to increasing uncertainty in the velocity estimation at depth.

While Gholami and Sacchi (2012) iteratively estimate reflectivity and wavelet, we assume the latter to be known a priori. This assumption is not stringent provided that the method is limited to weak dispersion cases and the outgoing wavelet is measured. The minimum L1/L2 norm

solution can be obtained by minimising the cost function:

$$J = \|\mathbf{W}\mathbf{r} - \mathbf{d}\|_2^2 + \lambda^2 \|\mathbf{r}\|_1^1 \quad (8.4)$$

where \mathbf{W} is the convolution matrix of the wavelet coefficients, \mathbf{r} represents the reflectivity, \mathbf{d} the recorded data and λ^2 the hyperparameter that weights the sparsity of the solution. The cost function 8.4 can be further amended to include a term related to the misfit of impedance constraints at depth and a term related to the lateral continuity of the reflectivity reconstruction. This leads to a cost function of kind

$$J = \|\mathbf{W}\mathbf{r} - \mathbf{d}\|_2^2 + \mu^2 \|\mathbf{K}\mathbf{r} - \mathbf{c}\|_2^2 + \nu^2 \|\mathbf{r} - \mathbf{r}_0\|_2^2 + \lambda^2 \|\mathbf{r}\|_1^1. \quad (8.5)$$

In equation 8.5 \mathbf{K} represents the integration operator that transforms reflectivity into impedance up to the arrival time of the constraint at depth, the value of which is indicated by the vector \mathbf{c} . The relative weight of the constraints at depth relatively to the data misfit is adjusted by the hyperparameter μ^2 . Lateral continuity is accounted for by the term $\nu^2 \|\mathbf{r} - \mathbf{r}_0\|_2^2$, where \mathbf{r}_0 represents the reconstruction on adjacent traces and the weight of this term is determined by the hyperparameter ν^2 .

In order to obtain more sensible estimates of velocity at depth, a second work-flow with a layer stripping approach has been devised. This workflow requires additional a priori information, more specifically an interpretation of the horizons on the GPR profile. Once those horizons have been picked, a windowing function mutes the parts of the traces that are sufficiently far from each pick. This muting corresponds to neglecting all the intra-layer information in terms of EM property variation. The minimum L1 norm solution, as described above, is obtained for the muted dataset. The mean value of the velocity obtained after the first layer boundary is kept as reference velocity for a new reflectivity reconstruction pass in which the first interface is stripped off the data. The lateral mean aims at stabilising the solution at depth, at the expenses of losing resolution on the lateral variation of velocity. The following layer-stripping pass estimates the third layer impedance, then the second horizon is removed and the process continues until the deepest interpreted horizon.

8.3 Case study: Boulder Clay Glacier

A GPR dataset was acquired in November 2017 to gain information about the Boulder Clay Glacier, which lies few kilometers from the Mario Zucchelli Italian base in Antarctica. GPR traces were acquired by Emanuele Forte by means of Malå Geoscience ProEx GPR system with 250 MHz nominal peak frequency. Trace interval is 10 cm and time sampling is 0.399 ns for a total trace length of 400 ns. A portion consisting of 2501 GPR traces has been singled out from line 4734 to study the feasibility of the amplitude inversion for velocity field reconstruction.

A direct wave has been registered by the antenna pairs. The acquisition device is the same as detailed by Dossi, Forte, and Pipan (2018) where an estimation of the reference amplitude at 1 meter ($A_0 = 136518[1/m]$) is provided for the direction of the maximum intensity and the

decay function

$$A(r) = \frac{A_0}{1+r} + B \quad (8.6)$$

This value (A_0) remains valid for all the family of functions of parameter p of the kind:

$$A(r) = \frac{A_0}{1+r^p}. \quad (8.7)$$

Equation 8.7 describes a power decay with distance (r) and it neglects the contribution of B . The goal of the exponent p is to account not only for spherical divergence, but also for transmission losses, scattering and absorption within the travel path. It is therefore sensible to consider p slightly larger than 1. A statistical analysis on the input data has been carried out to estimate sensible values for p . The findings are presented in Figure 8.1. The standard deviation of the samples across traces has been analysed by letting the parameter p vary from 1 to 2.25. After outlier removal, $p = 2$ is the value that shows the smallest trend of the resulting standard deviation of the data amplitude with depth (see Figure 8.1). Therefore, a gain recovery with $p = 2$ has been applied in what follows.

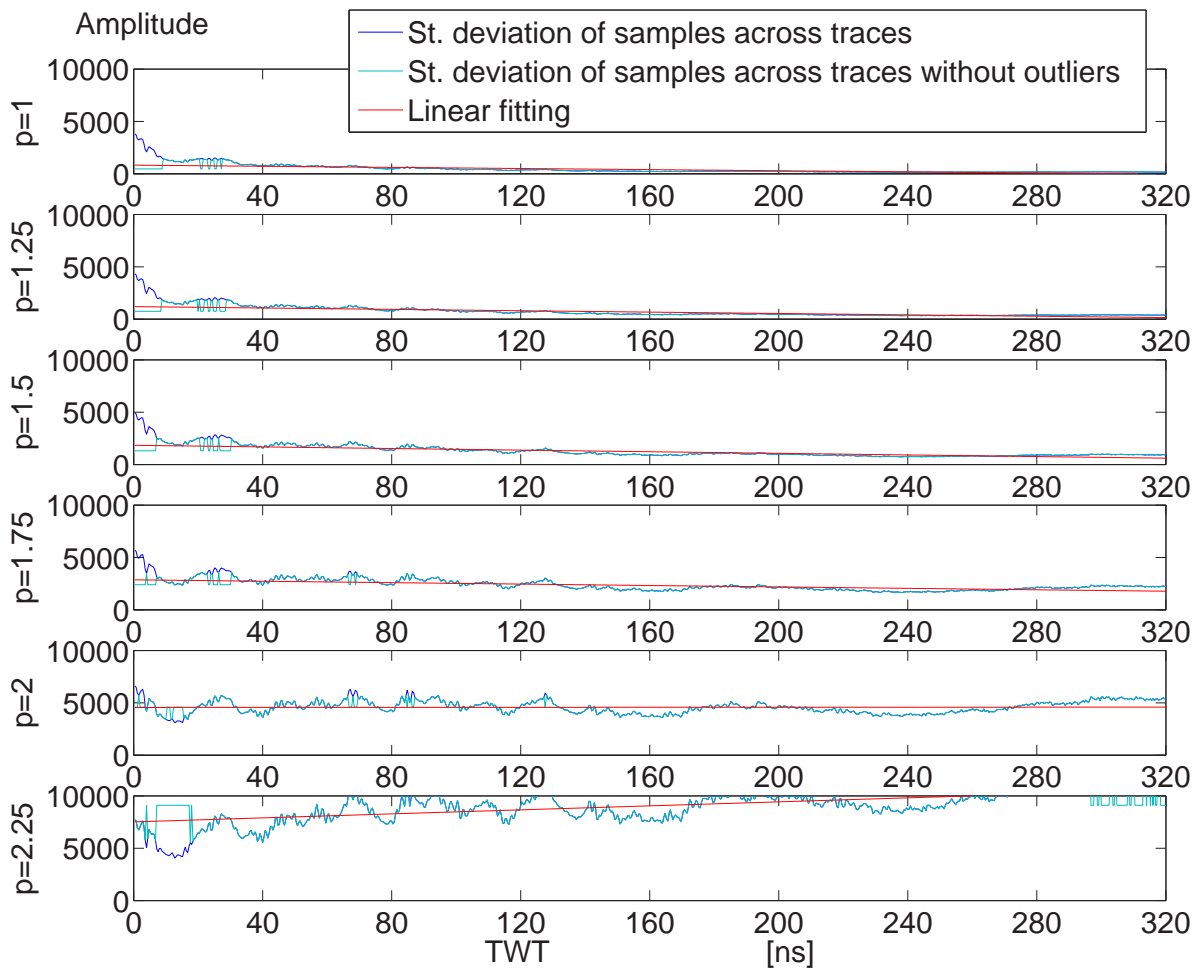


FIGURE 8.1: Standard deviation measure of GPR mean amplitudes as function of travel-time for different gain functions. A linear fitting (red line) has been superimposed on each panel to the blue curve corresponding to the standard deviation of the trace amplitudes for each time sample. The fourth panel ($p=2$) shows the best balancing in terms of amplitudes between the shallowest and the deepest part of the trace.

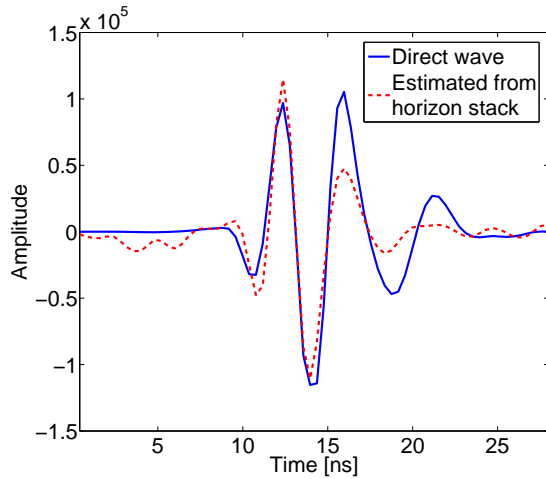


FIGURE 8.2: Wavelet estimation. Direct wave recorded from the GPR instrument in blue. Wavelet extracted from snow-firn horizon-stack in red dots. A certain degree of dispersion is evident in the tail of the dotted wavelet. The Amplitude is displayed for source to receiver distance equal to 1 m, in other terms the peak amplitude is A_0 from equation 8.6.

The recorded direct wave is shown in Figure 8.2 and the input dataset is shown before (Figure 8.3) and after (Figure 8.4) gain recovery. Some additional processing steps have been carried out by means of Matlab routines which have been modified from Sacchi and SAIG (*SeismicLab*) under the GNU v.3.0 license. High amplitude vertical stripes are evident in the shallow (Figure 8.4) and have been tackled with a mild f-x interpolation (Soubaras (2005)) in the frequency range 200-360 MHz that removes all the frequency components of linear events whose energy is 5 times the median energy of a window consisting of 240 time samples and 40 traces. A Singular Spectrum Analysis (SSA) in frequency domain (see for reference Oropeza and Sacchi (2011)) on the f-x interpolation output has been applied to the frequency-domain

representation of overlapping windows (41x41 samples). 10 principal components have been kept. Lastly, a time variant low-pass filter has been applied below 160 ns with 10 ns transition. The cut-off frequency for this filter has been set to 500 MHz.

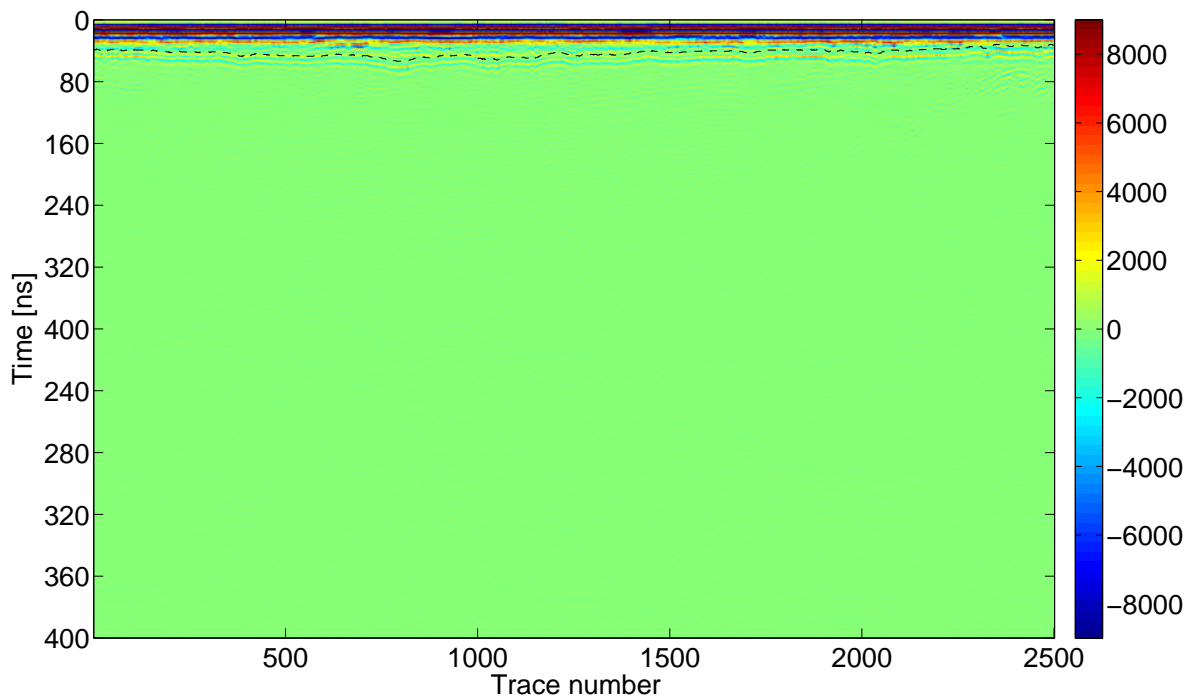


FIGURE 8.3: Raw data after Dewow and an Ormsby bandpass filter (zero phase, cut-off frequencies: 100 - 800 MHz). The dashed black line indicates the start of the target region and corresponds to 9 samples before the arrival time of one of interpreted horizons, presumably corresponding to the snow-firn discontinuity. All the processing that follows focuses on the 320 ns below the dashed line.

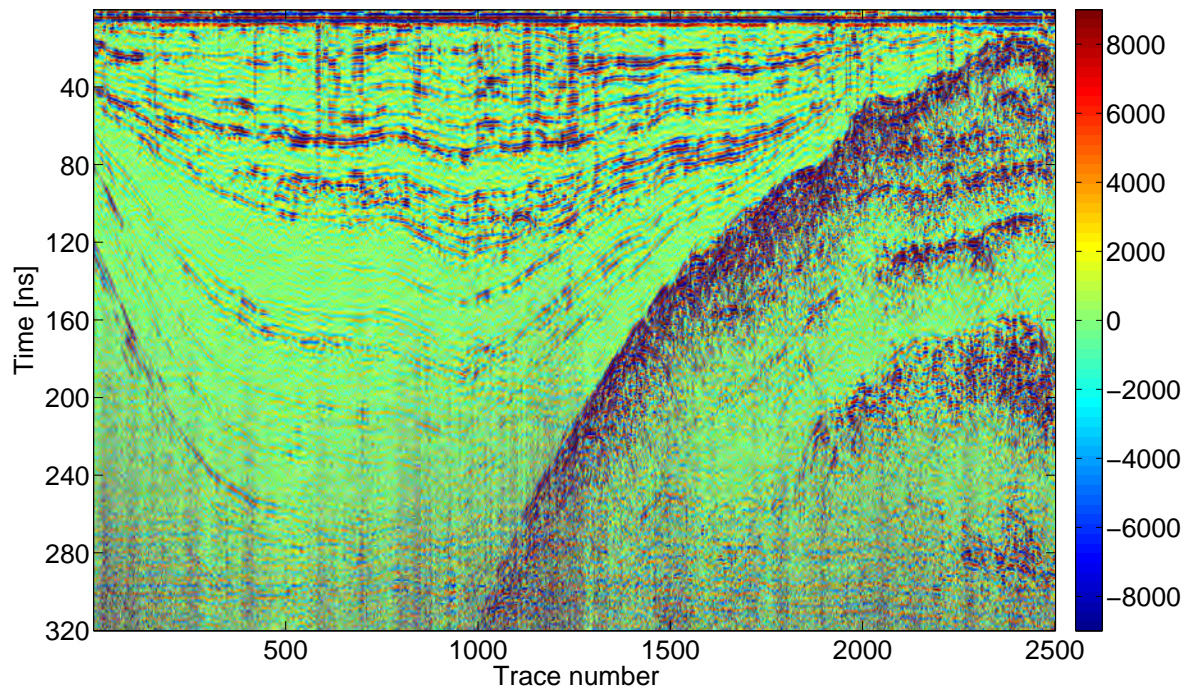


FIGURE 8.4: GPR section after divergence gain recovery with $p=2$. Data window shows the 320 ms below what has been interpreted as snow-firn interface.

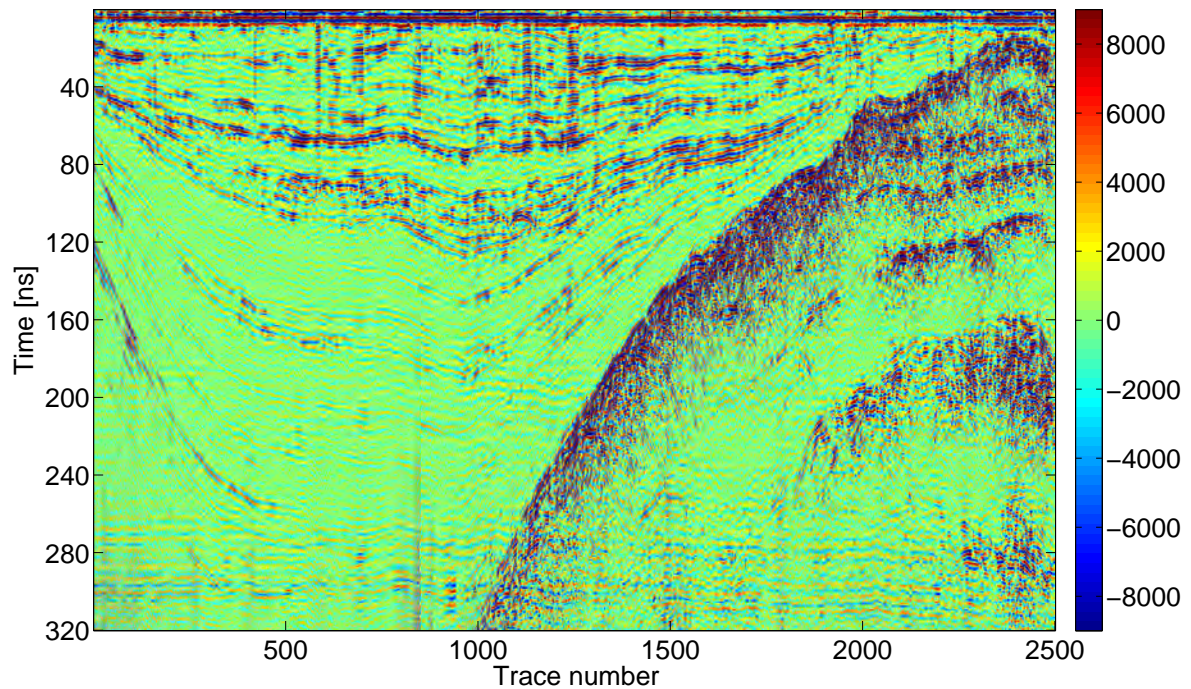


FIGURE 8.5: GPR section after one pass of f - x interpolation, an overlapping-window SSA that selects 10 principal components out of 41, and a time variant low-pass filter (500 MHz) which is active from 160 ns down to the end of the trace (10 ns transition).

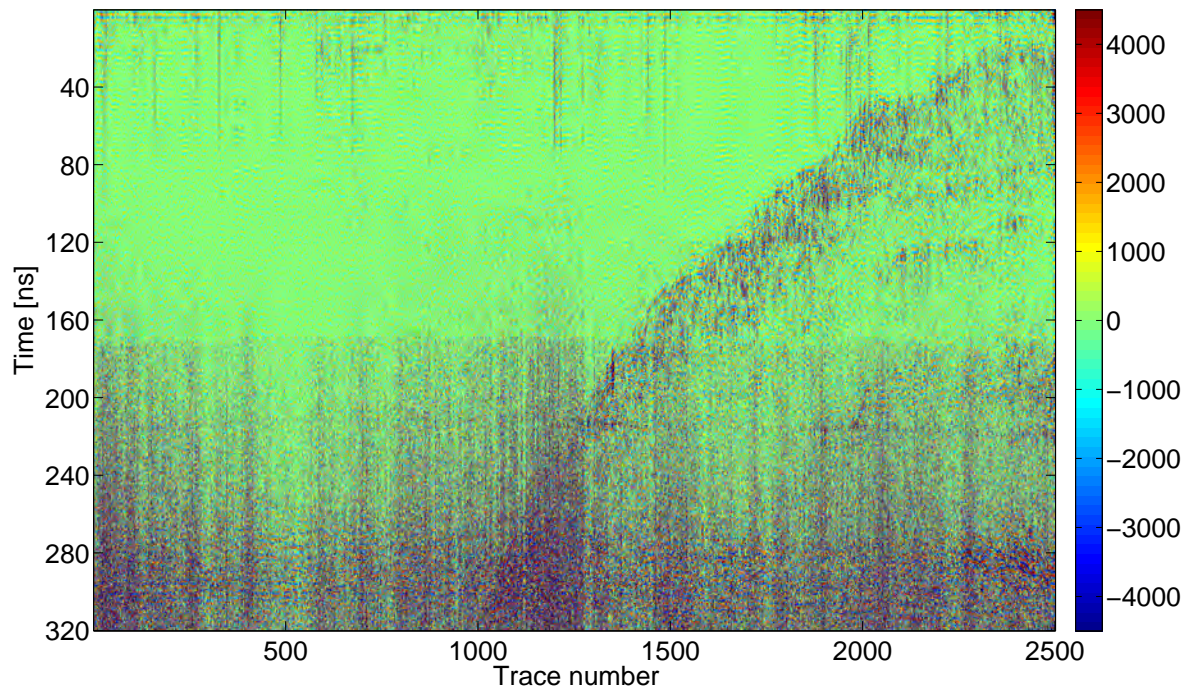


FIGURE 8.6: Difference (+6dB) between Figure 8.4 and 8.5: some damage is highlighted on the scattered contact between ice and the moraine on the right, which is of no interest for the inversion. Minor leakage on the first reflector (0-10 ns).

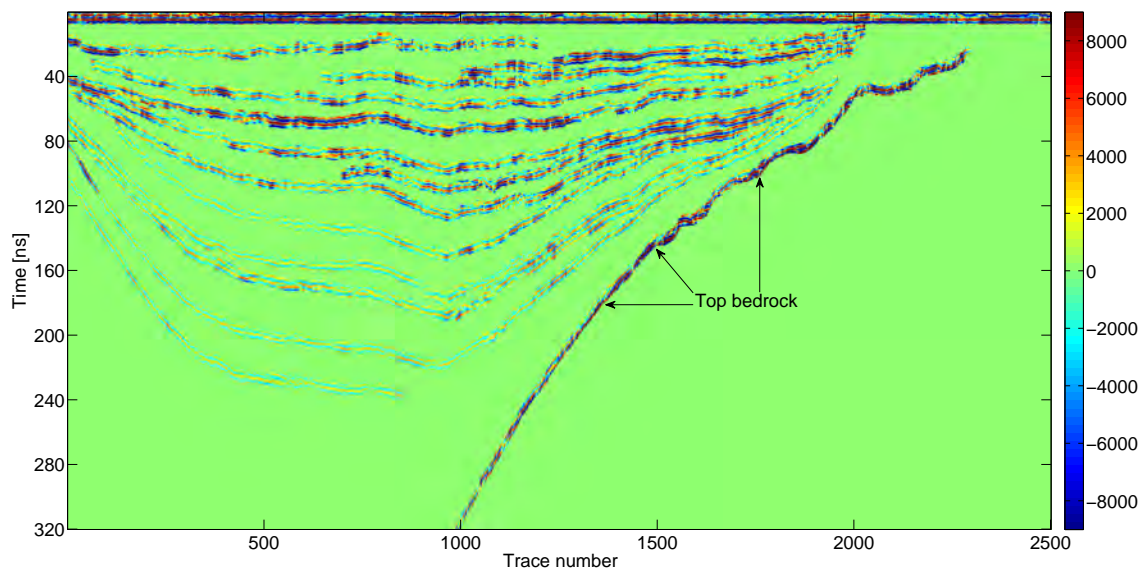


FIGURE 8.7: Simplified section after interpretation. A set of 8 ns windows centred on the picked horizons have been kept from the original data, while all the other samples have been zeroed. The deepest horizon separates the glacier and the bedrock.

8.4 Amplitude Inversion: Work-flow 1

The minimum L1-norm deconvolution described by equation 8.5 has been applied to the input data shown in Figures 8.4 and 8.5. I assumed the permittivity of the first sample to be homogeneous across the traces and equal to $18 \cdot 10^{-12} F/m$, which corresponds, under the low-conductivity hypothesis, to a propagation velocity of roughly 21 cm/ns. Some issues are found when using the measured wavelet for the inversion purpose. In fact, the reflectivity section of Figure 8.8 and the subsequent velocity of Figure 8.10 show the snow-firn event not resolved as a unique interface. The wavelet estimated from the snow-firn horizon stack resolves more precisely this event into a unique reflector with the expected polarity and a reasonable amplitude (Figure 8.9 and 8.12). However, some residual wavelet effects can be appreciated on deeper reflectors in this case. Deconvolution represents a difficult task on GPR data (Turner, 1994) and deterministic results are strongly influenced by the dispersive nature of the method (Economou and Vafidis, 2012). The reflectivity section in Figure 8.9 appears still reasonable, but the subsequent quantitative reconstruction of velocity shown in Figure 8.12 is strongly corrupted by trace-to-trace artefacts, which produce unrealistic lateral velocity variations. In order to reduce the problem, a solution with enhanced lateral continuity ($v \neq 0$ in equation 8.5) is proposed in Figure 8.13, but little improvement is obtained. The pre-processing is also helping in reducing the trace-to-trace artefacts, but no dramatic improvement is obtained (compare for reference the results of Figures 8.11 and 8.12). However, it is interesting to notice that both the general decreasing trend of the velocity and the overall velocity field values are in general realistic if we consider that a compacted snow at the surface is substituted by firn and by more and more compact ice (with lower and lower velocities) for increasing depths.

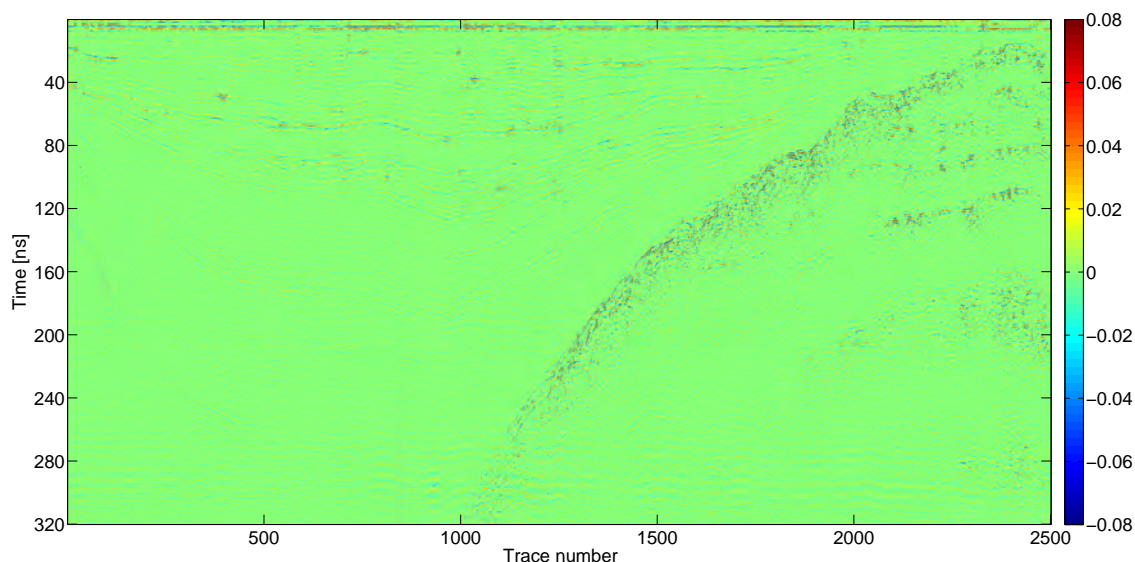


FIGURE 8.8: Reflectivity obtained from minimum L1-norm deconvolution out of the section of Figure 8.5 and the recorded wavelet. The event around 10 ns TWT in Figure 8.5 is re-defined as two different reflectors leading to an unreasonable reconstruction of the propagation velocity.

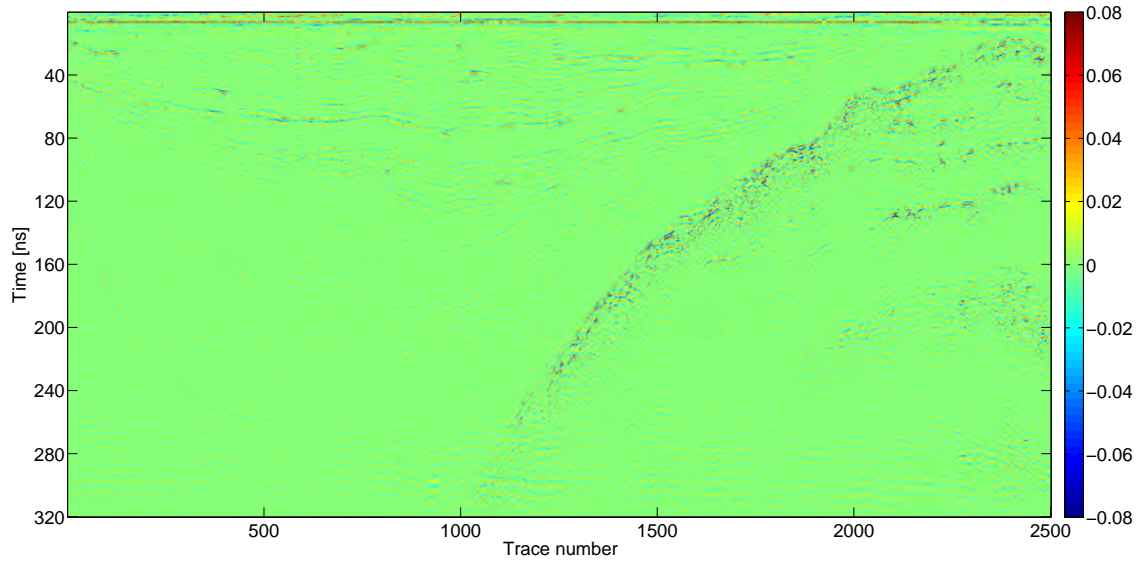


FIGURE 8.9: Reflectivity obtained from minimum L1-norm deconvolution out of the section of Figure 8.5 and a wavelet estimated from the snow-firn horizon stack. The event around 10 ns TWT in Figure 8.5 is better resolved than in Figure 8.8.

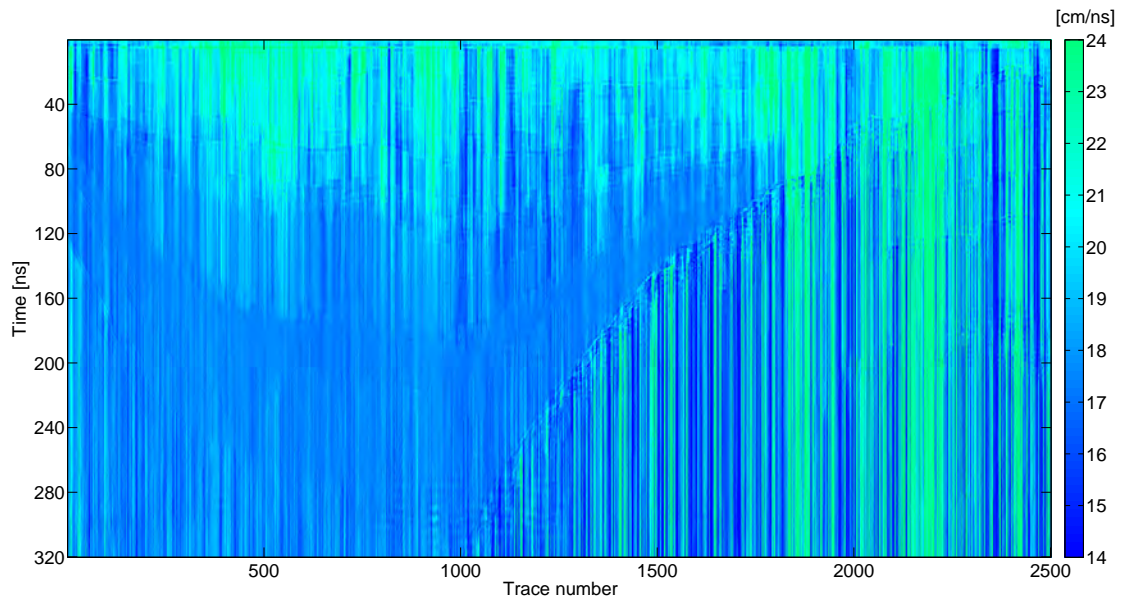


FIGURE 8.10: Velocity [cm/ns] obtained from inversion of the input of Figure 8.5. Recorded wavelet adopted for deconvolution. A mild weight on velocity (17 cm/ns) at depth around the travel-time of the deepest continuous horizon in Figure 8.7 has been imposed on the solution. A high velocity anomaly appears at 40-80 ns TWT for meeting the constraints at depth due to the high amplitude and poorly resolved reflectivity of the snow-firn discontinuity. Vertical bands are artefacts due to the 1-D approach of the inversion. The hyperparameter ν^2 that accounts for the lateral continuity of the solution has been set to 0.

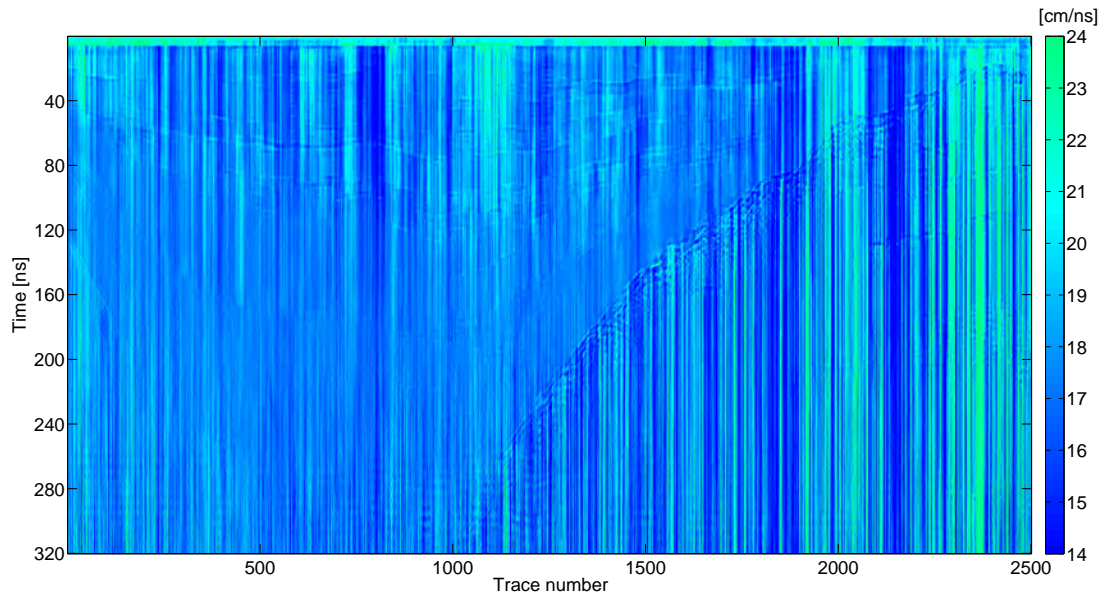


FIGURE 8.11: Velocity [cm/ns] obtained from inversion of the input of Figure 8.4. The inversion algorithm parametrisation is the same as in Figure 8.10, but the wavelet adopted for deconvolution is the one obtained by the snow-firn horizon stack. The proposed inversion shows a trend of decreasing velocity with depth which is reasonable for the dataset analysed.

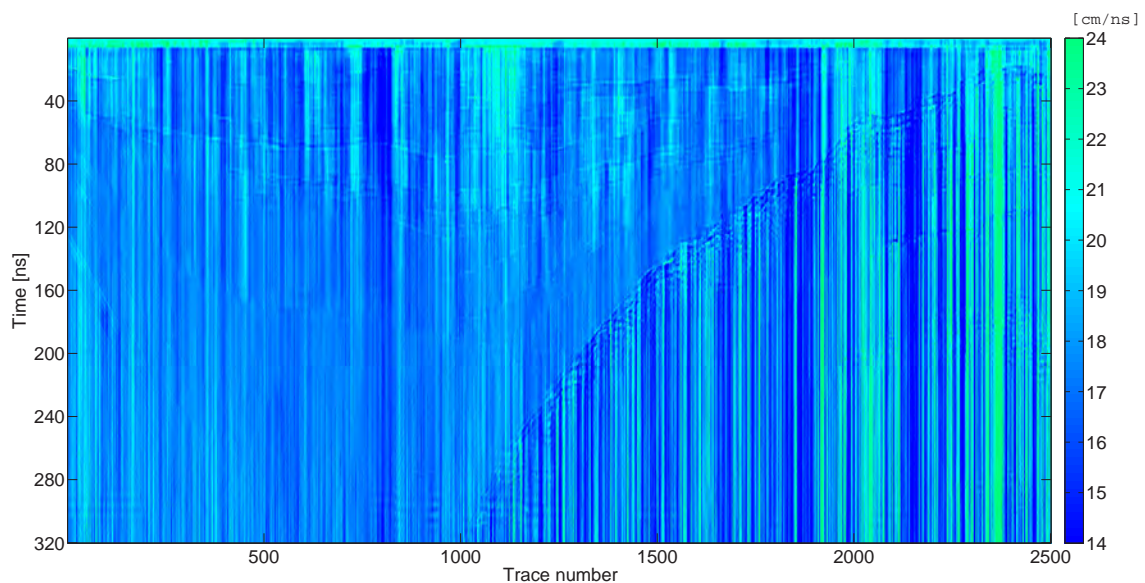


FIGURE 8.12: Velocity [cm/ns] obtained from time summation of the reflectivity presented in Figure 8.9 on the input of Figure 8.5. Same parametrisation as in Figure 8.11 (wavelet from snow-firn interface). By comparing this inverted section to the inverted section in Figure 8.11, little difference can be ascribed to the data filtering step.

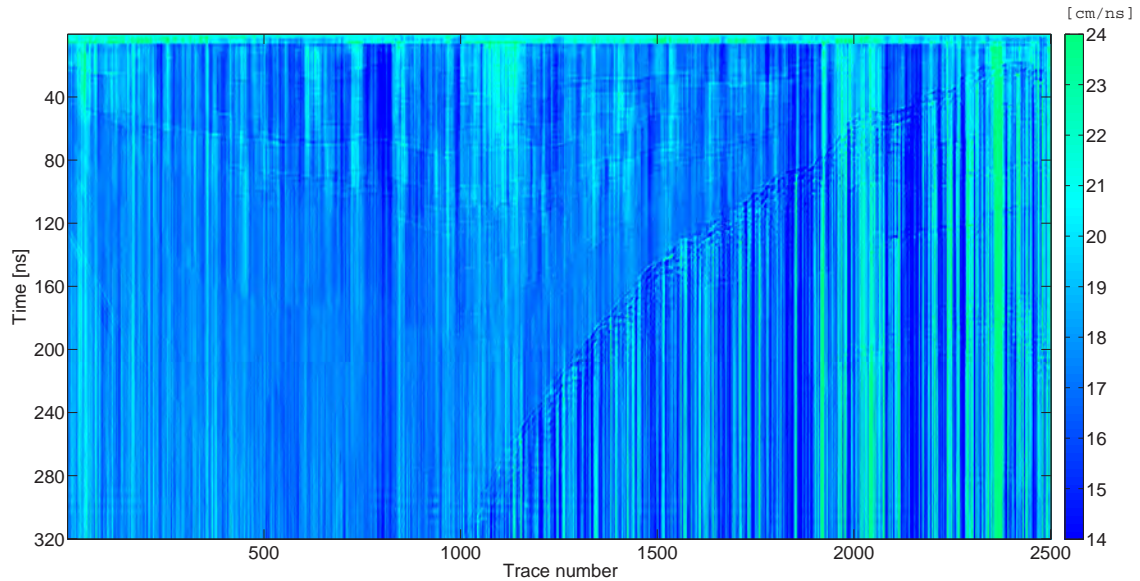


FIGURE 8.13: Velocity [cm/ns] obtained from the input of Figure 8.5. The inversion proposed accounts for a constraint on velocity at depth (same as in Figure 8.10) and a weight on the lateral variability of the solution. Little improvement on lateral continuity can be noticed with respect to the solution proposed in Figure 8.12.

Although the inverted velocities show unrealistic lateral variations, it is still possible to notice a degree of coherency within the icy layers. This does not happen within the bedrock whose velocities heavily depend on the diffracted energy, being the ice-bedrock contact a mixing of reflected and diffracted energy rather than a pure reflection. The strong velocity variation at the snow-firn interface is underlined by all the inversion estimates which use the wavelet extracted from the horizon for the purposes of deconvolution.

8.5 Amplitude Inversion: Work-flow 2

A layer stripping approach has also been attempted in order to reduce the trace-to-trace artefacts that affect the reconstruction of work-flow 1. A first approach towards a more stable solution was that of inverting the muted section in Figure 8.7. The obtained result shows similar issues to those presented in the previous section and it is reported for reference in Figure 8.14. The actual layer-stripping approach solution described in section 8.2 is presented in Figure 8.15. This result is not constrained at depth, and the reflectivity along the selected horizons is presumably reduced by the lateral averaging of events with different polarities. For this reason the reconstruction of velocity is much closer to the input velocity than in work-flow 1 results. However, a strong contrast is still visible around 10 ns with the deeper layers that follow, as expected, a general trend of decreasing velocity with depth.

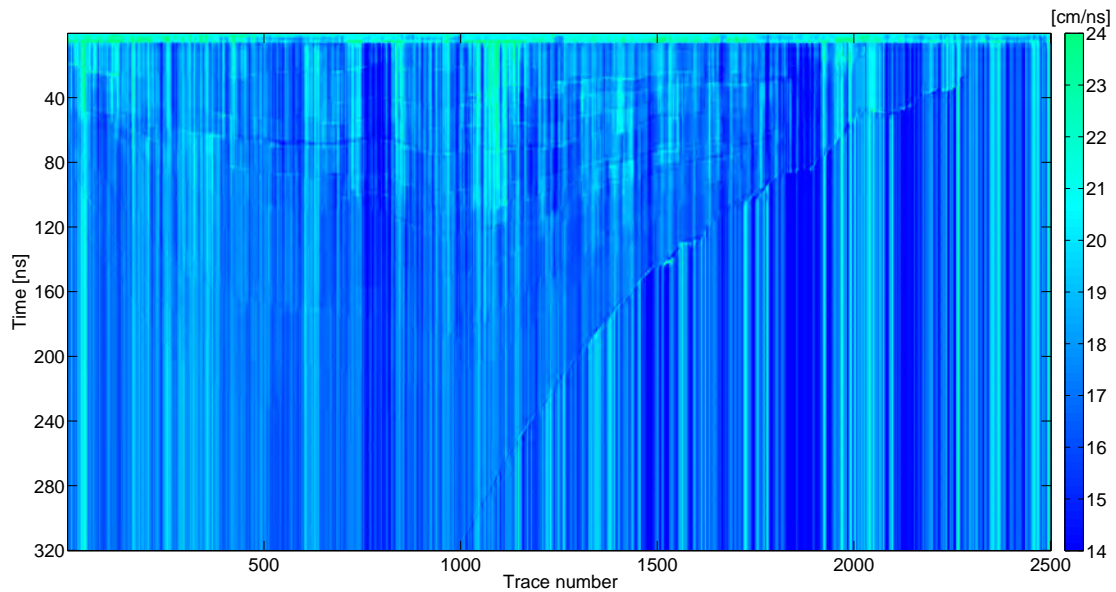


FIGURE 8.14: Estimation of propagation velocity [cm/ns] from the recursive summation of the reconstructed reflectivity. Input to the inversion algorithm is the section of Figure 8.7 and the parametrisation is the same as in Figure 8.13. The resulting velocity field shows similar artefacts that those obtained in Figure 8.13.

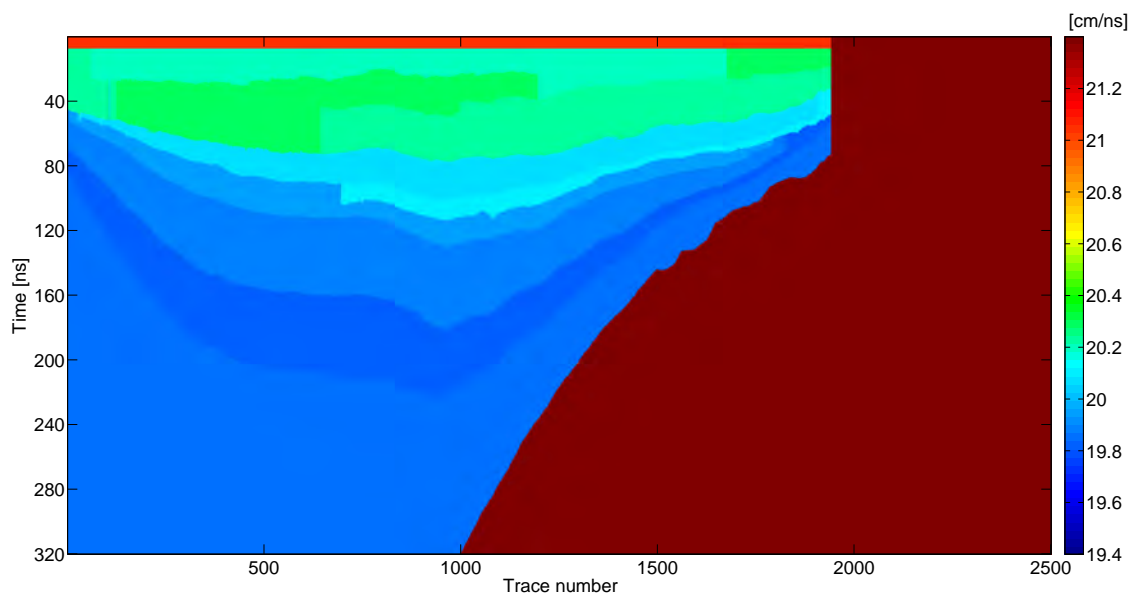


FIGURE 8.15: Layer-stripping inversion of the GPR profile from trace 1 to 1940. The largest variation in propagation velocity [cm/ns] happens around 10 ns TWT, and a trend of decreasing velocity with depth is apparent on the data. The actual values of velocity are probably biased toward the velocity of the first layer by traces with mixed polarity along the same reflector.

8.6 Discussion

From the Figures of the previous two sections is apparent that most of the local velocity variations are related either to diffractions (scattering) or to local effects within the shallowest layer.

Those high amplitudes propagate at depth as velocity vertical bands in the recursive inversion results. While the presence of diffractions in the GPR section is limited in number and in its effects (mainly within the bedrock), the reasons for the amplitude variation within the snow-firn event appear more elusive.

In fact, the GPR instrument should be almost perfectly repetitive (see Dossi, Forte, and Pipan (2018)) and, given the acquisition setting, the antenna-ground coupling should be even across traces. To this end, a quality control plot is shown in Figure 8.17. The amplitude of the direct arrival is fairly homogeneous across the section, while a stronger trace to trace variation is evidenced on the target horizon. A positive correlation between the amplitudes of the snow-firn event and the amplitude of the outgoing wavelet (estimated from the direct arrival) can be visually found. However, this does not explain all the trace-to-trace amplitude variability which stands out from the instantaneous amplitude section of Figure 8.16. Minor sources of amplitude bias for radar data may also be due to poor sampling interval (Dossi, Forte, and Pipan, 2018) and data processing (dewow, leakage due to noise attenuation).

Random noise and interference seem to be less problematic in this context because of the lateral coherency weight in the minimum L1-norm solution and the layer average in the layer-stripping solution.

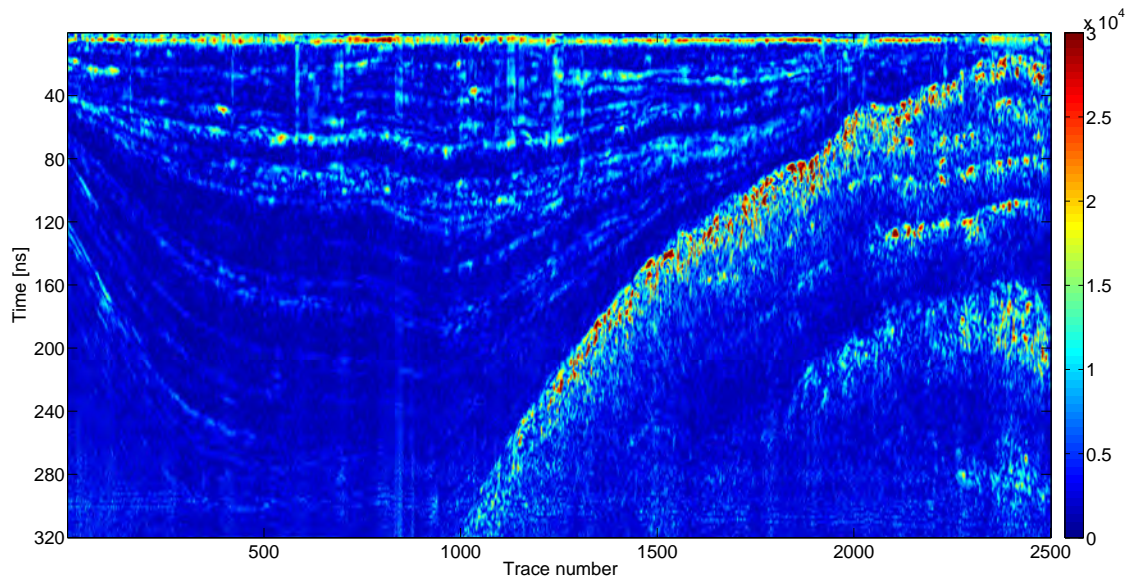


FIGURE 8.16: *Instantaneous amplitude of the GPR section 8.5. Amplitudes on the main events changes dramatically along the section, possibly leading to inaccurate dielectric property estimation.*

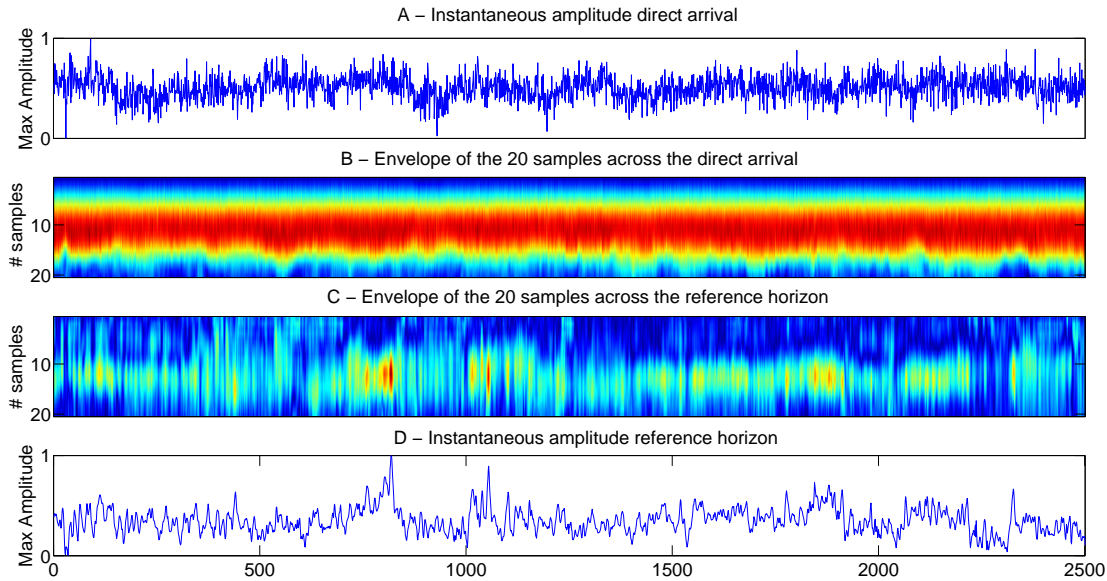


FIGURE 8.17: *Instantaneous amplitude of the of the direct arrival (Panel A and B) and the snow-firn discontinuity (Panel C and D). Peak amplitude normalised to 1 (red indicates high amplitude). Antenna elevation above the surface may play a role in the amplitude variations within the direct arrival. Although the instantaneous amplitude of the direct arrival is positively correlated with the instantaneous amplitude in the reference horizon amplitude, the latter is much more discontinuous and further factors should be considered in order to understand its behaviour. It is still noticeable that for the majority of the traces the maximum amplitude of the snow-firn event is close to the median value across the section.*

At the present stage the results of the GPR data inversion from the Boulder Clay Glacier suggest further investigation on the adopted techniques is required for obtaining quantitatively sound results. The first step towards a successful result appears the ability to deal with noise and amplitude bursts.

Chapter 9

Conclusions

9.1 Summary of the Results

The thesis provides an overview on the the spectral estimation methods applied to seismic data. In the author's perspective this review aims at clarifying the points related to spectral estimation for low frequency completion that were not fully detailed in the relevant literature to date. The review also analyses the factors affecting reflection seismic and GPR data amplitude, as a necessary feasibility study for a meaningful inversion.

Three main topics have been developed within the thesis.

The first refers to the estimation of the acoustic impedance from zero-offset seismic reflection data: the sparse-spike and the AR methods for low frequency extrapolation have been analysed to this end. The AR method has been stabilised with soft constraints at depth, with the information derived from the interval velocity field, and by accounting for the lateral continuity of the reflectivity. This led to what I called CARV method. The CARV method provides a more robust AI estimate than the original AR algorithm at the expense of larger amount of information required, additional pre-conditioning work, and more time-consuming parameter tuning. Robustness to the parametrization choice and to partially incorrect input data is demonstrated on synthetic examples characterized by sparsity in the time-domain representation of the reflectivity and on real seismic data. The CARV algorithm is able to highlight lateral variations of acoustic impedance on the marine dataset of Rockall Trough that cannot be obtained with the typical impedance inversion work-flows which derive the low frequency information from well-log data. The algorithm requires good data quality; in fact the estimations on the marine Penobscot test data could not be considered as adequate as in the case of the Rockall Trough test scenario. On land data, further problems arise from the large uncertainty on the AI reference value at depth, and for the generalized poorer S/N which characterizes this kind of surveys.

The second topic refers to the pre-stack low frequency reconstruction. The thesis presents two algorithms for the estimation of the full bandwidth of the elastic impedance and of a different set of elastic parameters. The success of the algorithms on synthetic examples has not prompted the same success on real data. Reasons for this behaviour must be sought in the S/N that characterises pre-stack gathers and in the problematic identification of stringent lithological constraints for some elastic parameters. Due to the linearisation of the governing law of the problem, which restricts the range of angles for the inversion, anomalies only on the s-wave velocity and on the density are not always singled out properly by the approach adopted in the thesis.

The third novel aspect delineated by the thesis consists of analysing the effects of correlations among the elastic parameters on the stability of the three-terms AVA inversion. The analysis has been performed as a function of the maximum incidence angle and of the background Poisson ratio and it assesses the role of the correlations due to Gardner and the Mudrock line relationships. The drawback of the proposed regularisation consists on obtaining solutions that show linear dependences between the elastic parameter reflectivities. This fact does not constitute a critical issue since most of the seismic events actually follow this background trend. However, it is worth acknowledging that exploration targets that show relevant anomalies on the background elastic properties represent a challenge for the method because an accurate a priori model for the target may not always be available. This analysis provides the means to determine the degree of correlation among the elastic parameters that is required to resolve the indeterminacy among them, depending on the S/N that characterises the seismic event, on the acquisition geometry, and on the background geology. From the point of view of feasibility studies, the analysis could provide an indication on the acquisition geometry that is required to solve the indeterminacy among the variation of mechanical properties of the subsurface, given the confidence on the a priori correlations on the target of interest.

TABLE 9.1: *Schematic summary of the advancements discussed in the thesis.*

Topic	State of the Art	Advancements	Future Work
Acoustic Impedance Inversion	Low-frequencies from well-log interpolation.	Low-frequencies from bandwidth extension and ancillary info.	Model in the inversion process non-stationary wavelet effects.
	Theoretical aspects of the AR reconstruction not fully described.	Overview on the details of the method.	Improve the model order choice.
	AR inversion unstable on real data.	Velocity-field regularisation and lateral smoothing partially mitigate the instability.	Include trace-varying scalar in the inversion.
	Sparse-spike inversion.	Sparse-spike inversion on GPR data acquired on a glacier.	Deal with noise of GPR profiles.
Elastic Parameter Inversion	Low-frequencies from well-log interpolation.	Low-frequencies from bandwidth extension and ancillary info.	Model in the inversion process the wavelet effects.
	No literature on low-frequency extension for elastic inversion.	Two work-flows proposed and tests on synthetic examples.	More work required for sensible results on real data.
	Instability of the linearised three-terms AVA.	Analysis on the stability of the regularised three-terms AVA.	Analysis on different parametrisation and prior information.

9.2 Future Work

The present work aims at reconstructing the mechanical properties of the subsurface investigated by an elastic wave-field. The extension of the techniques proposed in the thesis to electromagnetic wave-fields is only partially investigated: the present work could be further extended to the specific field of GPR data inversion only when the noise of this type of data is adequately reduced. The research is based on the assumption that the subsurface is made up of homogeneous, horizontally layered, blocks. This is a very stringent assumption that full-waveform inversion approaches might help to mitigate. The well-known problem of obtaining laterally smooth solutions via recursive methods was approached by globally smoothing either the input data, or the estimates. Smoothing kernels applied on dip-steered volumes could be a way to enhance the continuity of the estimates that I did not test in the thesis. Considering adaptive scalars or, even better, an adaptive wavelet for each seismic trace to account for all the

physical phenomena that happen to the wave-field other than the reflection at plane interfaces, could further enhance the continuity of the estimates.

As far as it concerns the pre-stack estimates, the governing law of the problem that I used in the thesis is a valid approximation only for small incidence angles. Considering a more complex relationship between the reflectivity at different angles and the mechanical properties of the subsurface would be an interesting topic to explore. The availability of s-wave reflection records could help to obtain more accurate results on real data.

The regularisation of the AVA inversion could be further extended to include the uncertainty on the Rock Physics coefficients. Finally, the extension of the analysis on the predictive power of the amplitude with angle information contained in the seismic records, to the prediction of litho-fluid properties such as porosity, clay content, or the type of fluid, could become, on specific targets, a new research objective.

Appendix A

Matlab code - Combined AR-velocity inversion of AI

A.1

The MATLAB function presented here below runs on version R2014a (8.3.0.532). The purposes of the function is to return the CARV reconstruction of the full-bandwidth of reflectivity and the subsequent AI inversion (see Chapter 3 for the details). The required input are described in the commented lines at the beginning of the code.

```

1  %-----
2  %-----AR RECOVERY OF AI -----
3  %-----
4  %---INPUT -----
5  %--- seismic: 2-D seismic line whose columns are the seismic traces-----
6  %--- scalar: Scalar to transform seismic amplitudes into reflectivity -----
7  %--- dt: Temporal sampling interval [ms] -----
8  %--- horizon_no: Number of horizon used to constrain the AI reconstruction
9  %--- horizon_name: Vector of strings containing the names of the horizons -
10 %--- parametrisation: path to a parametrisation file (see example below) --
11 %--- velocity_field: path to a csv file with a table for velocities -----
12 %--- Gardner: vector whose first element is alpha and second element c ----
13 %-----
14 %---OUTPUT -----
15 %---IMP: Acoustic Impedance estimated from the algorithm [rayl] -----
16 %---REF: Reflectivity estimated from the algorithm -----
17 %-----
18 %---Structure of the parameters file to be prompt or read: -----
19 %---1 Impedance of the first layer [rayl] -----
20 %---2 Order of the AR model -----
21 %---3 Low cut frequency for the AR model [Hz] -----
22 %---4 Bandpass flag -----
23 %---5 High cut frequency for the AR model [Hz] -----
24 %---6 Number of iterations of pass 3 -----
25 %---7 Number of constraints -----
26 %---8 Flag for the incorporation of velocity field -----
27 %---9 Regularisation parameter for incorporating the velocity field -----
28 %---6+4i Time of the i-th constraint [ms] -----
29 %---7+4i Uncertainty on the impedance of the i-th constraint [ms]-----

```

```

30 %---8+4i Impedance of the i-th constraint [ray1] -----
31 %---9+4i Uncertainty on the impedance of the i-th constraint -----
32 %-----
33 %---Reading the data -----
34 function [IMP,REF] = AR_RECOVERY_OF_AI ...
    (seismic,scalar,dt,horizon_no,horizon_name,parametrisation,velocity_field,Gardner)
35 IN=seismic./scalar;
36 siz=size(IN); %storing the number of samples/traces
37 IMP=zeros(siz(1),siz(2));
38 REF=zeros(siz(1),siz(2));
39 %---Preliminary check for amplitude -----
40 if max(max(abs(IN)))>1
41     scalar=max(max(abs(IN)));
42     IN=IN./scalar;
43 end
44 %---Reading the parametrization -----
45 fid=fopen(parametrisation);
46 [IO,M,iter,Fmin,Fmax,a,nc,tcons,etcons,vcons,econs,vflag,lambda,shift]=read_batch(fid);
47 %---Reading the horizon information as couples (TWT,trace_number) -----
48 for j=1:horizon_no
49 H{j}=csvread(horizon_name(j,:));
50 end
51 %--- INPUT THE VELOCITY FILE WHEN APPROPRIATE -----
52 if vflag ==1
53 Vint=csvread(velocity_field);
54 end
55 %---INITIALISATION-----
56 for w=1:siz(2);
57 tr=IN(1:end,w);
58 n=length(tr);
59 df=1/(n*dt/1000);
60 fn=1/(2*dt/1000);
61 fp=df.*[1:1:round(n/2)];
62 reg_flag=0; %Flag for pointing out issues in the the regularisation
63 TR=fftshift(fft(tr));
64 Fmina=round(Fmin/df);
65 Fmaxa=round(Fmax/df);
66 TRc=TR(ceil(n/2)+1+Fmina+1:ceil(n/2)+Fmaxa+1);
67 if a==0
68     Fmaxa=fn/df-1; %-1 is to avoid edge effects
69 end
70 for i=1:horizon_no
71     tcons(i)=dt*(round(H{i}(w,1)/dt))+shift;
72     end
73 %---WALKER AND ULRYCH AR FLOW (UNCONSTRAINED) -----
74 %---PASS 1 -----
75 g=aryule(TRc,M); %arburg,armcov possible
76 %---PASS 2 -----
77 xg=zeros(1,2*M+1);
78 xg=xcorr(g(1,:),g(1,:));
79 xg=conj(xg(ceil(length(xg)/2):end))/xg(ceil(length(xg)/2));
80 B=zeros(2*Fmina+1,1);
81 if 2*Fmina+1>M+1

```

```

82     xg(M+2:2*Fmina+1)=0;
83     G=toeplitz(xg(1:2*Fmina+1));
84 else
85     G=toeplitz(xg(1:2*Fmina+1));
86 end
87 if cond(G)>1000000
88     reg_flag=1;
89 end
90 for j=-Fmina:Fmina
91     j1=j+Fmina+1;
92     B(j1)=(conj(xg(1+j1:M+1))*conj(TRc(1:M-j1+1)));
93 end
94 C=conj(B(end:-1:1));
95 B=- (B+C);
96 clear C
97 TRint=G\B;
98 TRfill=[conj(TRc(end:-1:1)); TRint ; TRc];
99 %---PASS 3 (Many iterations are possible)-----
100 for iteration=1:iter
101 g3=aryule(TRfill,M); %arburg, armcov possible
102 %-----
103 xg3=xcorr(g3(:),g3(:));
104 xg3=conj(xg3(ceil(length(xg3)/2):end))/xg3(ceil(length(xg3)/2));
105 B3=zeros(2*Fmina+1,1);
106 if 2*Fmina+1>M+1
107     xg3(M+2:2*Fmina+1)=0;
108     G3=toeplitz(xg3(1:2*Fmina+1));
109 else
110     G3=toeplitz(xg3(1:2*Fmina+1));
111 end
112 if cond(G3)>100000
113     reg_flag=1;
114 end
115 for j=-Fmina:Fmina
116     j1=j+Fmina+1;
117     B3(j1)=(conj(xg3(1+j1:M+1) .')*(TRfill(Fmaxa-Fmina:-1:Fmaxa-Fmina-M+j1)));
118 end
119 C3=conj(B3(end:-1:1));
120 B3=- (B3+C3);
121 clear C3
122 TRint3=G3\B3;
123 TRfill=[conj(TRc(end:-1:1)); TRint3 ; TRc];
124 TRint=TRint3;
125 end
126 if iter>0
127     G=G3;
128     B=B3;
129 end
130 TRccons=[zeros(n/2-Fmaxa,1); -conj(TRc(end:-1:1)); zeros(2*Fmina+1,1); TRc; ...
          zeros(n/2-Fmaxa-1,1)];% High frequencies padded with zeroes
131 trccons=ifft(ifftshift(TRccons),'symmetric');
132 %-----
133 %--- INTRODUCTION OF THE TOMOGRAPHIC VELOCITY FIELD -----

```

```

134 if vflag==1
135     vint=Vint(:,w);
136     gamma=0.5*log(Gardner(1).*vint.^Gardner(2)./I0);
137     cv=floor(n/(2*Fmina+1));
138     for i=1:cv:n
139         ni((i-1+cv)/cv)=sum(trccons(1:i));
140     end
141     gamma2=gamma(1:cv:n)-(ni).';
142     L=zeros(Fmina,ceil(n/cv));
143     for i=1:1+Fmina
144         for j=1:cv:n
145             L(i,(j-1+cv)/cv)=sum(exp(2i*pi*(i-1)/(n+1)*(1:j)));
146         end
147     end
148     L=[conj(L(end:(-1):2,:));L]/(n+1).';
149     sca=max(eig(G))/max(eig(L'*L));
150     lambda2=lambda*sca;
151     G1=G+lambda2*(L')*L;
152     B1=B+lambda2*(L')*gamma2;
153     TRint=G1\B1;
154 else
155     G1=G;
156     B1=B;
157 end
158 TRfill13=[zeros(n/2-Fmaxa,1); conj(TRc(end:-1:1)); TRint ; TRc; ...
           zeros(n/2-Fmaxa-1,1)];
159 %-----
160 %---CONSTRAINTS ON IMPEDANCE -----
161 if nc>0
162     econs2=0.5*(log((vcons+econs)/I0)-log(vcons/I0)); %error on impedance constraint
163     vcons2=0.5*log(vcons/I0);
164     tcons2=round(tcons/dt);
165     etcons2=round(etcons/dt); %uncertainty on timings
166     mu=zeros(1,nc); %HYPOTHESIS: mu is reconstructed neglecting the high ...
           frequencies and applying the superposition principle
167     for i=1:nc
168         mu(i)=0.5*(sum(trccons(1:tcons2(i)))+sum(trccons(1:(tcons2(i)+etcons2(i)))));
169     end
170     beta=vcons2-mu;
171     H__1=zeros(n+1,nc);
172     for i=1:n+1
173         for j=1:nc
174             H__1(i,j)=0.5*((n+1)/(i-1)/pi/(2i)).*(exp((2i)*pi*(-1+i)/(n+1)*(tcons2(j))-1)+(n+1).
           INTEGRATION
175         end
176     end
177     for j=1:nc
178         H__1(1,j)=tcons2(j);
179         H__1(:,j)=(fftshift(H__1(:,j)))/(n+1).';
180         H__1(1:n/2,j)=conj(H__1(end:(-1):n/2+2,j));
181     end
182     H__1=H__1(n/2+1-Fmina:n/2+1+Fmina,:);
183 %-----

```

```

184 %--- SOLUTION OF THE OPTIMISATION PROBLEM -----
185 bc=[beta+econs2 -beta+econs2].';
186 Hc=[(H__1. '); -(H__1. ')];
187 options = optimset('LargeScale', 'off', 'Display', 'off');
188 Ygolub=lsqlin(G1,B1,Hc,bc, [], [], [], [], [], options); %The impedance (LOW AND ...
    MID FREQUENCY DERIVED) is constrained to lay between beta-econs and ...
    beta+econs
189 %-----
190 energy_mf=sum(TRc.*conj(TRc))/(Fmaxa-Fmina);
191 energy_lf=sum(Ygolub.*conj(Ygolub))/(2*Fmina+1);
192 if energy_lf>4*energy_mf
193     ['WARNING: The constraints are not compatible with the AR model of the ...
        seismogram.'];
194 reg_flag=1;
195 end
196 %-----
197 TRfillcons=[zeros(n/2-Fmaxa,1); conj(TRc(end:-1:1)); Ygolub ; TRc; ...
    zeros(n/2-Fmaxa-1,1)];
198 TRfull=TRfillcons;
199 O=ifftshift(TRfull);
200 o=ifft(O, 'symmetric');
201 else
202 TRfull=TRfill3;
203 O=ifftshift(TRfull);
204 o=ifft(O, 'symmetric');
205 TRfillcons=[];
206 end
207 %--- HIGH FREQUENCY EXTENSION (LOG NORM BY SACCHI) -----
208 if reg_flag~=1; %Avoid the high frequency reconstruction if the solution is a ...
    regularised one
209     [o, Ve, TRfull] = Sacchi_HF_extension (o,n,Fmaxa,nc,TRfill3,TRfillcons);
210 end
211 %-----
212 %--- Wavelet shaping control: control to avoid instabilities
213 f=find(o>0);
214 e=find(o<0);
215 if sign(o(n))>0;
216     q(1)=n-max(e);
217 else
218     q(2)=n-max(f);
219 end
220 m=max(f(2:end)-f(1:end-1));
221 p=max(e(2:end)-e(1:end-1));
222 if m>Fmina/2 | p>Fmina/2 | q>Fmina/2
223     ['REGULARISATION STILL NEEDED']
224 elseif nc>0
225     if energy_lf>c*energy_mf | energy_mf>c*energy_lf
226         ['REGULARISATION STILL NEEDED']
227     end
228 elseif imp_rec>10^8 | imp_rec<10^5 %On real data only
229     ['REGULARISATION STILL NEEDED']
230 end
231 %---CALCULATING THE OUTPUT IMPEDANCE -----

```

```

232 imp_rec=zeros(1,n);
233 imp_rec=I0.*exp(2.*cumsum(o));
234 IMP(:,w)=imp_rec;
235 REF(:,w)=o;
236 clearvars TR TRc tr g g3 sigg xg B G TRint TRfill xg3 B3 G3 TRint3
237 end
238 return
239
240 %-----
241 %--- FUNCTION TO READ THE PARAMETRISATION FILE -----
242 function ...
243     [I0,M,iter,Fmin,Fmax,a,nc,tcons,etcons,vcons,econs,vflag,lambda,shift]=read_batch(fid)
244     s=textscan(fid,'%s','delimiter',' ');
245     string=s{1};
246     for i=1:ceil(length(string))
247         stra(1:ceil(length(string)),1)=string(1:(length(string)));
248     end
249     fclose(fid);
250     for i=1:ceil(length(string))
251         aa=stra(i);
252         aaa(i)=str2double(aa);
253     end
254     I0=aaa(1);
255     M=aaa(2);
256     Fmin=aaa(3);
257     a=aaa(4);
258     Fmax=aaa(5);
259     iter=aaa(6);
260     nc=aaa(7);
261     vflag=aaa(8);
262     shift=aaa(10);
263     if nc~=0
264         for i=1:nc
265             tcons(i,:)=aaa(4*i+7);
266             etcons(i)=aaa(4*i+8);
267             vcons(i)=aaa(4*i+9);
268             econs(i)=aaa(4*i+10);
269         end
270     else
271         tcons=[];
272         etcons=[];
273         vcons=[];
274         econs=[];
275         lambda=[];
276     end
277     if vflag==1
278         lambda=aaa(9);
279     else
280         lambda=[];
281         Fvel=[];
282     end
283     return

```

```

284 %-----
285 %--- FUNCTION FOR THE HIGH FREQUENCY COMPLETION -----
286 function [o, Ve, TRfull] = Sacchi_HF_extension ...
      (o, n, Fmaxa, nc, TRfill13, TRfillcons)
287 Ve(1)=0;
288 Ve(2)=sum(o.^2.*(log(o.^2)-log(sum(o.^2/n)))/sum(o.^2/n))/(n*log(n));
289 energy=sum(o.^2)*n/(2*Fmaxa+1);
290 i=2;
291 while Ve(i-1)<Ve(i)
292     i=i+1;
293     q=o.^2/sum(o.^2)*n;
294     bh=(n).*(log(q)+1).*o/sum((log(q)+1).*q);
295     BH=fftshift(fft(bh));
296     if nc>0
297         TRfull=[BH(1:round(n/2)-Fmaxa); ...
                 (TRfillcons(round(n/2)-Fmaxa+1:round(n/2)+Fmaxa+1)); ...
                 BH(Fmaxa+round(n/2)+2:end)];
298     else
299         TRfull=[BH(1:round(n/2)-Fmaxa); ...
                 (TRfill13(round(n/2)-Fmaxa+1:round(n/2)+Fmaxa+1)); ...
                 BH(Fmaxa+round(n/2)+2:end)];
300     end
301     O=ifftshift(TRfull);
302     o=ifft(O, 'symmetric');
303     Ve(i)=(sum(o.^2.*(log(o.^2)-log(sum(o.^2/n)))/sum(o.^2/n))/(n*log(n));
304     en=sum(o.^2);
305     if energy < en
306         Ve(i)=Ve(i)-1;
307     end
308 end
309 return

```


References

- [1] H. Akaike. *Information Theory and an Extension of the Maximum Likelihood Principle*. Ed. by S. Kotz and N.L. Johnson. Springer-Verlag, 1992, p. 624.
- [2] K. Aki and P.G. Richards. *Quantitative Seismology: Theory and Methods*. Geology Series v. 2. W.H. Freeman, 1980. ISBN: 9780716710592.
- [3] M. Aleardi. “The importance of the V_p/V_s ratio in determining the error propagation, the stability and the resolution of linear AVA inversion: A theoretical demonstration”. In: *Bollettino di Geofisica Teorica ed Applicata* 56 (Oct. 2015).
- [4] W. Alemie and M.D. Sacchi. “High-resolution three-term AVO inversion by means of a Trivariate Cauchy probability distribution”. In: *Geophysics* 76.3 (2011), R43–R55. DOI: [10.1190/1.3554627](https://doi.org/10.1190/1.3554627).
- [5] A. Beck and M. Teboulle. “A Fast Iterative Shrinkage-Thresholding algorithm for linear inverse problems”. In: *SIAM Journal on Imaging Sciences* 2.1 (2009), pp. 183–202. DOI: [10.1137/080716542](https://doi.org/10.1137/080716542).
- [6] B.A. Bertheussen and B. Ursin. “Estimation of reflection coefficients from zero offset field data”. In: *Geophysics* 58(11).11 (1993), pp. 1634–1645. DOI: [10.1190/1.1443379](https://doi.org/10.1190/1.1443379).
- [7] L. Bianchin, E. Forte, and M. Pipan. “Acoustic impedance estimation from combined harmonic reconstruction and interval velocity”. In: *Geophysics* 84.3 (2019), R385–R400. DOI: [10.1190/geo2018-0296.1](https://doi.org/10.1190/geo2018-0296.1).
- [8] L. Bianchin and M.D. Sacchi. “Autoregressive low-frequency reconstruction for pre-stack inversion”. In: *80th EAGE Conference 2018 Extended Abstracts* (2018). DOI: [10.3997/2214-4609.201801542](https://doi.org/10.3997/2214-4609.201801542).
- [9] N. Bleistein, J.K. Cohen, and J.W.J. Stockwell. *Mathematics of Multidimensional Seismic Imaging, Migration, and Inversion*. Interdisciplinary Applied Mathematics. Springer-Verlag, New York, 2001. ISBN: 9780387950617.
- [10] A. Buland and H. Omre. “Bayesian linearized AVO inversion”. In: *Geophysics* 68.1 (2003), pp. 185–198. DOI: [10.1190/1.1543206](https://doi.org/10.1190/1.1543206).
- [11] J.P. Burg. “Maximum Entropy Spectral Analysis”. PhD thesis. Stanford University, Dept. of Geophysics, pp. 256, 1975.
- [12] J.A. Cadzow. “Spectral estimation: An overdetermined rational model equation approach”. In: *Proceedings of the IEEE* 70.9 (1982), pp. 907–939. ISSN: 0018-9219. DOI: [10.1109/PROC.1982.12424](https://doi.org/10.1109/PROC.1982.12424).
- [13] J.P. Castagna, M.L. Batzle, and R.L. Eastwood. “Relationships between compressional-wave and shear-wave velocities in clastic silicate rocks”. In: *Geophysics* 50.4 (1985), pp. 571–581. DOI: [10.1190/1.1441933](https://doi.org/10.1190/1.1441933).

- [14] B. Cerney and D.C. Bartel. "Uncertainties in low-frequency acoustic impedance models". In: *The Leading Edge* 26.1 (2007), pp. 74–87. DOI: [10.1190/1.2431834](https://doi.org/10.1190/1.2431834).
- [15] G. Chen et al. "Multi-scale signed envelope inversion". In: *Journal of Applied Geophysics* 153 (2018), pp. 113–126. ISSN: 0926-9851. DOI: <https://doi.org/10.1016/j.jappgeo.2018.04.008>.
- [16] K. Chen and M.D. Sacchi. "Making f-x projection filters robust to erratic noise". In: *SEG Technical Program Expanded Abstracts 2014* (2014), pp. 4371–4375. DOI: [10.1190/segam2014-0893.1](https://doi.org/10.1190/segam2014-0893.1).
- [17] J.F. Claerbout. *Fundamentals of Geophysical Data Processing*. New York: McGraw-Hill, 1976. ISBN: 9780070111172.
- [18] J.F. Claerbout. *Imaging the Earth's Interior*. Oxford, UK: Blackwell Scientific Publications, Ltd., 1985. ISBN: 0-86542-304-0.
- [19] P. Connolly. "Elastic impedance". In: *The Leading Edge* 18.4 (1999), pp. 438–452. DOI: [10.1190/1.1438307](https://doi.org/10.1190/1.1438307).
- [20] D.A. Cooke and W.A. Schneider. "Generalized linear inversion of reflection seismic data". In: *Geophysics* 48.6 (1983), pp. 665–676. DOI: [10.1190/1.1441497](https://doi.org/10.1190/1.1441497).
- [21] D.J. Daniels. *Surface-Penetrating Radar*. The Institution of Electrical Engineers, London, 1996. ISBN: 0852968620.
- [22] I. Daubechies. *Ten Lectures on Wavelets*. Society for Industrial and Applied Mathematics, 1992. ISBN: 978-0-89871-274-2. DOI: [10.1137/1.9781611970104](https://doi.org/10.1137/1.9781611970104).
- [23] J.L. Davis and A.P. Annan. "Ground penetrating radar for high-resolution mapping of soil and rock stratigraphy". In: *Geophysical Prospecting* 37 (1989), pp. 531–551.
- [24] C.G.M. de Bruin, C.P.A. Wapenaar, and A.J. Berkhout. "Angle-dependent reflectivity by means of prestack migration". In: *Geophysics* 55.9 (1990), pp. 1223–1234. DOI: [10.1190/1.1442938](https://doi.org/10.1190/1.1442938).
- [25] A. De Nicolao, G. Drufuca, and F. Rocca. "Eigenvalues and eigenvectors of linearized elastic inversion". In: *Geophysics* 58.5 (1993), pp. 670–679. DOI: [10.1190/1.1443451](https://doi.org/10.1190/1.1443451).
- [26] C.H. Dix. "Seismic velocities from surface measurements". In: *Geophysics* 20.1 (1955), pp. 68–86. DOI: [10.1190/1.1438126](https://doi.org/10.1190/1.1438126).
- [27] M. Dossi, E. Forte, and M. Pipan. "Quantitative analysis of GPR signals: transmitted wavelet, amplitude decay, and sampling-related amplitude distortions". In: *Pure and Applied Geophysics* 175.3 (2018), pp. 1103–1122. DOI: [10.1007/s00024-017-1752-2](https://doi.org/10.1007/s00024-017-1752-2).
- [28] J.E. Downton. "Seismic parameter estimation from AVO inversion". PhD thesis. University of Calgary, 2005.
- [29] J.E. Downton and L.R. Lines. "High-resolution AVO analysis before NMO". In: *SEG Technical Program Expanded Abstracts 2003*. 2005, pp. 219–222. DOI: [10.1190/1.1817781](https://doi.org/10.1190/1.1817781).
- [30] N. Economou and A. Vafidis. "GPR data time varying deconvolution by kurtosis maximization". In: *Journal of Applied Geophysics* 81 (June 2012).

- [31] G.G. Fahlman and T.J. Ulrych. "A new method for estimating the power spectrum of gapped data". In: *Mon. Not. Royal Astronomic Society* 199 (1982), pp. 53–65.
- [32] J.L. Fatti et al. "Detection of gas in sandstone reservoirs using AVO analysis: A 3-D seismic case history using the Geostack technique". In: *Geophysics* 59.9 (1994), pp. 1362–1376. DOI: [10.1190/1.1443695](https://doi.org/10.1190/1.1443695).
- [33] S. Fomel. "Seismic reflection data interpolation with differential offset and shot continuation". In: *Geophysics* 68.2 (2003), pp. 733–744. DOI: [10.1190/1.1567243](https://doi.org/10.1190/1.1567243).
- [34] G.H.F. Gardner, L.W. Gardner, and A.R. Gregory. "Formation velocity and density - the diagnostic basics for stratigraphic traps". In: *Geophysics* 39.6 (1974), pp. 770–780. DOI: [10.1190/1.1440465](https://doi.org/10.1190/1.1440465).
- [35] A. Gholami. "Nonlinear multichannel impedance inversion by total-variation regularization". In: *Geophysics* 80.5 (2015), R217–R224. DOI: [10.1190/geo2015-0004.1](https://doi.org/10.1190/geo2015-0004.1).
- [36] A. Gholami, H.S. Aghamiry, and M. Abbasi. "Constrained nonlinear amplitude variation with offset inversion using Zoeppritz equations". In: *Geophysics* 83.3 (2018), R245–R255. DOI: [10.1190/geo2017-0543.1](https://doi.org/10.1190/geo2017-0543.1).
- [37] A. Gholami and M.D. Sacchi. "A fast and automatic sparse deconvolution in the presence of outliers". In: *IEEE Transactions on Geoscience and Remote Sensing* 50.10 (2012), pp. 4105–4116. DOI: [10.1109/TGRS.2012.2189777](https://doi.org/10.1109/TGRS.2012.2189777).
- [38] A. Gholami and M.D. Sacchi. "Fast 3D blind seismic deconvolution via constrained Total Variation and GCV". In: *SIAM Journal on Imaging Sciences* 6(4).4 (2013), pp. 2350–2369. DOI: [10.1137/130905009](https://doi.org/10.1137/130905009).
- [39] G. Golub. "Numerical methods for solving linear least squares problems". In: *Numerische Mathematik* 7.3 (1965), pp. 206–216. ISSN: 0945-3245. DOI: [10.1007/BF01436075](https://doi.org/10.1007/BF01436075).
- [40] D. Grana and E. Della Rossa. "Probabilistic petrophysical-properties estimation integrating statistical rock physics with seismic inversion". In: *Geophysics* 75.3 (2010), O21–O37. DOI: [10.1190/1.3386676](https://doi.org/10.1190/1.3386676).
- [41] H. Hamid and A. Pidlisecky. "Multitrace impedance inversion with lateral constraints". In: *Geophysics* 80.6 (2015), pp. M101–M111. DOI: [10.1190/geo2014-0546.1](https://doi.org/10.1190/geo2014-0546.1).
- [42] H. Hamid and A. Pidlisecky. "Structurally constrained impedance inversion". In: *Interpretation* 4.4 (2016), T577–T589. DOI: [10.1190/INT-2016-0049.1](https://doi.org/10.1190/INT-2016-0049.1).
- [43] N. Hargreaves, S. Treitel, and M. Smith. "Frequency extension, resolution, and sparse inversion". In: *SEG Technical Program Expanded Abstracts 2013*. 2013, pp. 3345–3349. DOI: [10.1190/segam2013-0782.1](https://doi.org/10.1190/segam2013-0782.1).
- [44] N. Hendrick and S. Hearn. "Evaluation of seismic trace inversion techniques". In: *Exploration Geophysics* 24(3-4).3/4 (1993), pp. 549–560. DOI: [10.1071/EG993549](https://doi.org/10.1071/EG993549).
- [45] D.A. Herron. "Tutorial: Tying a well to seismic using a blocked sonic log". In: *Interpretation* 2.2 (2014), SD1–SD7. DOI: [10.1190/INT-2013-0123.1](https://doi.org/10.1190/INT-2013-0123.1).
- [46] S. Jazayeri, A. Ebrahimi, and S. Kruse. "Sparse blind deconvolution of common-offset GPR data". In: *SEG Technical Program Expanded Abstracts 2017*. 2017, pp. 5140–5145. DOI: [10.1190/segam2017-17791251.1](https://doi.org/10.1190/segam2017-17791251.1).

- [47] H.M. Jol. *Ground Penetrating Radar: Theory and Applications*. Elsevier Science, Amsterdam, 2009. ISBN: 978-0-444-53348-7.
- [48] S.T. Kaplan. "Principal and Independent Component Analysis for seismic data". MA thesis. University of British Columbia, Department of Earth and Ocean Sciences, pp. 86, 2002.
- [49] S.M. Kay and S.L. Marple. "Spectrum analysis - A modern perspective". In: *Proceedings of the IEEE* 69.11 (1981), pp. 1380–1419. ISSN: 0018-9219. DOI: [10.1109/PROC.1981.12184](https://doi.org/10.1109/PROC.1981.12184).
- [50] S. Lancaster and D. Whitcombe. "Fast-track 'coloured' inversion". In: *SEG Technical Program Expanded Abstracts 2000*. 2005, pp. 1572–1575. DOI: [10.1190/1.1815711](https://doi.org/10.1190/1.1815711).
- [51] A. Lesage et al. "Low-frequency reflection-data augmentation by an inpainting method: 1D acoustic media". In: *Geophysics* 80.4 (2015), R139–R153. DOI: [10.1190/geo2014-0352.1](https://doi.org/10.1190/geo2014-0352.1).
- [52] S.A. Levin. "Surface-consistent deconvolution". In: *Geophysics* 54.9 (1989), pp. 1123–1133. DOI: [10.1190/1.1442747](https://doi.org/10.1190/1.1442747).
- [53] S. Levy and P.K. Fullagar. "Reconstruction of a sparse spike train from a portion of its spectrum and application to high-resolution deconvolution". In: *Geophysics* 46.9 (1981), pp. 1235–1243. DOI: [10.1190/1.1441261](https://doi.org/10.1190/1.1441261).
- [54] S. Levy et al. "A linear programming approach to the estimation of the power spectra of harmonic processes". In: *IEEE Transactions on Acoustics, Speech, and Signal Processing* 30.4 (1982), pp. 675–679. ISSN: 0096-3518. DOI: [10.1109/TASSP.1982.1163928](https://doi.org/10.1109/TASSP.1982.1163928).
- [55] C. Liang, J. Castagna, and R.Z. Torres. "Tutorial: Spectral bandwidth extension — Invention versus harmonic extrapolation". In: *Geophysics* 82.4 (2017), W1–W16. DOI: [10.1190/geo2015-0572.1](https://doi.org/10.1190/geo2015-0572.1).
- [56] R.O. Lindseth. "Synthetic sonic logs—a process for stratigraphic interpretation". In: *Geophysics* 44.1 (1979), pp. 3–26. DOI: [10.1190/1.1440922](https://doi.org/10.1190/1.1440922).
- [57] H. Loseth et al. "Can hydrocarbon source rocks be identified on seismic data?" In: *Geology* 39.12 (2011), p. 1167. DOI: [10.1130/G32328.1](https://doi.org/10.1130/G32328.1).
- [58] G.S. Martin, K.J. Marfurt, and S. Larsen. "Marmousi-2: An updated model for the investigation of AVO in structurally complex areas". In: *SEG Technical Program Expanded Abstracts 2002* (2005), pp. 1979–1982. DOI: [10.1190/1.1817083](https://doi.org/10.1190/1.1817083).
- [59] A. Mazzotti and G. Ravagnan. "Impact of processing on the amplitude versus offset response of a marine seismic data set". In: *Geophysical Prospecting* 43.3 (1995), pp. 263–281. DOI: [10.1111/j.1365-2478.1995.tb00253.x](https://doi.org/10.1111/j.1365-2478.1995.tb00253.x).
- [60] W. Menke. *Geophysical Data Analysis: Discrete Inverse Theory*. Academic Press, Inc. San Diego, California, 1989. ISBN: 0-12-490921-3.
- [61] I.B. Morozov and J. Ma. "Accurate poststack acoustic-impedance inversion by well-log calibration". In: *Geophysics* 74.5 (2009), R59–R67. DOI: [10.1190/1.3170687](https://doi.org/10.1190/1.3170687).
- [62] D. Muerdter and D. Ratcliff. "Understanding subsalt illumination through ray-trace modeling, Part 1: Simple 2-D salt models". In: *The Leading Edge* 20.6 (2001), pp. 578–594. DOI: [10.1190/1.1438998](https://doi.org/10.1190/1.1438998).

- [63] R.F. O'Doerthy and N.A. Anstey. "Reflection on amplitudes". In: *Geophysical Prospecting* 19.3 (1974), pp. 430–458. DOI: [10.1111/j.1365-2478.1971.tb00610.x](https://doi.org/10.1111/j.1365-2478.1971.tb00610.x).
- [64] D.W. Oldenburg, S. Levy, and K. Stinson. "Root-mean-square velocities and recovery of the acoustic impedance". In: *Geophysics* 49.10 (1984), pp. 1653–1663. DOI: [10.1190/1.1441573](https://doi.org/10.1190/1.1441573).
- [65] D.W. Oldenburg, T. Scheuer, and S. Levy. "Recovery of the acoustic impedance from reflection seismograms". In: *Geophysics* 48.10 (1983), pp. 1318–1337. DOI: [10.1190/1.1441413](https://doi.org/10.1190/1.1441413).
- [66] M. Ooe and T.J. Ulrych. "Minimum entropy deconvolution with an exponential transformation". In: *Geophysical Prospecting* 27.2 (1979), pp. 458–473. DOI: [10.1111/j.1365-2478.1979.tb00979.x](https://doi.org/10.1111/j.1365-2478.1979.tb00979.x).
- [67] V. Oropeza and M.D. Sacchi. "Simultaneous seismic data denoising and reconstruction via multichannel singular spectrum analysis". In: *Geophysics* 76.3 (2011), pp. V25–V32. DOI: [10.1190/1.3552706](https://doi.org/10.1190/1.3552706).
- [68] R.L. Parker. *Geophysical Inverse Theory*. Princeton University Press, 1994, p. 386. ISBN: 0-691-03634-9.
- [69] E. Parzen. "Some recent advances in time series modeling". In: *IEEE Transactions on Automatic Control* 19.6 (1974), pp. 723–730. ISSN: 0018-9286. DOI: [10.1109/TAC.1974.1100733](https://doi.org/10.1109/TAC.1974.1100733).
- [70] D. Pereg, I. Cohen, and A.A. Vassiliou. "Multichannel sparse spike inversion". In: *Journal of Geophysics and Engineering* 14.5 (2017), p. 1290.
- [71] D.O. Perez, D.R. Velis, and M.D. Sacchi. "Three-term inversion of prestack seismic data using a weighted L2-L1 mixed norm". In: *Geophysical Prospecting* 65.6 (2017), pp. 1477–1495. ISSN: 1365-2478. DOI: [10.1111/1365-2478.12500](https://doi.org/10.1111/1365-2478.12500).
- [72] R.A. Peterson, W.R. Fillipone, and F.B. Coker. "The synthesis of seismograms from well log data". In: *Geophysics* 20 (1955), pp. 516–538. DOI: [10.1190/1.1438155](https://doi.org/10.1190/1.1438155).
- [73] V.F. Pisarenko. "On the estimation of spectra by means of non-linear functions of the covariance matrix". In: *Geophys. J. R. astr. Soc.* 28 (1972), pp. 511–531.
- [74] J.G. Proakis et al. *Advanced Digital Signal Processing*. Macmillan Publishing Company, New York, 1992, p. 590. ISBN: 0-02-396841-9.
- [75] T. Subba Rao. "The fitting of non-stationary time-series models with time-dependent parameters". In: *Journal of the Royal Statistical Society. Series B (Methodological)* 32(2).2 (1970), pp. 312–322. ISSN: 00359246.
- [76] A.E. Robinson. "Predictive decomposition of time series with applications to seismic exploration". PhD thesis. Massachusetts Institute of Technology, Dept. of Geology, pp. 256, 1954.
- [77] B.H. Russell. *Introduction to Seismic Inversion Methods*. Society of Exploration Geophysics, 1988, p. 172. ISBN: 9780931830655.
- [78] B.H. Russell and J. Hedlin. "Extended Poroelastic Impedance". In: *Geophysics* 84.2 (2019), N1–N14. DOI: [10.1190/GE02018-0311.1](https://doi.org/10.1190/GE02018-0311.1).

- [79] M.D. Sacchi. "Reweighting strategies in seismic deconvolution". In: *Geophysical Journal International* 129.3 (1997), pp. 651–656. DOI: [10.1111/j.1365-246X.1997.tb04500.x](https://doi.org/10.1111/j.1365-246X.1997.tb04500.x).
- [80] M.D. Sacchi and H. Kuehl. "FX ARMA filters". In: *SEG Technical Program Expanded Abstracts 2000* (2005), pp. 2092–2095. DOI: [10.1190/1.1815858](https://doi.org/10.1190/1.1815858).
- [81] M.D. Sacchi and SAIG. *SeismicLab*. Copyright (C) 2008. Distributed under the GNU version 3 or later.
- [82] M.D. Sacchi and T.J. Ulrych. "Recovery of near offsets using a F-X gap filling algorithm". In: *SEG Technical Program Expanded Abstracts 1997* (2005), pp. 1096–1099. DOI: [10.1190/1.1885580](https://doi.org/10.1190/1.1885580).
- [83] M.D. Sacchi, D.R. Velis, and A.H. Cominguez. "Minimum entropy deconvolution with frequency-domain constraints". In: *Geophysics* 59.6 (1994), pp. 938–945. DOI: [10.1190/1.1443653](https://doi.org/10.1190/1.1443653).
- [84] C. Sayers and S. Chopra. "Introduction to this special section: Seismic modeling". In: *The Leading Edge* 28.5 (2009), pp. 528–529. DOI: [10.1190/1.3124926](https://doi.org/10.1190/1.3124926).
- [85] L.E. Scales. *Introduction to non-linear optimization*. Springer-Verlag, New York, 1985. ISBN: 9781349177417.
- [86] R. Schmidt. "Multiple emitter location and signal parameter estimation". In: *IEEE Transactions on Antennas and Propagation* 34.3 (1986), pp. 276–280. ISSN: 0018-926X. DOI: [10.1109/TAP.1986.1143830](https://doi.org/10.1109/TAP.1986.1143830).
- [87] A. Schuster. "On the investigation of hidden periodicities with application to a supposed 26 day period of meteorological phenomena". In: *Terrestrial Magnetism* 3.1 (1898), pp. 13–41. DOI: [10.1029/TM003i001p00013](https://doi.org/10.1029/TM003i001p00013).
- [88] H. Schwetlick, T. Miyashita, and M. Schickert. "High resolution imaging with incomplete data". In: *Ultrasonic International 87 Conference Proceedings: London, UK, 6-9 July 1987*. Butterworth Scientific, 1987. ISBN: 0408023481.
- [89] R.E. Sheriff. "Factors affecting seismic amplitudes". In: *Geophysical Prospecting* 23.1 (1975), pp. 125–138. DOI: [10.1111/j.1365-2478.1975.tb00685.x](https://doi.org/10.1111/j.1365-2478.1975.tb00685.x).
- [90] R. Simm and M. Bacon. *Seismic Amplitude An Interpreter's Handbook*. Cambridge University Press, 2014, p. 283. ISBN: 9780511984501.
- [91] G.C. Smith and P.M. Gildow. "Weighted stacking for rock property estimation and detection of gas". In: *Geophysical Prospecting* 35.9 (1987), pp. 993–1014. ISSN: 1365-2478. DOI: [10.1111/j.1365-2478.1987.tb00856.x](https://doi.org/10.1111/j.1365-2478.1987.tb00856.x).
- [92] R. Soubaras. "Signal-preserving random noise attenuation by the f-x projection". In: *SEG Technical Program Expanded Abstracts 1994*. 2005, pp. 1576–1579. DOI: [10.1190/1.1822843](https://doi.org/10.1190/1.1822843).
- [93] R. Soubaras and Y. Lafet. "Variable-depth streamer acquisition: Broadband data for imaging and inversion". In: *SEG Technical Program Expanded Abstracts 2011* (2011), pp. 2364–2368. DOI: [10.1190/1.3627683](https://doi.org/10.1190/1.3627683).

- [94] S. Z. Sun et al. "Ultimate use of prestack seismic data: Integration of rock physics, amplitude-preserved processing, and elastic inversion". In: *The Leading Edge* 34.3 (2015), pp. 308–314. DOI: [10.1190/tle34030308.1](https://doi.org/10.1190/tle34030308.1).
- [95] A. Tarantola. *Inverse Problem Theory and Methods for Model Parameter Estimation*. Society for Industrial and Applied Mathematics, Philadelphia, 2005. 342 pp. ISBN: 978-0-89871-572-9.
- [96] A. Tarantola. "Inversion of seismic reflection data in the acoustic approximation". In: *Geophysics* 49.8 (1984), pp. 1259–1266. DOI: [10.1190/1.1441754](https://doi.org/10.1190/1.1441754).
- [97] J.B. Tary, R.H. Herrera, and M. Van der Baan. "Time-varying autoregressive model for spectral analysis of microseismic experiments and long-period volcanic events". In: *Geophysical Journal International* 196(1).1 (2014), pp. 600–611. DOI: [10.1093/gji/ggt400](https://doi.org/10.1093/gji/ggt400).
- [98] F. ten Kroode et al. "Broadband seismic data — The importance of low frequencies". In: *Geophysics* 78(2).2 (2013), WA3–WA14. DOI: [10.1190/geo2012-0294.1](https://doi.org/10.1190/geo2012-0294.1).
- [99] A.N. Tikhonov and V.Y. Arsenin. *Solutions of ill-posed problems*. Translated from the Russian, Scripta Series in Mathematics. Washington, D.C.: John Wiley & Sons, New York: V.H. Winston & Sons, 1977, pp. xiii+258.
- [100] Y. Tingyan. "Multistep Yule-Walker Estimation of Autoregressive Models". MA thesis. National University of Singapore, pp. 80, 2010.
- [101] G. Turner. "Subsurface radar propagation deconvolution". In: *Geophysics* 59.2 (1994), pp. 215–223. DOI: [10.1190/1.1443583](https://doi.org/10.1190/1.1443583).
- [102] T.J. Ulrych and T.N. Bishop. "Maximum entropy spectral analysis and autoregressive decomposition". In: *Reviews of Geophysics* 13.1 (1975), pp. 183–200. DOI: [10.1029/RG013i001p00183](https://doi.org/10.1029/RG013i001p00183).
- [103] T.J. Ulrych and R.W. Clayton. "Time series modelling and maximum entropy". In: *Physics of the Earth and Planetary Interiors* 12.2-3 (1976), pp. 188–200. ISSN: 00319201. DOI: [10.1016/0031-9201\(76\)90047-9](https://doi.org/10.1016/0031-9201(76)90047-9).
- [104] T.J. Ulrych and M.D. Sacchi. *Information-based Inversion and Processing with Applications*. Elsevier Science, Amsterdam, 2005, p. 436. ISBN: 9780080447216.
- [105] T.J. Ulrych, M.D. Sacchi, and A. Woodbury. "A Bayes Tour of Inversion: A tutorial". In: *Geophysics* 66.1 (2001), pp. 55–69. DOI: [10.1190/1.1444923](https://doi.org/10.1190/1.1444923).
- [106] T.J. Ulrych and C. Walker. "On a modified algorithm for the autoregressive recovery of the acoustic impedance". In: *Geophysics* 49.12 (1984), pp. 2190–2192. DOI: [10.1190/1.1441635](https://doi.org/10.1190/1.1441635).
- [107] C.P. Ursenbach and R.R. Stewart. "Two-term AVO inversion: Equivalences and new methods". In: *Geophysics* 73.6 (2008), pp. C31–C38. DOI: [10.1190/1.2978388](https://doi.org/10.1190/1.2978388).
- [108] B. Ursin. "Review of elastic and electromagnetic wave propagation in horizontally layered media". In: *Geophysics* 8.48 (1983), pp. 1063–1081. DOI: [10.1190/1.1441529](https://doi.org/10.1190/1.1441529).
- [109] M. Van der Baan and D. Pham. "Robust wavelet estimation and blind deconvolution of noisy surface seismics". In: *Geophysics* 73.5 (2008), pp. V37–V46. DOI: [10.1190/1.2965028](https://doi.org/10.1190/1.2965028).

- [110] P.C. Veeken and M. Da Silva. "Seismic inversion methods and some of their constraints". In: *First Break* 22.6 (2004), pp. 47–70. DOI: [10.3997/1365-2397.2004011](https://doi.org/10.3997/1365-2397.2004011).
- [111] P.C. Veeken et al. "Nonlinear multitrace genetic inversion applied on seismic data across the Shtokman field, offshore northern Russia". In: *Geophysics* 74.6 (2009), WCD49–WCD59. DOI: [10.1190/1.3223314](https://doi.org/10.1190/1.3223314).
- [112] J. Virieux and S. Operto. "An overview of full-waveform inversion in exploration geophysics". In: *Geophysics* 74.6 (2009), WCC1–WCC26. DOI: [10.1190/1.3238367](https://doi.org/10.1190/1.3238367).
- [113] J. Virieux et al. "6. An introduction to full waveform inversion". In: *Encyclopedia of Exploration Geophysics*. 2017, R1–1–R1–40. DOI: [10.1190/1.9781560803027.entry6](https://doi.org/10.1190/1.9781560803027.entry6).
- [114] A.T. Walden and J.W.J. Hosken. "An investigation on the spectral properties of primary reflection coefficients". In: *Geophysical Prospecting* 33.3 (1985), pp. 400–435. DOI: [10.1111/j.1365-2478.1985.tb00443.x](https://doi.org/10.1111/j.1365-2478.1985.tb00443.x).
- [115] C. Walker and T.J. Ulrych. "Autoregressive recovery of the acoustic impedance". In: *Geophysics* 48.10 (1983), pp. 1338–1350. DOI: [10.1190/1.1441414](https://doi.org/10.1190/1.1441414).
- [116] D. Wehner and M. Landrø. "Low-frequency acoustic signal created by rising air-gun bubble". In: *Geophysics* 82.6 (2017), P119–P128. DOI: [10.1190/geo2016-0674.1](https://doi.org/10.1190/geo2016-0674.1).
- [117] D. N. Whitcombe. "Elastic impedance normalization". In: *Geophysics* 67.1 (2002), pp. 60–62. DOI: [10.1190/1.1451331](https://doi.org/10.1190/1.1451331).
- [118] R.A. Wiggins. "Minimum entropy deconvolution". In: *Geoexploration* 16.1 (1978), pp. 21–35. ISSN: 0016-7142. DOI: [https://doi.org/10.1016/0016-7142\(78\)90005-4](https://doi.org/10.1016/0016-7142(78)90005-4).
- [119] R. Wu, J. Luo, and B. Wu. "Seismic envelope inversion and modulation signal model". In: *Geophysics* 79.3 (2014), WA13–WA24. DOI: [10.1190/geo2013-0294.1](https://doi.org/10.1190/geo2013-0294.1).
- [120] O. Yilmaz. *Seismic Data Analysis*. Society of Exploration Geophysicists, Tulsa, 2001, p. 2065. ISBN: 978-1-56080-098-8/9.
- [121] G. Yu. "Offset-amplitude variation and controlled-amplitude processing". In: *Geophysics* 50.12 (1985), pp. 2697–2708. DOI: [10.1190/1.1441890](https://doi.org/10.1190/1.1441890).
- [122] C. Zala, I. Barrodale, and J. Kennedy. "High-resolution signal and noise field estimation using the L1 (Least Absolute Values) norm". In: *IEEE Journal of Oceanic Engineering* 12.1 (1987), pp. 253–264. ISSN: 0364-9059. DOI: [10.1109/JOE.1987.1145232](https://doi.org/10.1109/JOE.1987.1145232).
- [123] K. Zoeppritz. "Über Reflexion ad Durchgang seismischer wellen durch Unstetigkeitsflächen". In: *Göttinger* (1919), pp. 66–84.